# Light-matter Interactions in Semiconductors and Metals: From Nitride Optoelectronics to Quantum Plasmonics

Thesis by

Prineha Narang

In Partial Fulfillment of the Requirements

for the Degree of

Doctor of Philosophy


California Institute of Technology

Pasadena, California

2016

(Defended May 18, 2015)

To my loving grandparents.

# Abstract

This thesis puts forth a theory-directed approach coupled with spectroscopy aimed at the discovery and understanding of light-matter interactions in semiconductors and metals.

The first part of the thesis presents the discovery and development of Zn-IV nitride materials. The commercial prominence in the optoelectronics industry of tunable semiconductor alloy materials based on nitride semiconductor devices, specifically InGaN, motivates the search for earth-abundant alternatives for use in efficient, high-quality optoelectronic devices. II-IV-$N_2$ compounds, which are closely related to the wurtzite-structured III-N semiconductors, have similar electronic and optical properties to InGaN namely direct band gaps, high quantum efficiencies and large optical absorption coefficients. The choice of different group II and group IV elements provides chemical diversity that can be exploited to tune the structural and electronic properties through the series of alloys. The first theoretical and experimental investigation of the $ZnSn_xGe_{1-x}N_2$ series as a replacement for III-nitrides is discussed here.

The second half of the thesis shows $ab-initio$ calculations for surface plasmons and plasmonic hot carrier dynamics. Surface plasmons, electromagnetic modes confined to the surface of a conductor-dielectric interface, have sparked renewed interest because of their quantum nature and their broad range of applications. The decay of surface plasmons is usually a detriment in the field of plasmonics, but the possibility to capture the energy normally lost to heat would open new opportunities in photon sensors, energy conversion devices and switching. A theoretical understanding of plasmon-driven hot carrier generation and relaxation dynamics in the ultrafast regime is presented here. Additionally calculations for plasmon-mediated upconversion as well as an energy-dependent transport model for these non-equilibrium carriers are shown.

Finally, this thesis gives an outlook on the potential of non-equilibrium phenomena in metals and semiconductors for future light-based technologies.

# List of Publications

## Published

1. Prineha Narang, Shiyou Chen, Naomi C. Coronel, Sheraz Gul, Junko Yano, Lin-Wang Wang, Nathan S. Lewis, and Harry A. Atwater, "Band Gap Tunability in Zn(Sn,Ge)$N_2$ Semiconductor Alloys" *Advanced Materials*, **2013**

2. Shiyou Chen, Prineha Narang, Harry A. Atwater, and Lin-Wang Wang, "Phase Stability and Defect Physics of a Ternary $ZnSnN_2$ Semiconductor: First Principles Insights" *Advanced Materials*, **2014**

3. Andrew J. Leenheer, Prineha Narang, Nathan S. Lewis, and Harry A. Atwater, "Solar Energy Conversion via Hot Electron Internal Photoemission in Metallic Nanostructures: Efficiency Estimates", *Journal of Applied Physics*, **2014**

4. Ravishankar Sundararaman*, Prineha Narang*, Adam S. Jermyn*,William A. Goddard III, and Harry A. Atwater, "Theoretical predictions for hot carrier generation from surface plasmon decay", *Nature Communications*, **2014**

5. Ana Brown, Ravishankar Sundararaman, Prineha Narang, William A. Goddard III, and Harry A. Atwater, "Non-Radiative Plasmon Decay and Hot Carrier Dynamics: Effects of Phonons, Surfaces and Geometry", *ACS Nano*, **2015**

6. Zeng-Hua Cai, Prineha Narang, Harry A. Atwater, Shiyou Chen, Chun-Gang Duan, Zi-Qiang Zhu, and Jun-Hao Chu, "Cation-Mutation Design of Quaternary Nitride Semiconductors Lattice-Matched to GaN", *Chemistry of Materials*, **2015**

7. Prineha Narang, Ravishankar Sundararaman and Harry A. Atwater, "Plasmonic hot carrier dynamics in solid-state and chemical systems for energy conversion", *Nanophotonics*, **2016** (Invited Review Article)

8. Ana M Brown, Ravishankar Sundararaman, Prineha Narang, William A Goddard III, and Harry A. Atwater, "*Ab initio* phonon coupling and optical response of hot electrons in plasmonic metals", arXiv preprint arXiv:1602.00625, **2016**

## Submitted

1. Prineha Narang, Sheraz Gul, Shiyou Chen, Lin-Wang Wang, Junko Yano, Nathan S. Lewis, and Harry A. Atwater, "Electronic Structure Studies of Zn-IV Nitrides Probed via X-ray Spectroscopy", **(2015)**

2. Prineha Narang, Ravishankar Sundararaman, Adam S. Jermyn, William A. Goddard III, and Harry A. Atwater, "Multiplasmon and nonlinear processes in plasmon decays", **(2015)**

3. Adam S. Jermyn, Prineha Narang, Ravishankar Sundararaman, William A. Goddard III, and Harry A. Atwater, "Transport and non-equilibrium behavior of plasmonic hot carriers", **(2015)**

# List of Figures

# List of Tables

# Contents

# 1

# Light-based Technologies and Materials Innovation

*A great deal of my work is just playing with equations and seeing what they give.*

– Paul A.M. Dirac

## 1.1 Introduction

On 20 December 2013, The United Nations (UN) General Assembly 68th Session proclaimed 2015 as the International Year of Light and Light-based Technologies (IYL 2015). This thesis introduction, written in 2015, presents a good opportunity to reflect on the current and future impact of light-based technologies and the role of physics in guiding that impact. For example, when we think of light and energy there are two approaches that come to mind: the here and now technologies (Si-based photovoltaics, solar thermal) and the "around the corner", high-risk, high-reward directions awaiting further development. A common link between both approaches is materials innovation and introducing new physics of light-matter interactions.

## 1.2 Discovery of new materials: Predictive materials physics

In many ways, the light-based technologies technologies in use today are limited by the performance of materials. This motivates the discovery of new materials, exploring materials physics of existing

materials and exploiting new device concepts.

Advanced materials share a common attribute: They are complex. Therefore achieving required performance depends on exploiting the many degrees of freedom of materials development including (but not limited to) multiple chemical components, nanoscale architectures, and tailored electronic structures. This introduces enormous complexity in the discovery process, complexity that must be understood and managed. A theory bias here would argue that we do not have the time or resources to explore all the options experimentally. However, our current computational methods confer upon us predictive power to accelerate discovery and innovation in materials.

During the past decade, computer simulations based on a quantum-mechanical description of the interactions between electrons and atomic nuclei have had an increasingly important impact on materials science, not only in fundamental understanding but also with a strong emphasis toward materials design for future technologies. While the current theory tools are not perfect, they do provide sufficient information for theory-directed design of new materials and new materials physics.

In addition to the computational design of materials for solar cells, artificial photosynthesis, and photochemical pathways to fuels, the need to computationally predict and optimize the light-matter interactions in materials is general and relevant to several light-based technologies including:

- Optical circuits
- Displays
- Solid-state lighting
- New light sources

A further link between established and to-be-developed technologies is that any new approaches must to some extent be integrable with dominant pervasive technologies and processes. This raises issues such as CMOS compatability and considerations of growth mechanisms, and on a more fundamental level the importance of both interface and volume effects in any new materials. This is particularly pertinent for nanostructured materials due to their increased surface-to-volume ratio. Hence, an adequate description of the physics occurring at interfaces of any new optoelectronic material must be taken into account in materials design and development from the start.

In many cases, a single theory method or approach may not be enough. A strategy of multiscale simulations must be used to translate the results of atomistic calculations to real-world scales. Some aspects of this thesis (especially the chapters on *ab initio* plasmonics) illustrate the need and use of multiscale theory.

## 1.3 Materials physics for energy

Solar technologies, whether photovoltaic or solar-fuel based, are ultimately limited by the efficiency of the light absorber. One of the primary goals of this thesis has been to investigate new light capture and conversion strategies through materials discovery. Artificial photosynthesis imposes unique demands on the light absorbers, relative to conventional photovoltaics. In artificial photosynthetic devices, either a single material, or two absorbers arranged in a tandem cell format (and current-matched spectrally), must at minimum provide the thermodynamically required voltage of 1.23 V to split water, and must provide comparable voltages to reduce $CO_2$ to methanol or other fuel. However, very few Earth-abundant materials have been identified that have band-gaps in the 1.5-2.2 eV range and satisfy the requirements for photoabsorbers in a solar fuels device. This presents a unique opportunity for exploring new materials physics especially in context of wide bandgap semiconductors. Optoelectronic properties and relaxation dynamics of these wide bandgap semiconductors would find applications beyond artificial photosynthesis in solid state lighting and photovoltaics.

## 1.4 High-throughput theory

As shown in recent work by Ceder, Jacobsen, Norskov, and others, it is now possible to scan hundreds of thousands of possible combinations of elements across the entire periodic table, suggesting many new materials solutions that far exceed the traditional intuition of experts in these fields. Even incomplete and low-level theories have suggested novel combinations of materials for new energy technologies. In principle, finding the best solution to solar harvesting and other issues related to composition-dependent property optimization can now be accomplished using this approach. Experimental synthesis and screening efforts to match the throughput of such computational approaches are underway within the Joint Center for Artificial Photosynthesis and within other

groups. The challenges associated with high-throughput theory (and to some extent experiments) are picking the "level of theory" commensurate with the complexity of the material and the property being screened for.

## 1.5 Optical phenomena in metals: Plasmonics

Prominent materials for photonic and optoelectronic components operating in the visible and near-infrared part of the electromagnetic spectrum comprise metals and semiconductors. Metals such as gold, silver, aluminium and copper are traditionally not materials of choice, due to their substantial absorption losses caused both by intraband and interband transitions. However, metals do provide a unique opportunity for photonics in this part of the spectrum, namely the existence of highly confined surface waves at interfaces with dielectrics. Here, the electromagnetic field can, under appropriate conditions, couple to the conduction electron plasma, setting up a hybrid mode, termed surface plasmon. For extended interfaces, propagating modes with mode areas below the diffraction limit are possible (surface plasmon polaritons), whereas metallic nanostructures act as optical nano resonators with minute sub-diffraction-limit mode volumes (localized surface plasmons).

The last two decades have seen an explosion of interest in surface plasmons, and a distinct research area of photonics, termed plasmonics, has emerged. This resurgence of interest in metal optics was to great extend facilitated by rapid advances in nano fabrication, near-field optical detection techniques, and computational modelling techniques taking the dispersion of the metal into account.

The high mode confinement that surface plasmons offer is made possible by a substantial penetration of the electric field into the metal itself, increasing with frequency until the surface plasma frequency is approached. This leads to unavoidable absorption losses and hence to a trade-off between localization and loss, which has hampered widespread applications of plasmonic waveguides and nano resonators for applications in integrated photonics. However, over the past few years it has been recognized that the optical losses also provide unique opportunities: Firstly, short dephasing times of only a couple of femtoseconds allow, under appropriate circumstances, for substantial emission enhancement of nearby (low internal quantum efficiency) nanoemitters. Secondly, decay of surface plasmons via absorption creates electron/hole pairs, and if these hot carriers can be harvested before thermalisation applications in hot carrier photodetector, catalysis, and nano chemistry seem

possible.

## 1.6 Optoelectronics and Nanophotonics

The potential for an order of magnitude improvement in size reduction of optoelectronic devices facilitated by plasmonic sub-diffraction-limit light confinement has intrigued researchers over the last decade. This directly addresses both the size mismatch between current electronic and photonic components, and furthermore promises substantial increases in modulation/switching speed, and potentially also lower energy consumption. Yet as described in the previous section, the unavoidable optical loss inherent in plasmonic light localization has to great extent hindered technological adoption of this approach. Since the physical limitations and parameter space for localisation and loss in plasmonic waveguides and nanostructures are well understood, focus has shifted to work on the underlying plasmonic materials for further improvements in performance. On the one hand, for the dominant plasmonic materials gold and silver, a substantial amount of research effort has been put into achieving higher crystallinity and hence less domain- and surface-induced optical losses. Examples include self-assembled-monolayer-assisted thin film growth for smoother films or back-etching of silicon in silicon/noble metal multilayers in order to expose an essentially single-crystal surface layer. At the same time, there is an active search for new plasmonic materials particularly in the near-infrared part of the spectrum underway. Here, materials with improved temperature stability such as TiN are attractive for applications such as Heat-assisted Magnetic Recording (HAMR), and also from the viewpoint of CMOS compatibility. Other candidate materials for applications in the near-to-mid-infrared are highly doped zinc oxides or perovskite-based ferroelectrics.

Apart from the physical properties plasmonic materials in isolation, it is also necessary to gain understanding and control over the materials physics at interfaces, particularly if both photonic and electronic phenomena associated with highly concentrated optical fields are to be exploited. Examples include plasmon-enhanced carrier transfer in Schottky-type photodetectors, or metallic nanostructures coated with molecular overlayers for catalytic applications. It is in all these areas that improvements in materials deposition and multilayer assembly go hand-in-hand with predictive theoretical studies enriching both our understanding of the underlying physics, and guiding further improvements. The employed methods necessarily are inherently quantum in nature, in contrast to the mainly classical modelling of plasmonic devices solely exploiting optical effects, which is firmly

based on the macroscopic Maxwell's equations, in most cases.

## 1.7 Contents of this thesis

The underlying theme of this thesis is exploring light-matter interactions, from a joint theory and experimental standpoint, in the context of high-risk, high-reward optoelectronic and nanophotonic technologies. This work is motivated in part by the materials-based challenges in current devices and in part by the search for new phenomena to enable novel optoelectronic and nanophotonic devices.

First part of the thesis presents the work my collaborators and I have done on Zn-IV nitrides, an example of theory-directed functional materials design. The second half of the thesis presents our work on *ab initio* calculations for plasmon decays and dynamics of hot carriers with a focus on understanding optical phemomena in metals. The chapters are organized as follows:

- In Chapter 2, theory and calculations to understand the stability and defect behavior of $ZnSnN_2$ are presented in context of Zn-IV nitride optoelectronics. The very small formation enthalpy of $ZnSnN_2$ and the donor defects in this semiconductor, with potential photovoltaic and solid state lighting applications, are discussed in detail.

- In Chapter 3, first-principles calculations as well as the synthesis and optoelectronic and spectroscopic characterization of a series of direct band-gap $Zn(Sn,Ge)N_2$ semiconductor alloys are presented.

- In Chapter 4, a theoretical evaluation of the energy-conversion efficiency of systems that rely on internal photoemission processes at metal-semiconductor Schottky-barrier diodes is discussed in addition to the drawbacks of such an approach to plasmon decays. This chapter sets the stage for the last chapters of this thesis.

- In Chapter 5, 'Theoretical predictions for hot carrier generation from surface plasmon decay in the interband limit', we present predictions for the prompt distributions of excited 'hot' electrons and holes generated by plasmon decay, prior to inelastic relaxation, using a quantized plasmon model with detailed electronic structure.

- In Chapter 6, we show the phonon-assisted and multi-plasmon contributions to plasmon decay and in general discuss optical processes in metals in the ultrafast regime.

- Finally, Chapter 7 summarizes the work done and future research directions for exploiting light-matter interactions both in the II-IV nitrides and in metals.

# 2

# Zn-IV Nitride Optoelectronics

*How wonderful that we have met with a paradox. Now we have some hope of making progress.*

– Niels Bohr

## 2.1 Chapter Overview:

$ZnSnN_2$ is an earth-abundant and visible-light-absorbing semiconductor, and has recently been synthesized, exhibiting an unexpectedly high electron concentration. Using first-principles calculations, we find that $ZnSnN_2$ has a very small formation enthalpy, so it is challenging to synthesize single-phase $ZnSnN_2$ without the coexistence of secondary phases. Based on the calculated formation energy of defects, we showed that $Sn_{Zn}$ (Sn on Zn antisite) is the dominant intrinsic defect with a high concentration, and $O_N$ (O on N antisite) is a possible dopant. Both defects are donors, and the high concentration of donor states form a defect band below the conduction band, making the material degenerately n-type, which explains the observed high electron concentration. The existence of the donor defect band does not induce any direct absorption of low-energy photons, so $ZnSnN_2$ is a degenerately doped metal-like semiconducting material with an optical bandgap around 2 eV, which is narrower than the bandgaps of conventional transparent conducting oxides.

## 2.2 Introduction

Direct bandgap, earth abundant semiconductors with $E_g$ around 1.5 eV are essential for both photovoltaic and solar to fuel (photocatalytic) energy conversion.[20, 6] Among the conventional semiconductors, such as element Si and Ge, binary III-V (III=B, Al, Ga, In; V=N, P, As, Sb) and II-VI (II=Zn, Cd; VI=O, S, Se, Te), only a limited number of candidates have suitable bandgaps in the range 1.0-2.0 eV.[12] This motivates the search for earth-abundant alternatives to current semiconductors for efficient, high-quality optoelectronics devices, photovoltaics and photocatalytic energy conversion. One methodology for the search is to study ternary and multi-ternary semiconductors with more elements and more flexible opto-electronic properties.

## 2.3 II-IV nitrides

Fifty years ago, the design of ternary and quaternary semiconductors through the cation mutation in binary II-VI and III-V semiconductors was proposed by Goodman and Pamplin:[5, 15, 1] (i) Through replacing two Zn atoms in ZnSe by one Cu and one In atom, ZnSe is mutated into ternary $CuInSe_2$, and if further replacing two In by Zn and Sn, $CuInSe_2$ is mutated into quaternary $Cu_2ZnSnSe_4$. Both $CuInSe_2$ and $Cu_2ZnSnSe_4$ are high-efficiency light-absorber semiconductors for thin film solar cells, which have been under intensive study during the past 30 years.[2, 25] (ii) Similarly through replacing two Ga in GaN by Zn and Sn, GaN can be mutated into $ZnSnN_2$, as shown in Fig. 2.1. In fact this cation mutation, a cross substitution, leads to a class of ternary II-IV-$V_2$ semiconductors with II=Zn, Cd, IV=Si, Ge, Sn and V=N, P, As, Sb, e.g., $ZnGeN_2$ and $ZnSnP_2$. II-IV-$N_2$ compounds are closely related to the wurtzite-structure III-N semiconductors, but have a mixed A-site composition. The choice of different group II and group IV elements provides chemical diversity that can be exploited to tune structural and electronic properties through the series.

Compared to the well studied $CuInSe_2$ (I-III-$VI_2$ class), the II-IV-$V_2$ semiconductors have not been studied extensively, e.g., the crystal structures and bandgaps of some II-IV-$V_2$ have been determined until quite recently.[16, 19] One possible reason for the slow progress in the study of II-IV-$V_2$ materials may be related to the difficulty in synthesis of electronic quality samples. With additional elements, it is more challenging to control the composition and to synthesize single-phase and stoichiometric ternary compounds.

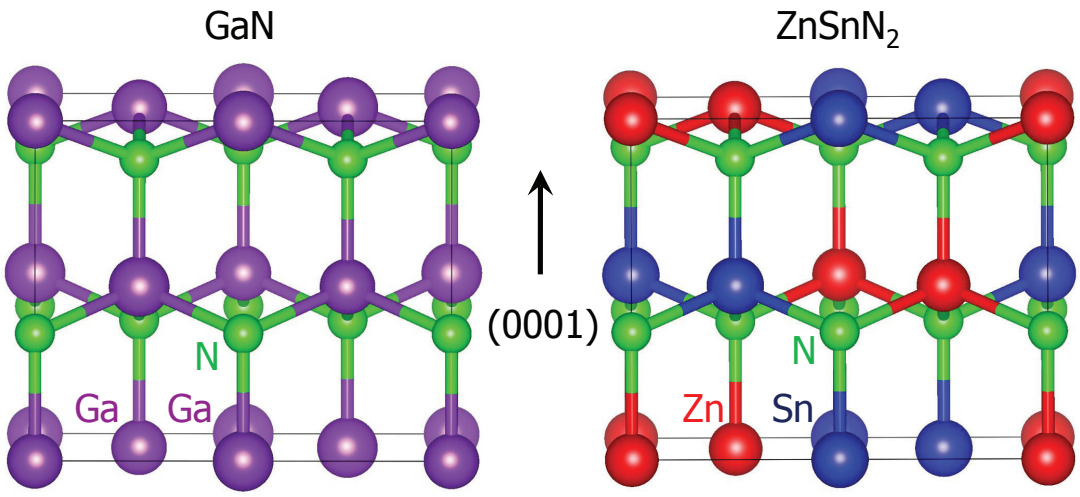


Figure 2.1: The crystal structure plot of wurtzite GaN and $ZnSnN_2$. Here GaN is plotted in a supercell with the same size as the primitive cell of $ZnSnN_2$ in the $Pna2_1$ symmetry. The $Pna2_1$ structure of $ZnSnN_2$ is equivalent to the wurtzite-kesterite $I_2$-II-IV-$VI_4$ structure through replacing I by Zn, II and IV by Sn, and VI by N.[3]

Using RF Magnetron Sputter Deposition, we recently synthesized a new II-IV-$V_2$ compound, $ZnSnN_2$, for which the optical measurements reveal a direct bandgap about 2.0 eV.[10] This successful synthesis of $ZnSnN_2$ indicates that a series of II-IV-$V_2$ semiconductors may be synthesized in the future and a rich space of the material properties may be explored for different functionalities.

## 2.4 Phase Stability and formation of $ZnSnN_2$

### 2.4.1 Phase Stability:

At the ground state, $ZnSnN_2$ crystalizes in a structure in the $Pna2_1$ symmetry with a 16-atom primitive cell,[16, 10] as shown in Fig. 2.1(b). To study its thermodynamic stability, we first calculated its formation energy, $\Delta H_f(ZnSnN_2)$, which is defined as the total energy change of the following reaction,

$$Zn(hcp) + Sn(diamond) + N_2(gas) \rightarrow ZnSnN_2 \tag{2.1}$$

where Zn is in the hexagonal-close-packed (HCP) structure, Sn is in the diamond structure and $N_2$ is at the gas molecule state. Using the hybrid functional with $\alpha$=0.31 (see the Experimental Section

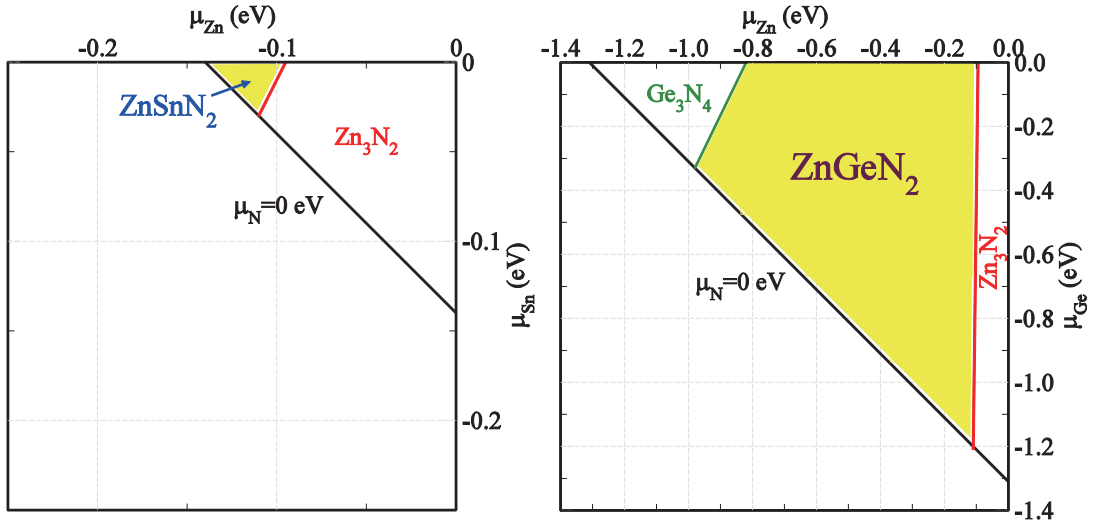


Figure 2.2: (a) and (b) The calculated chemical potential range (in yellow shadow) that stabilize single-phase $ZnSnN_2$ (a) and $ZnGeN_2$ (b). Outside the yellow region, different secondary phases as labeled will form.

for details), a very small $\Delta H_f(ZnSnN_2)$=-0.17 eV/f.u. (-3.92 kcal/mol) is found. Since the calculated formation energy of compound semiconductors are sensitive to the specific pseudopotentials and functionals,[4, 21] we also used a recently developed scheme which can predict the formation energy of compound semiconductors with a high accuracy (the test calculations on 55 ternary compounds show that the mean absolute error is only 0.048 eV/atom),[21] in order to evaluate the influence of the calculation methods. Using the new scheme, $\Delta H_f(ZnSnN_2)$=-0.14 eV/f.u., in good agreement with the value from the hybrid functional calculation. To compare with the experimental values, similar calculations are performed for other compounds, $\Delta H_f(Zn_3N_2)$=-0.33 eV/f.u. (experimental: -0.25 eV/f.u.[21]), $\Delta H_f(GaN)$=-1.43 eV/f.u. (experimental: -1.62 eV/f.u.[21]) Considering the small error with the new scheme, we believe the small formation energy of $ZnSnN_2$ has a high reliability. We notice that a large $\Delta H_f(ZnSnN_2)$=-2.32 eV/f.u. had been reported from the calculation using the linearized gradient muffin-tin orbital (LMTO) method,[17] which is in contrast with the present results using the plane-wave pseudopotential method and the new scheme, and the origin of the inconsistence is so far not clear.

Now we will discuss how the small formation energy influences the synthesis of $ZnSnN_2$. In the synthesis environment, the "richness" or partial pressure of the component elements can be

tuned, which can be quantitatively described by the chemical potentials of the component elements, $\mu_{Zn}$, $\mu_{Sn}$, $\mu_N$. $\mu_{Zn}$=0, $\mu_{Sn}$=0, $\mu_N$=0 are defined when Zn, Sn and N are so rich that their pure elemental phase like HCP Zn, diamond Sn, $N_2$ molecule can be formed. To avoid the formation of secondary phase such as the elemental phases and binary compound $Zn_3N_2$, the following conditions should be satisfied,

$$\begin{aligned} &\mu_{Zn} < 0,\ \mu_{Sn} < 0,\ \mu_N < 0 \\ &3\mu_{\mathrm{Zn}} + 2\mu_{\mathrm{N}} < \Delta \mathrm{H_f}(\mathrm{Zn_3N_2}) \end{aligned} \tag{2.2}$$

Under the thermodynamic equilibrium state that stabilizes $ZnSnN_2$, the following equation should also be satisfied,

$$\mu_{\mathrm{Zn}} + \mu_{\mathrm{Sn}} + 2\mu_{\mathrm{N}} = \Delta \mathrm{H_f}(\mathrm{ZnSnN_2}) \tag{2.3}$$

With all these requirements satisfied, $\mu_{Zn}$ and $\mu_{Sn}$ are limited in a certain region in the ($\mu_{Zn}$, $\mu_{Sn}$) plane as shown in Fig. 2.2(a), and $\mu_N$ depends on them according Eq. 2.3. As a result of the small $\Delta \mathrm{H_f}(\mathrm{ZnSnN_2})$, the stable region of $ZnSnN_2$ is quite narrow, and the tunable range of $\mu_{Zn}$ and $\mu_{Sn}$ is less than 0.05 eV. In contrast, another closely related II-IV-$V_2$ semiconductor $ZnGeN_2$ has a much larger formation energy (-1.31 eV/f.u.) and wider stable region in the ($\mu_{Zn}$, $\mu_{Ge}$) plane, as shown in Fig. 2.2(b). The obvious difference indicates that it is much more difficult to synthesize single-phase $ZnSnN_2$ than $ZnGeN_2$. Actually in the literature, $ZnGeN_2$ had been synthesized for decades while $ZnSnN_2$ was synthesized recently. The reason for the large difference may be related to the weaker Sn-N bond than Ge-N, which also causes the Sn-N compound $Sn_3N_4$ to have a positive formation energy (so not shown in Fig. 2.2, the experimental value is still unavailable) while $Ge_3N_4$ have a negative formation energy -0.98 eV/f.u. The much smaller formation energy of $ZnSnN_2$ than that of $ZnGeN_2$ is comparable with the situation between InN (-0.06 eV/f.u.) and GaN (-1.43 eV/f.u.).[21] As a result of narrow small stable region, the coexistence of secondary phases such as Zn, Sn metals and $Zn_3N_2$ is highly possible in the synthesized smaples. The coexisting Zn or Sn metal can be one possible origin of the high electron concentration. Based on these results, strategies to avoid the formation and exclude the coexistence of these secondary phases are critical to future applications and improvement of the $ZnSnN_2$ semiconductor.

## 2.5 $ZnSnN_2$ defect physics

Alternative to the formation of secondary phases, the formation of point defects in the $ZnSnN_2$ lattice is also possible, and influences its properties. Whether a point defect $\alpha$ in the charge state $q$ will form or not depends on its formation energy, $\Delta H(\alpha, q)$, which is a function of the chemical potential of elements and chemical potential of electrons (Fermi energy), as described by,

$$\Delta H(\alpha, q) = \Delta H_0(\alpha, q) + \sum_i n_i \mu_i + q E_F, \tag{2.4}$$

where $\Delta H_0(\alpha, q)$ is the formation energy when the chemical potentials $\mu_i$ of all elements $i$ ($i$=Zn, Sn, N) are zero and the Fermi energy $E_F$=0 ($E_F$ is referenced to the valence band maximum (VBM) eigenenergy of the host semiconductor), and can be calculated using the supercell model.[24, 22] $n_i$ is the number of atom $i$, and $q$ is the number of electrons exchanged between the semiconductor and the atmosphere in forming the defect.

The calculated formation energies of six possible defects in $ZnSnN_2$ is shown in Fig. 2.2(c), where the lowest-energy charge state is shown for each defect at a certain Fermi energy and the chemical potentials of the elements are set at the center of the stable region in Fig. 2.2(a). Two obvious characters can be identified: (i) the donor defects such as $Sn_{Zn}$ antisite (Sn substituing Zn), $V_N$ (N vacancy) and $Zn_i$ (Zn on the interstitial site surrounded by four N anions) have much lower formation energy than the acceptor defects, such as $Zn_{Sn}$, $V_{Zn}$ and $N_i$. The much lower formation energies of these donor defects determine the intrinsic n-type conductivity (self-doping) of $ZnSnN_2$. The values become negative when the Fermi energy approaches zero (VBM), i.e., they will form spontaneously in p-type samples, quenching mobile hole conductivity and pinning the Fermi energy close to the conduction band minimum (CBM) emergy, so the p-type doping is impossible based on this thermodynamic analysis. This can also be understood according to the low VBM energy of $ZnSnN_2$ (the GaN/$ZnSnN_2$ valence band offset calculation shows that the VBM of $ZnSnN_2$ is as low as that of GaN[13]) and the conventional doping limit rule, which states that a semiconductor is difficult to be doped p-type if the valence band is too low in energy.

(ii) $Sn_{Zn}$ antisite has the lowest formation energy through the whole Fermi energy range, so it is the dominant intrinsic defect of this ternary semiconductor. At the neutral charge state ($q$=0), the formation energy is only 0.13 eV, which corresponds to a population around $10^{20}$ cm$^{-3}$ at the room

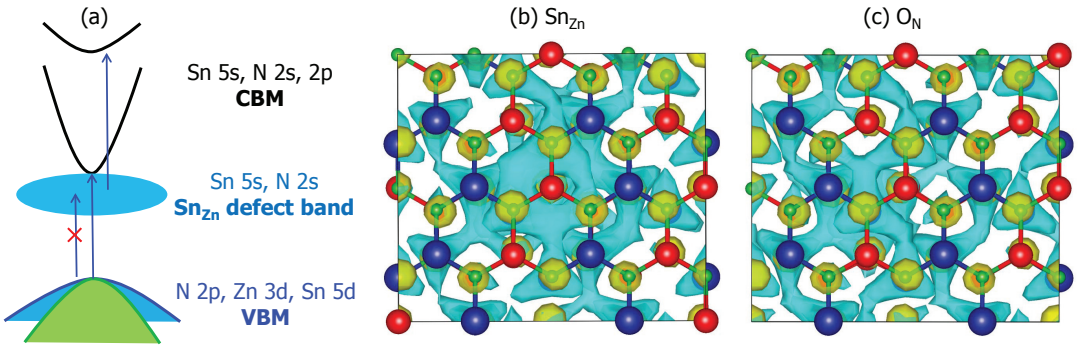


Figure 2.3: (a) Schematic plot of $ZnSnN_2$ band structure, with the $Sn_{Zn}$ defect band below the lowest conduction band. (b) Calculated band structure of $ZnSnN_2$ along high-symmetry lines in the Brillouin zone. (c) the wavefunction of $Sn_{Zn}$ donor state, (d) the wavefunction of $O_N$ donor state. For (c) and (d), the defect and dopant concentration is $5.6\times10^{20}$ cm$^{-3}$.

temperature, and a even higher population at higher growth temperature. As a donor defect, $Sn_{Zn}$ induces a donor level below the CBM state, which are occupied by two electrons (Sn has two more valence electrons than Zn). The calculated (0/2+) transition energy level of $Sn_{Zn}$ is 0.37 eV below CBM, i.e., when the Fermi energy is below this level, $Sn_{Zn}$ will be ionized and the two electrons on the donor level will be donated to the system. Since it has a much lower formation energy and thus much higher population than any other intrinsic defects, the Fermi energy of the $ZnSnN_2$ samples is pinned by $Sn_{Zn}$ to above the (0/2+) transition energy level.

Although the transition energy level of $Sn_{Zn}$ is not shallow, the corresponding donor state is not localized, as shown by the delocalized wave-function over the whole supercell in Fig. 2.3(c). This can be understood according to its component. The bandgap of $ZnSnN_2$ is opened between the valence band states composed of N-2$p$ +Zn-3$d$ orbitals and the conduction band states composed of Sn-5$s$+N-2s orbitals (see Fig. 2.3(a)).[13] The donor state of $Sn_{Zn}$ has the similar component to the lowest conduction band states, and is distributed on all Sn and N atoms in the whole supercell. Considering that the concentration of $Sn_{Zn}$ can be as high as $10^{20}$ cm$^{-3}$ (one defect among hundreds of atoms), the interaction between the nearby defects makes the donor states be continuous to form an occupied defect band, as shown schematically in Fig. 2.3(a). Our calculation with one $Sn_{Zn}$ defect in an 128-atom supercell and 2×2×2 k-point mesh shows that the $Sn_{Zn}$ defect band has a large dispersion (2 eV band width) and overlaps with the conduction bands. Because of the overlapping, the electrons in this defect band can be taken as the electron carriers (Note, this is insensitive to

the calculated (0/2+) level, and different from the situation when the defect concentration is low and the electrons on the donor states need to be ionized to the conduction band to become the electron carriers) and the system becomes almost metallic, which gives an explanation to the high concentration of electron carriers revealed by the Hall measurement.[10] Since the tunable chemical potential range of Zn and Sn is very narrow (less than 0.05 eV), it is limited to increase the $Sn_{Zn}$ formation energy by changing the chemical potential of elements, and thus it is difficult to suppress the electron concentration in $ZnSnN_2$ by changing the growth environment.

With the possible origin of the high electron concentration attributed to high population of $Sn_{Zn}$ defects, we need to revisit the Burstein-Moss effect in $ZnSnN_2$ samples,[10] which means that when the free electrons fill the conduction bands, the absorption onset shifts to higher energy. However, in $ZnSnN_2$ the electrons are actually occupying the donor defect bands below the CBM, rather than filling the conduction band as shown schematically in Fig. 2.3(a), so the absorption onset of photons will not shift up significantly with the electron concentration, i.e., the high electron concentration produced by the $Sn_{Zn}$ defects in $ZnSnN_2$ does not result in obvious Burstein-Moss effect. On the other hand, possible absorption may also happen through the electron excitation from the occupied defect band to the higher-energy conduction band. However, both our calculated band structure (Fig. 2.3(b)) and previously calculated band structure using different functionals show that the second conduction band is more than 2.5 eV higher than the lowest conduction band,[16, 10] so there is no direct absorption of lower-energy photons. Based on this analysis, the bandgap (about 2.0 eV) revealed by optical measurements[10] should be close to the fundamental bandgap of the defect-free $ZnSnN_2$. Because of the coexistence of metal-like high electron concentration and the 2.0 eV absorption onset (bandgap), $ZnSnN_2$ can be taken as a new conducting material, which has a narrower bandgap than the conventional wide-gap transparent conducting oxides.[23]

In addition to the intrinsic defects, unintentional doping by extrinsic impurity atoms is also possible, e.g., the O impurity atom may exist in the lattice. The calculated formation energy of $O_N$ is shown in Fig. 2.2(c) when the oxygen chemical potential $\mu_O$=$\Delta H_f$(ZnO)-$\mu_{Zn}$=-3.43 eV, and the value can be decreased significantly as $\mu_O$ increases (the oxygen partial pressure increases). Therefore, a very low partial pressure of oxygen is required to suppress the formation of $O_N$ ansites,[9] otherwise, $O_N$ donors can also cause a high electron concentration. The (0/+) transition energy level of $O_N$ is 0.21 eV below CBM and the corresponding donor state is also delocalized over the whole supercell, as shown in Fig. 2.3(d), so the $O_N$ states can also form a defect band, similar to

the $Sn_{Zn}$ states. Therefore the above discussion about the donor defect band and optical transitions work also for the $O_N$ impurities.

## 2.6 Conclusions

In conclusion, we find that $ZnSnN_2$ has a very narrow stable region in the element chemical potential space, so its single-phase synthesis is a challenge. The study of defect properties shows that the semiconductor is intrinsically self-doped to n-type by high population of defects such as $Sn_{Zn}$ and $O_N$ impurities. The high population of these donor defects results in a high concentration of electron carriers, and make the system almost metallic, explaining the experimental observation. Since these electrons stay on the donor defect band below the CBM, they do not influence the onset of the optical absorption (optical bandgap). Therefore $ZnSnN_2$ can be regarded as a new material that combines a metallic conductivity with a direct semiconductor bandgap.

## 2.7 Computational details:

The structural relaxation and electronic structure calculations are performed within the density functional theory (DFT) formalism as implemented in the VASP code.[7] The frozen-core projector augmented-wave potentials[8] were employed with an energy cutoff of 400 eV for the plane wave basis set. A 6×6×6 Monkhorst-Pack k-point mesh is included in the Brillouin zone integration for the 16-atom primitive cell and single k-point is included for the 128-atom supercell, which is used for the simulation of defects. Test calculations with denser k-point mesh show the calculated results are well converged. For the exchange-correlation functional, we used the non-local hybrid functional (HSE[14]) in which a percentage (known as the mixing parameter $\alpha$) of the semi-local GGA exchange potential is replaced by screened Fock exchange. Here based on the similarity in the crystal and electronic structure between GaN and $ZnSnN_2$, the mixing parameter $\alpha$ is set to 0.31, following the previous calculation setup which predicts a bandgap of 3.5 eV for GaN, in good agreement with the experimental value.[11, 18] It predicts a direct bandgap of 1.84 eV for $ZnSnN_2$, close to the value from the optical measurement (2.0 eV).[10] We notice that there are contradictive results in the calculated bandgaps from different level of approximations to the exchange-correlation functional,

from 1.42 eV (HSE with $\alpha$ =0.25[10]) to 2.02 eV (GW[16, 17]). To see if such approximations influence the conclusions of the current paper, test calculations are also performed with different $\alpha$ parameters ($\alpha$=0, 0.25), which show that the conclusions are independent of the specific functionals.

# Bibliography

Chen, Shiyou et al. In: *Phys. Rev. B* 79 (2009), p. 165211 (cit. on p. 9).

— "Crystal and electronic band structure of $Cu_2ZnSnX_4$ (X = S and Se) photovoltaic absorbers: First-principles insights". In: *Appl. Phys. Lett.* 94 (2009), p. 041903 (cit. on p. 9).

Chen, Shiyou et al. "Wurtzite-derived polytypes of kesterite and stannite quaternary chalcogenide semiconductors". In: *Phys. Rev. B* 82 (2010), p. 195203 (cit. on p. 10).

Fuchs, M. et al. "Cohesive properties of group-III nitrides: A comparative study of all-electron and pseudopotential calculations using the generalized gradient approximation". In: *Phys. Rev. B* 65 (24 2002), p. 245212 (cit. on p. 11).

Goodman, C. H. L. "The prediction of semiconductor properties in inorganic compounds". In: *J. Phys. Chem. Solids* 6 (1958), p. 305 (cit. on p. 9).

Gratzel, M. "Photoelectrochemical cells". In: *Nature* 414.6861 (2001), p. 338 (cit. on p. 9).

Kresse, G. and J. Furthmueller. In: *Phys. Rev. B* 54 (1996), p. 11169 (cit. on p. 16).

Kresse, G. and D. Joubert. In: *Phys. Rev. B* 59 (1999), p. 1758 (cit. on p. 16).

Kuwabara, Akihide. "Theoretical investigation to thermal equilibrium concentration of point defect through first-principles calculation". In: *Science and Technology of Advanced Materials* 8.6 (2007), p. 519 (cit. on p. 15).

Lahourcade, Lise et al. "Structural and Optoelectronic Characterization of RF Sputtered ZnSnN2". In: *Advanced Materials* 25 (2013), pp. 2562–2566 (cit. on pp. 10, 15–17).

Lyons, J. L., A. Janotti, and C. G. Van de Walle. "Carbon impurities and the yellow luminescence in GaN". In: *Appl. Phys. Lett.* 97 (2010), p. 152108 (cit. on p. 16).

Madelung, O. M. *Semiconductors: Data Handbook*. 3rd. Berlin: Springer, 2004 (cit. on p. 9).

Narang, P. et al. "Quasiparticle band structure of Zn-IV-N-2 compounds". In: *Un Published* (2013) (cit. on pp. 13, 14).

Paier, J. et al. “Screened hybrid density functionals applied to solids”. In: *J. Chem. Phys.* 124.15 (2006), p. 154709 (cit. on p. 16).

Pamplin, B. R. “deriving new semi. compounds by structural analogy”. In: *J. Phys. Chem. Solids* 25 (1964), p. 675 (cit. on p. 9).

Punya, Atchara, Walter R. L. Lambrecht, and Mark van Schilfgaarde. “Quasiparticle band structure of Zn-IV-N-2 compounds”. In: *Phys. Rev. B* 84 (2011), p. 165204 (cit. on pp. 9, 10, 15, 17).

Punya, Atchara, Tula R. Paudel, and Walter R. L. Lambrecht. “Electronic and lattice dynamical properties of II-IV-N2 semiconductors”. In: *physica status solidi (c)* 8.7-8 (2011), pp. 2492–2499. ISSN: 1610-1642 (cit. on pp. 11, 17).

Qimin Yan et al. “Role of nitrogen vacancies in the luminescence of Mg-doped GaN”. In: *Appl. Phys. Lett.* (2012), p. 142110 (cit. on p. 16).

Scanlon, David O. and Aron Walsh. “Bandgap engineering of ZnSnP2 for high-efficiency solar cells”. In: *Appl. Phys. Lett.* 100 (2012), p. 251911 (cit. on p. 9).

Shockley, W. and H. J. Queisser. In: *J. Appl. Phys.* 32 (1961), p. 510 (cit. on p. 9).

Stevanovi ć, Vladan et al. “Correcting density functional theory for accurate predictions of compound enthalpies of formation: Fitted elemental-phase reference energies”. In: *Phys. Rev. B* 85 (11 2012), p. 115104 (cit. on pp. 11, 12).

Van de Walle, C. G. and Neugebauer J. In: *J. Appl. Phys.* 95 (2004), p. 3851 (cit. on p. 13).

Walsh, Aron et al. “Nature of the Band Gap of $In_2O_3$ Revealed by First-Principles Calculations and X-Ray Spectroscopy”. In: *Phys. Rev. Lett.* 100 (16 2008), p. 167402 (cit. on p. 15).

Wei, Su-Huai. In: *Comp. Mater. Sci.* 30 (2004), p. 337 (cit. on p. 13).

Zhang, S. B. et al. “Defect physics of the CuInSe2 chalcopyrite semiconductor”. In: *Phys. Rev. B* 57.16 (1998), p. 9642 (cit. on p. 9).

# 3

# $Zn(Sn,Ge)N_2$ Semiconductor Alloys

*I think nature's imagination is so much greater than man's,*
*she's never going to let us relax.*

– R. P. Feynman

### 3.0.1 Chapter Overview

This chapter describes the first-principles calculations as well as the synthesis and optoelectronic and spectroscopic characterization of a series of direct band-gap semiconductor alloys, $ZnSn_(1-x)Ge_xN_2$. These materials have a crystal structure and electronic structure similar to that of the InGaN alloys. $ZnSn_(1-x)Ge_xN_2$ alloys with various compositions were synthesized, with the elements fully miscible across the composition range without evidence for phase separation, as shown by X-ray diffraction and X-ray absorption fine-structure spectroscopy. The optical band gaps of the $ZnSn_(1-x)Ge_xN_2$ alloys range from $\sim 2.0$ to $\sim 3.1$ eV, and nitrogen $K$-edge X-ray absorption and emission spectroscopy showed that the conduction-band minimum shifted to higher energy with the addition of Ge, while the valence-band maximum remained at constant energy. Relatively small values were measured (0.29 eV) and calculated (0.67 eV) for the band-bowing parameters for the band gaps of the $ZnSn_(1-x)Ge_xN_2$ alloys, indicating that the band gaps of the $ZnSn_(1-x)Ge_xN_2$ alloy series could be tuned almost monotonically by control of the Sn/Ge ratio.

## 3.1 Introduction

InGaN-based semiconductor materials have attained commercial prominence in optoelectronics in part due to the large range in electronic band gaps facilitated by tuning the In/Ga ratio of InGaN alloys.[14, 15] The experimentally determined fundamental gap of GaN is 3.51 eV[14], while that of InN is 0.69 eV.[7, 10], Hence, InGaN alloys provide a simple class of semiconductors whose fundamental band gap can, in principle, span the entire visible spectrum and beyond. However the InGaN semiconductors are difficult to synthesize as homogeneous alloys, without phase separation, across the full range of In/Ga ratios. This behavior has limited the compositional range for which InGaN typically exhibits high radiative efficiency, in turn limiting the range of light-emitting, photovoltaic or photoelectrochemical device applications of such materials. The large volume difference between InN and GaN[15] promotes clustering to relieve internal strains, and precludes the straightforward synthesis of high-quality crystals that have sufficiently high In concentrations to produce a band gap of the alloy in the green range of the color spectrum.[15] Additionally, the reliance on indium, with its limited economically viable sources, could potentially limit the large-scale incorporation of InGaN in solar energy-conversion applications. These factors motivate the search for alternatives to current III-nitride semiconductors for both optoelectronics and solar energy-conversion applications.

## 3.2 Tunability in Zn(Sn,Ge)$N_2$

The II-IV-$N_2$ compounds, closely related to the wurtzite-structured III-N semiconductors, have similar electronic and optical properties to InGaN, e.g. direct band gaps and large optical absorption coefficients.[9, 11, 5, 13] The choice of different group II and group IV elements provides chemical diversity that can be exploited to tune the structural and electronic properties through the series of alloys.

$ZnSnN_2$ ($ZnGeN_2$) can be considered as derived from binary GaN by the replacement of two Ga atoms by Zn+Sn (Zn+Ge) atoms.[2, 1] GaN is more stable in the wurtzite structure, therefore $ZnSnN_2$ and $ZnGeN_2$ can crystallize in the wurtzite-derived structure with two primitive cells, (i) the one with the $Pna2_1$ symmetry, shown in Fig 3.1(a(i)) (called wurtzite-chalcopyrite structure[2, 1] ) and (ii) the one with the $Pmc2_1$ symmetry (called wurtzite-CuAu structure[2, 1] , shown in

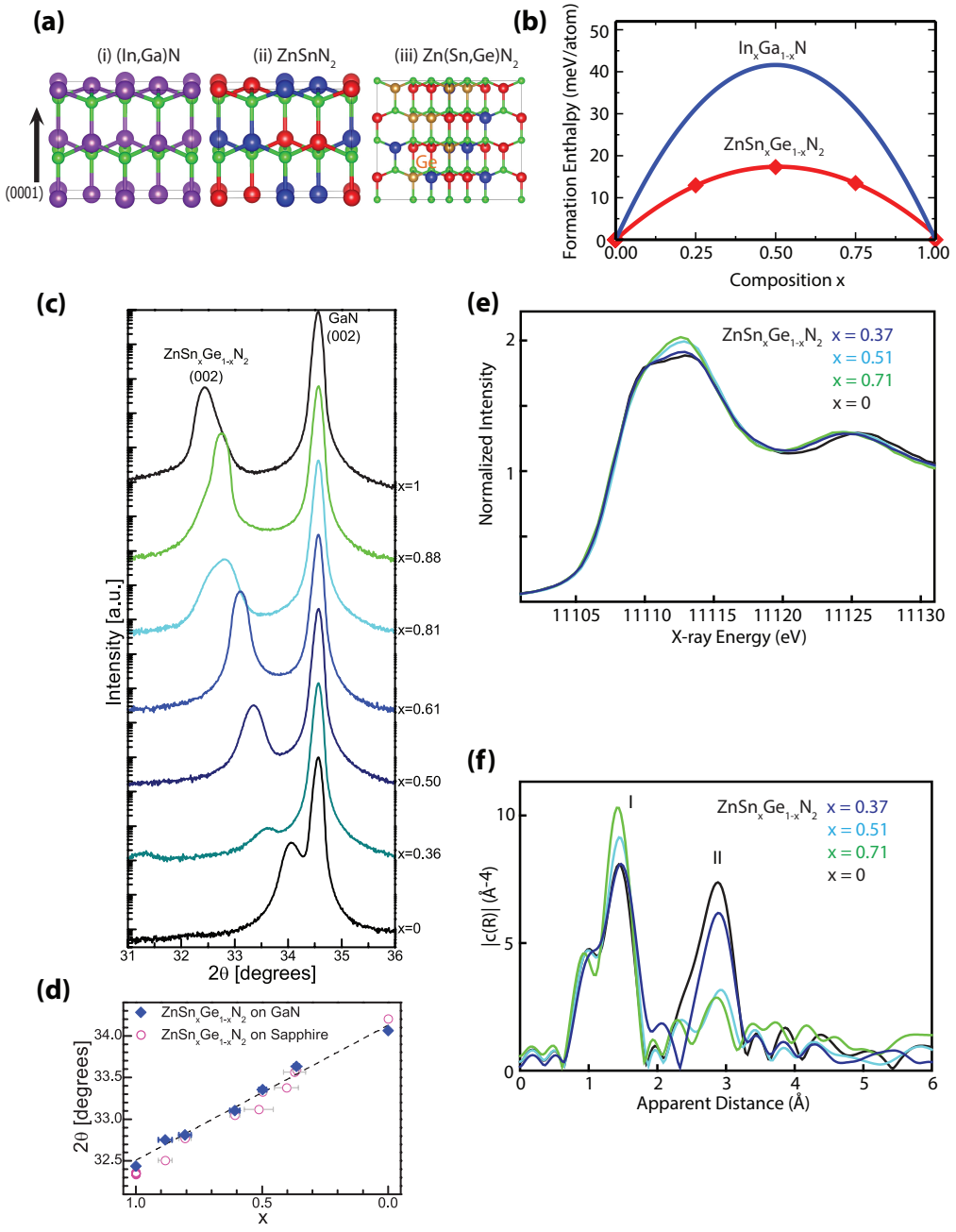


Figure 3.1: (a) The crystal structure of (i) a random $In_xGa_{(}1-x)N$ alloy, (ii) $ZnSnN_2$ ground-state structure with the $Pna2_1$ symmetry, and (iii) the special quasi-random structure of $ZnSn_0.5Ge_0.5N_2$. The structures can be derived from the GaN wurtzite structure by replacement of the Ga cations by different cations: (i) In, (ii) Zn and Sn, and (iii) Zn, Sn and Ge; The green, purple, red, blue and yellow balls show the N, Ga (In), Zn, Sn and Ge atoms in order. (b) The calculated formation enthalpies of $ZnSn_xGe_{(}1-x)N_2$ alloys with different compositions x (x = 0, 0.25, 0.5, 0.75 and 1). Sn and Ge atoms are randomly distributed on the Sn sites in the $ZnSnN_2$ structure with $Pna2_1$ symmetry. The red line shows the fit according to Equation **??**, with the interaction parameters $\Omega$ = 67 meV/atom, and the blue line shows the formation enthalpies of $In_xGa_{(}1-x)N$ alloys, with the interaction parameter $\Omega$ = 166 meV/ atom taken from Ref. [2] (c) XRD $\Theta$-$2\Theta$ scans around the (002) reflection for films with various compositions grown on *c*-plane GaN template substrates. For comparison, data points are also shown for films grown on sapphire (d) Linear relationship between the (002) peak position and the alloy composition. (e) Ge XANES and (f) FT EXAFS ($k^3$-weighted) spectra of $ZnGeN_2$ and $Zn(Ge,Sn)N_2$.

Fig 3.1(a(ii))). Other structures have larger primitive cells than these two structures and thus can be considered a mixing of these two structures, with intermediate properties.

Because our calculations, as well as previous calculations,[9, 13, 12] have shown that the wurtzite-chalcopyrite structure has a lower energy than the wurtzite-CuAu structure, our theoretical investigation of the $ZnSn_(1-x)Ge_xN_2$ alloys focused on the wurtzite-chalcopyrite structure, with Sn and Ge randomly distributed on the Sn/Ge sublattice. Calculations of disordered semiconductor alloys must realistically describe the random cation lattice site occupancy for the isovalent elements (Sn and Ge here). Hence we used the well-developed special-quasi-random structures (SQS[18, 17]) approach to describe the disordered occupation of Sn and Ge on cation sites. For a given supercell size, special quasi-random structures (SQS) have site occupations (the Sn/Ge sites in this chapter) optimized to best reproduce the structural correlation functions of a completely random alloy, so the calculated formation energy and the calculated band gaps should also be close to those of the random alloys. Fig 3.1(a(iii)) illustrates the SQS model having a composition x=0.5, for which the Sn and Ge were randomized on the 16 Sn/Ge cation sites. Detailed structural information of SQS are given in the computational details section.

Fig 3.1(b) shows the calculated formation enthalpy of the $ZnSn_xGe_(1-x)N_2$ and $In_(1-x)Ga_xN$ alloys, describing the solubility of mixing of Sn and Ge in their sublattice. The formation enthalpy of the alloys is given by:

$$\Delta H_f(x) = E(x) - (1-x)E(0) - xE(1) \tag{3.1}$$

where E(x) is the total energy of the alloy having the compositional parameter x, i.e., E(0) and E(1) are the total energies of $ZnSnN_2$ and $ZnGeN_2$ respectively. The values of E(x) were calculated using standard first-principles methods. The calculated formation enthalpies exhibited an upward bowing in the dependence on the composition, x, indicating that these materials are expected to prefer to phase separate at 0 K into $ZnSnN_2$ and $ZnGeN_2$. The calculated additional energy cost for mixing Sn and Ge cations is given by the calculated formation enthalpies.

To compare these quantities with the formation enthalpies of other alloys, the calculated formation enthalpies were fitted to Equation 3.2, to yield the interaction parameter, $\Omega$, of the Sn/Ge-mixed alloys:

$$\Delta H_f(x) = \Omega x(1-x) \tag{3.2}$$

The fit shown by the lines in Fig 3.1(b) indicated that the calculated data were in accord with the relationship of Equation 3.2. The interaction parameter was calculated to be 67 meV/atom (268 meV/mixed-atom). For comparison, Fig 3.1(b) also plots the calculated formation enthalpies of the $In_(1-x)Ga_xN$ alloy series using an interaction parameter of 166 meV/atom (332 meV/mixed-atom). 11 The smaller calculated interaction parameter of the $ZnSn_(1-x)Ge_xN_2$ alloys indicates that Sn and Ge are expected to be more easily mixed in the Sn/Ge sublattice than in the In/Ga sublattice of the $In_(1-x)Ga_xN$ alloys. Hence a higher compositional uniformity can be expected in the $ZnSn_(1-x)Ge_xN_2$ alloys relative to that of the $In_(1-x)Ga_xN$ alloys.

The theoretically predicted compositional uniformity of the $ZnSn_(1-x)Ge_xN_2$ alloys was in accord with the structural characterization data of the experimentally synthesized alloys. X-ray diffraction was used to characterize the long-range order of the materials, to thereby determine if the material was a continuous alloy or a mixture of different phases. The observation of a strong peak corresponding to the (002) reflection of $ZnSn_xGe_(1-x)N_2$, coupled with weak peaks or no peaks in any other crystallographic directions, indicated that the films were strongly textured, with the (001) planes oriented parallel to the surface of the substrate. The (002) peak positions for $ZnSnN_2$ and $ZnGeN_2$ were confirmed by calculations based on theoretical lattice parameters (a=6.70, b=5.81, c=5.42 Å for $ZnSnN_2$, and a=6.39, b=5.41, c=5.15 Å for $ZnGeN_2$), and the intermediate compositions of $ZnSn_xGe_(1-x)N_2$ are expected to have peaks with 2Θ positions in between those of $ZnSnN_2$ and $ZnGeN_2$. Fig 3.1(c) presents X-ray diffraction Θ-2Θ scans around the (002) reflection for films with various compositions grown on *c*-plane GaN template substrates. The (002) peak position increased steadily with increasing germanium content in the alloy series, indicating an apparent lack of phase separation in the material. Additionally, the 2Θ position of the (002) peak increased monotonically with increasing germanium content, implying that the unit cell continuously expanded and contracted as the composition was changed, which is consistent with the calculated volume change of the alloys with varied composition. Fig 3.1(d) further highlights the continuous nature of the alloying of the films, indicated by the linear relationship between the (002) peak position and the alloy composition. Data are shown from many samples with various compositions, with a linear fit of the data for films grown on GaN templates. For comparison, data points are also

shown for films grown on sapphire. The films grown on GaN were of higher crystalline quality than those grown on sapphire30 because the lattice mismatch between GaN and $ZnSn_xGe_(1-x)N_2$ is about half of the mismatch between sapphire and $ZnSn_xGe_(1-x)N_2$.

The observed compositional uniformity is in contrast to the behavior of the $In_xGa_(1-x)N$ alloys, in which the large lattice mismatch between InN and GaN causes the indium to segregate, resulting in phase separation and the consequent formation of distinct domains of InN and GaN in alloys with high indium content.[15] X-ray diffraction measurements for phase-separated $In_xGa_(1-x)N$ showed two separate peaks, representing the two different lattice parameters present in the material. In contrast, one prominent peak was observed for $ZnSn_xGe_(1-x)N_2$ in the $2\Theta$ range of the (002) reflection, and no peaks were observed at the $2\Theta$ positions of $ZnSnN_2$ or $ZnGeN_2$ for films with 0 $<$ x $<$ 1. The existence of a single (002) peak reinforces the conclusion that $ZnSn_xGe_(1-x)N_2$ is an alloy with continuous variable composition and is not a mixture of different phases. Hence this materials system should allow access to the entire range of band gap values by use of existing growth strategies.

Fig 3.1 (e)-(f) show the Ge X-ray absorption near-edge structure (XANES) and extended- edge X-ray absorption fine structure (EXAFS) spectra of the $Zn(Sn)GeN_2$ alloys as a function of changes in the Sn:Ge ratio. For comparison, the X-ray absorption spectrum of $ZnGeN_2$ is also displayed (Ge K-edge). Although the rising edge energy of Ge stayed constant as the Sn loading increased, the EXAFS spectra clearly showed the structural changes of the alloys. In Fig 3.1(f), the intensity of the first peak that corresponds to the Ge-N interactions increased when the Sn to Ge ratio was increased above 50 percent (Fig 3.1 d). Additionally, the intensity of the second peak, that contained contributions from Ge-Ge, Ge-Sn, and Zn-Ge interactions around 3.2 – 3.3 Å(note that the x-axis of Fig 3.1 f is an apparent distance, and it is 0.5Å shorter than the actual distances), decreased significantly. The EXAFS curve-fitting results are shown in the Appendix A. Figure A.1, with the fitting parameters summarized in Appendix A. For $ZnGeN_2$, the initial fitting parameters were taken from the crystal structure, and the coordination number (N) was fixed accordingly. The fitted result agrees well with the experimental data shown in Appendix **??**. For $ZnSn_xGe_(1-x)N_2$, a Ge-Sn path around 3.3 Å was included for the curve fitting, and the coordination numbers for the Ge-Ge and Ge-Sn interactions were varied during the fitting. As the fraction of Sn increased, the N number of Ge-Sn increased, while that of Ge-Ge decreased. However, the Debye-Waller factors ($\sigma^2$) of the Ge-Ge, Ge-Zn, and Ge-Sn interactions become large in the presence of Sn, as evidenced by

the weak peak intensity around the peak II region (Fig 3.1(f)). The data therefore indicate that a large distance heterogeneity around 3.3 Å was present in these samples, presumably due to the presence of Ge-Ge, Ge-Zn, and Ge-Sn interactions.

Spectroscopic ellipsometric measurements were used to probe the optical absorption properties of the alloys, particularly near the absorption onset of the materials. The absorption exhibited an obvious blue shift as the Ge composition increased (Fig 3.2a). For direct band-gap semiconductors, the value of the band gap can be estimated by linear extrapolation to the energy axis of a plot of the square of the absorption coefficient ($\alpha^2$) versus the photon energy. The fitted gaps are 2.0 eV for $ZnSnN_2$ [3, 9] and 3.1 eV for $ZnGeN_2$. These values are close to those measured previously for different samples, around 2.0 eV (2.0 eV, 1.7 eV, and 2.12-2.38 eV) for $ZnSnN_2$ and around 3.2-3.4 eV [4, 13, 12, 3, 5] for $ZnGeN_2$. As we can see, there is still uncertainty in the exact values of the gaps, but it is safe to say that the gap of $ZnSnN_2$ is around 2.0 eV and that of $ZnGeN_2$ is around 3.2 eV. Fig 3.2(b) shows the change in optical band gap as a function of composition, with the band gap ranging from 2.0 to 3.1 eV and thereby allowing access to the entire range of band gaps between $ZnSnN_2$ and $ZnGeN_2$, the two end-point compositions. For comparison, Fig 3.2(b) also presents the experimental band gap change for the $In_(1-x)Ga_xN$ alloys (cited from Ref. [15]). The band gap range spanned by the $ZnSn_(1-x)Ge_xN_2$ alloys (2.0-3.2 eV from the experiments and 1.84 to 3.89 eV from the calculations) is much narrower than that of the $In_(1-x)Ga_xN$ alloys (about 0.6-3.4 eV from experiments). This difference can primarily be related to the higher band gap of $ZnSnN_2$ relative to that of InN (replacement of two In in InN by Zn and Sn produces an increase of about 1.4 eV in the band gap).

The band gap of the alloy series clearly depended nearly linearly on the composition x, as evidenced by the bowing parameter b, defined as:

$$E_g(x) = xE_g(1) + (1-x)E_g(0) - bx(1-x) \tag{3.3}$$

A bowing parameter of b = 0.29 eV was determined from the measured band gaps of $ZnSn_(1-x)Ge_xN_2$, whereas a value of b = 0.67 eV was obtained from the calculated band gaps of the same alloy series (b = 0.3 eV was also predicted by Punya and Lambrecht for the x=0.5 alloy[12]), as shown in Fig 3.2(c). Despite an obvious difference, both b values are small, and are significantly smaller than b for the $In_(1-x)Ga_xN$ alloy series. The small value of b indicates that the $ZnSn_(1-x)Ge_xN_2$

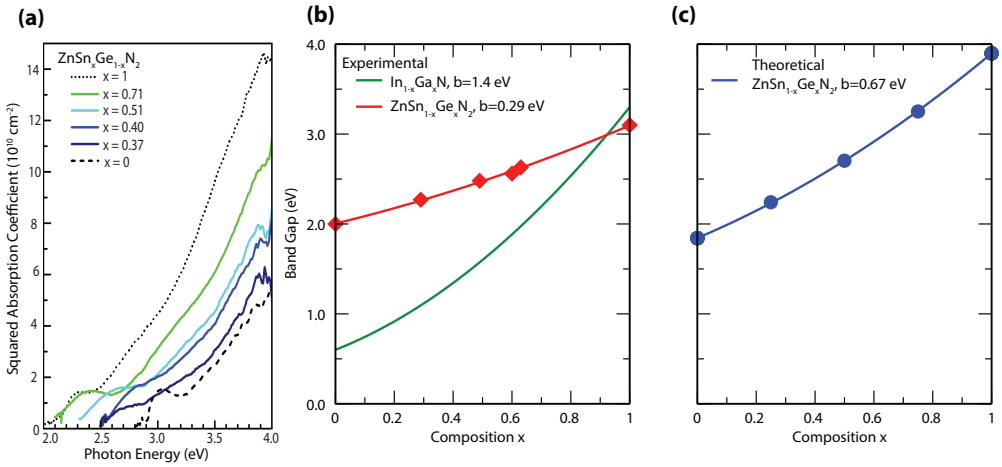


Figure 3.2: (a) Spectroscopic ellipsometry of $ZnSn_(1-x)Ge_xN_2$ alloys showing the tunability from 2-3.1 eV of the optical band gap, as a function of composition in the alloy series. The dependence of the band gap of the $ZnSn_(1-x)Ge_xN_2$ alloys and $In_(1-x)Ga_xN$ alloys on the composition parameter, x: (b) experimental data, and (c) calculated results. The filled diamonds and circles are taken from the experimental measurements and the alloy calculations respectively, and the lines show the fits according to Equation 3.3. The experimental data for $In_(1-x)Ga_xN$ are from Ref. [9]

alloy band gaps can be tuned almost linearly by control over the Sn/Ge composition.

Fig 3.3(a,b) presents the calculated band structures for the two end-point compounds, $ZnSnN_2$ and $ZnGeN_2$. The two band structures were similar in that both materials have direct band gaps. Additionally both materials have a lowest conduction band with a large dispersion, with the width of the band about 2 eV, while the highest valence bands are relatively flat in both cases. This behavior is consistent with the orbital component of the two bands, in that (i) the lowest conduction band is composed mainly of the antibonding state of the hybridization between Sn $5s$ (Ge $4s$) and N $2s$ orbitals, so this band is delocalized with a significant dispersion, and (ii) the highest valence bands are composed mainly of the N $2p$ states, with a weaker hybridization with Zn $3d$ states (because the Zn $3d$ eigenenergy is low and deep in the valence band, the hybridization is weaker, and the Sn $4d$ eigenenergy is much lower, so the hybridization is negligible). Hence the states are localized and have a small dispersion.

The primary difference between the band structure of $ZnSnN_2$ and $ZnGeN_2$ is in the value of the band gap of each system. Calculations using the hybrid functional (mixing parameter=0.31) yielded a band gap of 1.84 eV for $ZnSnN_2$, which is much smaller than the band gap of $ZnGeN_2$ (3.89 eV ). Because both compounds have the top part of their valence bands determined by the N $2p$ and Zn $3d$ states, the valence band offset should be small. This expectation is supported by the direct valence band offset calculations, and a valence band offset about 0.4 eV has been found.[12] The much smaller band gap of $ZnSnN_2$ compared to $ZnGeN_2$ is therefore derived from the much lower conduction-band minimum state, i.e., the large conduction-band offset between $ZnGeN_2$/$ZnSnN_2$. This behavior occurs because the conduction-band minimum state is the antibonding state of Sn $5s$ (Ge $4s$)+N $2s$ hybridization. In addition, (i) the Sn $5s$ orbital energy is much lower than Ge $4s$ orbital energy; and (ii) the Sn atom has much larger radius than Ge, so the Sn-N bond length is much larger than the Ge-N bond length, thus the Sn $5s$ + N $2s$ hybridization is weaker than the Ge $4s$ +N $2s$ hybridization, resulting in a lower energy antibonding state for $ZnSnN_2$ relative to $ZnGeN_2$.

Because the band-gap difference is about 1.6-2.0 eV and valence-band offset is only 0.4 eV, we estimate that the $ZnGeN_2$/$ZnSnN_2$ conduction-band offset is large, i.e., larger than 1.2 eV. When the Sn/Ge composition is changed in the $ZnSn_(1-x)Ge_xN_2$ alloys, the band gap change therefore results mainly from the shift in the position of the conduction band. Furthermore, because the band gap depends almost linearly on composition, the conduction-band edge should shift almost linearly

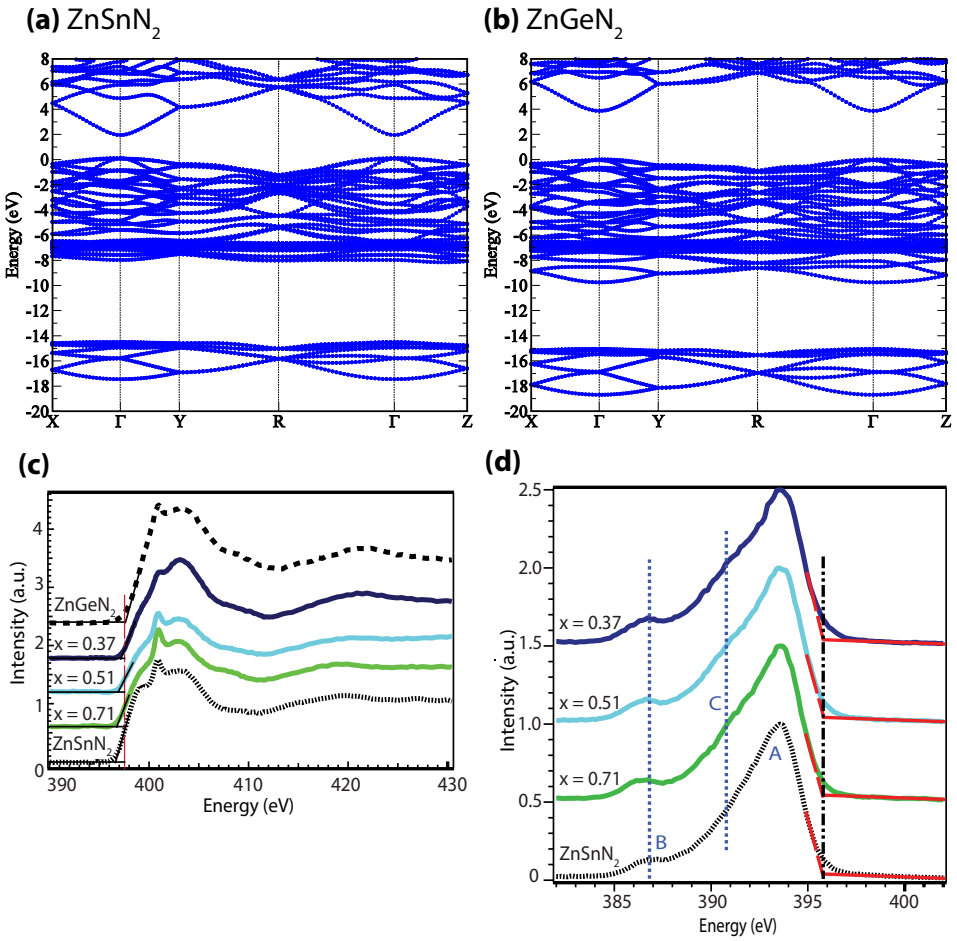


Figure 3.3: Calculated band structure of (a) $ZnSnN_2$ and (b) $ZnGeN_2$, along the high-symmetry lines of the Brillouin zone. (c) Nitrogen K-edge XANES spectra for samples with different Ge content as well as the end-point compositions, $ZnSnN_2$ and $ZnGeN_2$. The vertical line (red) indicates the evolution of the conduction-band minimum towards higher energies as a function of increasing Ge content. (d) Nitrogen K-edge X-ray emission spectra for samples with different Ge content. As indicated by the vertical line (black), little movement occurred in the valence-band maximum with varying Ge content.

with the composition parameter, x.

## 3.3 X-ray spectroscopy of Zn(Sn,Ge)$N_2$

The analysis described above was supported by X-ray spectroscopic data of the electronic structure of these alloys, which was used to complement the spectroscopic ellipsometry data. Ellipsometry is typically restricted to the region close to the band gap, and provides information about the position of energy levels but does not provide information about the localization or about the orbitals that characterize the electronic states. X-ray spectroscopy has element selectivity due to absorption via the core states, whereas chemical sensitivity is obtained due to the participation of valence electrons. Furthermore, due to the dipolar nature of the transitions, particular symmetry information can be obtained. X-ray absorption spectroscopy specifically probes the local unoccupied electronic structure, and is therefore related to the conduction band, whereas x-ray emission spectroscopy (XES) provides information about the local occupied electronic structure, and is therefore related to the valence band. Although the nitrogen K-edge XES/XAS spectra do not allow for direct determination of the band gap, due to the element specificity and selection rules of XES/XAS, the data do reflect the conduction and valence band characteristics and additionally provide information on the role that specific elements play in determining the electronic structure of the alloys. The spectral features are sensitive to changes in the chemical environment around the element being probed and also provide information about the oxidation state of the absorbing atom, the electronic configuration, and the site symmetry. Thus, X-ray spectroscopy provides a complementary picture of the conduction-band and valence-band states that is distinct from the information obtained via optical transitions.[6] Using the dipole selection rules, the nitrogen K-edge XAS involves transitions from localized N 1$s$-like state to unoccupied states with $p$-character in the CB, whereas XES involves transitions from occupied $p$ states in the VB to the 1$s$ core hole.

Fig 3.3(c) shows the X-ray absorption data for the $ZnSn_xGe_(1-x)N_2$ samples with varying Sn:Ge ratios, as well as the XAS data for pure $ZnSnN_2$ and $ZnGeN_2$. As indicated by the vertical line, the absorption threshold, which corresponds to the conduction-band minimum, shifted to higher energies as the Ge content increased. For $ZnSnN_2$, the absorption onset was around 396.6 eV whereas for $ZnGeN_2$ the onset was observed at approximately 397.5 eV, with the values for the alloys falling between these two extremes. This behavior is qualitatively consistent with the above

analysis based on the large conduction-band offset between $ZnSnN_2$ and $ZnGeN_2$.

Fig 3.3(d) presents the N K $\alpha$ emission spectra, which reflect the valence band partial density of states, for different samples with varying Ge concentration. Fig 3.3(d) also presents the X-ray emission spectrum of $ZnSnN_2$. Two features, labeled as A and B, were distinct in all of the spectra, but upon incorporation of Ge, a shoulder labeled as C appeared between A and B, with this shoulder becoming more prominent as the Ge content increased. Feature B also became more pronounced as the Ge content increased. Feature A, appearing at 393.6 eV, mainly corresponds to N $2p$ occupied states, whereas the low energy feature B, that appeared between 386.2 and 386.5 eV originates from nitrogen $2p$ states hybridized with Zn $3d$, Ge 4s and Sn 5s states. These assignments are in accord with previous results.[6, 13] The appearance of shoulder C with the addition of Ge is ascribable to the mixing of Ge 4p states with N $2p$ states, whereas the enhancement in feature B results from the contribution of Ge $4s$ states. This increase in the partial density of states observed in the lower energy part of the valence band below 392 eV, as displayed by the features B and C, indicates a stronger *s-p-d* hybridization in case of the alloy samples. As indicated by the vertical black line, the valence-band maximum did not shift upon addition of Ge, which is consistent with the calculated small valence-band offset. Thus, a gradual increase in the band gap with increasing Ge content primarily occurred by the reorganization of conduction-band minimum to higher energies.

## 3.4 Conclusions

In summary, the experimental observations and first principles calculations of the $ZnSn_xGe_(1-x)N_2$ semiconductors described herein have shown that the alloys can be tuned to span a large portion of the solar spectrum. The band gap in the $ZnSn_(1-x)Ge_xN_2$ is tunable from 2 eV ($ZnSnN_2$) to 3.1 eV ($ZnGeN_2$), with a linear dependence on the composition arising from the smaller lattice mismatch between $ZnSnN_2$ and $ZnGeN_2$ as compared to the lattice mismatch in the $In_xGa_(1-x)N$ alloys that span the same energy gap range, consistent with theoretical predictions. Thus, the $ZnSn_xGe_(1-x)N_2$ alloys potentially could be useful as earth-abundant light absorbers for artificial photosynthetic devices as well as a replacement for InGaN in nitride-based optoelectronic devices.

## 3.5 Calculation methods:

The structural relaxation and electronic structure were calculated within the density functional formalism as implemented in the VASP code. [8] For the exchange-correlation potential, both the generalized gradient approximation (GGA) in the PBE form, and the non-local hybrid functional, (HSE 23) in which 31 % (known as the mixing parameter) of the semi-local GGA exchange potential was replaced by screened Fock exchange, were used. For the 16-atom orthorhombic unit cells of $ZnSnN_2$ and $ZnGeN_2$, both the structural relaxation and electronic structural calculations were performed using the hybrid functional calculations. For the structural relaxation of the 64-atom special quasi-random structure (SQS) for the $ZnSn_xGe_(1-x)N_2$ alloys, the structural relaxation was performed using the PBE functional, due to the heavy calculation cost of the hybrid functional. The following electronic structure calculation was also performed using the hybrid functional. The d states of the group II and IV elements were treated explicitly as valence. The interaction between the core electrons and the valence electrons was included by the standard frozen-core projector augmented-wave potentials. An energy cut-off of 400 eV was applied in all cases. For Brillouin-zone integration, k-point meshes that were equivalent to the $6^3$ Monkhorst-Pack meshes for a 16-atom orthorhombic unit cell were used. All lattice vectors and atomic positions were fully relaxed by minimization of the quantum mechanical stresses and forces.

### 3.5.1 Calculated density of states

The calculated density of states for ZnSnN2 and ZnGeN2 is given ibelow, with the energy relative to the valence band maximum (VBM) eigen-energy.

## 3.6 Materials Synthesis

### 3.6.1 Deposition via Reactive RF Magnetron Sputtering

Thin films were synthesized in an AJA International sputtering chamber (base pressure $10^-8$ Torr) from a combined $Zn_0.75Sn_0.25$ target and an elemental Ge target in an $Ar/N_2$ gas mixture (3mTorr) with varying power on the Ge target to vary the composition. The films were deposited on *c*-sapphire and LUMILOG *c*-GaN template substrates.

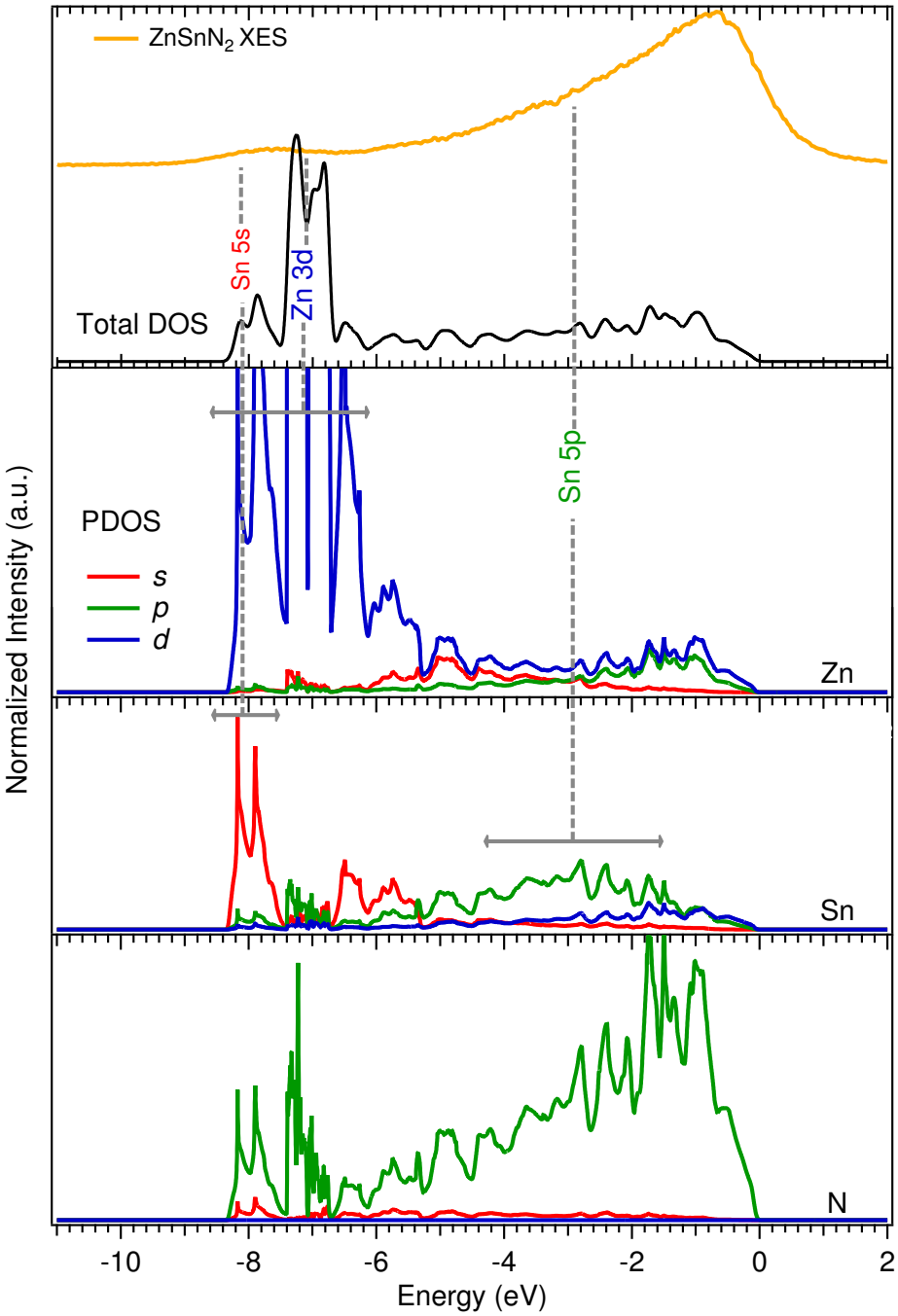


Figure 3.4: Calculated total and partial density of states of $ZnSnN_2$. The partial density of states is projected on Zn, Sn, Ge and N $s$, $p$, and $d$ orbitals respectively.

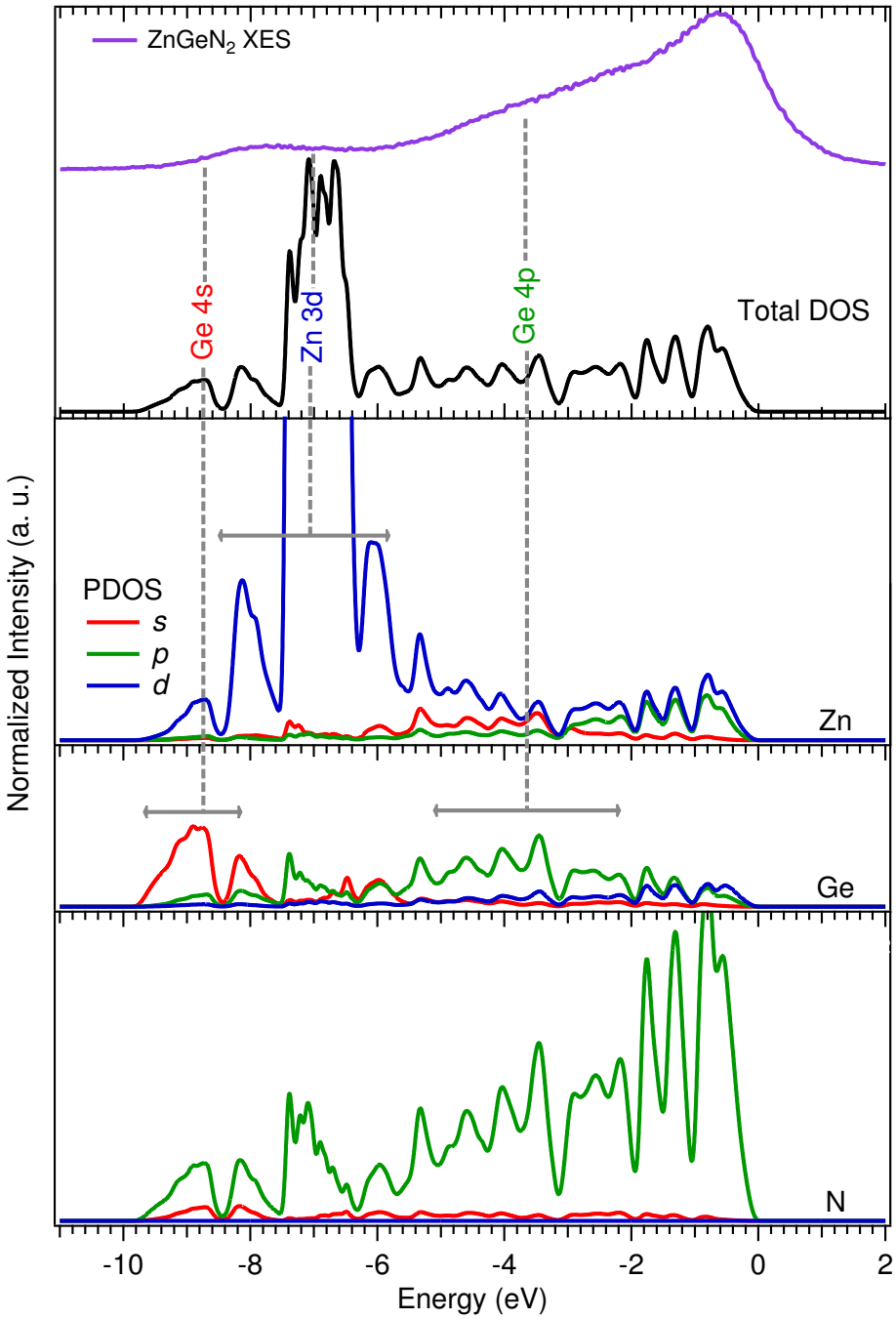


Figure 3.5: Calculated total and partial density of states of $ZnGeN_2$. The partial density of states is projected on Zn, Sn, Ge and N $s$, $p$, and $d$ orbitals respectively.

## 3.7 Experimental methods:

### 3.7.1 X-ray spectroscopy:

X-ray spectroscopic data were collected at the Advanced Light Source (ALS) at Lawrence Berkeley National Laboratory, with an electron energy of 1.9 GeV and an average current of 500 mA.

**Soft X-Ray Measurements:** Nitrogen K-edge XAS and XES measurements were performed using beamline 7.0.1. The beam line was equipped with a 99-pole, 5 cm period undulator and a spherical grating monochromator[16], and delivered intense radiation with a narrow band-pass. For x-ray absorption, the beam-line resolution was set to 0.15 eV at 400 eV. Spectra were recorded in total electron yield (TEY) mode by measurement of the sample drain current and total fluorescence yield (TFY) mode using a channeltron. The incident photon energy was calibrated by measurement of the X-ray absorption spectrum of hexagonal boron nitride (BN) during the experiment. The spectra were normalized to the photocurrent produced by a gold mesh that was inserted in the beamline between the last mirror and the sample. The incident radiation had a linear $p$-polarization (E vector in the plane of incidence), and samples were oriented at a grazing incidence with an angle of 20° with respect to the incident beam. X-ray emission spectra were recorded using a grazing incidence spectrometer16 that had a resolution of 0.4 eV at the N K-edge. With a Rowland circle geometry, the spectrometer consisted of a 20 $\mu$m wide and 2 cm long entrance slit, a spherical grating with a 5 m radius and 1200 lines mm$^{-}$1, and a two-dimensional detector. The emission spectra were measured with the spectrometer mounted at angle of 90° relative to the incident beam. The emission energies were calibrated using the elastic peaks of emission spectra of the N K-edge that were produced by the BN reference sample. All data were collected at room temperature.

**Hard X-Ray Measurements:** Hard X-ray absorption spectra (XAS) were collected at beam line 10.3.2. The radiation was monochromatized by a Si (111) double-crystal monochromator. The intensity of the incident X-ray beam was monitored by use of a $N_2$-filled ion chamber (I0) positioned in front of the sample. Fluorescence spectra were recorded using a seven-element Ge solid-state detector. The monochromator energy was calibrated relative to the rising-edge energy of a Ge foil (11103.00 eV). Data reduction of the XAS spectra was performed using custom-made software (Matthew Marcus). The pre-edge and post-edge contributions were subtracted from the XAS spectra,

and the results were normalized with respect to the edge jump. Background removal in k-space was performed by use of a five-domain cubic spline. Curve fitting was performed with Artemis and IFEFFIT software using ab initio calculated phases and amplitudes from the program FEFF 8.2. The details of the curve fitting are discussed in the Appendices.

### 3.7.2 X-ray Diffraction (XRD)

The structure and phase of the II-IV nitrides was evaluated by XRD obtained using a PANalytical X'Pert diffractometer with a Cu K $\alpha$ source ($\lambda = 1.5406$Å ), over a $2\Theta$ range of 30° to 43° for the thin films on a *c*-plane oriented sapphire substrate.

### 3.7.3 Spectroscopic Ellipsometry:

Spectroscopic ellipsometry was performed on samples grown on *c*-sapphire. Data were collected at an incidence angle of 70° for 250 nm $< \lambda <$ 2300 nm, with a Xe lamp visible light source and a Fourier-transform infrared spectrometer. The value of the band gap is estimated by linear extrapolation to the energy axis of a plot of the square of the absorption coefficient ($\alpha^2$) versus the photon energy as is typical for direct band-gap semiconductors.

# Bibliography

Chen, Shiyou et al. “Defect physics of the kesterite thin-film solar cell absorber Cu2ZnSnS4”. In: *Applied Physics Letters* 96.2, 021902 (2010), pages. DOI: http://dx.doi.org/10.1063/1.3275796. URL: http://scitation.aip.org/content/aip/journal/apl/96/2/10.1063/1.3275796 (cit. on p. 21).

— “Electronic structure and stability of quaternary chalcogenide semiconductors derived from cation cross-substitution of II-VI and I-III-$VI_2$ compounds”. In: *Phys. Rev. B* 79 (16 Apr. 2009), p. 165211. DOI: 10.1103/PhysRevB.79.165211. URL: http://link.aps.org/doi/10.1103/PhysRevB.79.165211 (cit. on pp. 21, 22).

Deng, Fuling et al. “Determination of the basic optical parameters of ZnSnN2”. In: *Opt. Lett.* 40.7 (Apr. 2015), pp. 1282–1285. DOI: 10.1364/OL.40.001282. URL: http://ol.osa.org/abstract.cfm?URI=ol-40-7-1282 (cit. on p. 26).

Du, K. et al. “Synthesis and characterization of ZnGeN2 grown from elemental Zn and Ge sources”. In: *Journal of Crystal Growth* 310.6 (Mar. 15, 2008), pp. 1057–1061. DOI: http://dx.doi.org/10.1016/j.jcrysgro.2007.12.042. URL: http://www.sciencedirect.com/science/article/pii/S0022024807012560 (cit. on p. 26).

Feldberg, N. et al. “Growth of ZnSnN2 by Molecular Beam Epitaxy”. In: 43.4 (2014), pp. 884–888. DOI: 10.1007/s11664-013-2962-8. URL: http://dx.doi.org/10.1007/s11664-013-2962-8 (cit. on pp. 21, 26).

Groot, Frank de. “High-Resolution X-ray Emission and X-ray Absorption Spectroscopy”. In: *Chemical Reviews* 101.6 (2001). PMID: 11709999, pp. 1779–1808. DOI: 10.1021/cr9900681. eprint: http://dx.doi.org/10.1021/cr9900681. URL: http://dx.doi.org/10.1021/cr9900681 (cit. on pp. 30, 31).

Ishitani, Yoshihiro. "Carrier dynamics and related electronic band properties of InN films". In: *Japanese Journal of Applied Physics* 53.10 (2014), p. 100204. URL: http://stacks.iop.org/1347-4065/53/i=10/a=100204 (cit. on p. 21).

Kresse, G. and J. Furthmüller. "Efficient iterative schemes for *ab initio* total-energy calculations using a plane-wave basis set". In: *Phys. Rev. B* 54 (16 Oct. 1996), pp. 11169–11186. DOI: 10.1103/PhysRevB.54.11169. URL: http://link.aps.org/doi/10.1103/PhysRevB.54.11169 (cit. on p. 32).

Lahourcade, Lise et al. "Structural and Optoelectronic Characterization of RF Sputtered ZnSnN2". In: *Advanced Materials* 25.18 (2013), pp. 2562–2566. ISSN: 1521-4095. DOI: 10.1002/adma.201204718. URL: http://dx.doi.org/10.1002/adma.201204718 (cit. on pp. 21, 23, 26, 27).

Miller, Nate et al. "Effect of charged dislocation scattering on electrical and electrothermal transport in *n*-type InN". In: *Phys. Rev. B* 84 (7 Aug. 2011), p. 075315. DOI: 10.1103/PhysRevB.84.075315. URL: http://link.aps.org/doi/10.1103/PhysRevB.84.075315 (cit. on p. 21).

Narang, Prineha et al. "Bandgap Tunability in Zn(Sn,Ge)N2 Semiconductor Alloys". In: *Advanced Materials* 26.8 (2014), pp. 1235–1241. ISSN: 1521-4095. DOI: 10.1002/adma.201304473. URL: http://dx.doi.org/10.1002/adma.201304473 (cit. on p. 21).

Punya, Atchara and Walter R. L. Lambrecht. "Band offsets between $ZnGeN_2$, GaN, ZnO, and $ZnSnN_2$ and their potential impact for solar cells". In: *Phys. Rev. B* 88 (7 Aug. 2013), p. 075302. DOI: 10.1103/PhysRevB.88.075302. URL: http://link.aps.org/doi/10.1103/PhysRevB.88.075302 (cit. on pp. 23, 26, 28).

Punya, Atchara, Walter R. L. Lambrecht, and Mark van Schilfgaarde. "Quasiparticle band structure of Zn-IV-$N_2$ compounds". In: *Phys. Rev. B* 84 (16 Oct. 2011), p. 165204. DOI: 10.1103/PhysRevB.84.165204. URL: http://link.aps.org/doi/10.1103/PhysRevB.84.165204 (cit. on pp. 21, 23, 26, 31).

S. Nakamura S. J. Pearton, G. Fasol. *The Blue Laser Diode: The Complete Story*. 2nd. Springer, 2000 (cit. on p. 21).

Singh, R. et al. "Phase separation in InGaN thick films and formation of InGaN/GaN double heterostructures in the entire alloy composition". In: *Applied Physics Letters* 70.9 (1997), pp. 1089–1091 (cit. on pp. 21, 25, 26).

Warwick, Tony et al. "A new bend-magnet beamline for scanning transmission X-ray microscopy at the Advanced Light Source". In: *Journal of Synchrotron Radiation* 9.4 (July 2002), pp. 254–257.

DOI: 10.1107/S0909049502005502. URL: http://dx.doi.org/10.1107/S0909049502005502 (cit. on p. 35).

Wei, S.-H. et al. "Electronic properties of random alloys: Special quasirandom structures". In: *Phys. Rev. B* 42 (15 Nov. 1990), pp. 9622–9649. DOI: 10.1103/PhysRevB.42.9622. URL: http://link.aps.org/doi/10.1103/PhysRevB.42.9622 (cit. on p. 23).

Zunger, Alex et al. "Special quasirandom structures". In: *Phys. Rev. Lett.* 65 (3 July 1990), pp. 353–356. DOI: 10.1103/PhysRevLett.65.353. URL: http://link.aps.org/doi/10.1103/PhysRevLett.65.353 (cit. on p. 23).

# 4

# Decay of surface plasmons

*Make things as simple as possible, but not simpler.*

– Albert Einstein

## 4.1 Chapter Overview

The decay of surface plasmon resonances into hot electron-hole pairs has recently been utilized in Schottky barrier optical detectors and energy conversion devices, in contrast to many applications where damping is to be ardently avoided. Collection of hot electrons generated by the efficient absorption of light in metallic nanostructures in contact with semiconductor substrates can provide a basis for the construction of solar energy-conversion devices. In this chapter we evaluate theoretically the energy-conversion efficiency of systems that rely on internal photoemission processes at metal-semiconductor Schottky-barrier diodes. In this calculation, the current-voltage characteristics are given by the internal photoemission yield as well as by the thermionic dark current over a varied-energy barrier height. The Fowler model in all cases predicts solar energy-conversion efficiencies of less than 1 % for such systems. However, relaxation of the assumptions regarding constraints on the escape cone and momentum conservation at the interface yields solar energy-conversion efficiencies as high as 1-10%, under some assumed (albeit optimistic) operating conditions. Under these conditions, the energy-conversion efficiency is mainly limited by the thermionic dark current, the distribution of hot electron energies, and hot-electron momentum considerations. Drawbacks of the IPE model and the question of quantum effects in describing plasmon decays will be addressed

in this chapter.

## 4.2 Introduction

### 4.2.1 Device physics motivated use of plasmon decays

The energy-conversion efficiencies of record-setting pn-junction photovoltaics are rapidly approaching the theoretical single-bandgap Shockley-Queisser limit of 32 % under unconcentrated sunlight.[20] Multi-junction solar cells (that still operate within the Shockley-Queisser limitations for each absorber and junction) can provide much higher efficiencies partly by reducing the amount of sub-bandgap light lost, but such devices also have much higher costs than single-bandgap devices due to the need to produce multiple high-purity semiconductor materials to capture the incident light and convert it into a collected electrical current. Another possible device architecture considered here consists of a single band gap semiconductor homojunction or heterojunction device used in combination with a metal-semiconductor Schottky junction formed from that same light absorber. In such an approach, in addition to collection of above band-gap carriers generated in the semiconductor (again subject to the Shockley-Queisser limit), the metal would additionally serve to generate "hot "electron-hole pairs in the metal which would then be emitted into the semiconductor and collected as an additional photocurrent. The process of hot carrier internal photoemission (IPE) from the metal to the semiconductor over a tunable Schottky barrier has therefore been proposed as a possible solar energy conversion device formation strategy.[22] This metal-absorber device structure (similar in some ways to a dye-sensitized solar cell) could therefore provide an interesting device integration possibility when placed optically behind a single-junction solar cell, serving to increase the overall efficiency of the whole system by virtue of the presence of this second capture and conversion system in the overall device structure. Though referred to as "hot electron" or "hot hole" emission/capture, we emphasize that the device physics are different from "hot carrier" solar cells.[19] Such hot carrier metal/semiconductor device structures could in principle be beneficially used in solid-state[22, 4, 13] or photoelectrochemical systems[15, 16, 5, 14] to collect photons having energies lower than the energy band gap of a semiconductor, in essence serving as the second junction in a tandem structure but not requiring necessarily a second pure semiconductor light absorber as in a conventional tandem cell arrangement. Plasmonic structures have been demonstrated to provide highly efficient light

scattering and trapping elements, in some cases providing enhancements in solar energy conversion.[2, 1, 17] In the context of hot-electron devices, the large extinction cross-section at a surface plasmon resonance enables very thin films of nanostructures to absorb a significant fraction of the solar spectrum.[17]The collective plasmon oscillation may also play a role in increasing the photoemission yield,[10, 12] though the details of the hot-carrier dynamics after surface plasmon decay are still under study. At the small dimensions of plasmonic structures, the effects of electron scattering at surfaces strongly modifies the yield even in the semiclassical IPE model.[12]

In this chapter an analysis of the efficiency limits for energy conversion via IPE, capturing the key optical and electronic processes in such devices is presented. Section 4.3 presents the current-voltage characteristics and energy-conversion efficiency based on simple Fowler theory and thermionic emission; section 4.4 reviews the three-step model of internal photoemission and describes explicitly the inherent assumptions of Fowler theory; section 4.5 refines the yield including the effect of phonon scattering and thin-film enhancement; section 4.6 presents example calculations of the limiting efficiency under various assumptions; and the discussion section goes over the application of these approaches to plasmonic structures. Previous estimates of the internal photoemission (IPE) yield and energy-conversion efficiency of such systems have used simple Fowler theory and/or have used a simplified treatment of the carrier dynamics, with a recent study by White and Catchpole consequently calculating a maximum best case solar energy-conversion efficiency of 8% for such systems.[23] In contrast, we describe the situation in which realistic assumptions are made and the carrier dynamics are fully treated. Our most generous efficiency estimates agree with previous "absolute upper-limit" efficiency values,[12, 23, 4] which assumed that the momentum requirements at the interface governing emission (the hot electron escape cone) can be relaxed for nanostructures. However, our more in-depth analysis shows that even for nanostructures of dimensions on the order of 20 nm, the practically obtainable efficiency is lowered by orders of magnitude due to the limiting effects of the hot electron mean free path in conjunction with the requirement of a critical momentum normal to the interface. The lowered efficiency limits calculated herein thus serve as a more realistic framework for establishing the expected efficiencies, design parameters, and performance characteristics, of an actual energy-conversion system based on metallic hot-carrier internal photoemission.

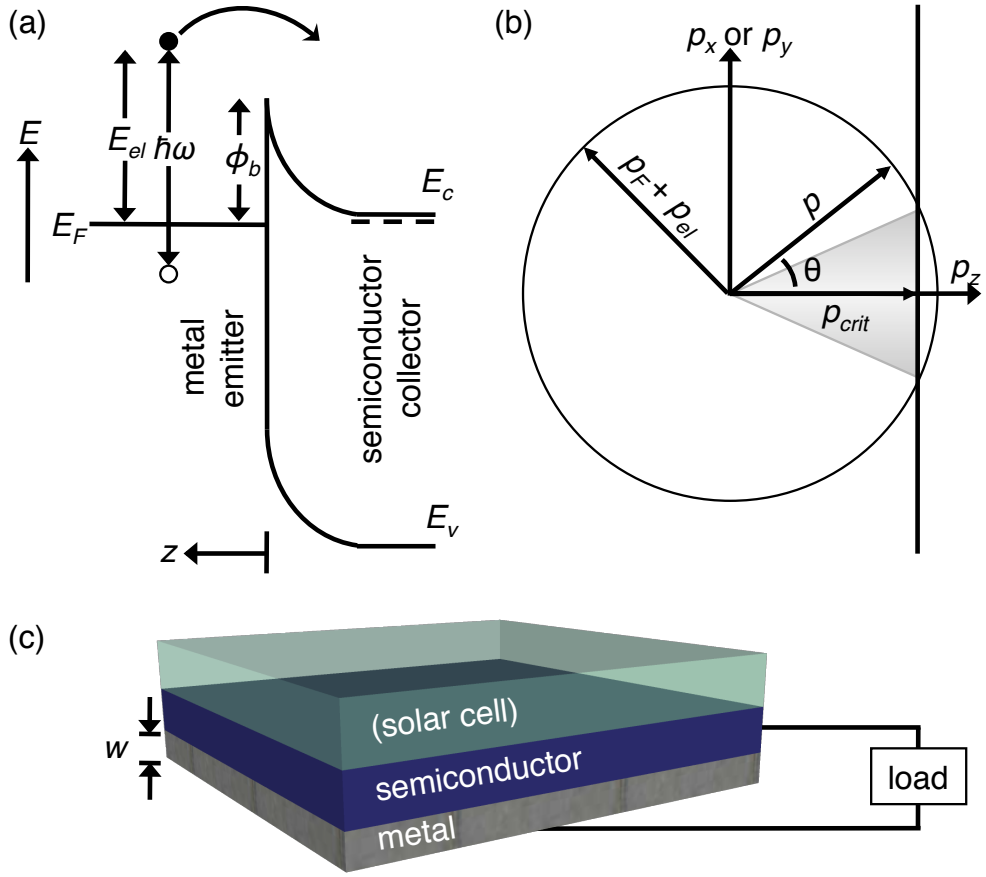


Figure 4.1: (a) Internal photoemission band diagram for hot electrons emitted from a metal into an n-type semiconductor. (b) Schematic of isotropic distribution of hot electron momentum on a sphere in momentum space with a limited escape cone. (c) Sketch of a possible energy conversion device layout where light passing through a photovoltaic solar cell and the semiconductor collector is absorbed in the metal emitter.

## 4.3 Internal photoemission and efficiency

Fowler developed the basic theory of photon-induced emission of electrons from metals in the early 20th century.[7] Though refinements have been made,[23, 10] the simple Fowler equation has proven to be in accord with experimental data for the internal photoemission yield26 in both magnitude and spectral behavior:

$$Y_{\mathrm{Fow}}(\hbar\omega) \approx \frac{1}{8E_F}\frac{(\hbar\omega - \phi_b)^2}{\hbar\omega} \tag{4.1}$$

where $\hbar$ is the reduced Planck constant, $\omega$ is the incident light frequency, $\phi_b$ is the barrier height (in units of energy), and $\mathrm{E}_F$ is the Fermi energy of the emitter, with the value of $\mathrm{E}_F$ describing the curvature of the conduction band in momentum space (Fig. 4.1(a)). The Fowler yield is based on a semiclassical model of hot electrons emitted over an energetic barrier, with the critical assumption that the kinetic energy normal to the barrier must be greater than the barrier height. As depicted in Fig. 4.1(b), for a spherical Fermi surface, this assumption gives rise to a limited escape cone for hot electrons, because the momentum normal to the interface must be larger than a critical value, $\mathrm{p}_crit$. The escape cone limitation results in zero yield at the threshold photon energy as well as a slow rise with photon energy if the Fermi energy is large compared to the photon energies of interest. This latter condition is true for visible light incident on noble metal emitters; for instance, both silver and gold have a Fermi energy near 5.5 eV (which was the value for $\mathrm{E}_F$ used in our calculations).

The collector material can be either an insulator or a semiconductor, and the built-in electric fields of metal-semiconductor Schottky barriers assist in the collection of the emitted hot carriers. In principle a metal-insulator-metal diode could also be used for energy conversion, but in our calculations the maximum energy-conversion efficiency was found to be equivalent to that of a metal-semiconductor diode, so the conceptually and notationally simpler Schottky barrier case will be discussed here, in which the metal is the emitter and the semiconductor is the collector. Considering hot-electron emission, the optimal semiconductor will be a highly doped n-type material, and the Fermi energy in the semiconductor should be nearly equal to the conduction-band energy. Equivalent considerations apply to a p-type semiconductor that would collect hot holes, but here for clarity we consider only the n-type case. To operate in power-generation mode, the diode must be forward-biased (by applying a positive voltage to the metal), in contrast to most internal photoemission detection experiments in which reverse bias aids in extracting the carriers. The

current-voltage characteristics can be determined by considering the reverse photocurrent density due to internal photoemission $J_{photo}$, the dark forward current density due to thermionic emission from the collector to the emitter $J_{dark}$, and the properties of the illumination source. The efficiency is given by:

$$\text{Percent Efficiency} = \frac{|J_{\text{photo}} + J_{\text{dark}}|V}{P_{\text{ill}}} X100 \tag{4.2}$$

$$= \frac{\left| -\int_0^{\hbar\omega_{\max}} I_{\text{ill}} Y(\hbar\omega) \left(\frac{q}{\hbar\omega}\right) d(\hbar\omega) + J_{\text{dark}}(V) \right| V}{\int_0^{\hbar\omega_{\max}} I_{\text{ill}} d(\hbar\omega)} X100 \tag{4.3}$$

where V is the operating voltage, $P_{ill}$ is the illumination irradiance, $I_{ill}$ is the spectral irradiance, and the integration is performed up to a maximum energy. Note that here the yield Y is the external quantum yield, but Y is assumed to be equal to the internal quantum yield under the condition of negligible optical reflection losses. To model the AM1.5 solar spectrum, the spectral irradiance was assumed to be a 5800 K blackbody with a total irradiance of 95 mW cm$^{-}$2. which provides an easily integratable function that generally matches the shape and irradiance of the AM1.5 spectrum. The thermionic dark current is given by:

$$J_{\text{dark,therm}} = A^* T^2 e^{\frac{q(V-\phi_b)}{kT}} \tag{4.4}$$

where A* is the Richardson's constant, T is the absolute temperature, and $k$ is Boltzmann's constant. Here we are assuming that the operating voltage is less than the barrier height but a few times greater than the thermal voltage $k$T. Though Richardson's constant is given as 120 A cm$^{-}$2 K$^{-}$1, in our calculations we generously assumed the more optimistic value of A*= 50 A cm$^{-}$2K$^{-}$1 which applies for thermionic emission involving a semiconductor like silicon; however, this more optimistic value only results in a maximum of 10% relative efficiency increase relative to the more stringent condition with A*=120 A cm$^{-}$2K$^{-}$1.

Fig. 4.2(a) displays the efficiency for hot carrier internal photoemission assuming the simple Fowler yield based on equations refeqn:JAPeqn1,eqn:JAPeqn2, eqn:JAPeqn3. Because one application of this concept involves capture of sub-bandgap illumination below a traditional photovoltaic

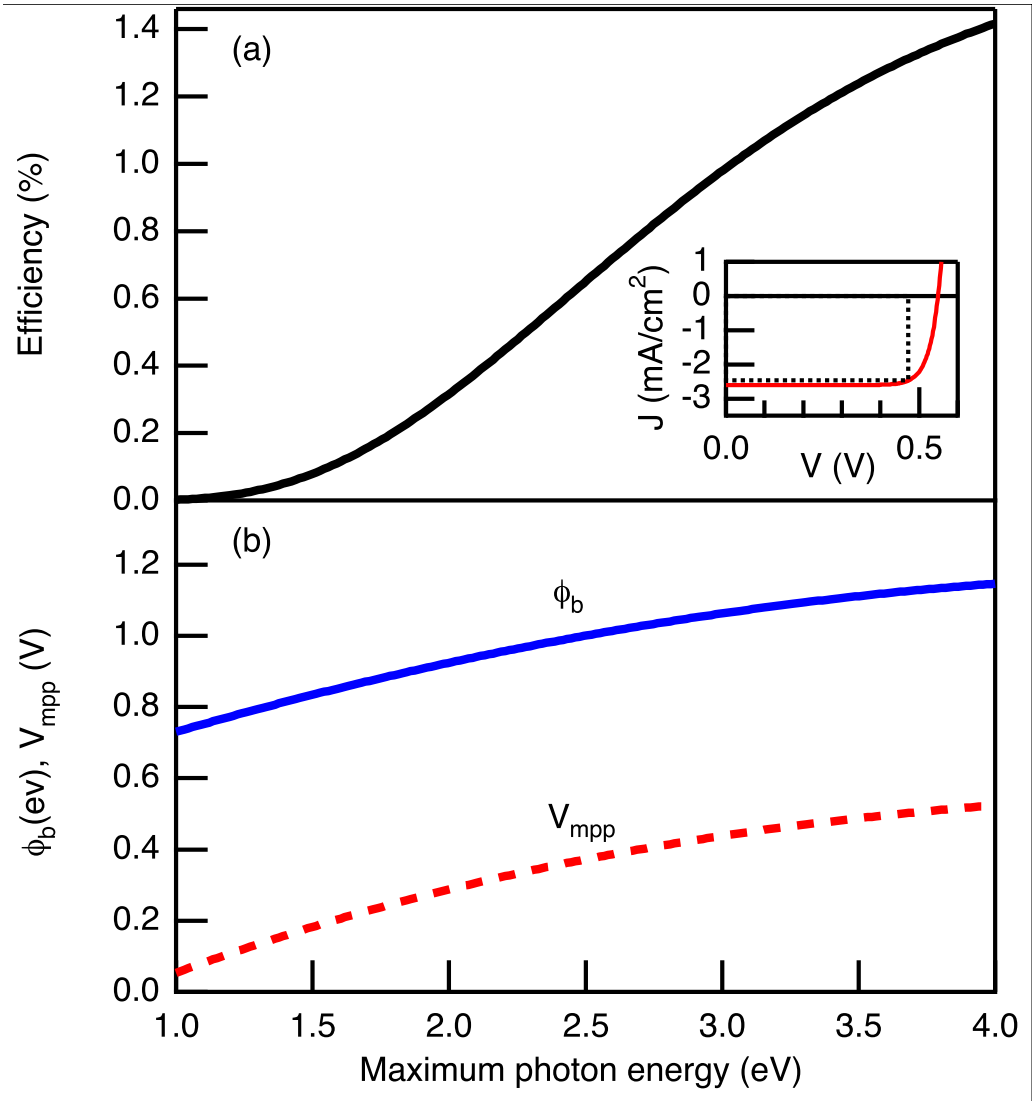


Figure 4.2: (a) Solar conversion efficiency for internal photoemission over a metal-semiconductor Schottky barrier based upon the simple Fowler equation. (b) Optimized barrier height and maximum power point voltage ($V_{mpp}$) used to calculate the curve in (a). Inset: Example current-voltage curve with maximum power shown as the dotted box.

cell as shown schematically in Fig. 4.1(c), the efficiency is plotted as a function of maximum photon energy. Hence the maximum photon energy would be 1.1 eV for a Si solar cell, 3.0 eV for a $TiO_2$ photoelectrochemical device, or about 4 eV for the entire solar spectrum. The inset shows an example current-voltage behaviour, which has a shape that is similar to a standard pn-junction or Schottky solar cell, but at a much lower operating voltage and current. Fig. 4.2(b) displays the barrier height and voltage at the maximum power point, Vmpp for the maximum efficiency values displayed in Fig. 4.2(a). The yield is highest for a small energy barrier, but avoiding the thermionic dark current requires a larger barrier. Specifically, for operation at 1 sun and 300 K, a difference of approximately 0.7 eV between barrier height and $V_{mpp}$ is required to keep the thermionic dark current less than the photocurrent. The thermionic dark current for metal-semiconductor Schottky barrier solar cells can be reduced by introducing a higher barrier for majority carriers, but internal photoemission is entirely a majority-carrier process, so any extra barrier will also reduce the photocurrent.

## 4.4 The three-step model for internal photoemission

Because the simple Fowler equation predicts that the maximum efficiency of an energy-conversion device based on internal photoemission is approximately 1%, it is useful to analyze the assumptions and mechanisms involved in derivation of the Fowler theory to determine the conditions, if any, that could result in higher efficiencies. The semiclassical model of internal photoemission involves three steps: hot-electron excitation, hot-electron transport to the interfacial barrier, and hot-electron emission over the energetic barrier from the emitter material into the collector material. Although the actual processes of light absorption and excitation of the collective electron cloud are quantum-mechanical phenomena, we assume herein that after light absorption, the "hot electron" behaves as a quasiparticle whose transport can be described semiclassically within a free-electron-like band structure. Light is absorbed in the metal when the photon's perturbing electric field causes electronic transitions. Consequently the material response is described macroscopically by a frequency-dependent dielectric constant, $\epsilon$, determined empirically for bulk materials. Assuming that this local, linear permittivity is a valid description for nanoscale structures such as plasmonic absorbers, Maxwell's equations yield the spectral power absorption as:

$$P_{\text{abs}} = -\frac{1}{2}\,\text{Re}[-\nabla.S] \tag{4.5}$$

$$= -\frac{1}{2}\omega|E|^2\,\text{Im}[\epsilon] \tag{4.6}$$

$$\propto \eta_e \tag{4.7}$$

where S is the Poynting vector, E is the electric field of the incident electromagnetic wave, and $\eta_e$ is the hot electron generation rate per length. The spatial distribution of absorbed power is obtained from equation 4.7, and for antenna-like structures, the absorbed power is highest near the surfaces around the midpoint where the highest currents flow. Assuming that the probability is low for an absorbed photon to couple directly to phonons or multiple electron excitations (because many-body excitations are not very probable), the spatial power absorption normalized by the incident power then directly corresponds to the spatial distribution of hot-electron generation. Such calculations are readily performed using e.g. full-field finite difference time domain simulations, but the generation profile depends significantly on the geometry of the antenna and system as a whole. Hence, for simplicity, the generation profile was assumed herein to be uniform throughout a film of thickness d, i.e. $\eta_e$= 1/d. The electron-hole pair excited by light was assumed to have a total energy equal to the photon energy, so the hot electron energy, $E_{el}$, can range from 0 to max photon energy. In the simplest approximation, the distribution of energies would be uniform in this range. However, considering the electronic density of states g(E) and nondirect transitions in which momentum can be supplied by surfaces, defects, or phonons, the probability of excitation to a certain energy E=$E_F$ + $E_{el}$ is just the multiplied probability of the existing initial and final states, normalized to the total number of transitions possible:

$$P_0(E_{\text{el}})dE = \frac{g(E)g(E-\hbar\omega)dE}{\int_{E_F}^{E_F+\hbar\omega} g(E')g(E'-\hbar\omega)\,\text{dE}'} \tag{4.8}$$

For a free-electron-like metal with a parabolic band structure at low temperature, such that the tails of the Fermi distribution can be ignored, the hot electron energy distribution becomes

$$P_0(E_{\text{el}})dE = \frac{\sqrt{E_F+E_{\text{el}}}\sqrt{E_F+E_{\text{el}}-\hbar\omega}dE}{\int_{E_F}^{E_F+\hbar\omega}\sqrt{E'}\sqrt{E'-\hbar\omega}dE'} \tag{4.9}$$

which was used in these calculations. Many metals are free-electron like near the Fermi energy, e.g. for gold the bands with *d*-orbital character lie about 1.6 eV below the Fermi level, so this approximation is most valid for low photon energy excitation. The relative distribution of hot electrons and hot holes varies depending on the material, and low-lying bands could favor hot holes over hot electrons due to the increased density of states below the Fermi level; modification of the "electron distribution joint density of states" could in principle enhance (or decrease) the yield and efficiency. After excitation, the hot electron quasiparticle must move through the material to reach a collecting interface. Because phonon scattering is a quasielastic process, only electron-electron scattering is assumed to cause significant energy loss of the hot electrons. Typically about half of the hot electron's energy is lost in an electron-electron scattering event, and the resulting electron can no longer surmount the barrier. The mean free path for electron-electron scattering therefore determines the probability $\mathrm{P}_{int}$ that the hot electron will reach the interface, if starting at a depth z at an angle $\theta$ away from normal:

$$P_{\mathrm{int}} \sin\theta d\theta = \frac{1}{2} e^{-\frac{z}{\lambda_{e-e}(E_{\mathrm{el}})\cos\theta}} \sin\theta d\theta \tag{4.10}$$

where the factor of half results from half of the electrons initially travelling away from the interface. A suitable analytical model for the electron-electron scattering mean free path was developed by Quinn and is given as:

$$\lambda_{e-e}(E_{\mathrm{el}}) = \frac{24 a_0 \sqrt{\alpha_e r_s/\pi}(3E_F/E_{\mathrm{el}}^2 + 2/E_{\mathrm{el}})}{\tan^{-1}\sqrt{\frac{\pi}{\alpha_e r_s}} + \sqrt{\frac{\alpha_e r_s/\pi}{1+\alpha_e r_s/\pi}}} \tag{4.11}$$

where $\mathrm{a}_0$ is the Bohr radius (0.0529 nm), $\alpha_e = (4/(9\pi))1/2$, and $\mathrm{r}_s$ is the radius of a sphere equal to the volume of one conduction electron in units of the Bohr radius; for gold $\mathrm{r}_s = 3$. The value of $\lambda_e - e$ approximately follows a $\mathrm{E}_e l$-sqaured behavior, with some example values being 100 nm at 1 eV to 10 nm at 3.5 eV. Thus, the details of the spatial hot electron generation profile are not critical, because the distances travelled are relatively long compared to the nanoscale dimensions of exemplary plasmonic structures. Though the mean free path can be longer than the characteristic dimension of the metallic nanostructure, the escape cone restriction (vide infra) dictates that, in general, multiple reflections within the metal will occur before the hot electron can be emitted. When the hot electron encounters the surface and energy barrier, Fowler's theory asserts that the

component of kinetic energy normal to the barrier must equal the barrier energy. This requirement is illustrated as the limited momentum escape cone in Fig. 4.1(b), with the maximum angle of approach for which a hot electron can escape given by:

$$\begin{aligned} \cos\theta_{\max} &= p_{\mathrm{crit}}/p & (4.12)\\ &= \sqrt{\frac{E_F+\phi_b}{E_F+E_{\mathrm{el}}}} & (4.13)\\ &\approx 1-\frac{E_{\mathrm{el}}-\phi_b}{2E_F} & (4.14) \end{aligned}$$

where the approximation holds if barrier height, $\mathrm{E}_{el} << \mathrm{E}_F$. This angle defines the maximum angle allowed in equation 4.9. Note that the fraction of hot electrons reflected by the barrier $\mathrm{R}_{elec}$ can be written as

$$\begin{aligned} R_{\mathrm{elec}} &= 1-T_{\mathrm{elec}} & (4.15)\\ &= 1-\int_0^{\theta_{\max}}\sin\theta d\theta & (4.16)\\ &\approx 1-\frac{E_{\mathrm{el}}-\phi_b}{2E_F} & (4.17) \end{aligned}$$

where $\mathrm{T}_{elec}$ is the transmitted fraction. For large Fermi energies compared to the excitation energy, the reflected fraction is nearly unity. The internal photoemission yield as a function of energy is obtained by combining the probabilities of absorption, transport to the barrier, and emission over the barrier:

$$Y(\hbar\omega)=\int_{\phi_b}^{\hbar\omega}\mathrm{dE}_{\mathrm{el}}\int_0^{\theta_{\max}}\sin\theta d\theta\int_0^{\infty}dzP_0(E_{\mathrm{el}})P_{\mathrm{int}}(z,\theta,E_{\mathrm{el}})\eta_e(z) \quad (4.18)$$

Under the conditions of $\mathrm{p}_crit = \mathrm{p}_F$ so that the escape cone is small, a small absorption length compared to $\lambda_{e-e}$, and a constant distribution of hot electron energies, the integrals are easily evaluated and result in the Fowler yield, 4.1, which is a good approximation for light incident on a bulk slab of metal.

## 4.5 Enhancements due to scattering

For thin metal emitters that have a thickness on the order of $\lambda_{e-e}$, the yield can be enhanced significantly due to Lambertian reflections at the interfaces. Electron-phonon scattering with a mean free path $\lambda_{e-p}$ 20 nm (used in the calculations here) can additionally enhance the yield, because the hot electron momentum can be redirected into the escape cone with little loss of energy in the quasi-elastic collisions. Again considering the case above, Dalal has derived an enhanced yield expression that takes into account both phonon and back-surface scattering. In this model, the angular integral of $P_{int}$ is replaced with a more detailed function q(z) due to a sum over multiple reflections at various scattering angles, producing the following expression for enhanced yield:

$$Y_{\rm enh}(\hbar\omega) = \int_{\phi_b}^{\hbar\omega} {\rm dE_{el}} \int_0^{\infty} dz P_0(E_{\rm el}) q(E_{\rm el}, z) \eta_e(z) \tag{4.19}$$

$$q(E_{\rm el}, z) = A_w e^{\mu z} + B_w e^{-\mu z} \tag{4.20}$$

$$A_w = e^{-2\mu w} B_w \tag{4.21}$$

$$B_w = \frac{1 - R_{\rm elec}}{(1 - R_{\rm elec})(1 + e^{-2\mu w}) + (1 + \lambda_{e-e}/\lambda_{e-p})^{-1/2}(1 + R_{\rm elec})(1 - e^{-2\mu w})} \tag{4.22}$$

$$\mu = \sqrt{(\lambda_{e-e}^{-1} + \lambda_{e-p}^{-1})^2 - \lambda_{e-p}^{-1}(\lambda_{e-e}^{-1} + \lambda_{e-p}^{-1})} \tag{4.23}$$

## 4.6 Theoretical efficiencies

Based on the equations for yield outlined in Sections 4.3 and 4.4, the efficiency given by equation 4.1 can be numerically evaluated for a variety of conditions and assumptions. Figure 4.3 shows the optimized efficiency as a function of maximum photon energy, assuming that the incident light is completely and uniformly absorbed over the film thickness with no reflection losses. Figure 4.3 includes (on a logarithmic scale) the result from Figure 4.1 (a) based on the Fowler yield but also shows results for a 100 nm metal film ($E_F$ = 5.5 eV) at 300 K, a 20 nm film at 300 K, a 20 nm film at 300 K for which $R_{elec}$=0, and a 20 nm film at 77 K, as well as the best-case scenario at both 300 and 77 K for which the hot electron mean free path is much longer than the film thickness. Note that when the momentum escape cone restriction is included, with either finite film thickness, the calculated efficiency is much lower than the best-case scenario in which the escape cone restriction is not explicitly included in the analysis. The 100 nm and 20 nm cases at 300 K

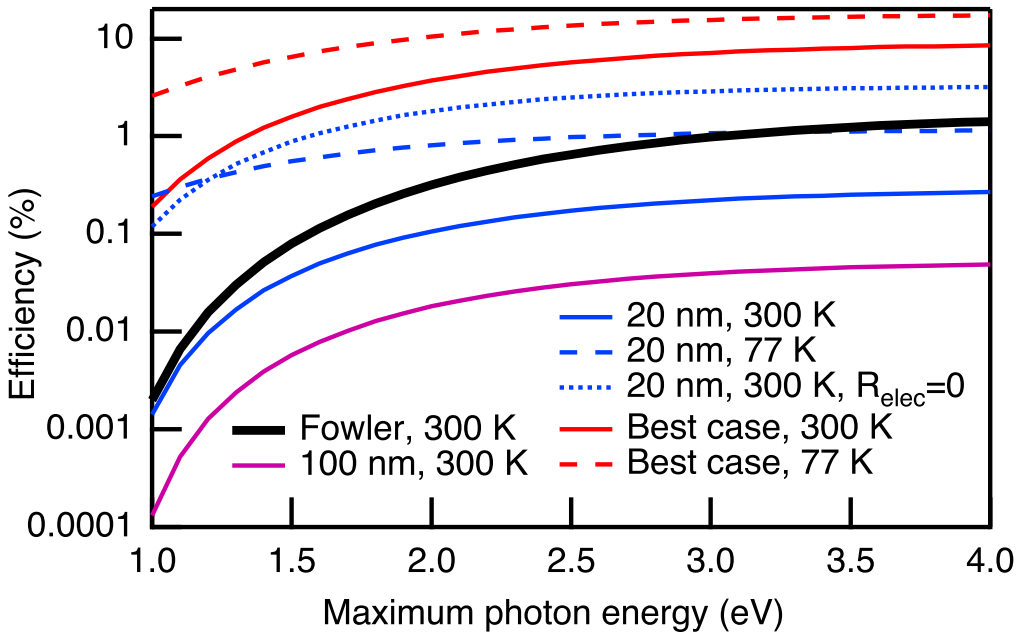


Figure 4.3: Solar conversion efficiency for IPE considering a 5800 K blackbody spectrum up to a given maximum photon energy fully absorbed in an Au-like metal considering different film thicknesses (colors), operating temperatures (dashed lines), and escape cone limitations (dotted line). The simple Fowler case from Fig. 4.1 is included as the bold black line, and "best case" represents a very long hot electron mean free path compared to the dimensions of the structure itself.

show lower efficiency than the simple estimate from the Fowler equation, due to the inclusion of a finite electron mean free path, which affects light absorbed deeply in the metal. In contrast, the Fowler case assumed absorption at the surface. Operation of such devices at lower temperature enhances the efficiency, because the dark current from thermionic emission is lowered significantly as the temperature decreases. Clearly the efficiency reaches values significantly in excess of 1% only if the escape cone restriction is lifted in the best-case scenario and if photon energies above 1.5 eV are included.

### 4.6.1 Discussion of IPE results

In this semiclassical model of hot electron internal photoemission, the energy-conversion efficiency is low for two primary reasons. First, the diode must be operated in forward bias to capture the reverse photocurrent, so the thermionic current of electrons flowing from the collector to the emitter strongly reduces the net current. Second, each photon creates a hot electron and a hot hole, and the hot electron energy can easily be less than the photon energy. In contrast to a semiconductor photovoltaic device in which the internal energy of the minority carriers is nearly equal to the bandgap, the internal energy of the hot electrons involved here is distributed from zero to the photon energy. Although the most optimistic assumptions were used in most cases, the results could be modified by explicit consideration of some other effects. The band structure of real materials can change the distribution of hot electron (and hot hole) energy, so the transition probabilities linking initial and final electronic band states should be calculated to determine the excitation probabilities as a function of both the hot electron/hole energy and momentum. An optimized band structure or device layout may allow higher efficiency than that calculated herein. We have used reasonable numbers for a Au/n-Si junction, but the efficiency estimates here should be applicable to a wide range of metal/semiconductor materials because the hot electron mean free paths do not vary wildly for various metals. Also, the efficiencies presented here are not true detailed-balance efficiencies, because no re-radiation of light was considered. Considering optical reflection and photon emission would further lower the efficiencies. Another limitation exists due to the requirement of critical momentum normal to the interface, which leads to a small escape cone for hot electrons having an energy just larger than the barrier energy. For an interface that is rough on the scale of the electron wavelength, this classical restriction may be relaxed. Indeed, some vacuum photoemission experiments have seen anomalously high yields from

nanoparticles,[15] with a variety of explanations involving geometry, escape cone relaxation, and surface chemistry modification.[5] In theory, the quantum mechanical details of plasmon-mediated hot carrier production may introduce a momentum-polarization correlation. Qualitatively, this coupling may enhance photocurrent along certain geometry-dependent directions at specific polarizations. This coupling tends to relax the escape cone considerations, by allowing final electron momenta that are usually disallowed by regular IPE processes. As a result, the yield may be increased up to the $R_{elec}$=0 case. However, simply relaxing the escape cone restriction without addressing the dark current and hot electron energy distribution limitations still results in energy-conversion efficiencies of a few percent at best (Figure 4.3). Because conventional photovoltaic cells do not absorb light below the bandgap energy, exploitation of IPE might be a potentially interesting method for capturing the otherwise unutilized part of the solar spectrum by placing the device behind a solar cell. In this arrangement, use of the metal/semiconductor device would be analogous to placing another, low band gap, semiconductor absorber and associated metallurgical junction in the optical path. The system instead relies on optical absorption and charge carrier excitation in the metal portion of the metal/semiconductor system (with a large band gap semiconductor, in principle), to produce the additional current and thus augment the device efficiency. As displayed in Figure 4.3, however, the yield and efficiency increase strongly as the photon energy is increased, and IPE is particularly inefficient for a spectrum that only includes energies below 1-2 eV. Hence such an approach would be more appropriate for larger-bandgap devices that normally only absorb ultraviolet light, such as a $TiO_2$-based photoelectrochemical system than for an additional absorber approach to a conventional solar cell arrangement. The metallic emitter was implicitly assumed to be a nanostructure that possessed plasmonic resonances so as to provide high absorption in a very thin structure and additionally to take advantage of the enhancements in scattering. The spatial distribution of hot electron generation may vary for such nanostructures, likely depending on the position of absorption based on the Poynting vector (Eqn 4.7). For example, a dipole antenna has the highest current and dissipation of energy near its center. The hot electrons may possibly instead be generated near areas of high field enhancement. Regardless, for these relatively low-energy hot electrons, the electron-electron scattering mean free path is on the same order as a plasmonic nanoparticle's dimensions, so the specific location of hot electron generation is of minor importance. The hot electron's initial momentum is however very important for the yield, as particles with a momentum vector inside the escape cone have a much higher probability of escape than those with

momentum vectors outside the escape cone.

### 4.6.2 Discussion of Efficiencies

The efficiencies presented here are somewhat lower than some previous published calculations. Wang and Melosh [22] considered power conversion using Kretschmann coupling to surface plasmon polaritons in a symmetric metal-insulator-metal geometry and obtained a calculated maximum efficiency of 2.7%. Their calculation assumed no escape cone restriction, no carrier reflections, a uniform energy distribution of excited carriers, and an energy-independent $\lambda_{e-e} = 56$ nm. The result is on the same order as that calculated here including however the assumption (for which the justification is unclear) of no escape cone restriction; similarly, White and Catchpole calculated a maxiumum efficiency of 8% by assuming that all hot electrons with sufficient energy in a perfect absorber were emitted.[23] Although it is tempting to assume that for nanostructured metallic absorbers the hot electron mean free path will be sufficiently longer than the device dimension and thus that the momentum escape cone restriction can be neglected, we have shown herein that even a small non-zero thickness (of 20 nm) of metal lowers the efficiency from 8% to 0.25% (c.f. Figure 4.3 blue solid line).

### 4.6.3 Drawbacks of the model

Finally, some deleterious effects were not included in our model. Scattering of hot electrons back into the emitter from the collector will reduce the yield, especially for diodes operated in forward bias with a weak electric field in the collector. Similarly, internal photoemission from the nominal collector to the emitter reduces the net photocurrent. Energetic losses due to phonon scattering also could somewhat reduce the yield. Emission of hot holes into the same material could take place if the collector is a low-bandgap semiconductor, reducing the yield. Last, interfacial and bulk defects present in real materials will lower the hot electron mean free paths and collection efficiency, decreasing the device efficiency.

## 4.7 Conclusions of IPE model calculations

The process of internal photoemission in which the absorbing material is a metal rather than a semiconductor was evaluated as a candidate for utilization in solar energy-conversion devices.

The semiclassical three-step model of internal photoemission for hot electrons over an energetic Schottky barrier was reviewed, and the energy-conversion efficiency was calculated considering the IPE photocurrent produced by complete absorption of a 5800 K blackbody spectrum in a nanoscale metal and the thermionic emission dark current as a function of voltage. The optimum efficiency values were found to be about 1 % for room-temperature operation with a metal similar to Au or Ag. The efficiency could approach 10 % if the escape cone restriction is removed, the mean free path of hot electrons is very long compared to the metal dimensions, and the illumination spectrum includes visible and ultraviolet light, in which case the efficiency is still limited by the thermionic dark current as well as by the distribution of hot electron energies (without modifying the metal's joint density of states). We have shown that from a semiclassical standpoint considering the momentum escape cone imposes a significant limit on efficiency even for nanostructures. Additional work to determine the applicability of this admittedly semiclassical model would be useful because the normal momentum requirement might be relaxed when considering quantum effects or surface chemistry. Alternatively, a device geometry in which light capture is decoupled from hot electron-hole generation in a metal bi-layer could possibly reduce the emitter thickness to the nm-size thickness required to justify neglecting the escape cone restriction.

## 4.8 Addressing drawbacks of the model: Can semiclassical calculations describe plasmon decays?

One of the biggest criticisms of the model and conclusions presented in this chapter has been the applicability of Fowler theory to describe plasmon decays and the use of experimental (and in some cases steady state) values for electron-electron and electron-phonon scattering. Subsequent chapters deal with quantum calculations of plasmonic hot carrier generation.

### 4.8.1 Quantum plasmonics and plasmon decays

A fundamental aspect of quantum plasmonics is the description of surface plasmons using quantum mechanics and the various size/time and experimental regimes where such descriptions are applicable. Treating the plasmon quantum mechanically, especially in the lossy regime is challenging.

Much of the work laying the foundations for quantization was carried out in the 1950s by Bohm and Pines, with work by Pines providing the very first model for quantizing plasma waves in metals[3]. Here, electrons in the conduction band were considered to be free electrons in an electron gas and the long-range correlations in their positions treated in terms of collective oscillations of the system as a whole. The quantized form of these collective matter oscillations plasmons were found to be bosons, with both wave-like and particle-like behavior, as expected for quantum excitations. The 'polariton', a joint state of light and matter was introduced by Hopfield[8], who provided a quantum model for the polarization field describing the response of matter to light. Depending on the type of matter, Hopfield called the field a 'phonon-polariton', 'plasmon-polariton' and so on, with the quanta as bosons. The concept of a surface plasma wave (SPW) was proposed soon after by Ritchie.[18] Several years later, Elson and Ritchie[6], and others used Hopfield's approach to provide the first quantized description of SPWs as 'SPPs'. Hydrodynamic effects were also included in the quantization[9]. Despite its great success, Hopfield's approach did not consider loss, which is caused by the scattering of electrons with background ions, phonons and themselves in the conduction band (ohmic loss) and at high frequencies by interband transitions.[21, 9]

### 4.8.2 Landau Damping

Landau damping [11] is a quantum mechanical process in which a plasmon quantum is transferred into a single electron–hole pair excitation on a timescale $\tau_L$ ranging from 1 to 100 fs. The plasmon-induced electric field, which represents a time-dependent perturbation on the conduction electrons of the metal, can induce transitions of electrons from occupied to unoccupied states. Landau damping is the typically invoked physical mechanism to describe contributions to the imaginary part of the dielectric permittivities of a metal. The link between Landau damping and calculations for generation of hot carriers perfomed (following the work in this chapter) are the subject of Chapter 6.

# Bibliography

Andrew, P. and W. L. Barnes. “Energy Transfer Across a Metal Film Mediated by Surface Plasmon Polaritons”. In: *Science* 306.5698 (Nov. 2004), pp. 1002–1005 (cit. on p. 42).

Atwater, Harry A. and Albert Polman. “Plasmonics for improved photovoltaic devices”. In: *Nat Mater* 9.3 (Mar. 2010), pp. 205–213. URL: http://dx.doi.org/10.1038/nmat2629 (cit. on p. 42).

Bohm, David and David Pines. “A Collective Description of Electron Interactions: III. Coulomb Interactions in a Degenerate Electron Gas”. In: *Phys. Rev.* 92 (3 Nov. 1953), pp. 609–625. DOI: 10.1103/PhysRev.92.609. URL: http://link.aps.org/doi/10.1103/PhysRev.92.609 (cit. on p. 57).

Brongersma, Mark L., Naomi J. Halas, and Peter Nordlander. “Plasmon-induced hot carrier science and technology”. In: *Nat Nano* 10.1 (Jan. 2015), pp. 25–34. URL: http://dx.doi.org/10.1038/nnano.2014.311 (cit. on pp. 41, 42).

Clavero, Cesar. “Plasmon-induced hot-electron generation at nanoparticle/metal-oxide interfaces for photovoltaic and photocatalytic devices”. In: *Nat Photon* 8.2 (Feb. 2014), pp. 95–103. URL: http://dx.doi.org/10.1038/nphoton.2013.238 (cit. on pp. 41, 54).

Elson, J. M. and R. H. Ritchie. “Photon Interactions at a Rough Metal Surface”. In: *Phys. Rev. B* 4 (12 Dec. 1971), pp. 4129–4138. DOI: 10.1103/PhysRevB.4.4129. URL: http://link.aps.org/doi/10.1103/PhysRevB.4.4129 (cit. on p. 57).

Fowler, R. H. “The Analysis of Photoelectric Sensitivity Curves for Clean Metals at Various Temperatures”. In: *Phys. Rev.* 38 (1 July 1931), pp. 45–56. DOI: 10.1103/PhysRev.38.45. URL: http://link.aps.org/doi/10.1103/PhysRev.38.45 (cit. on p. 44).

Hopfield, J. J. "Theory of the Contribution of Excitons to the Complex Dielectric Constant of Crystals". In: *Phys. Rev.* 112 (5 Dec. 1958), pp. 1555–1567. DOI: 10.1103/PhysRev.112.1555. URL: http://link.aps.org/doi/10.1103/PhysRev.112.1555 (cit. on p. 57).

Huttner, Bruno and Stephen M. Barnett. "Quantization of the electromagnetic field in dielectrics". In: *Phys. Rev. A* 46 (7 Oct. 1992), pp. 4306–4322. DOI: 10.1103/PhysRevA.46.4306. URL: http://link.aps.org/doi/10.1103/PhysRevA.46.4306 (cit. on p. 57).

Inouye, Hideyuki et al. "Ultrafast dynamics of nonequilibrium electrons in a gold nanoparticle system". In: *Phys. Rev. B* 57 (18 May 1998), pp. 11334–11340. DOI: 10.1103/PhysRevB.57.11334. URL: http://link.aps.org/doi/10.1103/PhysRevB.57.11334 (cit. on pp. 42, 44).

Landau, L. "On the vibration of the electronic plasma". In: *J. Phys. USSR* 10 (1946) (cit. on p. 57).

Leenheer, Andrew J. et al. "Solar energy conversion via hot electron internal photoemission in metallic nanostructures: Efficiency estimates". In: *Journal of Applied Physics* 115.13, 134301 (2014), pages. DOI: http://dx.doi.org/10.1063/1.4870040. URL: http://scitation.aip.org/content/aip/journal/jap/115/13/10.1063/1.4870040 (cit. on p. 42).

McFarland, Eric W. and Jing Tang. "A photovoltaic device structure based on internal electron emission". In: *Nature* 421.6923 (Feb. 6, 2003), pp. 616–618. URL: http://dx.doi.org/10.1038/nature01316 (cit. on p. 41).

Moskovits, Martin. "The case for plasmon-derived hot carrier devices". In: *Nat Nano* 10.1 (Jan. 2015), pp. 6–8. URL: http://dx.doi.org/10.1038/nnano.2014.280 (cit. on p. 41).

Mukherjee, Shaunak et al. "Hot Electrons Do the Impossible: Plasmon-Induced Dissociation of H2 on Au". In: *Nano Letters* 13.1 (Jan. 2013), pp. 240–247. DOI: 10.1021/nl303940z. URL: http://dx.doi.org/10.1021/nl303940z (cit. on pp. 41, 54).

Mukherjee, Shaunak et al. "Hot-Electron-Induced Dissociation of H2 on Gold Nanoparticles Supported on SiO2". In: *Journal of the American Chemical Society* 136.1 (Jan. 2014), pp. 64–67. DOI: 10.1021/ja411017b. URL: http://pubs.acs.org/doi/abs/10.1021/ja411017b (cit. on p. 41).

Pillai, S. et al. "Surface plasmon enhanced silicon solar cells". In: *Journal of Applied Physics* 101.9, 093105 (2007), pages. DOI: http://dx.doi.org/10.1063/1.2734885. URL: http://scitation.aip.org/content/aip/journal/jap/101/9/10.1063/1.2734885 (cit. on p. 42).

Ritchie, R. H. "Plasma Losses by Fast Electrons in Thin Films". In: *Phys. Rev.* 106 (5 June 1957), pp. 874–881. DOI: 10.1103/PhysRev.106.874. URL: http://link.aps.org/doi/10.1103/PhysRev.106.874 (cit. on p. 57).

Ross, Robert T. and Arthur J. Nozik. "Efficiency of hot-carrier solar energy converters". In: *Journal of Applied Physics* 53.5 (1982), pp. 3813–3818 (cit. on p. 41).

Shockley, William and Hans J. Queisser. "Detailed Balance Limit of Efficiency of p-n Junction Solar Cells". In: *Journal of Applied Physics* 32.3 (1961), pp. 510–519 (cit. on p. 41).

Sundararaman, Ravishankar et al. "Theoretical predictions for hot-carrier generation from surface plasmon decay". In: *Nat Commun* 5 (Dec. 16, 2014). URL: http://dx.doi.org/10.1038/ncomms6788 (cit. on p. 57).

Wang, Fuming and Nicholas A. Melosh. "Plasmonic Energy Collection through Hot Carrier Extraction". In: *Nano Letters* 11.12 (2011). PMID: 22023372, pp. 5426–5430. DOI: 10.1021/nl203196z. eprint: http://dx.doi.org/10.1021/nl203196z. URL: http://dx.doi.org/10.1021/nl203196z (cit. on pp. 41, 55).

White, Thomas P. and Kylie R. Catchpole. "Plasmon-enhanced internal photoemission for photovoltaics: Theoretical efficiency limits". In: *Applied Physics Letters* 101.7, 073905 (2012), pages. DOI: http://dx.doi.org/10.1063/1.4746425 (cit. on pp. 42, 44, 55).

# 5

# Theoretical Predictions for Hot-carrier Generation from Surface Plasmon Decay

*All that glisters may not be gold, but at least it contains free electrons.*
*(Lecture at Birkbeck College, University of London, 1960)*

– John Desmond Bernal

## 5.1 Chapter Overview:

Decay of surface plasmons to hot carriers finds a wide variety of applications in energy conversion, photocatalysis and photodetection. However, a detailed theoretical description of plasmonic hot carrier generation in real materials has remained incomplete. Here we report predictions for the prompt distributions of excited 'hot' electrons and holes generated by plasmon decay, prior to inelastic relaxation, using a quantized plasmon model with detailed electronic structure. We find that carrier energy distributions are sensitive to the electronic band structure of the metal: gold and copper produce holes hotter than electrons by 1-2 eV, while silver and aluminum distribute energies more equitably between electrons and holes. Momentum-direction distributions for hot carriers are anisotropic, dominated by the plasmon polarization for aluminum and by the crystal orientation for noble metals. We show that in thin metallic films, intraband transitions can alter the carrier distributions, producing hotter electrons in gold, but interband transitions remain dominant.

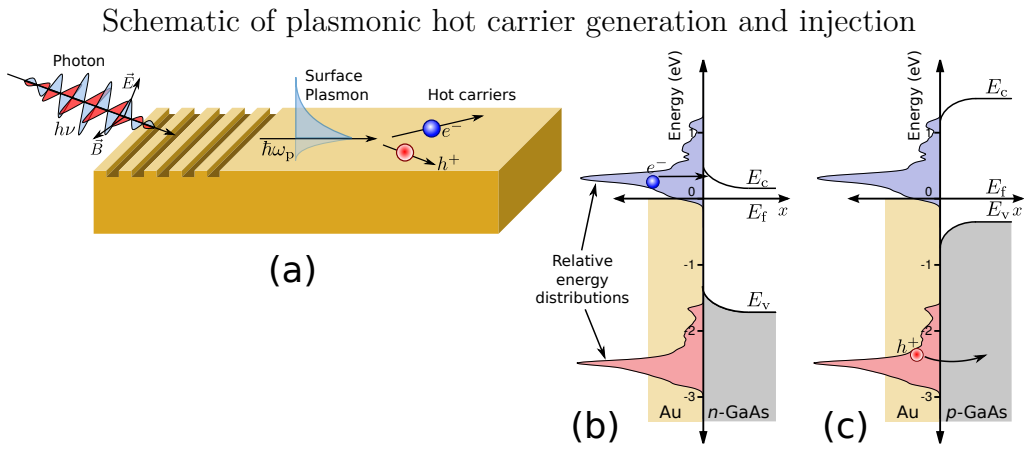


Figure 5.1: (a) Schematic for optical excitation of surface plasmons followed by decay to hot carriers, (b) tunneling of plasmonic hot electrons from gold through a Schottky barrier into $n$-type Gallium Arsenide using the predicted carrier distribution from Figure 5.3(d) and typical experimental band offsets [24], and (c) barrier-less injection of plasmonic hot holes from gold into $p$-type Gallium Arsenide. ($E_f$ is the Fermi energy, $E_c$ the conduction band minimum and $E_v$ the valence band maximum energy.)

## 5.2 Decay of surface plasmons in the interband limit

Plasmons are collective oscillations of electrons that couple to electromagnetic fields. They exhibit wave-like as well as particle-like behavior[15], support intense electromagnetic field concentrations[28], and provide a pathway to couple optical energy from free space in nanoscale systems[2]. Surface plasmons, electromagnetic modes confined to the surface of a conductor-dielectric interface, have sparked recent interest because of their quantum nature[12, 34] and their broad range of applications, including solar energy harvesting[17], non-linear optics, tunable-photodetectors[14], and spectroscopy. Decay of plasmons to hot carriers has recently attracted considerable interest[4] due to applications in energy conversion, photocatalysis and photodetection[29].

Surface plasmons can decay either radiatively[10] via emission of a photon or non-radiatively through the generation of excited carriers, typically referred to as hot carriers. These photo-excited hot carriers in metals could be used to directly drive energetically demanding chemical reactions[23], or they could be transferred to a semiconductor for use in photovoltaics[33, 35] and photoelectrochemical systems[22, 17]. At a metal-semiconductor interface, plasmonic hot-carrier collection over a tunable Schottky barrier allows the collection of photons with energies lower than

the interband threshold of the semiconductor, thereby enabling additional energy harvesting[]. These excited carriers, both electrons and holes, can be injected into other materials for example graphene[9] and $MoS_2$[13] thereby enabling plasmonic hot carrier induced doping and phase transitions.

Despite the significant experimental work in this direction, a complete theoretical understanding of plasmon-driven hot carrier generation with electronic structure details has been evasive. Understanding the initial energy distribution of carriers generated by plasmon decay, before inelastic relaxation, is the first key step towards exploiting these phenomena. Theoretical studies of plasmonic systems have traditionally focused on their optical response, including quantum jellium models of nanostructured systems such as nanoparticle dimers[30, 38, 18, 8], and detailed time-dependent density-functional calculations of short-wavelength surface plasmons on noble metal surfaces[37]. Recently, the initial hot carrier distribution generated by plasmon decay has been estimated within a simple electron gas model for various geometries[11], and within a jellium model for silver nanoparticles and nanoshells.[19] These models provide insight into the mechanisms of plasmonic hot carrier generation, but do not capture the material dependence of this process and miss interband transitions in noble metals since they preclude transitions involving $d$ bands.

In this Chapter we combine quantized plasmon modes from experimental dielectric functions with electronic states from first-principles density functional theory, in order to calculate the initial distribution of hot carriers in *real* materials. We first examine direct electron excitations generated by the decay of surface plasmon polaritons on planar metal-dielectric interfaces, as shown schematically in Figure 6.1(a). (Note that the surface plasmon and the initial photon have the same energy, and a coupling geometry such as a grating provides the change in momentum.[6]) This allows us to explore the effects of the electronic structure of the metal on the generated carrier distributions, independent from other effects such as geometry. Additionally, we focus on interband transitions which dominate at higher plasmon energies since these are expected to be more sensitive to the electronic structure than intraband transitions; the latter dominate at lower plasmon energies and have been described within simplified jellium models.[19] Finally, we analyze the effects of geometry on the generated hot carrier distribution in real materials by studying the decay of plasmon modes in thin metallic films of varying thickness.

## 5.3 Interband transition rate formalism

We describe the surface plasmon using an explicit quantization of the surface modes [Tame:2008kl, Archambault:2010kl, Elson:1971fk] derived from an experimental dielectric function [ExptDielFunc-AppliedOptics98].

The vector potential operator for plasmons on the surface of a semi-infinite slab (with normal along the $z$-direction) is $\hat{\mathbf{A}}(\mathbf{r},t) = \sum_{\mathbf{k}} \mathbf{u}_{\mathbf{k}}(\mathbf{r},t)\hat{\mathbf{a}}_{\mathbf{k}} + h.c.$, in terms of creation and annihilation operators, $\hat{\mathbf{a}}^{\dagger}_{\mathbf{k}}$ and $\hat{\mathbf{a}}_{\mathbf{k}}$, and the normalized mode functions of wave-vector $\mathbf{k}$ and angular frequency $\omega$,

$$\mathbf{u}_{\mathbf{k}}(\mathbf{r},t) = \sqrt{\frac{2\pi\hbar}{\omega S L(\omega)}}\left(\hat{\mathbf{k}} - \frac{k\hat{\mathbf{z}}}{\gamma(z)}\right) e^{i(\gamma(z)z + \mathbf{k}\cdot\mathbf{r} - \omega t)}. \tag{5.1}$$

The modes satisfy the dispersion relation $k = \frac{\omega}{c}\sqrt{\epsilon(\omega)/(\epsilon(\omega)+1)}$, where $\epsilon(\omega)$ is the experimental dielectric function of the metal. The $z$-wavenumber satisfies $\gamma^2(z) = \epsilon(z)\omega^2/c^2 - k^2$, where $\epsilon(z) = \epsilon(\omega)$ for $z < 0$ and 1 for $z > 0$, and with the sign of $\mathrm{Im}\gamma(z)$ set so that the modes decay away from the surface. Above, $S$ is a test area with periodic boundary conditions for discretizing the modes and $L(\omega)$ is a normalization length chosen so that each mode has energy $\hbar\omega$. (See Ref. Archambault:2010kl for details.) While this neglects the possibility of nonlocal effects in the dielectric matrix, such an approximation is valid at the wavelengths of interest.

Next, given an approximation of the quasiparticle orbitals $\psi^{\sigma}_{\mathbf{q}n}(\mathbf{r})$ and energies $\varepsilon_{\mathbf{q}n}$ of the metal, the electron field operator is $\hat{\mathbf{\Psi}}_{\sigma}(\mathbf{r},t) = \sum_{\mathbf{q}n} \psi^{\sigma}_{\mathbf{q}n}(\mathbf{r}) e^{-i\varepsilon_{\mathbf{q}n}t/\hbar}\hat{\mathbf{c}}_{\mathbf{q}n}$. Here, $\hat{\mathbf{c}}_{\mathbf{q}n}$ and $\hat{\mathbf{c}}^{\dagger}_{\mathbf{q}n}$ are Fermionic creation and annihilation operators for electrons with wave-vector $\mathbf{q}$ and band-index $n$. We have included the spinor index $\sigma$ in the orbitals in order to fully treat relativistic effects such as spin-orbit coupling, when necessary.

Finally, we approximate the plasmon-quasiparticle interaction Hamiltonian using the lowest order unrenormalized vertex, $\hat{\mathbf{H}}_{\mathrm{int}} = \frac{e}{2m_e}\sum_{\sigma}\int d\mathbf{r}\hat{\mathbf{\Psi}}^{\dagger}_{\sigma}\hat{\mathbf{A}}\cdot\hat{\mathbf{p}}\hat{\mathbf{\Psi}}_{\sigma}$, where $\hat{\mathbf{p}}$ is the electronic momentum operator. Fermi's golden rule for the decay of a single plasmon with wave-vector $\mathbf{k}$ and angular frequency $\omega$ to electron-hole pairs via interband transitions then reduces to

$$\Gamma = \frac{\pi^2}{2\omega L(\omega)|\gamma(z<0)|}\int_{\mathrm{BZ}}\frac{d\mathbf{q}}{(2\pi)^3}\sum_{n'n}(1-f_{\mathbf{q}n'})f_{\mathbf{q}n}\delta(\varepsilon_{\mathbf{q}n'}-\varepsilon_{\mathbf{q}n}-\hbar\omega) \times\left|\left(\hat{\mathbf{k}}-\frac{k\hat{\mathbf{z}}}{\gamma(z<0)}\right)\cdot\sum_{\sigma}\int_{\Omega}d\mathbf{r}\psi^{\sigma *}_{\mathbf{q}n'}(\mathbf{r})\frac{e\hbar\boldsymbol{\nabla}}{im_{\mathrm{e}}}\psi^{\sigma}_{\mathbf{q}n}(\mathbf{r})\right|^2, \quad (5.2)$$

where $f_{\mathbf{q}n}$ are the occupation factors of the quasiparticles in the Fermi sea. The key approximation above is that the plasmon mode function varies slowly on the atomic scale (interband approximation).

## 5.4 Electronic structure method selection

To calculate the carrier distributions from plasmon decays in real materials using (5.2), we need a sufficiently accurate prescription for the quasiparticle orbitals and energies. Figure 5.2 compares the accuracy of different electronic structure methods for the noble metals copper, silver and gold. The different methods produce identical results for aluminum since it is a nearly-free electron metal; we omit that comparison for brevity and select the PBEsol generalized-gradient approximation[25] within density-functional theory.

In contrast, for the noble metals, generalized-gradient approximations such as PBEsol predict the $d$-band positions to be closer to the Fermi level than experiment because of the self-interaction error for localized electrons. The GLLB-sc orbital-dependent functional[16] partially remedies this situation, as shown by a recent density-functional study of plasmon dispersions on noble metal surfaces.[37] However, Figure 5.2 shows that the band structure predicted by this functional still exhibits significant deviations from angle-resolved photoemission measurements.[5, 36, 21] These deviations are largest ($\sim 0.5$ eV) near the $L$-point in the Brillouin zone, and this region of the Brillouin zone is particularly active for interband transitions in these metals. Many-body perturbation theory methods, such as the quasiparticle self-consistent $GW$ approximation, significantly improve the agreement with experiment as shown for gold in Figure 5.2(c) ($GW$ results from Rangel et al.[27]), however the error near the $L$-point remains large ($\sim 0.5$ eV).

We find that the DFT+$U$ method,[7] which improves the description of localized electrons with a local semi-empirical correction on each atom, yields the best agreement ($\sim 0.1$ eV) to the quasiparticle bandstructure of all three noble metals (indicated by PBEsol+$U$ in Figure 5.2, since we

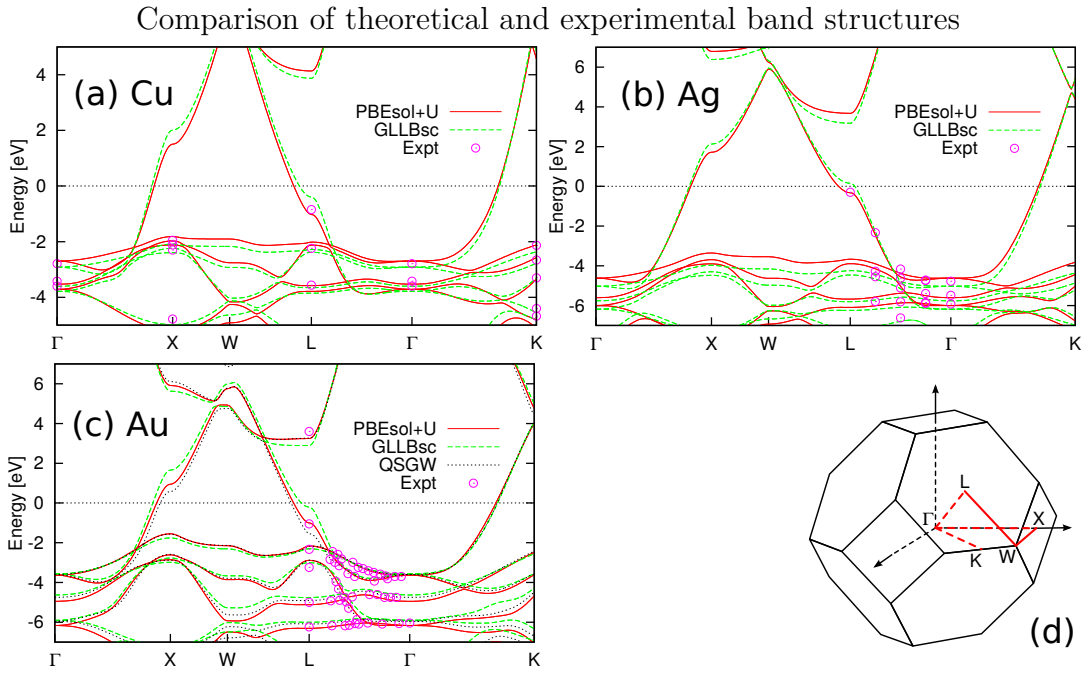


Figure 5.2: Theoretical band structures for (a) copper (b) silver and (c) gold as predicted by different density functional approximations, compared to angle-resolved ultraviolet photoemission measurements[5, 36, 21] and quasiparticle self-consistent GW calculations[27]. Panel (d) shows the high symmetry paths in the Brillouin zone along which the band structures are plotted. All calculations account for relativistic effects including spin-orbit coupling. The PBEsol+$U$ approximation, with $U$ fit to the experimental Γ-point energies, provides the best overall agreement with the experimental data for all three noble metals and particularly improves upon the accuracy of the other methods near the L-point.

combine the $U$ correction with the PBEsol density functional). We pick the value of $U$ to reproduce the experimental energies at the Γ-point, which results in $U = 1.63$, 2.45 and 2.04 eV for copper, silver and gold respectively.

The calculations presented here account for relativistic effects including spin-orbit coupling fully self-consistently. The spin-orbit splitting at the $X$-point is particularly relevant, since it determines the inter-band threshold energy. The magnitude of the effect is $\sim 0.5$ eV in gold, $\sim 0.2$ eV in silver and $\sim 0.1$ eV in copper. Therefore, the inclusion of spin-orbit splitting is critical in calculations of optical transitions in gold, still quite significant for silver and negligible at the achievable accuracy for copper (and aluminum).

## 5.5 Hot carrier distributions from surface plasmon decay

Substituting the electronic states and energies from the PBEsol+U density functional method in (5.2), allows us to predict accurate carrier distributions. We histogram the contributions to the decay rate Γ by the electron (final state) and hole (initial state) energies to generate the distributions shown in Fig 5.3, and by the carrier energies as well as momentum directions to generate Fig 5.4. Energy conservation determines which regions of the Brillouin zone contribute to the plasmon decay, and the top panels of Fig 5.3 annotate the allowed transitions for each metal at selected energies.

For aluminum, the band crossing close to the Fermi level near the W point allows interband transitions that originate from valence band states with energies ranging continuously from the Fermi level to $\hbar\omega$ below it. Consequently, surface plasmon decay results in both hot electrons and holes with continuous energy distributions that extend from zero energy to the plasmon energy, as seen in the bottom panel of Fig 5.3(a). Additional transitions near the K point contribute predominantly to hot holes with energies $> 2$ eV, and lead to the moderate asymmetry between the electron and hole energy distributions.

For silver, the lowest energy interband transitions, originating from the $d$ bands at the X and L points as well as from the Fermi level at the L point, all appear at $\sim 3.6$ eV. Consequently the decay of a plasmon of that energy produces bimodal energy distributions for both the electrons and holes as shown in Fig 5.3(b).

In copper and gold, the allowed interband transitions near the resonant surface plasmon polariton

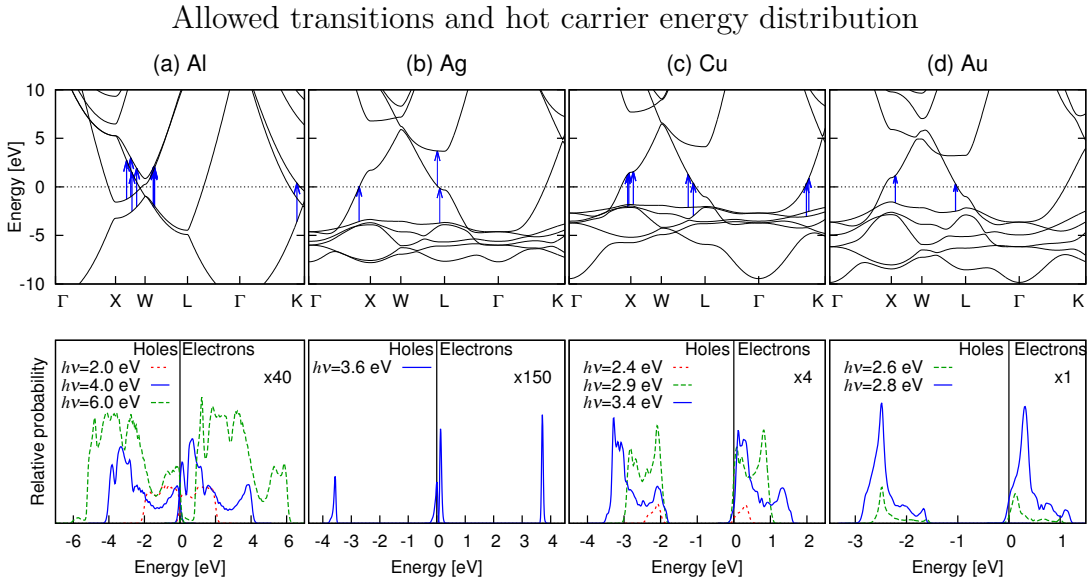


Figure 5.3: PBEsol+$U$ band structure and predicted plasmonic hot carrier energy distributions for (a) aluminum (b) silver (c) copper and (d) gold. The bottom panels show the energy distribution of hot electrons (positive energies relative to Fermi level at 0) and hot holes (negative energies) for various photon and plasmon energies, $h\nu$. The top panels show the band-structure and arrows mark the allowed transitions for the plasmon energy plotted with a solid line in the corresponding bottom panel. Contrast the almost uniform energy distribution of electron and hole energies in aluminum, with the hole-dominant energy distribution in copper and gold and the bimodal hot-hole and hot-electron distributions in silver due to the position of the $d$-bands.

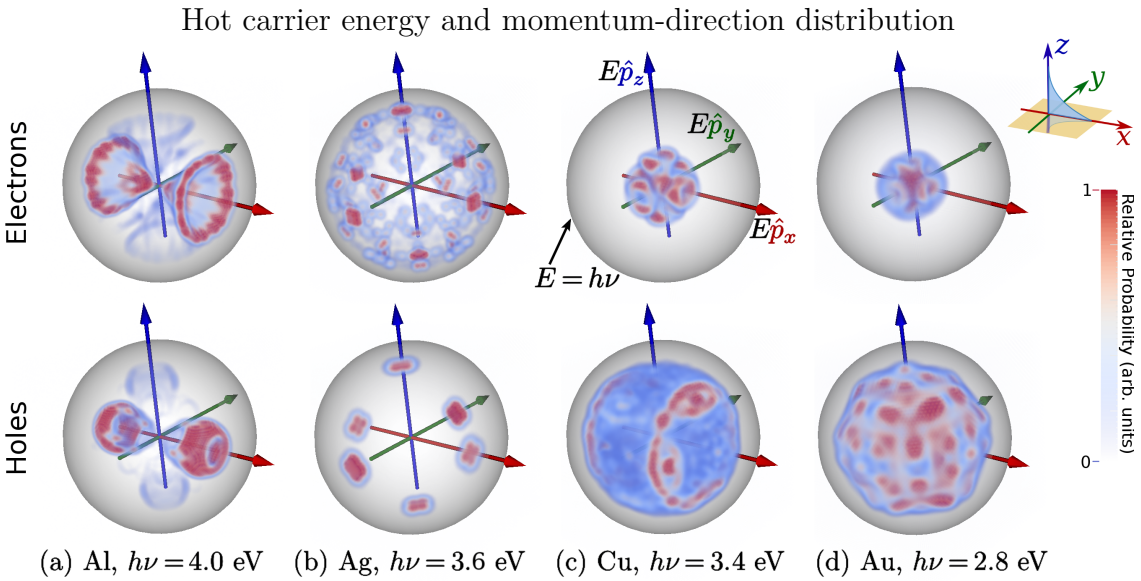


Figure 5.4: Plasmonic hot carrier energy and momentum-direction distribution in (a) aluminum (b) silver (c) copper and (d) gold. The radial coordinate in each panel is the carrier energy relative to the Fermi level with the spherical shell indicating the plasmon (photon) energy, $h\nu$, while the angular coordinates correspond to the carrier momentum direction. The asymmetry in electron and hole energies in the noble metals from Fig 5.3 is manifest in the radial extent of the corresponding probability clouds here. None of the metals exhibit the isotropic orientation distribution assumed in the Fowler theory.

energies occur near the X and L points for both metals, and additionally near the K point for copper, as shown in Fig 5.3(c) and (d). Notice that all these transitions originate in the $d$-bands that are approximately $E_t = 2$ eV below the Fermi level. Consequently, for these metals, the generated holes are on average more energetic than the electrons by $E_t$.

The asymmetry between energy distributions for plasmonic hot electrons and holes in copper and gold has important consequences for collection efficiencies across a metal-semiconductor interface. Consider, for example, the gold to n-type gallium arsenide Schottky junction in Fig 6.1(b), which includes the predicted hot carrier distributions from Fig 5.3(d). Most of the hot electrons are not sufficiently energetic to overcome the Schottky barrier, and would either have to tunnel through the barrier or would require an additional thermal boost to overcome it. In contrast, in the corresponding junction to p-type gallium arsenide shown in Fig 6.1(c), all the holes are sufficiently energetic to cross into the semiconductor. This barrier-less collection of holes would exhibit significantly higher efficiency and would require lower biases than electron collection. Combining the results of Fig 5.3 with this picture, gold and copper are ideally suited for hot hole injection, whereas silver and aluminum are capable of both.

The nature of transitions accessible by the plasmon also affects the angular distribution of the excited carriers. For the four metals considered above, Fig 5.4 illustrates the momentum direction and energy distribution for hot carriers generated by the decay of a surface plasmon polariton propagating on a [001] surface along the $x$-direction. The radial direction indicates carrier energy whereas the orientation indicates the carrier momentum direction. The maximum energy, illustrated by the gray sphere, corresponds to the photon energy, and the color scheme indicates the relative probability density of carriers at that energy and momentum direction.

The electric field due to such a plasmon is predominantly along the $x$-direction, and for a free-electron metal we expect a dipole-antenna like momentum distribution that peaks along the field directions. Only the electron and hole distributions in aluminum exhibit such an orientation dependence; the remaining metals deviate significantly from that idealized prediction. For the noble metals, the allowed transitions are on a surface in $k$-space containing the X and L points, which contributes carriers in all directions, but with a strong anisotropy dominated by the crystal directions rather than the plasmon field.

The collection efficiency of hot carriers in plasmonic structures depends on both the initial distribution and transport of the carriers. In faceted structures smaller than the carrier mean free

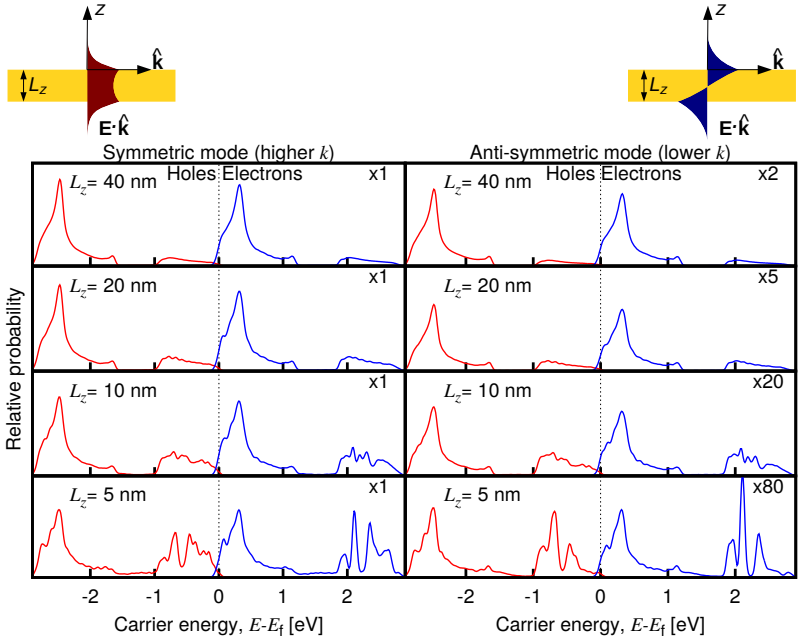


Figure 5.5: Energy distributions of hot carriers (electrons in blue, holes in red) generated by the decay of symmetric and antisymmetric plasmon modes of energy 2.8 eV on gold thin films of various thicknesses. As the film thickness decreases, the relative probability for generating hot electrons via geometry-assisted intraband transitions (compared to hot holes generated via interband transitions) increases.

path, ballistic transport, which preserves the momentum direction, is significant compared to diffusive transport. The crystal-orientation dependent anisotropy in the initial momentum distribution would therefore become particularly important for such structures.

## 5.6 Geometry effects in decay of thin-film plasmons

Above, we considered the decay of surface plasmon polaritons on semi-infinite metal slabs in order to minimize geometry effects and focus on the effects of electronic structure. In nano-confined geometries, crystal momentum or $\mathbf{q}$ is no longer a good quantum number due to the uncertainty principle and therefore the transitions excited by plasmon decay no longer need to be vertical unlike the situation in Figure 5.3. This opens up the possibility of geometry-assisted intraband transitions without involving phonons. This mode of localized plasmon decay has been studied within the

context of jellium models with simplified electronic structure;[11, 19] here we analyze this decay mode including the full electronic structure of the plasmonic metal.

Direct electronic structure calculations for nanoparticles require significant computational effort, however, and we therefore make two simplifications to enable practical calculations for systems of experimentally relevant sizes. First, we consider thin films which are of finite thickness along one dimension; the electronic structure calculation can then exploit Bloch's theorem in the remaining two periodic directions. The resulting predictions would then be a lower bound on the corresponding geometry effect in nanoparticles which are confined in all three dimensions. Second, we adopt an *ab initio* tight-binding approximation for the electronic structure of the thin film using the density-functional Hamiltonian expressed in the basis of maximally localized Wannier functions.[20, 31] This approach reproduces the full density-functional band structure of the bulk material exactly by construction, but approximates geometry effects since changes in orbital shapes within a unit cell are neglected.

A metal film of finite thickness supports symmetric and antisymmetric plasmon modes (with respect to $\mathbf{E} \cdot \hat{\mathbf{k}}$, the electric field along the propagation direction) as shown schematically in the top insets of Figure 5.5. We analytically construct the vector potential for one quantum of each of these modes,[3] analogous to (5.1), and use Fermi's golden rule to calculate the rate of their direct decay to electron hole-pairs with the matrix elements and electronic energies obtained from the Wannier representation. See the Methods section for details.

Figure 5.5 shows the resulting electron and hole energy distributions generated from the decay of plasmons in gold films. The results for both the symmetric and antisymmetric plasmon modes on a film of thickness 40 nm resemble that for the semi-infinite slab from Figure 5.3(d): most of the energy is deposited in the hot holes. However, with decreasing film thickness, the finite-thickness geometrical effects become stronger and the probability of generating hot electrons via intraband transitions increases. The effect is particularly pronounced for the antisymmetric mode because this lower wave-vector mode becomes more light-like with a smaller fraction of the field in the interior of the metal which lowers the contribution of the interband transitions (note the scale factors in the right hand panels of Figure 5.5).

This analysis allows one to weigh the relative importance of the interband transitions and geometry-assisted intraband transitions. Confining geometries smaller than 10 nm enable finite probabilities of intraband transitions and allow the generation of hotter electrons than allowed in

the hole-dominant bulk copper or gold. However, interband transitions are still responsible for a significant fraction of the generated carriers, and hence an appropriate choice of material (as discussed in section 5.5) is important to maximize the efficiency of hot electron or hole generation.

## 5.7 Discussion

We have reported first-principles calculations that describe plasmon-mediated hot carrier generation in aluminum, gold, silver and copper. These calculations illustrate that the generated carrier profile is extremely sensitive to the details of the electronic band structure, especially to the position of the *d*-bands in silver, copper and gold relative to unoccupied states above the Fermi level. Copper and gold generate hot holes that are much more energetic than the electrons, silver produces narrow energy distributions of hot holes as well as hot electrons, while aluminum generates continuous energy distributions of holes and electrons. These findings inform material selection for efficiently collecting carriers of a specific type and energy at metal-semiconductor interfaces or in surface-adsorbed molecular species.

Geometry of the plasmonic structure also plays an important role in determining the efficiency of carrier generation and collection. Nano-confinement effects allow the generation of hotter electrons in copper and gold via geometry-induced intraband transitions. However, interband transitions, which depend strongly on the electronic band structure, still dominate the initial energy distribution. The initial momentum distribution of the carriers depends on both the crystallographic orientation of the metal and plasmon polarization. The net efficiency of carrier collection in a specific geometry depends on this initial distribution as well as the subsequent transport of the carriers to the surface. Therefore, assessing and optimizing carrier collection efficiency of plasmonic nano-structures additionally require models for the transport of hot carriers, a subject for future study.

# Methods

## 5.8 Computational details

We perform density-functional calculations for face-centered cubic aluminum, silver, copper and gold in the plane-wave electronic density functional software, JDFTx [32], using full-relativistic

norm-conserving pseudopotentials at a kinetic energy cutoff of 30 Hartrees (816 eV) and at the experimental lattice geometry. We use the PBEsol[25] exchange-correlation approximation along with a rotationally-invariant DFT+U correction[7] for the $d$-electrons, with $U = 1.63$ eV for copper, 2.45 eV for silver and 2.04 eV for gold fit to reproduce experimental photoemission data (no $U$ correction for aluminum).

We use Kohn-Sham eigenvalues, Fermi occupations and momentum matrix elements on a dense $128^3$ sampling of the Brillouin zone to calculate the inter-band transition rate of plasmon mode equation (5.1) using equation (5.2). We use experimental dielectric functions from Ref. [26], parametrized as a sum of Lorentz-Drude responses, to determine the plasmon mode. We replace the energy-conserving $\delta$-function in equation (5.2) with a normalized Gaussian of width $\sim k_{\mathrm{B}}T = 0.026$ eV in order to accommodate the discrete $k$-point sum that replaces the Brillouin-zone integral. We histogram the contributions to the total transition rate $\Gamma$ in terms of the electron and hole energies and momenta to generate the distributions plotted in Figs 5.3 and 5.4.

For the thin-film calculations, we generate the Wannier functions, Hamiltonian and matrix elements using a coarser $10^3$ sampling of the Brillouin zone, which results in an *ab initio* tight-binding like Hamiltonian with a range of approximately 5 unit cells in each direction. We then calculate the electronic states of the thin film in the Wannier basis and calculate the transition rate of plasmon modes equations (5.8–5.13) using equation (5.14), histogrammed by electron and hole energies to generate the distributions shown in 5.5.

## Surface plasmon polariton decay rate

Here we sketch the derivation of equation (5.2), the decay rate of a single surface plasmon to electron-hole pairs via interband transitions. The initial state for this decay is the Fermi sea of quasiparticles and a single surface plasmon with wave vector $\mathbf{k}$, which we can denote by $|\mathbf{k}\rangle = \hat{\mathbf{a}}^\dagger_{\mathbf{k}}|0\rangle$, if we define $|0\rangle$ to consist of the vacuum of surface plasmons and the Fermi sea. The possible final states each consist of a single electron-hole pair on the Fermi sea and no plasmon, $|\mathbf{q}n, \mathbf{q}'n'\rangle = \hat{\mathbf{c}}^\dagger_{\mathbf{q}'n'}\hat{\mathbf{c}}_{\mathbf{q}n}|0\rangle/\sqrt{(1-f_{\mathbf{q}'n'})f_{\mathbf{q}n}}$, and are therefore labeled by the electron and hole wave-vectors $\mathbf{q}, \mathbf{q}'$ and band indices $n, n'$. (The occupation factors normalize the final states, since $\{\hat{\mathbf{c}}_{\mathbf{q}n}, \hat{\mathbf{c}}^\dagger_{\mathbf{q}'n'}\} = \delta_{\mathbf{q}\mathbf{q}'}\delta_{nn'}$ and $f_{\mathbf{q}n} \equiv \langle 0|\hat{\mathbf{c}}^\dagger_{\mathbf{q}n}\hat{\mathbf{c}}_{\mathbf{q}n}|0\rangle$.)

Fermi's golden rule for this decay process is therefore

$$\Gamma = \frac{2\pi}{\hbar} \sum_{\mathbf{q}'\mathbf{q}n'n} \delta(\varepsilon_{\mathbf{q}'n'} - \varepsilon_{\mathbf{q}n} - \hbar\omega) \left| M^{\mathbf{k}}_{\mathbf{q}n,\mathbf{q}'n'} \right|^2, \tag{5.3}$$

with the transition matrix element

$$\begin{aligned} M^{\mathbf{k}}_{\mathbf{q}n,\mathbf{q}'n'} &:= \langle \mathbf{q}n, \mathbf{q}'n' | \hat{\mathbf{H}}_{\text{int}} | \mathbf{k} \rangle \\ &= \frac{\langle 0 | \hat{\mathbf{c}}^\dagger_{\mathbf{q}n} \hat{\mathbf{c}}_{\mathbf{q}'n'}}{\sqrt{(1 - f_{\mathbf{q}'n'}) f_{\mathbf{q}n}}} \left[ \frac{e}{2m_{\text{e}}} \sum_\sigma \int d\mathbf{r} \hat{\mathbf{\Psi}}^\dagger_\sigma \hat{\mathbf{A}} \cdot \hat{\mathbf{p}} \hat{\mathbf{\Psi}}_\sigma \right] \hat{\mathbf{a}}^\dagger_{\mathbf{k}} | 0 \rangle \\ &= \sqrt{(1 - f_{\mathbf{q}'n'}) f_{\mathbf{q}n}} \left[ \frac{\Omega}{L_z S} \sum_\sigma \int_{L_z S} d\mathbf{r} \psi^{\sigma *}_{\mathbf{q}'n'}(\mathbf{r}) \frac{e}{2m_{\text{e}}} \mathbf{u}_{\mathbf{k}}(\mathbf{r}, 0) \cdot \frac{\hbar \nabla}{i} \psi^\sigma_{\mathbf{q}n}(\mathbf{r}) \right]. \end{aligned} \tag{5.4}$$

The expectation value of the plasmon and quasiparticle creation and annihilation operators in the second line above against the vacuum and Fermi sea reduces to $(1 - f_{\mathbf{q}'n'}) f_{\mathbf{q}n}$. In the final line above, $S$ is the surface area for plasmon quantization [1] and we quantize the electrons on a box of area $S$ on the surface that extends a depth $L_z$ into the surface, with $L_z \gg 1/|\gamma(z < 0)|$, the decay length of the plasmon mode in the metal. The factor $\Omega/(L_z S)$ above accounts for the fact that the orbitals are normalized on the unit cell of volume $\Omega$ instead of on the quantization volume.

Substituting the plasmon mode function given by (5.1), noting that it varies slowly on the length scale of the orbitals (both $\mathbf{k}$ and $|\gamma(z < 0)|$ are small in atomic units), and splitting $\mathbf{q} = q_z \hat{\mathbf{z}} + \mathbf{q}_\parallel$, the normal and surface-plane components, the matrix element reduces to

$$\begin{aligned} M^{\mathbf{k}}_{\mathbf{q}n,\mathbf{q}'n'} := \sqrt{(1 - f_{\mathbf{q}'n'}) f_{\mathbf{q}n}} \frac{d_z}{2L_z} \sqrt{\frac{2\pi\hbar}{\omega S L(\omega)}} \left( \hat{\mathbf{k}} - \frac{k\hat{\mathbf{z}}}{\gamma(z < 0)} \right) \cdot \delta_{\mathbf{q}'_\parallel \mathbf{q}_\parallel} \\ \times \frac{1}{1 - e^{-d_z(|\gamma(z<0)| + i(q_z - q'_z))}} \sum_\sigma \int_\Omega d\mathbf{r} \psi^{\sigma *}_{\mathbf{q}'n'}(\mathbf{r}) \frac{e\hbar\nabla}{i m_{\text{e}}} \psi^\sigma_{\mathbf{q}n}(\mathbf{r}), \end{aligned} \tag{5.5}$$

where $d_z$ is the separation between lattice planes. The term with the exponential in the denominator arises from the sum of a geometric series over lattice planes and is a sharply peaked function of $q_z - q'_z$ with width $\sim |\gamma(z < 0)|$. We can therefore approximate it by $\delta_{q_z q'_z}$ in the total transition rate with weight equal to

$$\sum_{q'_z} \left| \frac{1}{1 - e^{-d_z(|\gamma(z<0)| + i(q_z - q'_z))}} \right|^2 \approx \frac{N_z}{2d_z |\gamma(z < 0)|}, \tag{5.6}$$

where $N_z = L_z/d_z$ is the number of lattice planes in the quantization volume. Reducing the double sum over $\mathbf{q}$ using $\delta_{\mathbf{q}'_\parallel \mathbf{q}_\parallel}$ and $\delta_{q_z q'_z}$, the total transition rate simplifies to

$$\Gamma = \frac{\pi^2}{2\omega L(\omega)|\gamma(z<0)|}\frac{1}{L_z S}\sum_{\mathbf{q}n'n}(1-f_{\mathbf{q}n'})f_{\mathbf{q}n}\delta(\varepsilon_{\mathbf{q}n'}-\varepsilon_{\mathbf{q}n}-\hbar\omega) \times\left|\left(\hat{\mathbf{k}}-\frac{k\hat{\mathbf{z}}}{\gamma(z<0)}\right)\cdot\sum_\sigma\int_\Omega d\mathbf{r}\psi^{\sigma *}_{\mathbf{q}n'}(\mathbf{r})\frac{e\hbar\nabla}{im_{\mathrm{e}}}\psi^{\sigma}_{\mathbf{q}n}(\mathbf{r})\right|^2 \quad (5.7)$$

Finally, replacing the discrete average over wave-vectors $\frac{1}{L_z S}\sum_{\mathbf{q}}$ by its continuum limit $\int\frac{d\mathbf{q}}{(2\pi)^3}$, gets rid of all dependence on the fictitious plasmon quantization area and electron quantization volume, and results in equation (5.2) in the main text.

## Thin-film plasmon decay rate

Here we briefly sketch the construction of the plasmon mode functions, the Wannier basis approximation to the electronic states and the Fermi golden rule calculation for the surface plasmon decay in thin metallic films (section 5.6).

Given a thin metal film of thickness $L_z = 2H$ centered at $z = 0$ described by a local dielectric function $\epsilon(\omega)$, we can solve Maxwell's equations analytically to obtain the symmetric mode

$$\mathbf{u}^{\mathrm{sym}}_{\mathbf{k}}(\mathbf{r},t) = \sqrt{\frac{2\pi\hbar}{\omega L_{\mathrm{sym}}(\omega)S}}e^{i(\mathbf{k}\cdot\mathbf{r}-\omega t)}\underbrace{\begin{cases} e^{-\gamma_{\mathrm{out}}(|z|-H)}\left(\hat{\mathbf{k}}+\hat{\mathbf{z}}\frac{ik}{\gamma_{\mathrm{out}}}\mathrm{sign}(z)\right), & |z|>H \\ \frac{1}{\cosh(\gamma_{\mathrm{in}}H)}\left(\hat{\mathbf{k}}\cosh(\gamma_{\mathrm{in}}z)-\hat{\mathbf{z}}\frac{ik}{\gamma_{\mathrm{in}}}\sinh(\gamma_{\mathrm{in}}z)\right), & |z|\le H \end{cases}}_{\equiv\mathbf{u}^{\mathrm{sym0}}_{\mathbf{k}}(z)}, \quad (5.8)$$

and the antisymmetric mode

$$\mathbf{u}^{\mathrm{asym}}_{\mathbf{k}}(\mathbf{r},t) = \sqrt{\frac{2\pi\hbar}{\omega L_{\mathrm{asym}}(\omega)S}}e^{i(\mathbf{k}\cdot\mathbf{r}-\omega t)}\underbrace{\begin{cases} e^{-\gamma_{\mathrm{out}}(|z|-H)}\left(\hat{\mathbf{k}}\mathrm{sign}(z)+\hat{\mathbf{z}}\frac{ik}{\gamma_{\mathrm{out}}}\right), & |z|>H \\ \frac{1}{\sinh(\gamma_{\mathrm{in}}H)}\left(\hat{\mathbf{k}}\sinh(\gamma_{\mathrm{in}}z)-\hat{\mathbf{z}}\frac{ik}{\gamma_{\mathrm{in}}}\cosh(\gamma_{\mathrm{in}}z)\right), & |z|\le H \end{cases}}_{\equiv\mathbf{u}^{\mathrm{asym0}}_{\mathbf{k}}(z)}. \quad (5.9)$$

Here, $\gamma_{\text{out}} = \sqrt{k^2 - \omega^2/c^2}$ and $\gamma_{\text{in}} = \sqrt{k^2 - \epsilon(\omega)\omega^2/c^2}$, where $k$ satisfies the dispersion relation

$$k = \frac{\omega}{c}\sqrt{\frac{\epsilon(\omega)(\epsilon(\omega)\tanh^2(\gamma_{\text{in}}H) - 1)}{\epsilon^2(\omega)\tanh^2(\gamma_{\text{in}}H) - 1}} \tag{5.10}$$

for the symmetric mode and

$$k = \frac{\omega}{c}\sqrt{\frac{\epsilon(\omega)(\epsilon(\omega)\coth^2(\gamma_{\text{in}}H) - 1)}{\epsilon^2(\omega)\coth^2(\gamma_{\text{in}}H) - 1}} \tag{5.11}$$

for the antisymmetric mode (obtained by imposing continuity of $\mathbf{D}\cdot\hat{\mathbf{z}}$ across the interface).

Above, the prefactors in (5.8) and (5.9) normalize the energy of the plasmon modes on an area $S$ to that of a single quantum, $\hbar\omega$. (See Ref. [3] for more details about quantization of surface plasmons on thin films.) Integrating the field intensities and enforcing this normalization then results in

$$L_{\text{sym}}(\omega) = \frac{\left[(\gamma_{\text{in}}^2 + k^2)\sinh(\gamma_{\text{in}}L_z) + (\gamma_{\text{in}}^2 - k^2)\gamma_{\text{in}}L_z\right]\frac{d(\omega\epsilon)}{d\omega} + \left(\frac{\omega\epsilon}{c}\right)^2\left[\sinh(\gamma_{\text{in}}L_z) - \gamma_{\text{in}}L_z\right]}{2\gamma_{\text{in}}^3\left(\cosh(\gamma_{\text{in}}L_z) + 1\right)} + \frac{k^2}{2\gamma_{\text{out}}^3} \tag{5.12}$$

for the symmetric mode and

$$L_{\text{asym}}(\omega) = \frac{\left[(\gamma_{\text{in}}^2 + k^2)\sinh(\gamma_{\text{in}}L_z) - (\gamma_{\text{in}}^2 - k^2)\gamma_{\text{in}}L_z\right]\frac{d(\omega\epsilon)}{d\omega} + \left(\frac{\omega\epsilon}{c}\right)^2\left[\sinh(\gamma_{\text{in}}L_z) + \gamma_{\text{in}}L_z\right]}{2\gamma_{\text{in}}^3\left(\cosh(\gamma_{\text{in}}L_z) - 1\right)} + \frac{k^2}{2\gamma_{\text{out}}^3} \tag{5.13}$$

for the antisymmetric mode.

As for the electronic states, we start by computing the maximally localized Wannier functions[20, 31] $w_a^\sigma(\mathbf{r}-\mathbf{R}) = \frac{1}{N_{\mathbf{q}}}\sum_{\mathbf{q}b} U_{ab}^{\mathbf{q}} e^{-i\mathbf{q}\cdot(\mathbf{r}-\mathbf{R})}\psi_{\mathbf{q}b}^\sigma(\mathbf{r})$ for the bulk metal, which involves finding the unitary rotations $U_{ab}^{\mathbf{q}}$ that minimize the spatial variance of $w_a^\sigma(\mathbf{r}-\mathbf{R})$. Here, $\psi_{\mathbf{q}b}^\sigma(\mathbf{r})$ are the eigen-orbitals of the bulk metal and let $\epsilon_{\mathbf{q}b}$ be the corresponding eigen-energies. Now, we can use the unitary transformations to construct the Hamiltonian in the basis of Wannier functions, $H_{\mathbf{R}a,\mathbf{R}'a'} = \frac{1}{N_{\mathbf{q}}}\sum_{\mathbf{q}b} U_{a'b}^{\mathbf{q}} U_{ab}^{\mathbf{q}} \epsilon_{\mathbf{q}b} e^{i\mathbf{q}\cdot(\mathbf{R}-\mathbf{R}')}\epsilon_{\mathbf{q}b}$. The fact that the Wannier functions are localized then implies that the elements of $H_{\mathbf{R}a,\mathbf{R}'a'}$ decrease rapidly with increasing $|\mathbf{R}-\mathbf{R}'|$ and can be truncated after a finite number of sites. This is therefore a multi-orbital tight-binding-like model (with many neighbors) that exactly reproduces the original eigenfunctions and eigenvalues since it is obtained from a unitary transformation of the original Hamiltonian. See Ref. [31] for a detailed exposition.

Next, we approximate the Hamiltonian for the thin film by starting with the above Wannier basis

Hamiltonian for the bulk system and setting any matrix elements that involve a site outside the film to zero. Diagonalizing this discrete Hamiltonian then gives us the eigenvalues $\epsilon_{\mathbf{q}n}$ and eigenfunctions $\psi^{\sigma}_{\mathbf{q}n} = \sum_{a\mathbf{R}} C_{\mathbf{q}naZ} e^{i\mathbf{q}\cdot\mathbf{R}} w^{\sigma}_{a}(\mathbf{r}-\mathbf{R})$ as a linear combination of the localized Wannier functions on various atom sites $\mathbf{R}$. Here, we have used Bloch's theorem in the two periodic directions to obtain the diagonalizing factor $e^{i\mathbf{q}\cdot\mathbf{R}}$ where $\mathbf{q}$ is a wave vector in the two-dimensional Brillouin zone. The coefficients $C_{\mathbf{q}naZ}$ (where $Z = \hat{\mathbf{z}}\cdot\mathbf{R}$) are obtained from numerical diagonalization of the discrete Hamiltonian matrix constructed above.

Finally, we apply Fermi's golden rule to calculate the transition rates using the vector potentials for the thin film plasmon modes and the eigenfunctions in the Wannier basis. Assuming that $\mathbf{u}^{\mathrm{sym/asym}}_{\mathbf{k}}$ vary slowly on the atomic scale in the two periodic directions, we can show analogously to the previous section that the transition rates for the symmetric/antisymmetric modes are

$$\Gamma_{\mathrm{sym/asym}} \approx \frac{\pi^2\hbar^2 e^2}{\Omega_{\parallel} m_{\mathrm{e}}^2 \omega L_{\mathrm{sym/asym}}(\omega)} \sum_{n'n} \int \frac{d\mathbf{q}}{(2\pi)^2} (1 - f_{\mathbf{q}n'}) f_{\mathbf{q}n} \delta(\varepsilon_{\mathbf{q}n'} - \varepsilon_{\mathbf{q}n} - \hbar\omega) \times \left| \sum_{a'aZ'Z} C^{*}_{\mathbf{q}n'a'Z'} C_{\mathbf{q}naZ} \mathbf{u}^{\mathrm{sym0/asym0}}_{\mathbf{k}}(\bar{z}^{Z'Z}_{a'a}) \cdot \sum_{\mathbf{R}_{\parallel}} e^{i\mathbf{q}\cdot\mathbf{R}_{\parallel}} \langle i\boldsymbol{\nabla}\rangle^{\mathbf{R}_{\parallel}}_{a'a} \right|^2 . \quad (5.14)$$

Here, $\Omega_{\parallel}$ is the area of the two-dimensional surface unit cell, $\bar{z}^{Z'Z}_{a'a}$ is the $z$-center of the product density of the Wannier basis functions indexed by $aZ$ and $a'Z'$, and $\langle i\boldsymbol{\nabla}\rangle^{\mathbf{R}_{\parallel}}_{a'a}$ is the momentum matrix element between Wannier functions $a$ and $a'$ at two sites separated by $\mathbf{R}_{\parallel}$, a lattice vector parallel to the surface. As before, we generate the carrier energy distributions by histogramming contributions to the integral in the above expression in terms of the initial and final electronic state energies.

# Bibliography

Archambault, Alexandre et al. “Quantum theory of spontaneous and stimulated emission of surface plasmons”. In: *Physical Review B* 82.3 (July 12, 2010), pp. 035411–. URL: http://link.aps.org/doi/10.1103/PhysRevB.82.035411 (cit. on p. 75).

Atwater, Harry A. and Albert Polman. “Plasmonics for improved photovoltaic devices”. In: *Nat Mater* 9.3 (Mar. 2010), pp. 205–213. URL: http://dx.doi.org/10.1038/nmat2629 (cit. on p. 62).

Ballester, D. et al. “Long-range surface-plasmon-polariton excitation at the quantum level”. In: *Physical Review A* 79.5 (May 26, 2009), pp. 053845–. URL: http://link.aps.org/doi/10.1103/PhysRevA.79.053845 (cit. on pp. 72, 77).

Clavero, Cesar. “Plasmon-induced hot-electron generation at nanoparticle/metal-oxide interfaces for photovoltaic and photocatalytic devices”. In: *Nat Photon* 8.2 (Feb. 2014), pp. 95–103. URL: http://dx.doi.org/10.1038/nphoton.2013.238 (cit. on p. 62).

Courths, R. and S. H ufner. “Photoemission experiments on copper”. In: *Physics Reports* 112.2 (1984), pp. 53–171. ISSN: 0370-1573. DOI: http://dx.doi.org/10.1016/0370-1573(84)90167-4. URL: http://www.sciencedirect.com/science/article/pii/0370157384901674 (cit. on pp. 65, 66).

Di Martino, Giuliana et al. “Quantum Statistics of Surface Plasmon Polaritons in Metallic Stripe Waveguides”. In: *Nano Letters* 12.5 (2014/10/20 2012), pp. 2504–2508. DOI: 10.1021/nl300671w. URL: http://dx.doi.org/10.1021/nl300671w (cit. on p. 63).

Dudarev, S. L. et al. “Electron-energy-loss spectra and the structural stability of nickel oxide: An LSDA+U study”. In: *Phys. Rev. B* 57 (3 Jan. 1998), pp. 1505–1509. DOI: 10.1103/PhysRevB.57.1505. URL: http://link.aps.org/doi/10.1103/PhysRevB.57.1505 (cit. on pp. 65, 74).

Esteban, Ruben et al. “Bridging quantum and classical plasmonics with a quantum-corrected model”. In: *Nat Commun* 3 (May 8, 2012), p. 825. URL: http://dx.doi.org/10.1038/ncomms1806 (cit. on p. 63).

Fang, Zheyu et al. “Plasmon-Induced Doping of Graphene”. In: *ACS Nano* 6.11 (2014/08/28 2012), pp. 10222–10228. DOI: 10.1021/nn304028b. URL: http://dx.doi.org/10.1021/nn304028b (cit. on p. 63).

Giannini, Vincenzo et al. “Plasmonic Nanoantennas: Fundamentals and Their Use in Controlling the Radiative Properties of Nanoemitters”. In: *Chemical Reviews* 111.6 (2014/08/28 2011), pp. 3888–3912. DOI: 10.1021/cr1002672. URL: http://dx.doi.org/10.1021/cr1002672 (cit. on p. 62).

Govorov, Alexander O., Hui Zhang, and Yurii K. Gun’ko. “Theory of Photoinjection of Hot Plasmonic Carriers from Metal Nanostructures into Semiconductors and Surface Molecules”. In: *The Journal of Physical Chemistry C* 117.32 (2013/11/11 2013), pp. 16616–16631. DOI: 10.1021/jp405430m. URL: http://dx.doi.org/10.1021/jp405430m (cit. on pp. 63, 72).

Jacob, Zubin and Vladimir M. Shalaev. “Plasmonics Goes Quantum”. In: *Science* 334.6055 (Oct. 2011), pp. 463–464. URL: http://www.sciencemag.org/content/334/6055/463.short (cit. on p. 62).

Kang, Yimin et al. “Plasmonic Hot Electron Induced Structural Phase Transition in a MoS2 Monolayer”. In: *Advanced Materials* 26.37 (2014), pp. 6467–6471. ISSN: 1521-4095. DOI: 10.1002/adma.201401802. URL: http://dx.doi.org/10.1002/adma.201401802 (cit. on p. 63).

Knight, Mark W. et al. “Photodetection with Active Optical Antennas”. In: *Science* 332.6030 (May 2011), pp. 702–704. URL: http://www.sciencemag.org/content/332/6030/702.abstract (cit. on p. 62).

Kolesov, Roman et al. “Wave-particle duality of single surface plasmon polaritons”. In: *Nat Phys* 5.7 (July 2009), pp. 470–474. URL: http://dx.doi.org/10.1038/nphys1278 (cit. on p. 62).

Kuisma, M. et al. “Kohn-Sham potential with discontinuity for band gap materials”. In: *Phys. Rev. B* 82 (11 Sept. 2010), p. 115106. DOI: 10.1103/PhysRevB.82.115106. URL: http://link.aps.org/doi/10.1103/PhysRevB.82.115106 (cit. on p. 65).

Linic, Suljo, Phillip Christopher, and David B. Ingram. “Plasmonic-metal nanostructures for efficient conversion of solar to chemical energy”. In: *Nat Mater* 10.12 (Dec. 2011), pp. 911–921. URL: http://dx.doi.org/10.1038/nmat3151 (cit. on p. 62).

Manjavacas, A., F. J. Garcia de Abajo, and P. Nordlander. "Quantum plexcitonics: strongly interacting plasmons and excitons". In: *Nano Lett.* 11.6 (June 2011), pp. 2318–2323 (cit. on p. 63).

Manjavacas, Alejandro et al. "Plasmon-Induced Hot Carriers in Metallic Nanoparticles". In: *ACS Nano* 8.8 (2014/08/28 2014), pp. 7630–7638. DOI: 10.1021/nn502445f. URL: http://dx.doi.org/10.1021/nn502445f (cit. on pp. 63, 72).

Marzari, Nicola and David Vanderbilt. "Maximally localized generalized Wannier functions for composite energy bands". In: *Phys. Rev. B* 56 (20 Nov. 1997), pp. 12847–12865. DOI: 10.1103/PhysRevB.56.12847. URL: http://link.aps.org/doi/10.1103/PhysRevB.56.12847 (cit. on pp. 72, 77).

Mills, K. A. et al. "Angle-resolved photoemission determination of Λ-line valence bands in Pt and Au using synchrotron radiation". In: *Phys. Rev. B* 22 (2 July 1980), pp. 581–592. DOI: 10.1103/PhysRevB.22.581. URL: http://link.aps.org/doi/10.1103/PhysRevB.22.581 (cit. on pp. 65, 66).

Mubeen, Syed et al. "An autonomous photosynthetic device in which all charge carriers derive from surface plasmons". In: *Nat Nano* 8.4 (Apr. 2013), pp. 247–251. URL: http://dx.doi.org/10.1038/nnano.2013.18 (cit. on p. 62).

Mukherjee, Shaunak et al. "Hot Electrons Do the Impossible: Plasmon-Induced Dissociation of H2 on Au". In: *Nano Letters* 13.1 (2013/07/23 2012), pp. 240–247. DOI: 10.1021/nl303940z. URL: http://dx.doi.org/10.1021/nl303940z (cit. on p. 62).

Okumura, T. and K. N. Tu. "Electrical characterization of Schottky contacts of Au, Al, Gd, and Pt on n-type and p-type GaAs". In: *Journal of Applied Physics* 61.8 (1987), pp. 2955–2961. DOI: http://dx.doi.org/10.1063/1.337843. URL: http://scitation.aip.org/content/aip/journal/jap/61/8/10.1063/1.337843 (cit. on p. 62).

Perdew, John P. et al. "Restoring the Density-Gradient Expansion for Exchange in Solids and Surfaces". In: *Phys. Rev. Lett.* 100 (13 Apr. 2008), p. 136406. DOI: 10.1103/PhysRevLett.100.136406. URL: http://link.aps.org/doi/10.1103/PhysRevLett.100.136406 (cit. on pp. 65, 74).

Rakic, Aleksandar D. et al. "Optical Properties of Metallic Films for Vertical-Cavity Optoelectronic Devices". In: *Appl. Opt.* 37.22 (Aug. 1998), pp. 5271–5283. DOI: 10.1364/AO.37.005271. URL: http://ao.osa.org/abstract.cfm?URI=ao-37-22-5271 (cit. on p. 74).

Rangel, T. et al. “Band structure of gold from many-body perturbation theory”. In: *Phys. Rev. B* 86 (12 Sept. 2012), p. 125125. DOI: 10.1103/PhysRevB.86.125125. URL: http://link.aps.org/doi/10.1103/PhysRevB.86.125125 (cit. on pp. 65, 66).

Schuller, Jon A. et al. “Plasmonics for extreme light concentration and manipulation”. In: *Nat Mater* 9.3 (Mar. 2010), pp. 193–204. URL: http://dx.doi.org/10.1038/nmat2630 (cit. on p. 62).

Sobhani, Ali et al. “Narrowband photodetection in the near-infrared with a plasmon-induced hot electron device”. In: *Nat Commun* 4 (Mar. 27, 2013), p. 1643. URL: http://dx.doi.org/10.1038/ncomms2642 (cit. on p. 62).

Song, P., P. Nordlander, and S. Gao. “Quantum mechanical study of the coupling of plasmon excitations to atomic-scale electron transport”. In: *J Chem Phys* 134.7 (Feb. 2011), p. 074701 (cit. on p. 63).

Souza, Ivo, Nicola Marzari, and David Vanderbilt. “Maximally localized Wannier functions for entangled energy bands”. In: *Phys. Rev. B* 65 (3 Dec. 2001), p. 035109. DOI: 10.1103/PhysRevB.65.035109. URL: http://link.aps.org/doi/10.1103/PhysRevB.65.035109 (cit. on pp. 72, 77).

Sundararaman, R. et al. *JDFTx*. http://jdftx.sourceforge.net. 2012 (cit. on p. 73).

Takahashi, Yukina and Tetsu Tatsuma. “Solid state photovoltaic cells based on localized surface plasmon-induced charge separation”. In: *Applied Physics Letters* 99.18 (Oct. 31, 2011), pp. 182110–3. URL: http://dx.doi.org/10.1063/1.3659476 (cit. on p. 62).

Tame, M. S. et al. “Quantum plasmonics”. In: *Nat Phys* 9.6 (June 2013), pp. 329–340. URL: http://dx.doi.org/10.1038/nphys2615 (cit. on p. 62).

Wang, Fuming and Nicholas A. Melosh. “Plasmonic Energy Collection through Hot Carrier Extraction”. In: *Nano Letters* 11.12 (2013/07/23 2011), pp. 5426–5430. DOI: 10.1021/nl203196z. URL: http://dx.doi.org/10.1021/nl203196z (cit. on p. 62).

Wehner, P. S. et al. “Valence-band structure of silver along Λ from angle-resolved photoemission”. In: *Phys. Rev. B* 19 (12 June 1979), pp. 6164–6171. DOI: 10.1103/PhysRevB.19.6164. URL: http://link.aps.org/doi/10.1103/PhysRevB.19.6164 (cit. on pp. 65, 66).

Yan, Jun, Karsten W. Jacobsen, and Kristian S. Thygesen. “Conventional and acoustic surface plasmons on noble metal surfaces: A time-dependent density functional theory study”. In: *Phys. Rev. B* 86 (24 Dec. 2012), p. 241404. DOI: 10.1103/PhysRevB.86.241404. URL: http://link.aps.org/doi/10.1103/PhysRevB.86.241404 (cit. on pp. 63, 65).

Zuloaga, J., E. Prodan, and P. Nordlander. “Quantum description of the plasmon resonances of a nanoparticle dimer”. In: *Nano Lett.* 9.2 (Feb. 2009), pp. 887–891 (cit. on p. 63).

# 6

# Phonon-assisted and Multi-plasmon Contributions to Plasmon Decay

*All the cool electrons want to be in a band.*

– Ravishankar Sundararaman

## 6.1 Chapter Overview:

Behavior of metals across a broad frequency range from microwave to ultraviolet frequencies is of interest in plasmonics, nanophotonics and metamaterials. Depending on the frequency, losses of collective excitations in metals can be predominantly classical resistive effects or Landau damping. In this context, we present first principles calculations that capture all the significant microscopic mechanisms underlying surface plasmon decay and predict the initial excited carrier distributions so generated. Specifically we report the first *ab initio* calculations of phonon-assisted optical excitations in metals, which are critical to bridging the frequency range between resistive losses at low frequencies and direct interband transitions at high frequencies. In aluminum and the noble metals, commonly used plasmonic materials, we find that resistive losses compete with phonon-assisted carrier generation below the interband threshold, but hot carrier generation via direct transitions dominates above threshold. Finally, we predict energy-dependent lifetimes and mean free paths of hot carriers, accounting for electron-electron and electron-phonon scattering, to provide

insight toward transport of plasmonically-generated carriers at the nanoscale.

## 6.2 Introduction

Plasmons provide a pathway to manipulate electromagnetic radiation at nanometer length scales [2, 26] and at femtosecond time scales.[12] Illumination of a metallic structure produces strong optical near fields that initiate a cascade of processes with multiple outcomes, including the excitation of surface plasmons, their radiative decay to photons, and their non-radiative decay in the material.[18].

Non-radiative plasmon decay includes the generation of electron-hole pairs. These electron and hole energies depend on the material and the plasmon energy, and are considered 'hot' if significantly larger than those of thermal excitations at ambient temperatures. These hot carriers undergo fast internal relaxation, but can be ejected into semiconductor and molecular systems as clearly demonstrated in several recent device applications ranging from energy conversion and photocatalysis to photodetection. In particular, demonstrations of photochemistry driven by both hot electrons[21, 7] and hot holes[6] raise interesting questions regarding the timescales of plasmonic hot carrier generation and transport.

In addition to the visible and ultraviolet plasmonic response of metals, the behavior of metals at microwave and infrared frequencies is of broad interest.[28, 24, 10] Losses in metals can proceed either through classical resistive dissipation or single-particle excitations. For plasmons, the collective excitations of electrons in metals, these excitations constitute Landau damping that results in the generation of highly energetic carriers. Direct optical excitation of carriers in most metals is only allowed above an interband threshold energy due to crystal momentum conservation. Below this threshold, which typically corresponds to optical frequencies, phonons provide the necessary momentum to circumvent this selection rule. Additionally, in metals, confinement of fields to the surface breaks translational invariance that can also provide the momentum necessary to excite intraband transitions.[13] These 'surface-assisted' and phonon-assisted transitions are important contributors to losses in metals at infrared frequencies, and hence important to understand from both a fundamental and technological perspective.[32]

First principles calculations provide an opportunity to quantitatively analyze each microscopic mechanism underlying plasmon decay individually (Fig. 6.1(a)) and gauge their relative contributions in different materials and at different frequencies. These calculations can examine the process at

various time scales, separating effects due to the initial distribution of hot carriers and their subsequent transport. Such a detailed understanding, which is extremely challenging to extract from experiment, will elucidate opportunities to enhance plasmonic hot carrier devices as well as their fundamental limits.

Previously, we studied direct interband transitions in plasmonic metals in detail[33] and showed that the plasmon-generated hot carrier distribution is extremely sensitive to details of the electronic band structure. Specifically, we found that in noble metals, the positions of the $d$ bands relative to the Fermi level results in much hotter holes than electrons; subsequent studies confirmed these results.[3] We also showed that the decay of surface plasmon polaritons is representative of decays in plasmonic nanostructures and that effects of geometry on the generation of carriers are significant only at dimensions below 10 nm.

This Chapter completes the theoretical picture of surface plasmon decay by adding *ab initio* calculations of phonon-assisted transitions and resistive losses. Previous first principles calculations of phonon-assisted transitions treat indirect-gap semiconductors below their optical gap.[22, 14] In extending such calculations to metals, we show that it is necessary to carefully treat the energy-conserving 'on-shell' intermediate states, that correspond to sequential processes (Fig. 6.1(b)). We predict the relative contributions of these processes and direct transitions, and compare the absolute decay rates to those estimated from experimentally-measured complex dielectric functions for frequencies ranging from infrared to ultraviolet. Finally, we analyze the subsequent dynamics of the generated hot carriers, account for electron-electron and electron-phonon scattering and present *ab initio* predictions for the strongly energy-dependent lifetimes and mean free paths of hot carriers.

## 6.3 Results & Discussion

### 6.3.1 Plasmon decay

In order to compare various contributions to surface plasmon decay with experiment on equal footing, we calculate contributions to the imaginary part of the dielectric tensor $\Im\bar{\epsilon}(\omega)$ and relate the complex dielectric function to the plasmon decay rate. Specifically, the decay rate per unit volume is $\frac{1}{2\pi}\mathbf{E}^*(\mathbf{r})\cdot\Im\bar{\epsilon}(\omega)\cdot\mathbf{E}(\mathbf{r})$ at a point in the material where the electric field is $\mathbf{E}(\mathbf{r})$. For a surface plasmon polariton with wave vector $k$ and angular frequency $\omega$ on the surface of a semi-infinite

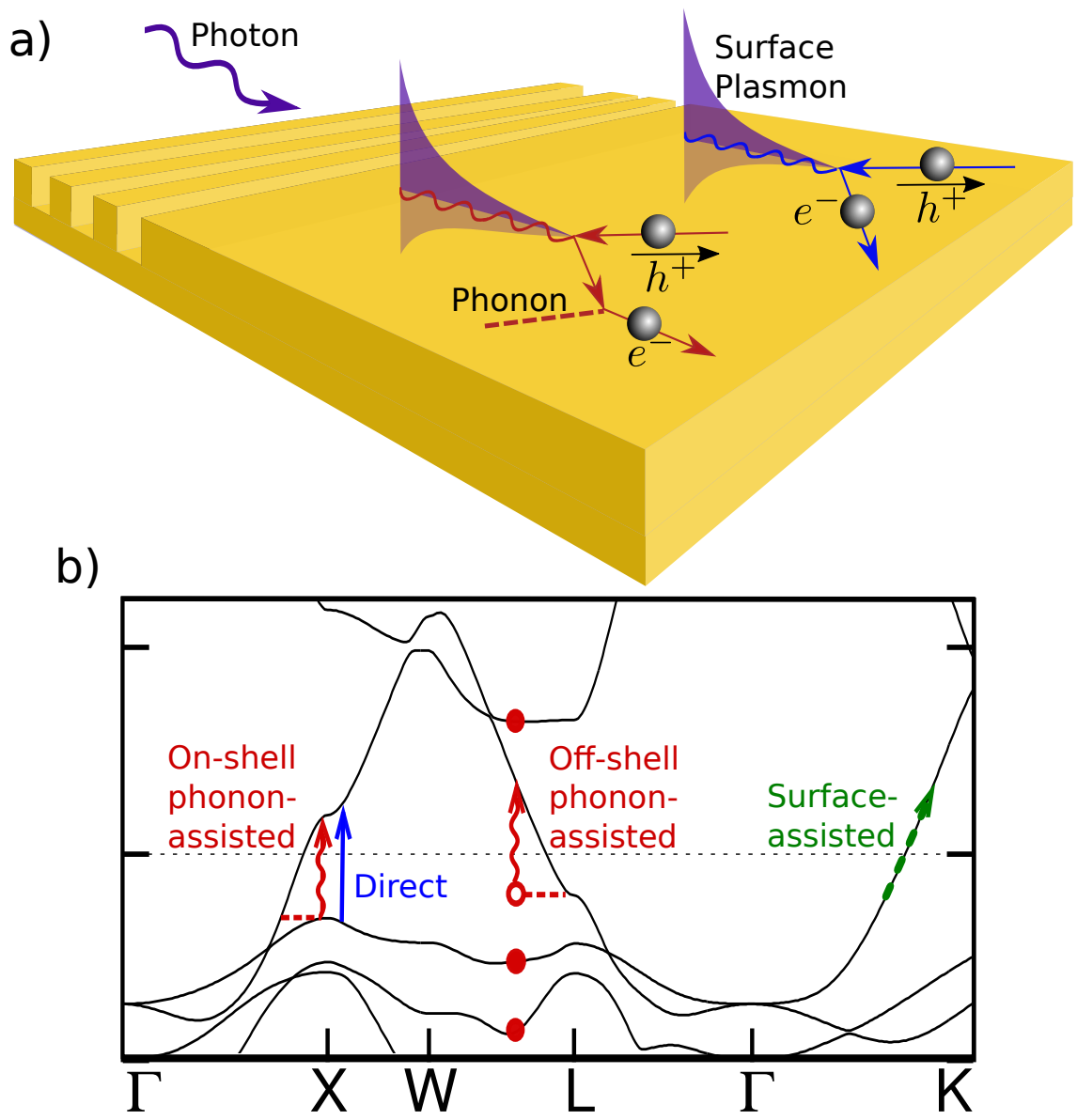


Figure 6.1: (a) Schematic for decay of surface plasmons via direct and phonon-assisted transitions to generate hot electrons and holes. (b) Illustrations of direct, surface-assisted and phonon-assisted transitions on the band structure of gold. Surface-assisted transitions constitute the small but non-zero probability of non-vertical transitions due to the momentum distribution of the plasmon. The intermediate virtual state (empty circle) requires a sum over states (filled circles) in perturbation theory. When the intermediate state is a real state on the band structure (goes 'on shell'), it corresponds to a sequential process of electron-phonon scattering followed by a direct transition (or vice versa).

metal slab extending over $z < 0$, substituting the electric field profile of a single quantum [1] and integrating over space yields the total decay rate

$$\Gamma = \frac{\omega}{2L(\omega)|\gamma(z<0)|}\boldsymbol{\lambda}^* \cdot \Im\bar{\epsilon}(\omega) \cdot \boldsymbol{\lambda}. \tag{6.1}$$

Here, $L(\omega)$ is the quantization length for the plasmon determined by normalizing the energy density of the mode, $|\gamma(z<0)|$ is the inverse decay length of the plasmon into the metal and $\boldsymbol{\lambda} \equiv \hat{\mathbf{k}} - \hat{\mathbf{z}}k/\gamma(z<0)$ is the polarization vector. All of these quantities are fully determined by the experimental dielectric function and described in detail in Refs. [1] and [33].

We calculate the total 'experimental' decay rate of plasmons as a function of frequency by using (6.1) directly with the complex dielectric functions measured by ellipsometry.[25]

Within the random phase approximation, direct interband transitions contribute

$$\boldsymbol{\lambda}^* \cdot \Im\bar{\epsilon}_{\text{direct}}(\omega) \cdot \boldsymbol{\lambda} = \frac{4\pi^2 e^2}{m_e^2\omega^2}\int_{\text{BZ}}\frac{d\mathbf{q}}{(2\pi)^3}\sum_{n'n}(f_{\mathbf{q}n} - f_{\mathbf{q}n'})\delta(\varepsilon_{\mathbf{q}n'} - \varepsilon_{\mathbf{q}n} - \hbar\omega)\left|\boldsymbol{\lambda}\cdot\langle\mathbf{p}\rangle^{\mathbf{q}}_{n'n}\right|^2, \tag{6.2}$$

where $\varepsilon_{\mathbf{q}n}$ and $f_{\mathbf{q}n}$ are the energies and occupations of electronic quasiparticles with wave-vectors $\mathbf{q}$ (in the Brillouin zone BZ) and band index $n$, and $\langle\mathbf{p}\rangle^{\mathbf{q}}_{n'n}$ are momentum matrix elements.

Substitution of (6.2) in (6.1) results exactly in the plasmon decay rate we previously derived using Fermi's Golden rule within a fully quantum many-body formalism of the electrons and plasmons.[33] We calculate the energies and matrix elements with the same relativistic DFT+$U$ method as Ref. [33] which produces band structures in excellent agreement with photoemission spectra. Since we use a spinorial electronic structure method to fully treat relativistic effects, the band indices include spin degrees of freedom.

Next, the contribution due to phonon-assisted transitions from second-order perturbation theory is [22, 14]

$$\begin{aligned}\boldsymbol{\lambda}^*\cdot\Im\bar{\epsilon}_{\text{phonon}}(\omega)\cdot\boldsymbol{\lambda} = \frac{4\pi^2e^2}{m_e^2\omega^2}\int_{\text{BZ}}\frac{d\mathbf{q}'d\mathbf{q}}{(2\pi)^6}\sum_{n'n\alpha\pm}(f_{\mathbf{q}n}-f_{\mathbf{q}'n'})\left(n_{\mathbf{q}'-\mathbf{q},\alpha}+\frac{1}{2}\mp\frac{1}{2}\right)\delta(\varepsilon_{\mathbf{q}'n'}-\varepsilon_{\mathbf{q}n}-\hbar\omega\mp\hbar\omega_{\mathbf{q}'-\mathbf{q},\alpha})\\ \times\left|\boldsymbol{\lambda}\cdot\sum_{n_1}\left(\frac{g^{\mathbf{q}'-\mathbf{q},\alpha}_{\mathbf{q}'n',\mathbf{q}n_1}\langle\mathbf{p}\rangle^{\mathbf{q}}_{n_1n}}{\varepsilon_{\mathbf{q}n_1}-\varepsilon_{\mathbf{q}n}-\hbar\omega+i\eta}+\frac{\langle\mathbf{p}\rangle^{\mathbf{q}'}_{n'n_1}g^{\mathbf{q}'-\mathbf{q},\alpha}_{\mathbf{q}'n_1,\mathbf{q}n}}{\varepsilon_{\mathbf{q}'n_1}-\varepsilon_{\mathbf{q}n}\mp\hbar\omega_{\mathbf{q}'-\mathbf{q},\alpha}+i\eta}\right)\right|^2,\end{aligned} \tag{6.3}$$

where $\hbar\omega_{\mathbf{k}\alpha}$ is the energy of a phonon with wave-vector $\mathbf{k}$ and polarization index $\alpha$, $n_{\mathbf{k}\alpha}$ is the

corresponding Bose occupation factor and $g^{\mathbf{k}\alpha}_{\mathbf{q}'n',\mathbf{q}n}$ is the corresponding electron-phonon matrix element with electronic states labeled by wave-vectors $\mathbf{q}, \mathbf{q}'$ and band indices $n, n'$ (with $\mathbf{k} = \mathbf{q}' - \mathbf{q}$ for crystal momentum conservation). The sum over $\pm$ accounts for phonon absorption as well as emission. Since the *ab initio* matrix elements couple all pairs of wave-vectors in the Brillouin zone, they implicitly account for wrap-around (Umklapp) processes.

We calculate the phonon energies and electron-phonon matrix elements consistently using the same relativistic DFT+$U$ approximation as for the electronic states. We use a Wannier representation to efficiently interpolate the phonon energies and matrix elements to calculate the Brillouin zone integrals in (6.3) accurately (See Methods section for details.)

The imaginary part of the energy denominator, $\eta$, in the second line of equation (6.3) corresponds to the linewidth of the intermediate electronic state (with band index $n_1$). The value of $\eta$ does not affect the phonon-assisted absorption at photon energies less than the optical gap of materials previously considered,[22, 14] and is usually treated as a numerical regularization parameter. However, above the optical gap (the interband threshold for metals), the real part of the denominator crosses zero and the resulting singular contributions are inversely proportional to $\eta$. These singular contributions correspond to sequential processes: electron-phonon scattering followed by a direct interband transition or vice versa (Fig. 6.1). For a metal, including contributions from these sequential processes would lead to a multiple counting of the direct transition. Scattering events preceding the optical transition are a part of the equilibrium Fermi distribution, while scattering events following the optical transition corresponds to the subsequent inelastic relaxation of the generated carriers. We eliminate this multiple counting by taking advantage of the $\eta$ independence of the non-singular part and the $\eta^{-1}$ variation of the singular part and extrapolating from calculations done using two values of $\eta$ (See Methods section for details.)

In metals, the strong confinement of fields at the surface introduces an additional mechanism for intraband transitions. The exponential decay of the fields in the metal with inverse decay length $|\gamma(z < 0)|$ introduces a Lorentzian distribution in the momentum of the plasmon normal to the surface with width $\sim |\gamma(z < 0)|$. (This can also be interpreted in terms of the uncertainty principle.) This momentum distribution allows diagonal intraband transitions on the band structure (Fig. 6.1(b)), which contributes a 'surface-assisted' loss[13]

$$\Im\epsilon_{\text{surface}}(\omega) = \frac{\omega_p^2}{\omega^3} \times \frac{3}{4}|\gamma(z < 0)|v_F. \tag{6.4}$$

Here, $\omega_p = \sqrt{4\pi ne^2/m_e}$ is the the bulk plasma frequency of the metal and $v_F = (\hbar/m_e)\sqrt[3]{n/(3\pi^2)}$ its Fermi velocity, where $n$ is the bulk carrier density of the metal. See Ref. [13] for a detailed derivation of this contribution.

The direct, surface-assisted and phonon-assisted transitions considered above are the lowest-order processes for the decay of a plasmon to single-particle excitations, which correspond to the Landau damping of the plasmon on the Fermi sea.[16, 4, 9] Higher-order processes including multiple electron-hole pairs or multiple phonons are suppressed by phase-space factors at low energies and become important only at higher energies that are not usually accessed by surface plasmons.[12]

Apart from Landau damping, an additional source of plasmon loss is the intrinsic lifetime of the electronic states comprising the collective oscillation. This corresponds to a resistive loss in the material which we calculate using a linearized Boltzmann equation with a relaxation time approximation. We show in the Methods section that

$$\Im\epsilon_{\text{resistive}}(\omega) = \frac{4\pi\sigma_0}{\omega(1+\omega^2\tau^2)}, \tag{6.5}$$

where the zero-frequency conductivity $\sigma_0$ and the momentum relaxation time $\tau$ are derived from *ab initio* electronic states and electron-phonon matrix elements.

Fig. 6.2 compares the plasmon linewidth and decay rates estimated directly from the experimentally-measured complex dielectric functions with theoretical predictions for cumulative contributions from direct, surface-assisted, phonon-assisted transitions and resistive losses. For all the common plasmonic metals, aluminum and the noble metals, we find that direct transitions dominate above the interband threshold ($\sim 1.6 - 1.8$ eV for aluminum, gold and copper and $\sim 3.5$ eV for silver). All other contributions add to less than 10% above threshold, and hence the cumulative results overlay the direct transition lines. In silver, the maximum plasmon frequency coincides with the interband threshold and hence there is no accessible frequency range for which direct transitions dominate. In aluminum, direct transitions are in fact possible at all frequencies due to a band crossing near the Fermi level,[33] but an additional channel for direct transitions with much higher density of states opens up at the effective threshold of $\sim 1.6$ eV.

Below the threshold, direct transitions are forbidden (or for aluminum, are weak) and the contributions due to the other processes become important. Surface-assisted processes only contribute a small fraction (at most 3%) of the experimental linewidth in the entire frequency range below

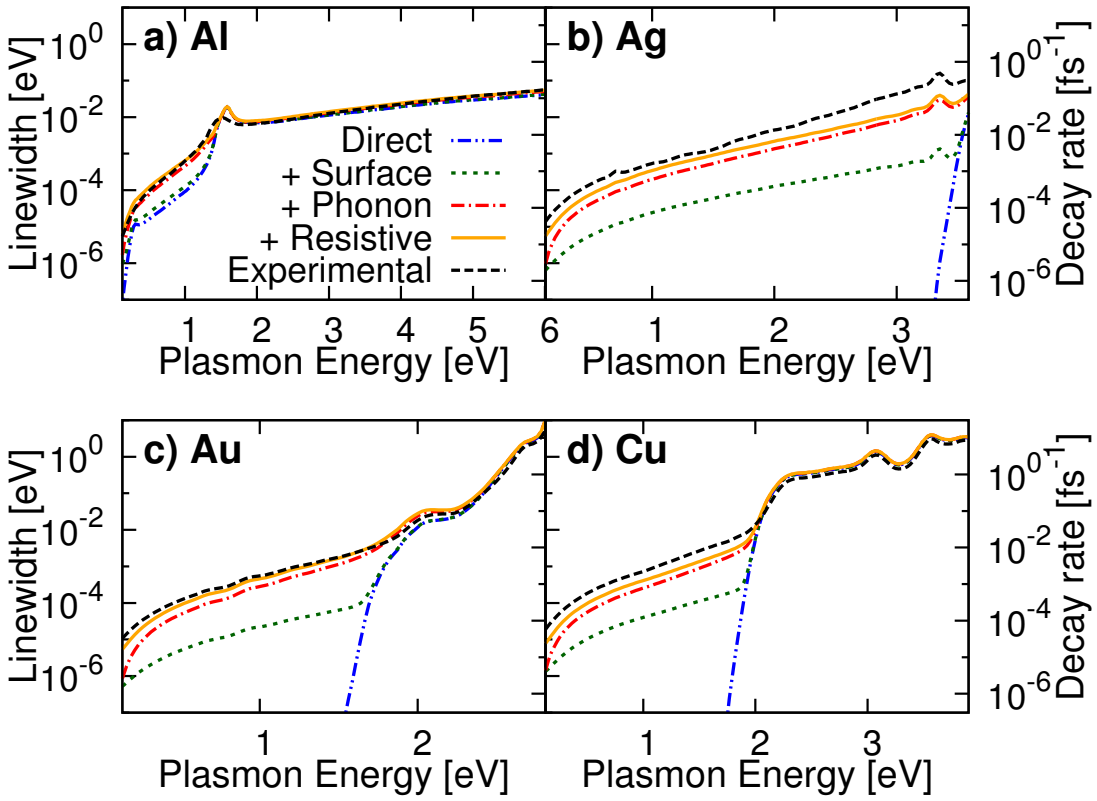


Figure 6.2: Comparison of calculated and experimental linewidths (left axis) and decay rates (right axis) in (a) Al (b) Ag (c) Au and (d) Cu. The theoretical curves indicate cumulative contributions from direct transitions alone ('Direct'), including surface-assisted transitions ('+Surface'), including phonon-assisted transitions ('+Phonon'), and including resistive losses ('+Resistive').

threshold. Phonon-assisted transitions and resistive losses compete significantly and dominate this frequency range. The relative importance of phonon-assisted transitions increases slightly with frequency, with resistive losses dominating at very low frequencies (close to 0 eV in these plots), an approximately even split at $\sim 1$ eV, and a greater contribution from phonon-assisted transitions just below threshold.

The total theoretical prediction including all these contributions agrees very well with experiment over the entire range of frequencies. Above threshold for the noble metals, the theoretical predictions overestimate experiment by $\sim 10 - 20\%$, which is the typical accuracy of optical matrix elements involving $d$ electrons in density-functional theory.[19] Below threshold, the total theory result underestimates the experimental value but is typically within a factor of two from it. This is, in part, because material non-idealities could contribute additional losses and our theoretical calculations estimate an ideal lower bound. In fact, the largest discrepancy is for silver because these ideal losses are the smallest and the non-idealities become more important relatively. Also note that there is significant spread in tabulated experimental dielectric functions for the noble metals,[25] with discrepancies a factor of two or higher in the imaginary parts at infrared frequencies. (We used the measurements that covered the greatest frequency range.) Therefore, more careful experimental measurements in that frequency range with higher quality samples would be necessary and useful for a stricter comparison.

The results in Fig. 6.2 are based on calculations at standard room temperature, $T = 298$ K. We expect the direct and surface-assisted contributions to be approximately independent of temperature, and the phonon-assisted and resistive contributions to decrease upon lowering the temperature. Therefore, at very low temperatures, we predict the cumulative direct and surface-assisted contribution (green dotted line in Fig. 6.2) to dominate the surface plasmon decay.

Fig. 6.3 shows the initial carrier distributions generated via direct and phonon-assisted transitions, which we calculate by histogramming the integrands in (6.2) and (6.3) by the initial (hole) and final (electron) state energies. The carrier distributions are plotted as a function of carrier energy (horizontal axis) and plasmon / photon energy (axis normal to the page). The color scale indicates the fraction of carriers generated by direct or phonon-assisted transitions.

Direct transitions, shown in blue, dominate at high energies and exhibit the strong material dependence we previously discussed in detail in Ref. [33]. For copper and gold, direct transitions occur from the $d$-bands to unoccupied states above the Fermi level, which results in holes that are

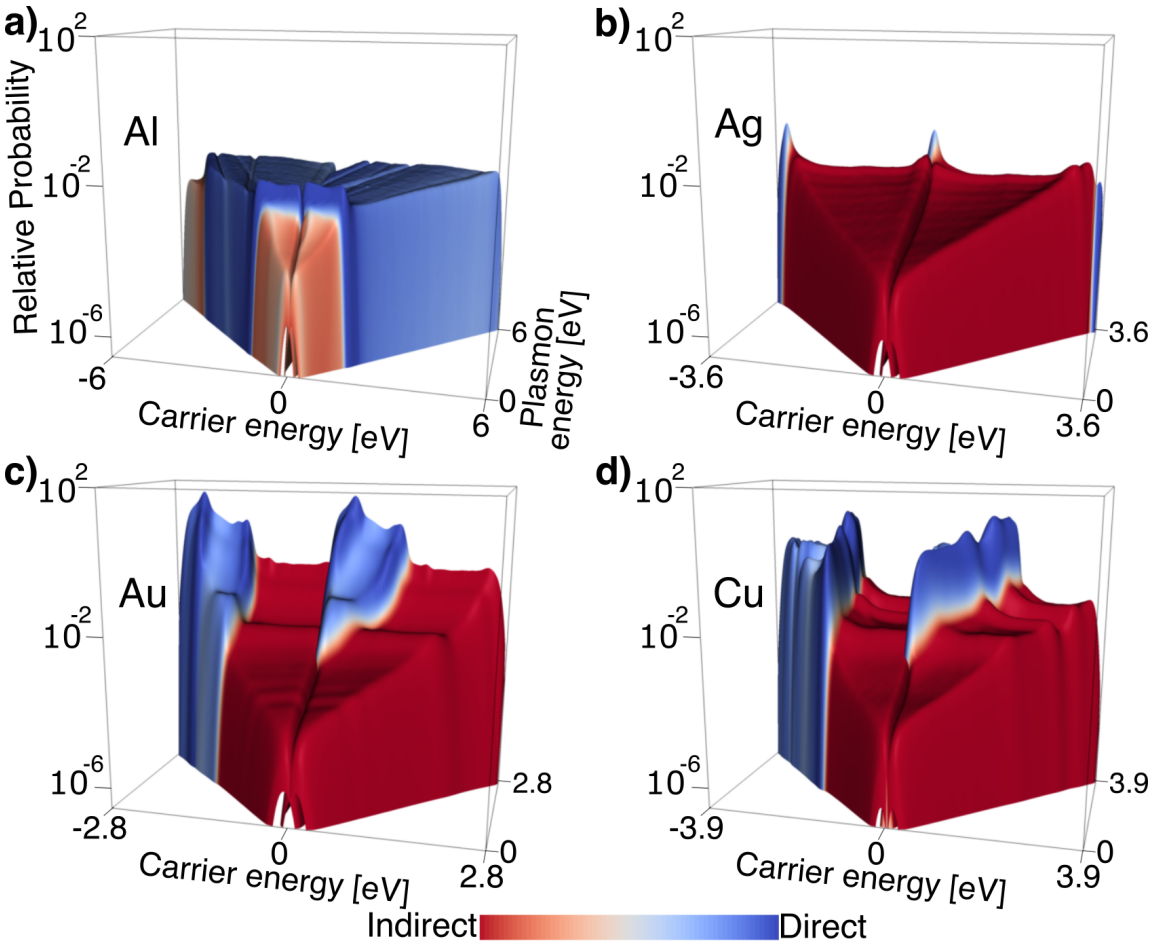


Figure 6.3: Energy distributions of hot carriers generated by to phonon-assisted and direct transitions in (a) Al (b) Ag (c) Au and (d) Cu. The color-scale indicates the fraction of carriers produced by phonon-assisted (red) or direct (blue) transitions.

much more energetic than electrons. Aluminum exhibits a relatively flat distribution of electrons and holes, while silver exhibits a bimodal distribution of hot electrons as well as holes from direct transitions in a very narrow frequency range close to the maximum plasmon frequency.

Phonon-assisted transitions, shown in red, exhibit a flat distribution of electrons and holes extending from zero to the plasmon energy for all the metals. In aluminum, direct transitions are also possible below the threshold at 1.6 eV and contribute $\sim 25\%$ of the generated carriers. For the other metals, phonon-assisted transitions generate a majority of the carriers since surface-assisted transitions are negligible at room temperature as discussed above. Resistive losses compete with phonon-assisted transitions, but dissipate thermally and do not generate energetic hot carriers. Due to this competition, only $\sim 50\%$ of the absorbed energy results in hot carrier generation below threshold. Therefore, plasmonic hot-carrier applications could benefit from the higher efficiency above threshold, where direct transitions dominate by far and result in high-energy carriers. Additionally, we predict aluminum to be an excellent candidate for general hot carrier applications since it allows direct transitions at all energies and has the smallest fraction of resistive loss (despite its absolute resistivity being higher than other metals).

### 6.3.2 Carrier Transport

In experiments, hot carriers generated by plasmon decay must live long enough or travel far enough to be collected or detected. The time and length scales of such non-equilibrium carrier transport has been the subject of much recent debate.[21, 5, 12] Here, we present *ab initio* predictions for the lifetimes and mean free paths of hot carriers as a function of energy in all four metals considered above, accounting for electron-phonon and electron-electron scattering.

For the electron-electron scattering contribution, we calculate the imaginary part of the quasiparticle self energy given by[15]

$$\Im\Sigma^{\text{e-e}}_{\mathbf{q}n} = \int_{\text{BZ}} \frac{d\mathbf{q}'}{(2\pi)^3} \sum_{n'} \sum_{\mathbf{G}\mathbf{G}'} \tilde{\rho}_{\mathbf{q}'n',\mathbf{q}n}(\mathbf{G}) \tilde{\rho}^*_{\mathbf{q}'n',\mathbf{q}n}(\mathbf{G}') \times \frac{4\pi e^2}{|\mathbf{q}' - \mathbf{q} + \mathbf{G}|^2} \Im\left[\epsilon^{-1}_{\mathbf{G}\mathbf{G}'}(\mathbf{q}' - \mathbf{q}, \varepsilon_{\mathbf{q}n} - \varepsilon_{\mathbf{q}'n'})\right], \quad (6.6)$$

where $\tilde{\rho}_{\mathbf{q}'n',\mathbf{q}n}(\mathbf{G})$ is the plane-wave expansion of the product density $\sum_\sigma u^{\sigma *}_{\mathbf{q}'n'}(\mathbf{r}) u^\sigma_{\mathbf{q}n}(\mathbf{r})$ of Bloch functions with reciprocal lattice vectors $\mathbf{G}$, and $\epsilon^{-1}_{\mathbf{G}\mathbf{G}'}(\mathbf{k}, \omega)$ is the microscopic dielectric function in

a plane-wave basis calculated within the random-phase approximation. See Ref. [15] for a detailed exposition including its connection to Fermi golden rule for electron-electron scattering. Here, we calculate (6.6) in JDFTx[34] using an explicit frequency integral with 0.1 eV resolution for the dielectric function, retaining local field effects with a kinetic energy cutoff of 200 eV. The remaining computational details are identical to the plasmon decay calculations described in the Methods section.

We calculate the electron-phonon scattering contribution to the electron linewidth using Fermi golden rule

$$\Im\Sigma^{\text{e-ph}}_{\mathbf{q}n} = \pi \int_{\text{BZ}} \frac{\Omega d\mathbf{q}'}{(2\pi)^3} \sum_{n'\alpha\pm} \left( n_{\mathbf{q}'-\mathbf{q},\alpha} + \frac{1}{2} \mp \frac{1}{2} \right) \times \delta(\varepsilon_{\mathbf{q}'n'} - \varepsilon_{\mathbf{q}n} \mp \hbar\omega_{\mathbf{q}'-\mathbf{q},\alpha}) \left| g^{\mathbf{q}'-\mathbf{q},\alpha}_{\mathbf{q}'n',\mathbf{q}n} \right|^2, \quad (6.7)$$

where the electronic states, phonon modes and electron-phonon matrix elements are computed exactly as for the phonon-assisted decay (see Methods section). Additionally, we use a dense $48 \times 48 \times 48$ grid to sufficiently resolve the $\mathbf{q}'$ integral with electron and phonon occupations at standard temperature, $T = 298$ K.

We then calculate the total carrier linewidth $\Im\Sigma_{\mathbf{q}n} = \Im\Sigma^{\text{e-e}}_{\mathbf{q}n} + \Im\Sigma^{\text{e-ph}}_{\mathbf{q}n}$, the carrier lifetime $\tau_{\mathbf{q}n} = \hbar/(2\Im\Sigma_{\mathbf{q}n})$ and mean free path $\lambda_{\mathbf{q}n} = v_{\mathbf{q}n}\tau_{\mathbf{q}n}$, where $\mathbf{v}_{\mathbf{q}n} \equiv \frac{\partial\varepsilon_{\mathbf{q}n}}{\partial\mathbf{q}}$ is the group velocity of electronic state $\mathbf{q}n$. Figure **??** shows the resulting carrier lifetimes and mean free paths as a function of carrier energy relative to the Fermi level, for aluminum and the noble metals. For each metal, the axes for lifetime and mean free paths have been scaled relatively by the Fermi velocity so that the two quantities approximately coincide for low energy carriers.

For all metals, we find that low energy carriers close to the Fermi level have the longest lifetime and mean free path. At these energies, electron-phonon scattering dominates while electron-electron scattering, which is nominally proportional to $(\varepsilon - \varepsilon_f)^2$ due to the phase space available for scattering,[15] is negligible. The noble metals have similar maximum carrier lifetimes $\sim 30$ fs and mean free paths $\sim 50$ nm in the order Ag > Cu > Au, while aluminum has a smaller maximum lifetime $\sim 10$ fs and mean free path of $\sim 20$ nm.

With increasing carrier energy away from the Fermi level, for both electrons and holes, the electron-phonon scattering rates remain nominally constant while the electron-electron scattering

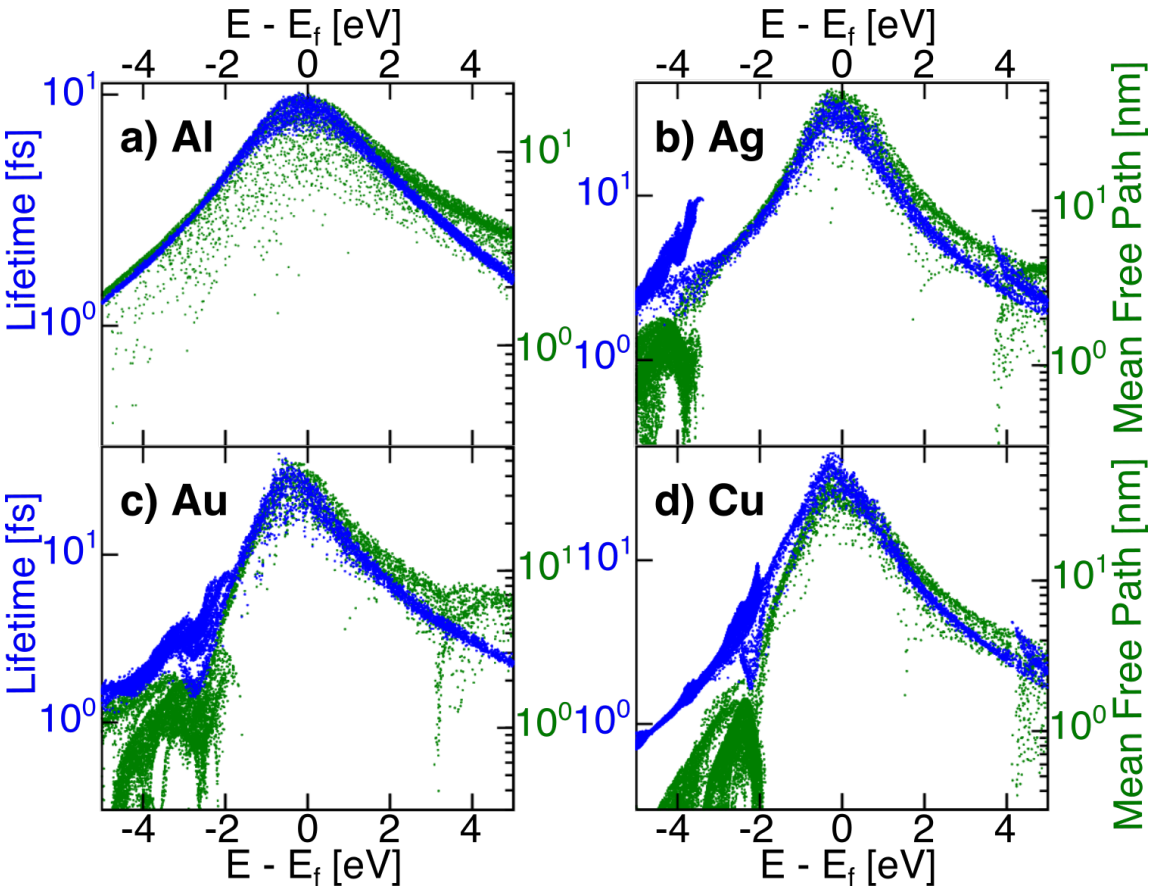


Figure 6.4: Comparison of total, e-e and e-phonon contributions to carrier line widths in (a) Al (b) Ag (c) Au and (d) Cu.

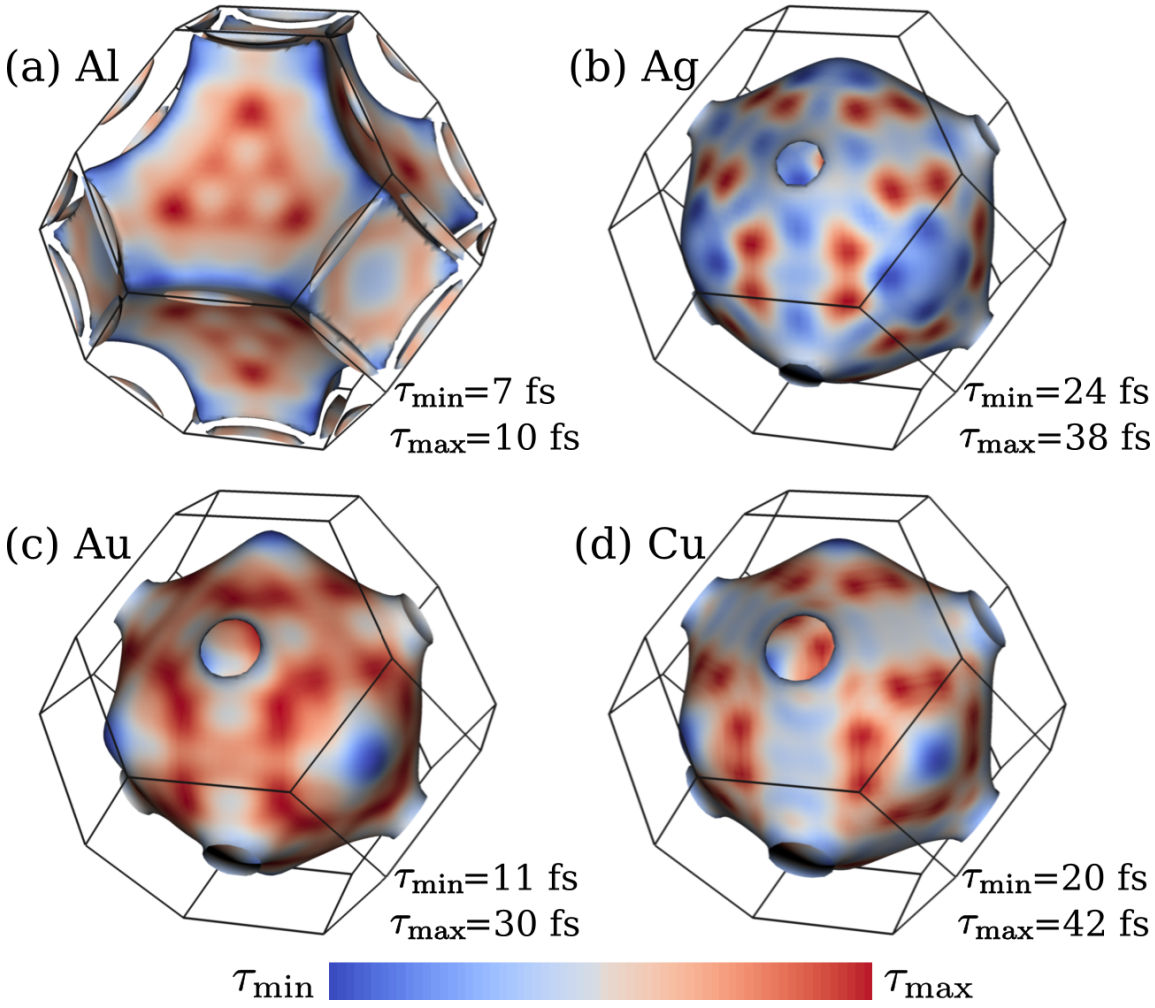


Figure 6.5: Anisotropy of hot carrier lifetimes on the Fermi surface of (a) Al (b) Ag (c) Au and (d) Cu, with variations of about a factor of two between regions of positive and negative curvature of the Fermi surface.

rates increase dramatically reducing the lifetimes and mean free paths. The electron-electron and electron-phonon contributions become comparable roughly at 1 eV away from the Fermi level for all four metals. The mean free paths drop to $\sim$ 10 nm in all four metals for 2 eV electrons.

Figure 6.4 also exhibits an asymmetry between electron versus hole transport in all the metals. Electrons and holes of similar energies have similar lifetimes, but electrons have higher group velocities, and hence higher mean free paths, because of the curvature of the dispersion relation. This effect is particularly drastic for $d$-band holes in the noble metals, which are relatively localized states with dramatically smaller group velocities. However, after the first scattering event, $d$-band holes result in $s$-band holes with half the energy on average, which can transport much further. Additionally, our results indicate that aluminum and silver are particularly attractive for the transport of high energy holes.

## 6.4 Conclusions

In this chapter we report the first *ab initio* calculations of phonon-assisted optical excitations in metals, allowing us to link the energy range between resistive losses at low energies (microwave-infrared) and direct interband transitions at high energies (visible-ultraviolet). Along with surface-assisted transitions due to field confinement in metals,[13] this completes the theoretical picture of surface plasmon decay, accounting for all relevant mechanisms.

We find good agreement with experimental measurements for the total decay rate, but we additionally predict the relative contributions of all these processes and the initial generation of hot carriers in plasmonic metals. We find that direct transitions dominate above threshold and generate hot carriers, while below threshold, hot carrier generation by phonon-assisted transitions is diminished by competition from resistive losses. We also find that surface-assisted transitions, which have been the subject of considerable recent debate, are negligible compared to phonon-assisted and resistive contributions at room temperature. However, we predict that they could be important below threshold at very low temperatures.

We suggest that aluminum is quite promising as a general-purpose plasmonic hot carrier generator since it generates hot carriers efficiently for the widest frequency range, and generates high-energy electrons and holes with equal probability. Compared to the noble metals, aluminum also exhibits the best transport properties for high energy holes. A detailed analysis of the transport of energetic

carriers in real metal nanostructures, based on the initial carrier distributions and scattering rates predicted here, now enable directed design of optimal hot carrier devices.

## 6.5 Methods

### 6.5.1 Electronic Structure

We require an approximation to quasiparticle energies and optical matrix elements to describe the decay of surface plasmons to quasiparticle excitations (6.2,6.3). We use the relativistic DFT+$U$ approach that we previously established[33] to best reproduce experimental photoemission spectra in contrast to semilocal density-functional or even quasiparticle self-consistent GW methods.[29] Strong screening in metals renders electron-hole interactions and excitonic effects negligible, so that we can work at the independent quasiparticle level rather than with the more expensive Bethe-Salpeter equation[30] that accounts for those effects.

Following Ref. [33], we perform density-functional calculations in the open-source code JDFTx[34] with full-relativistic norm-conserving pseudopotentials at a plane-wave cutoff of 30 $E_h$ (Hartrees). We use the PBEsol[27] exchange-correlation approximation and a rotationally-invariant DFT+U correction[8] for the $d$-electrons in noble metals ($U$ = 1.63 eV, 2.45 eV and 2.04 eV respectively for copper, silver and gold). See Ref. [33] for more details regarding the selection of the electronic structure method.

We perform the self-consistent ground state calculations using a $12\times12\times12$ uniform $k$-point mesh centered at the $\Gamma$ point along with a Fermi-Dirac smearing of 0.01 $E_h$ to resolve the Fermi surface. The optical matrix elements correspond to the momentum operator $\hat{\mathbf{p}} \equiv \frac{m_e}{i\hbar}[\mathbf{r}, \hat{\mathbf{H}}] = \frac{\hbar}{i}\boldsymbol{\nabla} + \frac{m_e}{i\hbar}[\mathbf{r}, \hat{\mathbf{V}}_{\mathrm{NL}}]$, which accounts for the fact that the nonlocal DFT+$U$ and pseudopotential contributions ($\hat{\mathbf{V}}_{\mathrm{NL}}$) to the DFT Hamiltonian ($\hat{\mathbf{H}}$), do not commute with the position operator, $\mathbf{r}$. These nonlocal corrections are usually insignificant for $s$ and $p$-like electrons, but are critical for describing optical transitions involving the $d$-electrons in the noble metals.[19]

Finally, we interpolate the electronic energies and matrix elements to arbitrary $k$-points in the Brillouin zone using a basis of maximally-localized Wannier functions.[20, 31] Specifically, we use an $sp^3$ basis with 4 Wannier bands for aluminum and a relativistic $d^5t^2$ basis with 14 Wannier bands for the noble metals (where $t$ is an orbital centered on the tetrahedral void sites of the face-centered

cubic lattice). These Wannier functions exactly reproduce the orbital energies and matrix elements within the maximum surface plasmon energy of the Fermi level for all metals. We then evaluate (6.2) by Monte Carlo sampling $6.4 \times 10^6$ $\mathbf{q}$ values in the Brillouin zone for the noble metals ($9.6 \times 10^7$ for aluminum), and histogram contributions by plasmon and carrier energies to get the direct-transition results in Figures 6.2 and 6.3. Note that aluminum requires more $\mathbf{q}$ samples to get similar statistics since it contributes fewer pairs of bands per $\mathbf{q}$.

### 6.5.2 Phonon modes and matrix elements

We calculate the *ab initio* force matrix for phonons and electron-phonon matrix elements from direct perturbations of atoms in a $4 \times 4 \times 4$ supercell using exactly the same electronic DFT parameters as above in JDFTx.[34] All four metals considered here have a single atom basis and hence exactly three acoustic phonon modes. We then cast these phonon energies and matrix elements into a Wannier basis to enable interpolation for a dense sampling of the Brillouin zone integrals. (See Ref. [11] for a detailed introduction; we implement an analogous method in JDFTx, with additional support for spinorial relativistic calculations.)

We use the aforementioned Wannier basis to cover the energy range close to the Fermi level, and add random-initialized maximally-localized Wannier orbitals orthogonal to the first set to extend the energy range of included unoccupied states. We use a total of 24 Wannier bands for aluminum and 46 spinorial Wannier bands for the noble metals that exactly reproduce the orbital energies, optical and phonon matrix elements up to at least 50 eV above the Fermi level. We find this energy range of unoccupied states sufficient to fully converge the sum over states in the second order perturbation theory expression (6.3) at all plasmon energies considered.

Finally, we evaluate the double integral over Brillouin zone in (6.3) by Monte Carlo sampling with $2 \times 10^7$ $\{\mathbf{q}, \mathbf{q}'\}$ pairs for the noble metals ($3 \times 10^8$ pairs for aluminum to get similar statistics). We use standard temperature, $T = 298$ K, to calculate the Fermi occupations for electrons and Bose occupations for phonons. Note that such low electronic temperatures (compared to the Fermi energy $\sim 10^5$ K) necessitate extremely dense Brillouin zone sampling, which is, in turn, made practical by the Wannier interpolation.[11] Histogramming by plasmon and carrier energies, we collect the phonon-assisted contributions to Figures 6.2 and 6.3 (after incorporating the extrapolation discussed below to eliminate sequential process contributions).

### 6.5.3 Extrapolation to eliminate sequential processes

In the results section, we pointed out that (6.3) contains singular contributions when the intermediate state conserves energy (is 'on shell') causing the denominators in the effective second-order matrix element to vanish. We examine these on-shell contributions in more detail here.

By taking the limit $\eta \to 0$ in (6.3) and noting that $|1/(x+i\eta)|^2 \to \pi\delta(x)/\eta$, we can show that

$$\begin{aligned}\boldsymbol{\lambda}^* \cdot \Im\bar{\epsilon}_{\text{phonon}}(\mathbf{q}'n', \mathbf{q}n) \cdot \boldsymbol{\lambda} \\ &= \frac{\Im\Sigma^{\text{e-ph}}_{\mathbf{q}n'}}{\eta} \left(\boldsymbol{\lambda}^* \cdot \Im\bar{\epsilon}_{\text{direct}}(\mathbf{q}n', \mathbf{q}n) \cdot \boldsymbol{\lambda}\right) \\ &+ \left(\boldsymbol{\lambda}^* \cdot \Im\bar{\epsilon}_{\text{direct}}(\mathbf{q}'n', \mathbf{q}'n) \cdot \boldsymbol{\lambda}\right) \frac{\Im\Sigma^{\text{e-ph}}_{\mathbf{q}n}}{\eta} \\ &+ O(\eta^0) + O(\eta^1) + \cdots, \quad (6.8)\end{aligned}$$

where $\Im\bar{\epsilon}(\mathbf{q}'n', \mathbf{q}n)$ denotes the contribution to $\Im\bar{\epsilon}$ due to a specific pair of initial and final electronic states. Here, $\Im\Sigma^{\text{e-ph}}_{\mathbf{q}n}$ is the electron line width due to electron-phonon scattering, given by (6.7).

The above expansion in $\eta$ clearly illustrates that the singular contributions correspond to sequential processes. The first term corresponds to a direct transition followed by electron-phonon scattering while the second term corresponds to the reverse. If we substitute the intermediate state linewidth $\Im\Sigma_{\mathbf{q}n}$ for $\eta$ as the formalism prescribes,[22, 14] and for simplicity focus only on electron-phonon scattering contributions $\Im\Sigma^{\text{e-ph}}_{\mathbf{q}n}$ (which is dominant for low energy carriers), then we see that the $\eta$-singular part reduces simply to twice the direct contribution (6.2). For a metal, this contribution should not be counted as a separate decay rate since scattering events preceding and following a transition are part of the initial Fermi distribution and the subsequent carrier transport respectively.

We eliminate the singular contributions using an extrapolation scheme designed to exploit the fact that the $\eta$ dependence is different for on-shell and off-shell processes. To retain the non-singular $O(\eta^0)$ terms while canceling the $O(\eta^{-1})$ singular terms discussed above, we modify equation (6.3) as

$$(6.3)_{\text{corrected}} = 2\,(6.3)|_{2\eta} - (6.3)|_{\eta}\,. \quad (6.9)$$

We find that $\eta = 0.1$ eV, which was previously used for semiconductors,[22] is sufficiently large to

keep the singular terms resolvable for effective subtraction and sufficiently small to have negligible impact on the physical non-singular contributions. We note that this extrapolation only has an effect and is necessary above the optical gap of the material. Previous *ab initio* studies of phonon-assisted processes did not deal with this issue since they focused on predictions for semiconductors above the indirect gap and below the direct (optical) gap.

### 6.5.4 *Ab initio* estimate of resistive losses

Single electron-hole pair generation dominate the plasmon decay at high frequencies. As the Results section discusses, resistive loss in the metal, which arises from the finite carrier lifetime and results in heating rather than few energetic carriers, dominates at frequencies close to 0 eV. Here, we estimate these losses from the frequency-dependent resistivity calculated *ab initio* within a linearized Boltzmann equation with a relaxation time approximation.

The Boltzmann equation for electron occupations $f_{\mathbf{q}n}(t)$ in a uniform time-dependent electric field $\mathbf{E}(t)$ is[23]

$$\frac{\partial f_{\mathbf{q}n}(t)}{\partial t} + e\mathbf{E}(t) \cdot \frac{\partial f_{\mathbf{q}n}(t)}{\partial \mathbf{p}} = \left.\frac{\partial f_{\mathbf{q}n}}{\partial t}\right|_{\text{coll}}. \tag{6.10}$$

We then substitute $f_{\mathbf{q}n}(t) = f_{\mathbf{q}n} + \delta f_{\mathbf{q}n}(t)$, where the first term is the equilibrium Fermi distribution and the second contains perturbations to linear order due to the applied electric field, and collect contributions at first order in $\mathbf{E}(t)$.

To first order, the collision integral on the right-hand side of (6.10) can be written as $-\delta f_{\mathbf{q}n}\tau_{\mathbf{q}n}^{-1}$, where $\tau_{\mathbf{q}n}^{-1}$ is the difference between rates of scattering out of and into the electronic state $\mathbf{q}n$. Within the relaxation time approximation, we assume that $\tau_{\mathbf{q}n}^{-1}$ is approximately constant for carriers near the Fermi level, and replace it by an average $\tau^{-1}$ (inverse of momentum relaxation time). This is an excellent approximation for metals where electron-phonon scattering dominates carrier relaxation near the Fermi level,[23] which is the case for most elemental metals (except those with partially occupied *d*-shells) including aluminum and the noble metals.

Switching (6.10) to the frequency domain, linearizing, invoking the relaxation time approximation, and rearranging, we get

$$\delta f_{\mathbf{q}n}(\omega) = \frac{-e f'_{\mathbf{q}n}}{\tau^{-1} - i\omega} \mathbf{v}_{\mathbf{q}n} \cdot \mathbf{E}(\omega), \tag{6.11}$$

where $\mathbf{v}_{\mathbf{q}n} \equiv \frac{\partial \varepsilon_{\mathbf{q}n}}{\partial \mathbf{q}}$ is the group velocity of electronic state $\mathbf{q}n$ and $f'_{\mathbf{q}n}$ is the energy derivative of the Fermi-Dirac distribution. We then calculate the current density $\mathbf{j} = \sum_{\mathbf{q}n} e f_{\mathbf{q}n} \mathbf{v}_{\mathbf{q}n}$, and obtain the

Table 6.1: *Ab initio* momentum relaxation times and resistivities of plasmonic metals at $T = 298$ K, compared to experimental resistivities from Ref. [17].

| Metal | $\tau$ [fs] | $\rho_0 = \sigma_0^{-1}$ [$\Omega$m] | Expt $\rho_0$ [$\Omega$m] |
|---|---|---|---|
| Al | 12.0 | $2.46 \times 10^{-8}$ | $2.71 \times 10^{-8}$ |
| Cu | 35.6 | $1.58 \times 10^{-8}$ | $1.71 \times 10^{-8}$ |
| Ag | 36.4 | $1.58 \times 10^{-8}$ | $1.62 \times 10^{-8}$ |
| Au | 26.3 | $2.23 \times 10^{-8}$ | $2.26 \times 10^{-8}$ |

conductivity tensor by factoring out $\mathbf{v}_{\mathbf{q}n}$. Averaging over directions, the isotropic conductivity is then

$$\sigma(\omega) = \frac{1}{1 - i\omega\tau} \underbrace{e^2\tau \int_{\mathrm{BZ}} \frac{d\mathbf{q}}{(2\pi)^3} \sum_n (-f'_{\mathbf{q}n}) \frac{v_{\mathbf{q}n}^2}{3}}_{\equiv \sigma_0}, \tag{6.12}$$

where $\sigma_0$ is the zero-frequency (DC) conductivity.

Finally we calculate the momentum relaxation time $\tau$ using Fermi golden rule for electron-phonon scattering. In the average, we weight the scattering rates by $(-f'_{\mathbf{q}n})\frac{v_{\mathbf{q}n}^2}{3}$ since that determines the relative contributions to the conductivity above. It is then straightforward to show that $\tau^{-1} = \Gamma_{\mathrm{sum}}/w_{\mathrm{sum}}$, where

$$\begin{aligned}\Gamma_{\mathrm{sum}} = \frac{2\pi}{\hbar} \int_{\mathrm{BZ}} \frac{\Omega d\mathbf{q} d\mathbf{q}'}{(2\pi)^6} \sum_{n'n\alpha\pm} (-f'_{\mathbf{q}n}) \frac{v_{\mathbf{q}n}^2 - \mathbf{v}_{\mathbf{q}n} \cdot \mathbf{v}_{\mathbf{q}'n'}}{3} \\ \times \left[ n_{\mathbf{q}'-\mathbf{q},\alpha} + \frac{1}{2} \mp \left( \frac{1}{2} - f_{\mathbf{q}'n'} \right) \right] \\ \times \delta(\varepsilon_{\mathbf{q}'n'} - \varepsilon_{\mathbf{q}n} \mp \hbar\omega_{\mathbf{q}'-\mathbf{q},\alpha}) \left| g_{\mathbf{q}'n',\mathbf{q}n}^{\mathbf{q}'-\mathbf{q},\alpha} \right|^2\end{aligned} \tag{6.13}$$

with all the *ab initio* electron and phonon properties defined exactly as before, and where the denominator for normalizing the weights is

$$w_{\mathrm{sum}} = \int_{\mathrm{BZ}} \frac{d\mathbf{q}}{(2\pi)^3} \sum_n (-f'_{\mathbf{q}n}) \frac{v_{\mathbf{q}n}^2}{3}. \tag{6.14}$$

Note that with this definition, we can simplify the DC conductivity, $\sigma_0 = e^2\tau w_{\mathrm{sum}} = e^2 w_{\mathrm{sum}}^2/\Gamma_{\mathrm{sum}}$.

Given the frequency-dependent conductivity of the metal, we can calculate the resistive losses $\Im\epsilon = \Im\left[4\pi i\sigma(\omega)/\omega\right]$, which results in (6.5) upon simplification. We calculate $w_{\mathrm{sum}}$ and $\Gamma_{\mathrm{sum}}$ using Monte Carlo sampling of the Brillouin zone integrals with $1.6 \times 10^6$ $\mathbf{q}$ values for the single integral

and $5 \times 10^7$ $\{\mathbf{q}, \mathbf{q}'\}$ pairs for the double integral, which converges $\tau$ and $\sigma_0$ within 1%. Table 6.1 lists the momentum-relaxation time and resistivity we predict for the common plasmonic metals. The excellent agreement with experimental resistivities demonstrates the quantitative accuracy of the *ab initio* electron-phonon coupling (better than 10% in all cases).

## 6.6 Multiplasmon and Nonlinear Processes

Now we focus on the imaginary part, $\Im\chi^3$, of the cubic susceptibility for two reasons. First, this corresponds physically to two plasmons (or photons) exciting an electronic transition in the material with the sum of their energies, resulting in higher energy carriers than the corresponding transitions induced by single plasmons which contribute to $\Im\chi^1$. This opens up the unique possibility of electrically detecting the two-plasmon process by discriminating carrier energies, as we discuss later. Second, the imaginary parts of the susceptibility have a closer connection to the electronic structure properties of the material such as the joint density of states at a given frequency. They are easier to calculate and interpret physically compared to the real parts which require additional frequency integrals.

We consider processes involving one or two plasmons of the same mode – frequency and polarization – in order to keep the number of variables explored below (material, geometry, frequency, carrier energy, intensity etc.) manageable. The extension to plasmons of different modes is straightforward but that does not lend any additional insight and we therefore omit such cases here for simplicity. With a single plasmon frequency $\omega$, the one plasmon process $\Im\chi^1$ then excites electronic transitions with energy $\hbar\omega$ whereas the two-plasmon process excites those with energy $2\hbar\omega$.

We previously analyzed the one-plasmon process ($\Im\chi^1$) in great detail and showed that we can quantitatively account for experimental decay rates with first principles calculations of direct and phonon-assisted transitions. Figure **??** shows the Feynman diagrams associated with these processes. The direct transition absorbs a plasmon and creates an electron-hole pair with net zero crystal momentum, which is possible only above the interband threshold energy $E_t$. Direct transitions dominate above this threshold, and are forbidden below it. Below threshold, $\Im\chi^1$ is dominated by phonon-assisted intraband transitions which derive momentum from the additional absorption or emission of phonons to excite an electron-hole pair with net crystal momentum.

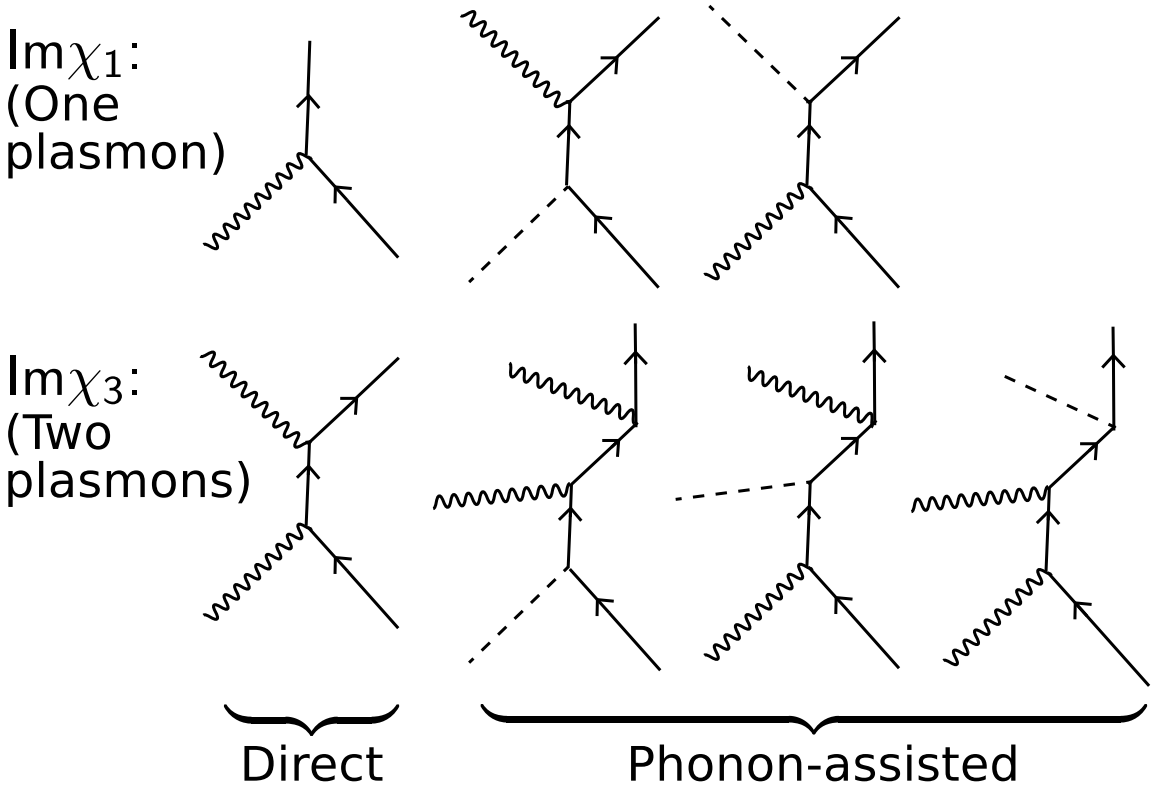


Figure 6.6: Analogously to the one-plasmon case, the Feynman diagrams for multiplasmon processes are shown here. The two-plasmon process ($\Im\chi^3$), similarly, includes direct and phonon-assisted contributions. The lowest order process involves two plasmons decaying together to excite an electronic transition with the sum of their energies. However, the total plasmon momentum is still negligible compared to electron momenta requiring the initial and final electron states to have the same crystal momentum, which implies that the total energy of the transition must exceed the interband threshold energy $E_t$. Therefore, this process dominates above plasmon energies $E_t/2$. Again, phonons can provide momentum to excite transitions with different initial and final electron crystal momenta and this process dominates below the two-plasmon threshold energy $E_t/2$.

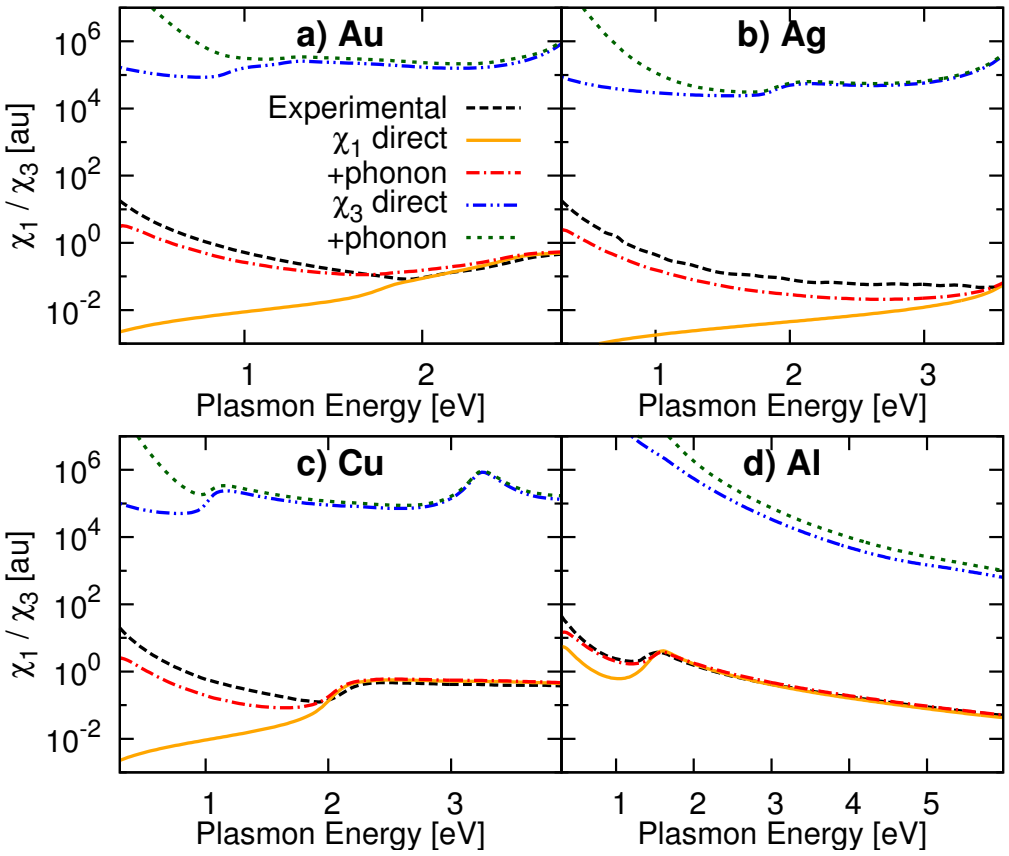


Figure 6.7: Comparison of contributions to linear and cubic susceptibilities, $\Im\chi^1$ and $\Im\chi^3$, as a function of frequency in (a) gold (b) silver (c) copper and (d) aluminum. Direct transitions dominate $\Im\chi^1$ above the interband threshold energy $E_t$ and $\Im\chi^3$ above $E_t/2$. The lines labeled '+phonon' show the total contributions from direct and phonon-assisted transitions, and the latter dominate $\Im\chi^1$ and $\Im\chi^3$ below $E_t$ and $E_t/2$ respectively. The experimental estimates for $\Im\chi^1$ are obtained from ellipsometry.[25]

Qualitatively, $\Im\chi^3$ exhibits a similar frequency dependence in all cases, except that the energy scale is halved since two plasmons combine to excite the transition: direct transitions are allowed and dominate above half the interband threshold energy, while phonon-assisted intraband transitions dominate below it. Measuring $\Im\chi^3$ of plasmonic metals is challenging because the field inside the metals is much smaller than exteral fields making it difficult to reliably access the nonlinear regime in continuous wave measurements.

### 6.6.1 One-plasmon decay in terms of $\mathbf{Im}\chi^1$

$\operatorname{Im}\chi$ differs from Fermi golden rule for decay rate in the following ways. Instead of $2\pi/\hbar$, we have just $\pi$ since $\hbar$ was to convert energy to rate and 2 to convert linewidth to rate. Additionally, the response is calculated at unit electric field i.e. $\mathbf{A} = \frac{1}{i\omega}\hat{\mathbf{E}}$ and we normalize to unit volume instead of per-unit-cell.

$$
\begin{aligned}
\operatorname{Im}\chi^1 &\equiv \frac{\pi}{\Omega}\sum_f \delta(E_i - E_f)|\mathcal{M}_{if}|^2 (\text{with } \mathcal{M}_{if} \text{ corresponding to } \hat{\mathbf{E}} \text{ perturbation}) \\
&= \frac{\pi}{\Omega}\frac{1}{N_q}\sum_{\mathbf{q}n'n}(f_{\mathbf{q}n} - f_{\mathbf{q}n'})\delta(\varepsilon_{\mathbf{q}n'} - \varepsilon_{\mathbf{q}n} - \hbar\omega)\left|\frac{e\hat{\mathbf{E}}}{i\omega}\cdot\langle\mathbf{v}\rangle^{\mathbf{q}}_{n'n}\right|^2 \\
&= \frac{\pi e^2}{\Omega\omega^2}\frac{1}{N_q}\sum_{\mathbf{q}n'n}(f_{\mathbf{q}n} - f_{\mathbf{q}n'})\delta(\varepsilon_{\mathbf{q}n'} - \varepsilon_{\mathbf{q}n} - \hbar\omega)|\hat{\mathbf{E}}\cdot\langle\mathbf{v}\rangle^{\mathbf{q}}_{n'n}|^2
\end{aligned}
$$

$$
\begin{aligned}
\Gamma^{1p}_{\mathrm{SPP}} &\equiv \frac{2}{\hbar}\int \mathrm{d}\mathbf{r}|\mathbf{E}(r)|^2 \operatorname{Im}\chi^1 \\
&= \frac{2}{\hbar}\int_S \mathrm{d}x\mathrm{d}y\int_{-\infty}^0 \mathrm{d}z\left|i\omega\sqrt{\frac{2\pi\hbar}{\omega L(\omega)S}}e^{|\gamma_-|z}\left(\hat{\mathbf{k}} - \frac{k}{\gamma_-}\hat{\mathbf{z}}\right)e^{i(\mathbf{k}\cdot\mathbf{r}-\omega t)}\right|^2 \operatorname{Im}\chi^1 \\
&= \frac{2}{\hbar}\omega^2\frac{2\pi\hbar}{\omega L(\omega)S}\left(\int_S \mathrm{d}x\mathrm{d}y\int_{-\infty}^0 \mathrm{d}z e^{2|\gamma_-|z}\right)\left|\left(\hat{\mathbf{k}} - \frac{k}{\gamma_-}\hat{\mathbf{z}}\right)\right|^2 \operatorname{Im}\chi^1 \\
&= \frac{2}{\hbar}\omega^2\frac{2\pi\hbar}{\omega L(\omega)S}S\frac{1}{2|\gamma_-|}\left|\left(\hat{\mathbf{k}} - \frac{k}{\gamma_-}\hat{\mathbf{z}}\right)\right|^2 \operatorname{Im}\chi^1 \\
&= \frac{2\pi\omega}{L(\omega)|\gamma_-|}\left|\left(\hat{\mathbf{k}} - \frac{k}{\gamma_-}\hat{\mathbf{z}}\right)\right|^2 \operatorname{Im}\chi^1 \\
&= \frac{2\pi\omega}{L(\omega)|\gamma_-|}|\boldsymbol{\lambda}|^2\frac{\pi e^2}{\Omega\omega^2}\frac{1}{N_q}\sum_{\mathbf{q}n'n}(f_{\mathbf{q}n} - f_{\mathbf{q}n'})\delta(\varepsilon_{\mathbf{q}n'} - \varepsilon_{\mathbf{q}n} - \hbar\omega)|\hat{\boldsymbol{\lambda}}\cdot\langle\mathbf{v}\rangle^{\mathbf{q}}_{n'n}|^2 \\
&= \frac{2\pi^2 e^2}{\omega L(\omega)|\gamma_-|\Omega}\times\frac{1}{N_q}\sum_{\mathbf{q}n'n}(f_{\mathbf{q}n} - f_{\mathbf{q}n'})\delta(\varepsilon_{\mathbf{q}n'} - \varepsilon_{\mathbf{q}n} - \hbar\omega)|\boldsymbol{\lambda}\cdot\langle\mathbf{v}\rangle^{\mathbf{q}}_{n'n}|^2
\end{aligned}
$$

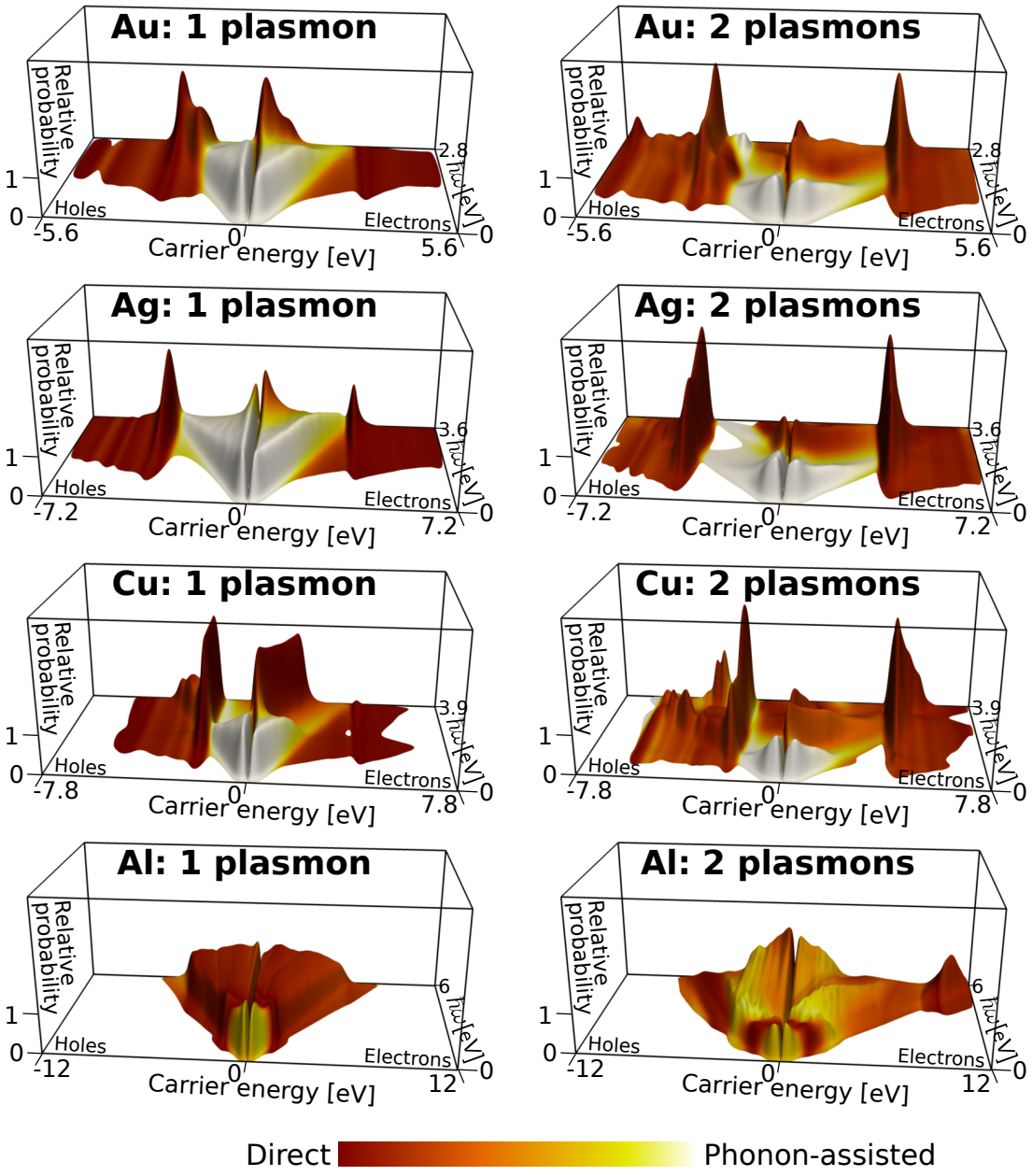


Figure 6.8: Energy distributions of hot electrons and holes generated due to single plasmon decay (left panels) and two-plasmon decay (right panels) in (a) gold (b) silver (c) copper and (d) aluminum. In each panel, the carrier energy varies from left to right and the plasmon energy from front to back. The color scale indicates the relative contributions of direct transitions (dark red) and phonon-assisted transitions (white). The carrier probabilities (vertical axis) are normalized for each plasmon energy such that a uniform distribution would be 1, as seen approximately for the single plasmon results of aluminium and below threshold for the noble metals.

### 6.6.2 Two-plasmon decay

$$
\begin{aligned}
\operatorname{Im}\chi^3 &\equiv \frac{\pi}{\Omega}\sum_f \delta(E_i-E_f)|\mathcal{M}_{if}|^2 (\text{with } \mathcal{M}_{if} \text{ corresponding to second order } \hat{\mathbf{E}} \text{ perturbation}) \\
&= \frac{\pi}{\Omega}\frac{1}{N_q}\sum_{\mathbf{q}n'n}(f_{\mathbf{q}n}-f_{\mathbf{q}n'})\delta(\varepsilon_{\mathbf{q}n'}-\varepsilon_{\mathbf{q}n}-2\hbar\omega)\left|\sum_l \frac{\left(\frac{e\hat{\mathbf{E}}}{i\omega}\cdot\langle\mathbf{v}\rangle^{\mathbf{q}}_{n'l}\right)\left(\frac{e\hat{\mathbf{E}}}{i\omega}\cdot\langle\mathbf{v}\rangle^{\mathbf{q}}_{ln}\right)}{\bar{\varepsilon}_{\mathbf{q}l}-\varepsilon_{\mathbf{q}n}-\hbar\omega}+(\omega_1\leftrightarrow\omega_2)\right|^2 \\
&= \frac{\pi}{\Omega}\frac{1}{N_q}\sum_{\mathbf{q}n'n}(f_{\mathbf{q}n}-f_{\mathbf{q}n'})\delta(\varepsilon_{\mathbf{q}n'}-\varepsilon_{\mathbf{q}n}-2\hbar\omega)\left|2\sum_l \frac{\left(\frac{e\hat{\mathbf{E}}}{i\omega}\cdot\langle\mathbf{v}\rangle^{\mathbf{q}}_{n'l}\right)\left(\frac{e\hat{\mathbf{E}}}{i\omega}\cdot\langle\mathbf{v}\rangle^{\mathbf{q}}_{ln}\right)}{\bar{\varepsilon}_{\mathbf{q}l}-\varepsilon_{\mathbf{q}n}-\hbar\omega}\right|^2 (\text{since } \omega_1=\omega_2) \\
&= \frac{\pi e^4}{\Omega\omega^4}\frac{1}{N_q}\sum_{\mathbf{q}n'n}(f_{\mathbf{q}n}-f_{\mathbf{q}n'})\delta(\varepsilon_{\mathbf{q}n'}-\varepsilon_{\mathbf{q}n}-2\hbar\omega)\left|2\sum_l \frac{(\hat{\mathbf{E}}\cdot\langle\mathbf{v}\rangle^{\mathbf{q}}_{n'l})(\hat{\mathbf{E}}\cdot\langle\mathbf{v}\rangle^{\mathbf{q}}_{ln})}{\bar{\varepsilon}_{\mathbf{q}l}-\varepsilon_{\mathbf{q}n}-\hbar\omega}\right|^2
\end{aligned}
$$

$$
\begin{aligned}
\Gamma^{2p}_{\mathrm{SPP}} &\equiv \frac{2}{\hbar}\int \mathrm{d}\mathbf{r}|\mathbf{E}(r)|^4 \operatorname{Im}\chi^3 \\
&= \frac{2}{\hbar}\int_S \mathrm{d}x\mathrm{d}y\int_{-\infty}^0 \mathrm{d}z\left|i\omega\sqrt{\frac{2\pi\hbar}{\omega L(\omega)S}}e^{|\gamma_-|z}\left(\hat{\mathbf{k}}-\frac{k}{\gamma_-}\hat{\mathbf{z}}\right)e^{i(\mathbf{k}\cdot\mathbf{r}-\omega t)}\right|^4 \operatorname{Im}\chi^3 \\
&= \frac{2}{\hbar}\omega^4\left(\frac{2\pi\hbar}{\omega L(\omega)S}\right)^2\int_S \mathrm{d}x\mathrm{d}y\int_{-\infty}^0 \mathrm{d}z e^{4|\gamma_-|z}|\boldsymbol{\lambda}|^4\operatorname{Im}\chi^3 \\
&= \frac{2}{\hbar}\omega^4\left(\frac{2\pi\hbar}{\omega L(\omega)S}\right)^2 S\frac{1}{4|\gamma_-|}|\boldsymbol{\lambda}|^4\operatorname{Im}\chi^3 \\
&= \frac{2\pi^2\hbar\omega^2}{L(\omega)^2|\gamma_-|S}|\boldsymbol{\lambda}|^4\operatorname{Im}\chi^3 \\
&= \frac{2\pi^2\hbar\omega^2}{L(\omega)^2|\gamma_-|S}|\boldsymbol{\lambda}|^4\frac{4\pi e^4}{\Omega\omega^4}\frac{1}{N_q}\sum_{\mathbf{q}n'n}(f_{\mathbf{q}n}-f_{\mathbf{q}n'})\delta(\varepsilon_{\mathbf{q}n'}-\varepsilon_{\mathbf{q}n}-2\hbar\omega)\left|\sum_l\frac{(\hat{\mathbf{E}}\cdot\langle\mathbf{v}\rangle^{\mathbf{q}}_{n'l})(\hat{\mathbf{E}}\cdot\langle\mathbf{v}\rangle^{\mathbf{q}}_{ln})}{\bar{\varepsilon}_{\mathbf{q}l}-\varepsilon_{\mathbf{q}n}-\hbar\omega}\right|^2 \\
&= \frac{2\pi^3\hbar e^4}{\omega^2L(\omega)^2|\gamma_-|\Omega S}\times\frac{1}{N_q}\sum_{\mathbf{q}n'n}(f_{\mathbf{q}n}-f_{\mathbf{q}n'})\delta(\varepsilon_{\mathbf{q}n'}-\varepsilon_{\mathbf{q}n}-2\hbar\omega)\left|\sum_l\frac{(\boldsymbol{\lambda}\cdot\langle\mathbf{v}\rangle^{\mathbf{q}}_{n'l})(\boldsymbol{\lambda}\cdot\langle\mathbf{v}\rangle^{\mathbf{q}}_{ln})}{\bar{\varepsilon}_{\mathbf{q}l}-\varepsilon_{\mathbf{q}n}-\hbar\omega}+(\leftrightarrow)\right|^2
\end{aligned}
$$

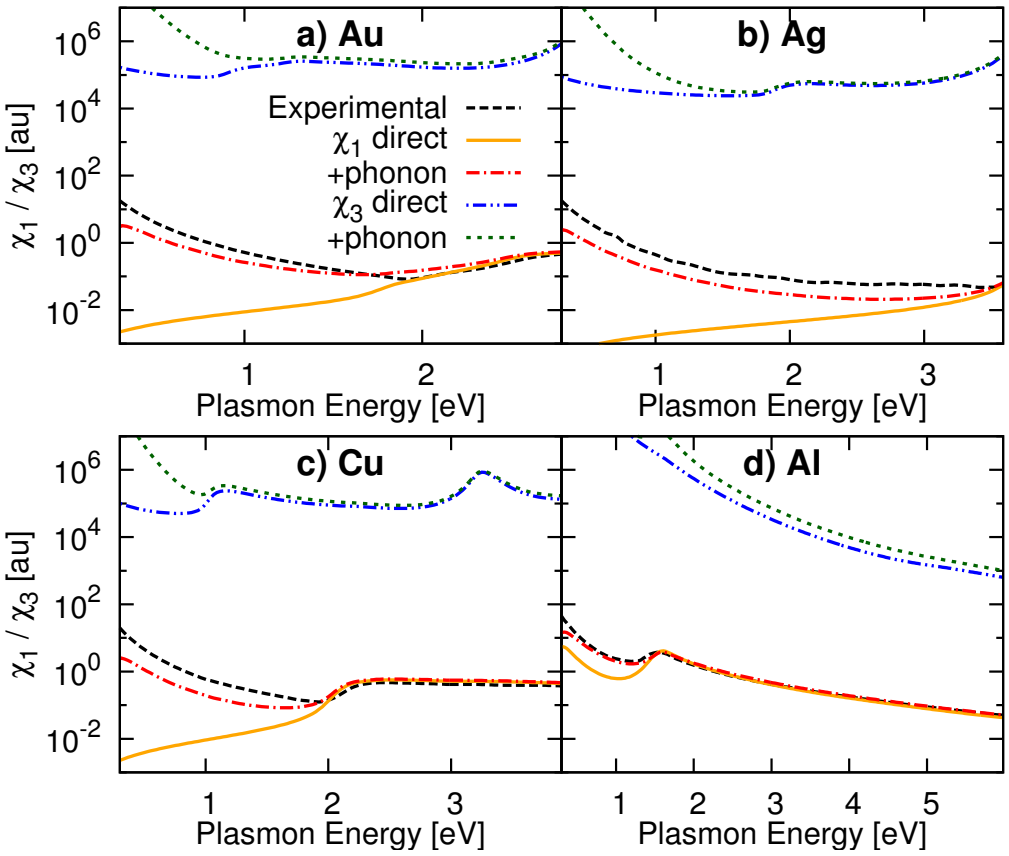


Figure 6.9: Comparison of contributions to linear and cubic susceptibilities, $\Im\chi^1$ and $\Im\chi^3$, as a function of frequency in (a) gold (b) silver (c) copper and (d) aluminum. Direct transitions dominate $\Im\chi^1$ above the interband threshold energy $E_t$ and $\Im\chi^3$ above $E_t/2$. The lines labeled '+phonon' show the total contributions from direct and phonon-assisted transitions, and the latter dominate $\Im\chi^1$ and $\Im\chi^3$ below $E_t$ and $E_t/2$ respectively. The experimental estimates for $\Im\chi^1$ are obtained from ellipsometry.[25]

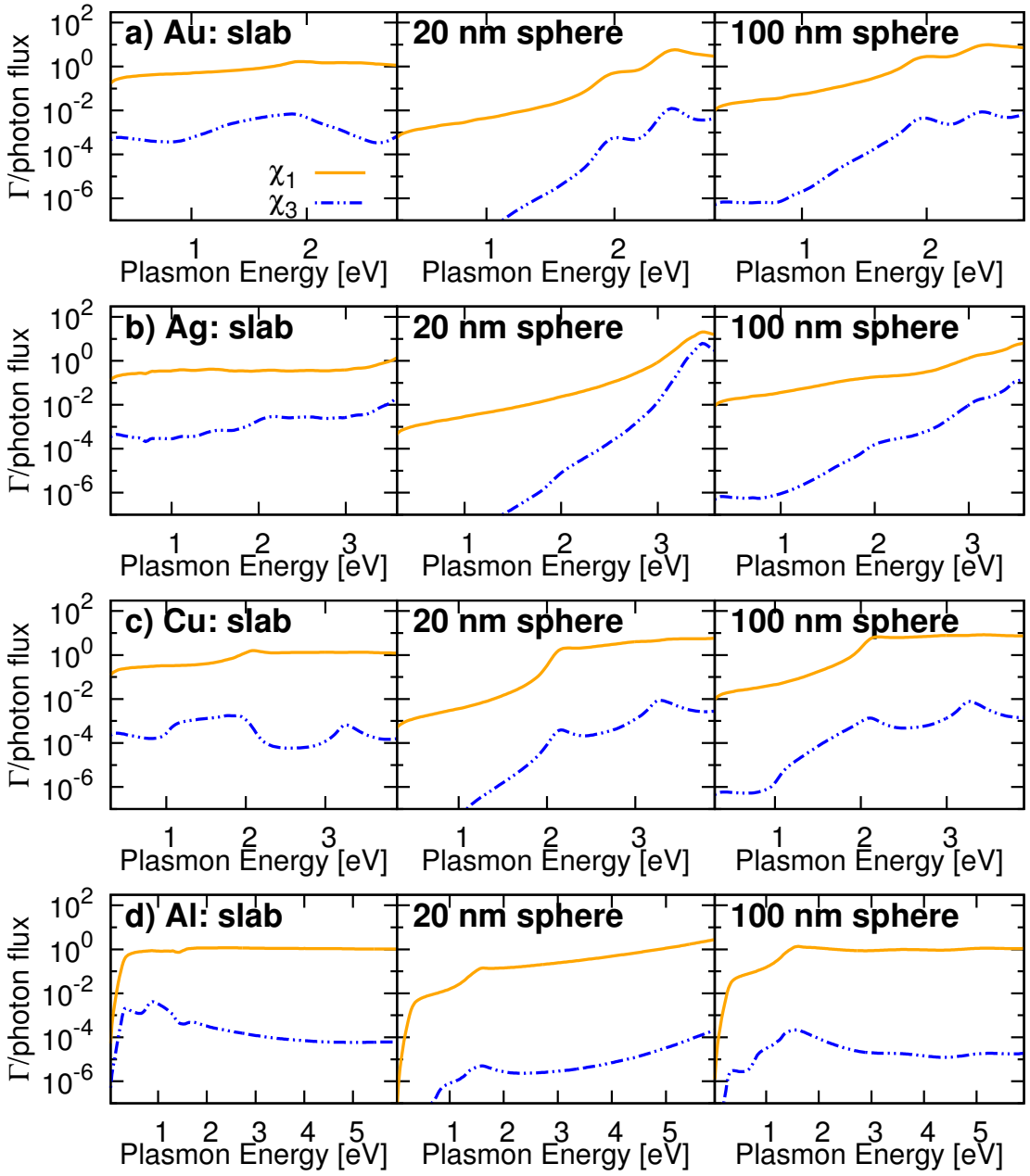


Figure 6.10: One and two-plasmon decay rates per photon flux for various geometries in (a) gold (b) silver (c) copper and (d) aluminum as a function of plasmon energy at a reference instantaneous intensity of $10^{12}$ W/m$^2$. The one-plasmon decay rates are independent of intensity and the two-plasmon decay rates increase proportionally with intensity. The geometries affect the instantaneous electric field and hence the relative contributions of one and two-plasmon processes: the left panels show results for a roughened metal surface assuming ideal coupling, the center panels for a 20 nm sphere and the right panels for a 100 nm sphere.

### 6.6.3 Planar geometry

For a given angle of incidence of light, solve optics problem to calculate surface electric field magnitude $E_0$ and decay constant $\gamma$ (of the field) i.e. $|\mathbf{E}(\mathbf{r})| = E_0 e^{\gamma z}$

$$\begin{aligned}
\Gamma^{1p} &= \frac{2}{\hbar}\int \mathrm{d}\mathbf{r}|\mathbf{E}(r)|^2 \,\mathrm{Im}\,\chi^1 \\
&= \frac{2}{\hbar} S \int_{-\infty}^{0} \mathrm{d}z E_0^2 e^{2\gamma z} \,\mathrm{Im}\,\chi^1 \\
&= \frac{2S}{\hbar} E_0^2 \frac{1}{2\gamma} \,\mathrm{Im}\,\chi^1
\end{aligned}$$

$$\begin{aligned}
\Gamma^{2p} &= \frac{2}{\hbar}\int \mathrm{d}\mathbf{r}|\mathbf{E}(r)|^4 \,\mathrm{Im}\,\chi^3 \\
&= \frac{2}{\hbar} S \int_{-\infty}^{0} \mathrm{d}z E_0^4 e^{4\gamma z} \,\mathrm{Im}\,\chi^3 \\
&= \frac{2S}{\hbar} E_0^4 \frac{1}{4\gamma} \,\mathrm{Im}\,\chi^3
\end{aligned}$$

$$\frac{\Gamma^{2p}}{\Gamma^{1p}} = \frac{E_0^2}{2}\frac{\mathrm{Im}\,\chi^3}{\mathrm{Im}\,\chi^1}$$

# Bibliography

Archambault, Alexandre et al. “Quantum theory of spontaneous and stimulated emission of surface plasmons”. In: *Physical Review B* 82.3 (July 12, 2010), pp. 035411–. URL: http://link.aps.org/doi/10.1103/PhysRevB.82.035411 (cit. on p. 88).

Barnes, William L., Alain Dereux, and Thomas W. Ebbesen. “Surface plasmon subwavelength optics”. In: *Nature* 424.6950 (Aug. 14, 2003), pp. 824–830. URL: http://dx.doi.org/10.1038/nature01937 (cit. on p. 85).

Bernardi, M. et al. “Theory and Computation of Hot Carriers Generated by Surface Plasmon Polaritons in Noble Metals”. In: *Nat. Commun.* In press (2015) (cit. on p. 86).

Bohm, David and David Pines. “A Collective Description of Electron Interactions: III. Coulomb Interactions in a Degenerate Electron Gas”. In: *Phys. Rev.* 92 (3 Nov. 1953), pp. 609–625. DOI: 10.1103/PhysRev.92.609. URL: http://link.aps.org/doi/10.1103/PhysRev.92.609 (cit. on p. 90).

Brongersma, Mark L., Naomi J. Halas, and Peter Nordlander. “Plasmon-induced hot carrier science and technology”. In: *Nat Nano* 10.1 (Jan. 2015), pp. 25–34. URL: http://dx.doi.org/10.1038/nnano.2014.311 (cit. on p. 94).

Christopher, Phillip, Hongliang Xin, and Suljo Linic. “Visible-light-enhanced catalytic oxidation reactions on plasmonic silver nanostructures”. In: *Nat Chem* 3.6 (June 2011), pp. 467–472. URL: http://dx.doi.org/10.1038/nchem.1032 (cit. on p. 85).

Clavero, Cesar. “Plasmon-induced hot-electron generation at nanoparticle/metal-oxide interfaces for photovoltaic and photocatalytic devices”. In: *Nat Photon* 8.2 (Feb. 2014), pp. 95–103. URL: http://dx.doi.org/10.1038/nphoton.2013.238 (cit. on p. 85).

Dudarev, S. L. et al. “Electron-energy-loss spectra and the structural stability of nickel oxide: An LSDA+U study”. In: *Phys. Rev. B* 57 (3 Jan. 1998), pp. 1505–1509. DOI: 10.1103/PhysRevB.57.1505. URL: http://link.aps.org/doi/10.1103/PhysRevB.57.1505 (cit. on p. 99).

Elson, J. M. and R. H. Ritchie. “Photon Interactions at a Rough Metal Surface”. In: *Phys. Rev. B* 4 (12 Dec. 1971), pp. 4129–4138. DOI: 10.1103/PhysRevB.4.4129. URL: http://link.aps.org/doi/10.1103/PhysRevB.4.4129 (cit. on p. 90).

Etchegoin, P. G., E. C. Le Ru, and M. Meyer. “An analytic model for the optical properties of gold”. In: *The Journal of Chemical Physics* 125.16, 164705 (2006), pages. DOI: http://dx.doi.org/10.1063/1.2360270 (cit. on p. 85).

Giustino, Feliciano, Marvin L. Cohen, and Steven G. Louie. “Electron-phonon interaction using Wannier functions”. In: *Phys. Rev. B* 76 (16 Oct. 2007), p. 165108. DOI: 10.1103/PhysRevB.76.165108. URL: http://link.aps.org/doi/10.1103/PhysRevB.76.165108 (cit. on p. 100).

Khurgin, Jacob B. “How to deal with the loss in plasmonics and metamaterials”. In: *Nat Nano* 10.1 (Jan. 2015), pp. 2–6. URL: http://dx.doi.org/10.1038/nnano.2014.310 (cit. on pp. 85, 90, 94).

Khurgin, J.B. “Ultimate limit of field confinement by surface plasmon polaritons”. preprint arXiv:1410.1226. 2014 (cit. on pp. 85, 89, 90, 98).

Kioupakis, Emmanouil et al. “Free-carrier absorption in nitrides from first principles”. In: *Phys. Rev. B* 81 (24 June 2010), p. 241201. DOI: 10.1103/PhysRevB.81.241201. URL: http://link.aps.org/doi/10.1103/PhysRevB.81.241201 (cit. on pp. 86, 88, 89, 101).

Ladstädter, Florian et al. “First-principles calculation of hot-electron scattering in metals”. In: *Phys. Rev. B* 70 (23 Dec. 2004), p. 235125. DOI: 10.1103/PhysRevB.70.235125. URL: http://link.aps.org/doi/10.1103/PhysRevB.70.235125 (cit. on pp. 94, 95).

Landau, L. “On the vibration of the electronic plasma”. In: *J. Phys. USSR* 10 (1946) (cit. on p. 90).

Lide, D.R. *CRC Handbook of Chemistry and Physics, 84th Edition*. CRC HANDBOOK OF CHEMISTRY AND PHYSICS. Taylor & Francis, 2003. ISBN: 9780849304842 (cit. on p. 103).

Maier, Stefan Alexander. *Plasmonics: fundamentals and applications*. Springer Science and Business Media, 2007 (cit. on p. 85).

Marini, Andrea, Giovanni Onida, and Rodolfo Del Sole. “Plane-wave DFT-LDA calculation of the electronic structure and absorption spectrum of copper”. In: *Phys. Rev. B* 64 (19 Oct. 2001),

p. 195125. DOI: 10.1103/PhysRevB.64.195125. URL: http://link.aps.org/doi/10.1103/PhysRevB.64.195125 (cit. on pp. 92, 99).

Marzari, Nicola and David Vanderbilt. "Maximally localized generalized Wannier functions for composite energy bands". In: *Phys. Rev. B* 56 (20 Nov. 1997), pp. 12847–12865. DOI: 10.1103/PhysRevB.56.12847. URL: http://link.aps.org/doi/10.1103/PhysRevB.56.12847 (cit. on p. 99).

Moskovits, Martin. "The case for plasmon-derived hot carrier devices". In: *Nat Nano* 10.1 (Jan. 2015), pp. 6–8. URL: http://dx.doi.org/10.1038/nnano.2014.280 (cit. on pp. 85, 94).

Noffsinger, Jesse et al. "Phonon-Assisted Optical Absorption in Silicon from First Principles". In: *Phys. Rev. Lett.* 108 (16 Apr. 2012), p. 167402. DOI: 10.1103/PhysRevLett.108.167402. URL: http://link.aps.org/doi/10.1103/PhysRevLett.108.167402 (cit. on pp. 86, 88, 89, 101).

Nozieres, P. and D. Pines. *Theory Of Quantum Liquids*. Advanced Books Classics Series. Westview Press, 1999. ISBN: 9780813346533 (cit. on p. 102).

Ordal, M. A. et al. "Optical properties of the metals Al, Co, Cu, Au, Fe, Pb, Ni, Pd, Pt, Ag, Ti, and W in the infrared and far infrared". In: *Appl. Opt.* 22.7 (Apr. 1983), pp. 1099–1119. DOI: 10.1364/AO.22.001099. URL: http://ao.osa.org/abstract.cfm?URI=ao-22-7-1099 (cit. on p. 85).

Palik, E. D. *Handbook of Optical Constants of Solids*. New York: Academic, 1985 (cit. on pp. 88, 92, 106, 110).

Pendry, John. "Playing Tricks with Light". In: *Science* 285.5434 (Sept. 1999), pp. 1687–1688. URL: http://www.sciencemag.org/content/285/5434/1687.short (cit. on p. 85).

Perdew, John P. et al. "Restoring the Density-Gradient Expansion for Exchange in Solids and Surfaces". In: *Phys. Rev. Lett.* 100 (13 Apr. 2008), p. 136406. DOI: 10.1103/PhysRevLett.100.136406. URL: http://link.aps.org/doi/10.1103/PhysRevLett.100.136406 (cit. on p. 99).

Rakić, Aleksandar D. et al. "Optical properties of metallic films for vertical-cavity optoelectronic devices". In: *Appl. Opt.* 37.22 (Aug. 1998), pp. 5271–5283. DOI: 10.1364/AO.37.005271. URL: http://ao.osa.org/abstract.cfm?URI=ao-37-22-5271 (cit. on p. 85).

Rangel, T. et al. "Band structure of gold from many-body perturbation theory". In: *Phys. Rev. B* 86 (12 Sept. 2012), p. 125125. DOI: 10.1103/PhysRevB.86.125125. URL: http://link.aps.org/doi/10.1103/PhysRevB.86.125125 (cit. on p. 99).

Salpeter, E. E. and H. A. Bethe. "A Relativistic Equation for Bound-State Problems". In: *Phys. Rev.* 84 (6 Dec. 1951), pp. 1232–1242. DOI: 10.1103/PhysRev.84.1232. URL: http://link.aps.org/doi/10.1103/PhysRev.84.1232 (cit. on p. 99).

Souza, Ivo, Nicola Marzari, and David Vanderbilt. "Maximally localized Wannier functions for entangled energy bands". In: *Phys. Rev. B* 65 (3 Dec. 2001), p. 035109. DOI: 10.1103/PhysRevB.65.035109. URL: http://link.aps.org/doi/10.1103/PhysRevB.65.035109 (cit. on p. 99).

Stanley, Ross. "Plasmonics in the mid-infrared". In: *Nat Photon* 6.7 (July 2012), pp. 409–411. URL: http://dx.doi.org/10.1038/nphoton.2012.161 (cit. on p. 85).

Sundararaman, Ravishankar et al. "Theoretical Predictions for Hot-carrier Generation from Surface Plasmon Decay". In: *Nat. Commun.* 5 (5788 Apr. 2014). DOI: 10.1038/ncomms6788. URL: http://dx.doi.org/10.1038/ncomms6788 (cit. on pp. 86, 88, 90, 92, 99).

Sundararaman, R. et al. *JDFTx*. http://jdftx.sourceforge.net. 2012 (cit. on pp. 95, 99, 100).

# 7

# Summary and Outlook

*Physics is really nothing more than a search for ultimate simplicity, but so far all we have is a kind of elegant messiness.*

– Bill Bryson

In summary, this thesis has explored various aspects of light-matter interactions in both metals and semiconductors. The work on Zn-IV nitrides has been from both an experimental and theory standpoint while the optical phenomena in metals have been approached from an *ab initio* plasmonics perspective.

Prior to this work, a complete theoretical understanding of plasmon decays from a microscopic perspective was missing. Chapters 4, 5, and 6 have established the various regimes of plasmon decays and applicability of semi-classical and quantum plasmonic calculations in those regimes.

A complete theoretical investigation of real plasmonic hot carrier based energy conversion devices is, however, extremely challenging. The optical response of these devices depends on length scales ranging from a few nanometers to hundreds of nanometers or microns, and this presents challenges even for classical electromagnetic simulations. On the other hand, carrier generation requires a quantum mechanical electronic structure treatment where the relevant length scales are in Angstroms, and the current practical upper limit for such theories is a few nanometers. Figure 7.1 illustrates this disparity in length scales, and also points out the disparate time scales ranging from carrier thermalization by electron-electron scattering tens of femtoseconds after excitation, to equilibration with lattice by electron-phonon scattering picoseconds later.

Specifically the branching and relative contributions of interband, phonon-assisted intraband,

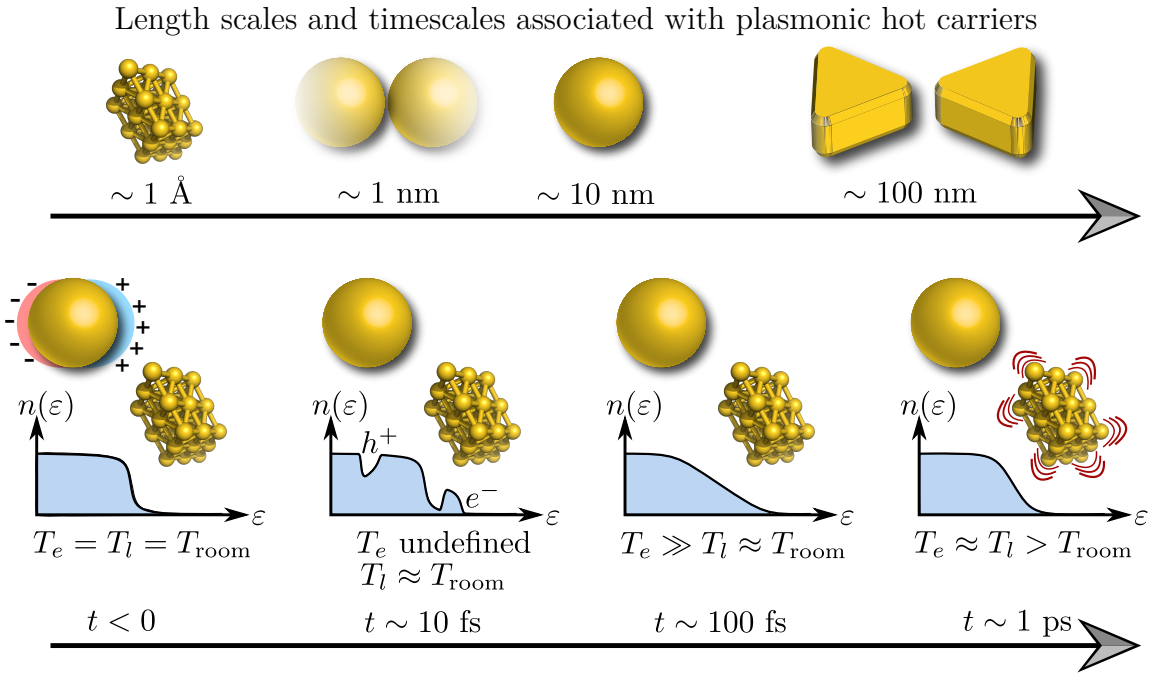


Figure 7.1: Top panel: length scales in plasmonics vary from the atomic to the mesoscale. Shown from left to right: atomic lattice, small gaps in nanoparticle dimers, nanoparticles and bowtie antennae. Lower panel: typical time scales for the the excitation of hot carriers and their subsequent relaxation. In the 10 fs regime, carrier distributions do not resemble Fermi distributions at any temperature, but at later times the dynamics can be described approximately by distinct electron and lattice temperatures, $T_e$ and $T_l$.

two-plasmon and geometry-assisted transitions have been explicitly calculated and compared with experimental results. Briefly, in the interband limit, we showed that (i) the plasmon generated 'hot' carrier profile is extremely sensitive to the details of energy band structure, especially to the position of the *d*-band in silver, copper and gold relative to unoccupied states above the Fermi level; (ii) copper and gold generate hot holes that are much more energetic than electrons; (iii) silver produces narrow energy distributions of hot holes as well as hot electrons; (iv) the hot carrier momentum distribution exhibits significant anisotropy dependent on the crystal orientation and plasmon field profile; (v) nano-confinement effects allow altering these distributions of charged carriers via geometry-induced intraband transitions. Our calculations show that direct interband transitions are the dominant avenue for plasmonic decay above the interband threshold. Below this threshold, the plasmon has roughly equal probability of decaying through phonon-assisted intraband transitions or classical drude losses (pure dephasing from a quantum mechanical perspective). Finally we have completed the picture of plasmon decays at a variety of intensity regimes and in different geometries by filling in multi-plasmon and higher order processes. Employing a Feynman diagram approach here has been critical to determine the relevant processes. Chapter 5 and 6 build on the conclusions (and drawbacks) of the calculations for internal photoemission processes at metal-semiconductor Schottky-barrier diodes presented in Chapter 4.

A complete understanding of plasmonic hot carrier generation requires accounting for material as well as geometry effects. The decay mechanisms in bulk materials, direct and phonon-assisted transitions, are strongly dependent on the electronic band structure of the metal, whereas the geometry-assisted transitions occur predominantly in the free-electron like conduction band. Theoretically, the former require detailed bulk electronic structure calculations, whereas the latter can be treated using free-electron-like jellium models but require explicit inclusion of geometry in the quantum mechanical method. Different theoretical approaches spanning different levels of detail and system size have been applied to different aspects of hot carrier generation, and we need a combination of these to understand the relative contributions of all mechanisms as a function of material, energy and geometry.

Overall, this work has provided useful quantitative insights about the energy and momentum distributions for excited 'hot' carriers with impact in a variety of fields where observation or exploitation of 'hot' carriers is important, including energy conversion devices, photodetection and spectroscopy.

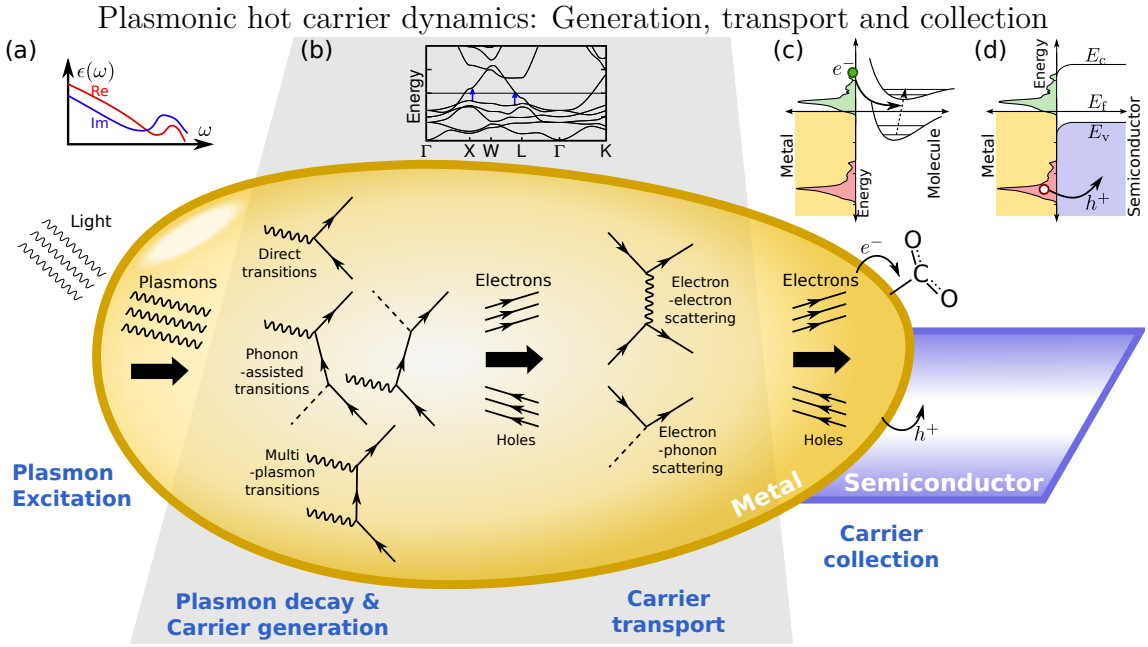


Figure 7.2: Processes involved in the excitation of plasmons, their decay to hot carriers, the transport of hot carriers in plasmonic nanostructures and their collection either in adsorbed molecules or semiconductors (lower part). The top part of the figure shows the theoretical methods with a level of detail appropriate for each stage: (a) dielectric functions for plasmon excitation (b) electronic structure theory for carrier generation and transport and (c) band / energy-level alignment analysis for collection. Feynman diagrams indicate the relevant processes at each stage: direct transitions, phonon-assisted transitions and multi-plasmon decay (in the high-intensity range only) for generation, and electron-electron and electron-phonon scattering for transport. Collection of hot carriers in solid-state systems can be used for solar energy conversion devices, sensitive photodetectors and nano-spectrometers. Hot carriers injected into molecules on a surface can induce photochemical reactions e.g. $CO_2$ reduction, which is mechanistically very different from solid state collection.

The work on II-IV nitrides has been a combination of materials physics calculations and spectroscopy aimed at the discovery of a new class of active optoelectronic materials. Based on the successful synthesis of $ZnSnN_2$, we emabrked on a project to explore a series of II-IV-$V_2$ semiconductors that may be synthesized and allow access to a rich space of the material properties for different functionalities. That culminated in the success (first) synthesis, optoelectronic and spectroscopic characterization of a series of direct band-gap semiconductors, $ZnSn_{1-x}Ge_xN_2$. The band gap in the $ZnSn_(1-x)Ge_xN_2$ is tunable from 2 eV ($ZnSnN_2$) to 3.1 eV ($ZnGeN_2$), with a linear dependence on the composition arising from the smaller lattice mismatch between $ZnSnN_2$ and $ZnGeN_2$ as compared to the lattice mismatch in the $In_xGa_(1-x)N$ alloys that span the same energy gap range, consistent with theoretical predictions. Thus, the $ZnSn_xGe_(1-x)N_2$ alloys potentially could be useful as earth-abundant light absorbers for artificial photosynthetic devices as well as a replacement for InGaN in nitride-based optoelectronic devices. Both $ZnSnN_2$ and $ZnSn_{1-x}Ge_xN_2$ semiconductor alloys are examples of theory-directed functional materials design.

## 7.1 Future Research Directions:

- Our work in plasmon decays and in understanding optical phenomena in metals sets the stage for nonequilibrium carrier transport in metal nanostructures. Definitive experiments and theory are both lacking in this direction which is of fundamental and technological importance. Beyond plasmonics, there is an opportunity here to develop a microscopic understanding of how optical excitations, in general, transfer energy in metals, on length-scales beyond 100nm and timescales ranging from the 100s of femtoseconds to beyond picosecond regime (where current theory methods stop) taking into account electron-photon, electron-electron and electron-phonon interactions. These calculations would directly intersect with ultrafast spectroscopy experiments and could be used to predict/interpret results.

- Hot carriers generated by plasmon decay are limited by the photon energy. A given energy-conversion process is usually associated with a characteristic energy, eg. semiconductor band gap in photovoltaics, such that lower-energy photons are incapable of driving the process, while the excess energy of higher-energy photons is wasted. The efficiency of solar energy conversion could be improved by harvesting the energy of these higher and lower energy photons, by producing multiple electron-hole pairs (down-conversion) or single electron-hole

pairs from multiple photons (up-conversion). Sub-band-gap injection from plasmonic metals to semiconductors can be used to achieve up-conversion, whereas careful design in geometry to optimize for a single electron-electron scattering event could in principle achieve the generation of two electron-hole pairs, analogous in effect to multiple exciton generation in semiconductors.

- As the fields of quantum plasmonics and quantum optics merge with electronic structure theory, there are many questions about the fundamental nature of plasmons to be answered, including a many-body understanding of plasmons in the dispersive regime. While there have been demonstrations of the quantum behavior of plasmons, being close to light-line has limited the insight we obtain of the quantum nature of 'lossy' plasmons.

- Plasmon driven catalysis is one of the most direct applications of our predictions. An interesting direction would be to evaluate the limitations of plasmonic photocatalysis and its potential to enhance carbon dioxide reduction for artificial photosynthesis.Photo-catalyzed carbon dioxide reduction is particularly challenging because it requires a minimum of six electrons and some of the steps have large barriers that require high overpotentials to achieve practical reaction rates. These potentials are difficult to achieve with carriers generated from single photons in the solar spectrum. Heterogeneous catalysts for carbon dioxide reduction additionally lack product selectivity. Plasmonic catalysis has the potential to address some of these issues. A promising direction could be to study the mechanisms by which hot electrons produced from surface plasmons are injected into the surface adsorbed molecules specifically on the surface of Cu and Cu alloys. Additionally, transport of hot carriers to the surface and carrier distributions after scattering is a key step towards understanding the enegetics of plasmon-driven catalysis.

- Building on the work done with II-IV nitrides, an interesting direction could be to look at new materials classes like mixed cation and anion (oxy)-nitrides that could merge the beneficial properties of oxides (stability) and nitrides (optical), like the $AMO_xN_y$ pervoskite oxynitrides that are expected to be stable under oxidative conditions. Metal oxynitrides are a promising class of emerging materials that, in optimal cases, would combine the advantages of oxides and nitrides. Previous work has shown that their stabilities in air and moisture are greater than those of the pure nitrides, but with smaller band gaps than those of comparable oxides. The wide band gap of oxides is primarily attributed to a low valence band (VB) energy derived from the $2p$ orbitals of the oxygen atoms whereas non-oxides such as nitrides have a higher

VB (thus smaller $E_g$), but are unstable under OER conditions. Oxynitrides could potentially retain the stability of oxides with an intermediate VB position that would give band gaps in the 1.8-2eV ranges.

# Appendix A

# EXAFS Analysis

## A.1 X-ray Absorption Fine Structure Spectroscopy Experimental Details

Curve fitting was performed with Artemis and IFEFFIT software using ab initio-calculated phases and amplitudes from the program FEFF 8.2. These ab initio phases and amplitudes were used in the EXAFS equation:

$$\chi(k) = S_0^2 \sum_j \frac{N_j}{kR_j^2} f_{\mathrm{eff}_j}(\pi, k, R_j) e^{-2\sigma_j^2 k^2} e^{-2\frac{R_j}{\lambda_j(k)}} \sin(2kR_j + \phi_{\mathrm{ij}}(k))$$

The neighboring atoms to the central atom(s) were divided into $j$ shells, with all atoms with the same atomic number and distance from the central atom grouped into a single shell. Within each shell, the coordination number $\mathrm{N}_j$ denoted the number of neighboring atoms in shell $j$ at a distance of $\mathrm{R}_j$ from the central atom. is the ab initio amplitude function for shell j, and the Debye-Waller term $e^{-2\sigma_j^2 k^2}$ accounted for damping due to static and thermal disorder in absorber-backscatterer distances. The mean free path term $e^{-2\frac{R_j}{\lambda_j(k)}}$ reflects losses due to inelastic scattering, where $\lambda_j(k)$ is the electron mean free path. The oscillations in the EXAFS spectrum are reflected in the sinusoidal term, $\sin(2kR_j + \phi_{\mathrm{ij}}(k))$ where $\phi_{\mathrm{ij}}(k)$ is the ab initio phase function for shell $j$. ${S_0}^2$ is an amplitude reduction factor due to shake-up/shake-off processes at the central atom(s). The EXAFS equation was used to fit the experimental data using N, R, and the EXAFS Debye-Waller factor $\sigma_j^2$ as variable

Table A.1: EXAFS fit details

| | Path | R(Å) | | N | $\sigma^2$(Å$^2$) | $R_f$(%) |
|---|---|---|---|---|---|---|
| | | EXAFS | XRD | | | |
| | Ge-N | 1.86 (0.03) | 1.84 | 4.0 | 0.004 (0.002) | 2.7 |
| $ZnGeN_2$ | Ge-Zn | 3.23 (0.08) | 3.14 | 8.0 | 0.011 (0.001) | $\Delta E_0(eV) = 2.3$ |
| | Ge-Ge | 3.20 (0.04) | 3.11–3.20 | 4.0 | 0.015 (0.005) | |
| | Ge-N | 1.88 (0.09) | | 4.0 | 0.004 (0.008) | 1.6 |
| $ZnGeSnN_2$ | Ge-Zn | 3.26 (0.14) | | 8.0 | 0.012 (0.013) | $\Delta E_0 = 4.3$ |
| (Ge:Sn=2:1) | Ge-Ge | 3.34 (0.01) | | 3.0 | 0.020 (0.001) | |
| | Ge-Sn | 3.28 (0.60) | | 1.0 | 0.016 (0.020) | |
| | Ge-N | 1.88 (0.08) | | 4.0 | 0.003 (0.007) | 1.7 |
| $ZnGeSnN_2$ | Ge-Zn | 3.28 (0.14) | | 8.0 | 0.020 (0.002) | $\Delta E_0 = 4.3$ |
| (Ge:Sn=1:1) | Ge-Ge | 3.24 (0.10) | | 2.0 | 0.020 (0.001) | |
| | Ge-Sn | 3.29 (0.44) | | 2.0 | 0.020 (0.003) | |
| | Ge-N | 1.87 (0.12) | | 4.0 | 0.002 (0.011) | 1.4 |
| $ZnGeSnN_2$ | Ge-Zn | 3.29 (0.01) | | 8.0 | 0.020 (0.012) | $\Delta E_0 = 3.7$ |
| (Ge:Sn=1:2) | Ge-Ge | 3.23 (0.01) | | 1.7 | 0.020 (0.012) | |
| | Ge-Sn | 3.33 (0.30) | | 2.3 | 0.020 (0.002) | |

parameters. For conversion of the energy (eV) to wave vector (k, Å$^{-1}$) axis, $E_0$ was defined as 11111.0 eV and the ${S_0}^2$ value was fixed at 1.0. All fits were performed in the R space.

EXAFS Analysis: Data and Fits

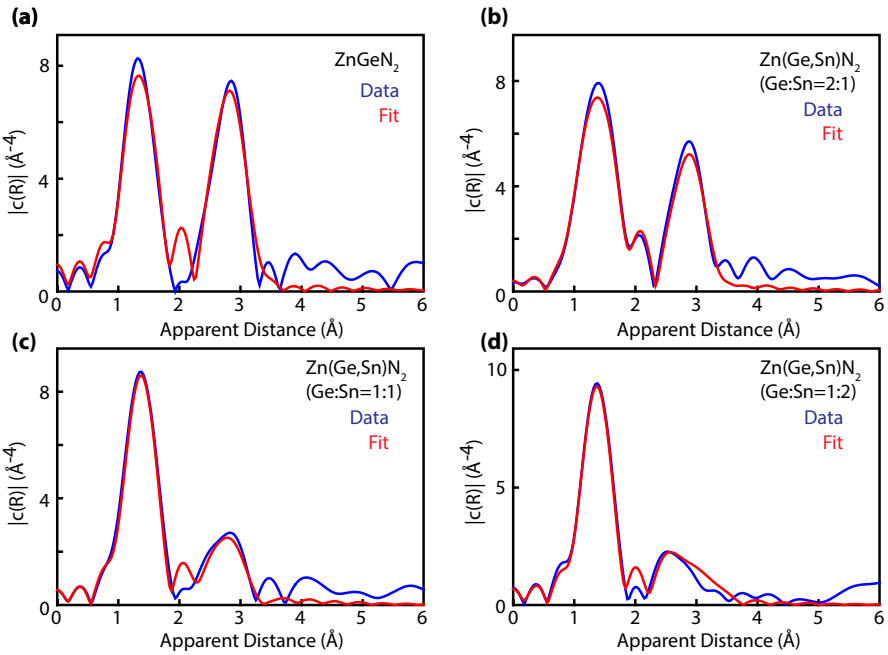


Figure A.1: (a)-(d) EXAFS curve-fitting results for $Zn(Sn,Ge)N_2$ alloys with fitting parameters summarized in Table 1

Table A.2: Basis vectors (in Angstrom) and atomic coordinates (relative to basis vectors) of the SQS used in our calculation for the $ZnSn_(1-x)Ge_xN_2$ alloys at concentration x=0.25, 0.50.

| x=0.50 | | x=0.25 | |
|---|---|---|---|
| a | -6.72 -5.81 5.47 | a | -6.72 -5.81 5.47 |
| b | 6.72 -5.81 5.47 | b | 6.72 -5.81 5.47 |
| c | 0.00 0.00 10.94 | c | 0.00 5.81 5.47 |
| Zn | 0.5000000 0.5000000 0.1875 | Zn | 1.09375000 0.09375000 0.1875000 |
| Zn | 0.1250000 0.3750000 0.1875 | Zn | -0.15625000 0.09375000 0.4375000 |
| Zn | 1.0833335 0.5833335 0.4375 | Zn | 0.88541675 0.38541675 0.6041665 |
| Zn | 0.7083335 0.4583335 0.4375 | Zn | 0.63541675 0.38541675 0.8541665 |
| Zn | 1.0000000 0 0.1875 | Zn | 0.59375000 0.59375000 0.1875000 |
| Zn | 0.6250000 0.8750000 0.1875 | Zn | 0.34375000 0.59375000 0.4375000 |
| Zn | 0.5833335 0.0833335 0.4375 | Zn | 0.38541675 0.88541675 0.6041665 |
| Zn | 0.2083335 0.9583335 0.4375 | Zn | 0.13541675 0.88541675 0.8541665 |
| Zn | 0.5000000 0.5000000 0.6875 | Zn | 0.34375000 0.34375000 0.6875000 |
| Zn | 0.1250000 0.3750000 0.6875 | Zn | 0.09375000 0.34375000 -0.0625000 |
| Zn | 1.0833335 0.5833335 0.9375 | Zn | 1.13541675 0.63541675 1.1041665 |
| Zn | 0.7083335 0.4583335 0.9375 | Zn | -0.11458325 0.63541675 0.3541665 |
| Zn | 1.0000000 0 0.6875 | Zn | 0.84375000 -0.15625000 0.6875000 |
| Zn | 0.6250000 0.8750000 0.6875 | Zn | 0.59375000 0.84375000 -0.0625000 |
| Zn | 0.5833335 0.0833335 0.9375 | Zn | 0.63541675 0.13541675 1.1041665 |
| Zn | 0.2083335 0.9583335 0.9375 | Zn | 0.38541675 1.13541675 0.3541665 |
| Sn | 0.2500000 0.7500000 0.1875 | Sn | 0.84375000 0.34375000 0.1875000 |
| Sn | 0.3333335 0.3333335 0.4375 | Sn | 0.13541675 0.13541675 0.6041665 |
| Sn | 0.8750000 0.6250000 0.1875 | Sn | 0.59375000 0.34375000 0.4375000 |
| Sn | 0.9583335 0.2083335 0.4375 | Sn | 0.88541675 0.13541675 0.8541665 |
| Sn | 0.3750000 0.1250000 0.1875 | Sn | 0.34375000 0.84375000 0.1875000 |
| Sn | 0.4583335 0.7083335 0.4375 | Sn | 0.63541675 0.63541675 0.6041665 |
| Sn | 0.2500000 0.7500000 0.6875 | Sn | 0.38541675 0.63541675 0.8541665 |
| Sn | 0.3333335 0.3333335 0.9375 | Sn | 0.09375000 0.59375000 0.6875000 |
| Ge | 0.7500000 0.2500000 0.1875 | Sn | 0.38541675 0.38541675 0.1041665 |
| Ge | 0.8333335 0.8333335 0.4375 | Sn | 0.84375000 0.59375000 0.9375000 |
| Ge | 0.8750000 0.6250000 0.6875 | Sn | 0.13541675 0.38541675 0.3541665 |
| Ge | 0.9583335 0.2083335 0.9375 | Sn | 0.59375000 0.09375000 0.6875000 |
| Ge | 0.7500000 0.2500000 0.6875 | Ge | 0.09375000 0.84375000 0.4375000 |
| Ge | 0.8333335 0.8333335 0.9375 | Ge | 0.88541675 0.88541675 0.1041665 |
| Ge | 0.3750000 0.1250000 0.6875 | Ge | 0.34375000 0.09375000 0.9375000 |
| Ge | 0.4583335 0.7083335 0.9375 | Ge | 0.63541675 0.88541675 0.354166 |

Table A.3: Atomic correlation functions for the atomic clusters $(k, m)$ with $k$ vertices and up to the $m$-th neighbor of the SQS used in our calculation, at the alloy concentration x=0.25, 0.5, and compared with the ideal values of the random alloy.

| (m,k) | (2,1) | (2,2) | (2,3) | (2,4) | (3,2) | (3,3) | (3,4) | (4,3) | (4,4) |
|---|---|---|---|---|---|---|---|---|---|
| x=0.50 | | | | | | | | | |
| Random | 0.0 | 0.0 | 0.0 | 0.0 | 0.0 | 0.0 | 0.0 | 0.0 | 0.0 |
| SQS | 0.0 | 0.0 | 0.0 | 0.0 | 0.0 | 0.0 | 0.0 | 0.0 | -1.0 |
| x=0.25 | | | | | | | | | |
| Random | 0.25 | 0.25 | 0.25 | 0.25 | - | 0.125 | 0.125 | 0.0625 | 0.0625 |
| SQS | 0.25 | 0.25 | 0.25 | 0.25 | - | 0.000 | 0.250 | 0.0000 | 0.2500 |

# Appendix B

# Plasmon decay rate derivations

## B.1 Decay rate details

Let us take an alternate and simpler route to calculating the decay rates. Let us neglect the photon momentum explicitly in the very first step. In the notation of our first paper's method section, the electric-dipole transition matrix element (neglecting the higher-order magnetic field coupling) is:

$$
\begin{aligned}
M^{k}_{qn,q'n'} &= \langle \mathbf{q}n, \overrightarrow{q}'n', \bar{k}|\hat{\mathbf{H}}_{e-\mathrm{pl}}|0\rangle \\
&= \frac{\langle 0|\hat{\mathbf{c}}^{\dagger}_{\mathbf{q}n}\hat{\mathbf{c}}_{\mathbf{q}'n'}a_k}{\sqrt{f_{\mathbf{q}n}(1-f_{\mathbf{q}'n'})n_{\mathrm{pl}}}}\left[\frac{e}{m_e}\sum_{\sigma}\int \mathrm{d}\mathbf{r}\Psi^{\dagger}_{\sigma}\hat{\mathbf{A}}\cdot\hat{\mathbf{p}}\Psi_{\sigma}\right]|0\rangle \\
&= \sqrt{f_{\mathbf{q}n}(1-f_{\mathbf{q}'n'})n_{\mathrm{pl}}}\left[\frac{\Omega}{L_zS}\sum_{\sigma}\int_{L_zS}\mathrm{d}\mathbf{r}\psi^{\sigma *}_{\mathbf{q}'n'}(\mathbf{r})\frac{e}{m_e}\mathbf{u}_{\mathbf{k}}(\mathbf{r})\cdot\left(\frac{\hbar\nabla+[\mathbf{r},\hat{\mathbf{V}}_{\mathrm{NL}}]}{i}\right)\psi^{\sigma}_{\mathbf{q}n}(\mathbf{r})\right] \\
&\approx \delta_{q'q}\sqrt{f_{\mathbf{q}n}(1-f_{\mathbf{q}n'})n_{\mathrm{pl}}\overline{\left(\frac{u_k(\mathbf{r})}{u_k(0)}\right)^2}_{L_zS}}\left[\mathbf{u}_{\mathbf{k}}(0)\cdot\sum_{\sigma}\int_{\Omega}\mathrm{d}\mathbf{r}\psi^{\sigma *}_{qn'}(\mathbf{r})\frac{e(\hbar\nabla+[\mathbf{r},\hat{\mathbf{V}}_{\mathrm{NL}}])}{im_e}\psi^{\sigma}_{\mathbf{q}n}(\mathbf{r})\right] \\
&= \delta_{q'q}\sqrt{f_{\mathbf{q}n}(1-f_{\mathbf{q}n'})n_{\mathrm{pl}}\frac{1}{2L_z|\gamma(z<0)|}}\left[\mathbf{u}_{\mathbf{k}}(0)\cdot\sum_{\sigma}\int_{\Omega}\mathrm{d}\mathbf{r}\psi^{\sigma *}_{\mathbf{q}n'}(\mathbf{r})\frac{e(\hbar\nabla+[\mathbf{r},\hat{\mathbf{V}}_{\mathrm{NL}}])}{im_e}\psi^{\sigma}_{\mathbf{q}n}(\mathbf{r})\right] \\
&= \delta_{q'q}\sqrt{f_{\mathbf{q}n}(1-f_{\mathbf{q}n'})n_{\mathrm{pl}}\frac{1}{2L_z|\gamma(z<0)|}}[\mathbf{u}_{\mathbf{k}}(0)\cdot e\langle\hat{\mathbf{v}}\rangle^{\mathbf{q}}_{n'n}] \\
\langle\hat{\mathbf{v}}\rangle^{\mathbf{q}}_{n'n} &\equiv \sum_{\sigma}\int_{\Omega}\mathrm{d}\mathbf{r}\psi^{\sigma *}_{\mathbf{q}n'}(\mathbf{r})\frac{\hbar\nabla+[\mathbf{r},\hat{\mathbf{V}}_{\mathrm{NL}}]}{im_e}\psi^{\sigma}_{\mathbf{q}n}(\mathbf{r})
\end{aligned}
$$

What we effectively showed painstakingly in the first paper is that the interband approximation for a plasmon yields a matrix element squared which is the bulk interband matrix element interacting

with the RMS plasmon vector potential. We can motivate this easily now, since that is the only form that will have the correct extensivity i.e. dependence on quantization box size in this case.

$$\begin{aligned}
\Gamma_{\text{direct}} &= \frac{2\pi}{\hbar}\sum_{\mathbf{q}n\mathbf{q}'n'}\delta(\varepsilon_{\mathbf{q}'n'}-\varepsilon_{\mathbf{q}n}-\hbar\omega)|M^{k}_{qn,q'n'}|^2 \\
&= \frac{2\pi}{\hbar}\sum_{\mathbf{q}n\mathbf{q}'n'}\delta(\varepsilon_{\mathbf{q}'n'}-\varepsilon_{\mathbf{q}n}-\hbar\omega)\delta_{q'q}\frac{f_{\mathbf{q}n}(1-f_{\mathbf{q}n'})n_{\text{pl}}}{2L_z|\gamma(z<0)|}\left|\sqrt{\frac{2\pi\hbar}{\omega SL(\omega)}}\left(\hat{\mathbf{k}}-\frac{k\hat{\mathbf{z}}}{\gamma(z<0)}\right)\cdot e\langle\hat{\mathbf{v}}\rangle^{\mathbf{q}}_{n'n}\right|^2 \\
&= \frac{2\pi^2e^2}{\omega L(\omega)|\gamma(z<0)|}\frac{1}{L_zS}\sum_{\mathbf{q}nn'}f_{\mathbf{q}n}(1-f_{\mathbf{q}n'})n_{\text{pl}}\delta(\varepsilon_{\mathbf{q}n'}-\varepsilon_{\mathbf{q}n}-\hbar\omega)\left|\left(\hat{\mathbf{k}}-\frac{k\hat{\mathbf{z}}}{\gamma(z<0)}\right)\cdot\langle\hat{\mathbf{v}}\rangle^{\mathbf{q}}_{n'n}\right|^2 \\
&= \frac{2\pi^2e^2}{\omega L(\omega)|\gamma(z<0)|\Omega}\times\frac{1}{N_{\mathbf{q}}}\sum_{\mathbf{q}nn'}f_{\mathbf{q}n}(1-f_{\mathbf{q}n'})n_{\text{pl}}\delta(\varepsilon_{\mathbf{q}n'}-\varepsilon_{\mathbf{q}n}-\hbar\omega)|\boldsymbol{\lambda}_{\mathbf{k}}\cdot\langle\hat{\mathbf{v}}\rangle^{\mathbf{q}}_{n'n}|^2
\end{aligned}$$

$$\boldsymbol{\lambda}_{\mathbf{k}} \equiv \hat{\mathbf{k}}-\frac{k\hat{\mathbf{z}}}{\gamma(z<0)}$$

This is the expression in the first paper, except for a factor of 4, and the extra nonlocal pseudopotential contribution to the matrix element. In the code, we add an extra factor of $w_\sigma = 1$ for relativistic (spinorial) and 2 for non-relativistic calculations (the variable we internally call "spinWeight"), because the above assumed that the different spin channels were accounted for explicitly, which is the case for relativistic calculations. Also, this is the more general many-body expression including the plasmon occupation number. (This therefore accounts for phenomena such as 'super-radiance' as well.)

## B.2 Phonon-assisted transitions

Next, for the phonon-assisted transition:

$$\Gamma_{\text{indirect}} = \frac{2\pi}{\hbar}\sum_{\mathbf{q}n\mathbf{q}'n'k'\alpha\pm}\delta(\varepsilon_{\mathbf{q}'n'}-\varepsilon_{\mathbf{q}n}-\hbar\omega\mp\hbar\omega_{\mathbf{k}'\alpha})|\mathcal{T}^{kk'\alpha\pm}_{qn,q'n'}|^2$$

where the second-order perturbation theory transition matrix elements are:

$$\begin{aligned}
\mathcal{T}^{kk'\alpha+}_{qn,q'n'} &= \sum_M \left[ \frac{\langle \mathbf{q}n, \overrightarrow{q}n', \bar{k}, \overline{k'\alpha}|\hat{\mathbf{H}}_{e-\mathrm{pl}}|M\rangle\langle M|\hat{\mathbf{H}}_{e-\mathrm{ph}}|0\rangle}{E_M - (\hbar\omega + \hbar\omega_{\mathbf{k}'\alpha})} + (\mathrm{pl} \leftrightarrow \mathrm{ph}) \right] \\
\mathcal{T}^{kk'\alpha-}_{qn,q'n'} &= \sum_M \left[ \frac{\langle \mathbf{q}n, \overrightarrow{q}n', \bar{k}, k'\alpha|\hat{\mathbf{H}}_{e-\mathrm{pl}}|M\rangle\langle M|\hat{\mathbf{H}}_{e-\mathrm{ph}}|0\rangle}{E_M - (\hbar\omega - \hbar\omega_{\mathbf{k}'\alpha})} + (\mathrm{pl} \leftrightarrow \mathrm{ph}) \right]
\end{aligned}$$

$$\begin{aligned}
\hat{\mathbf{H}}_{e-\mathrm{pl}} &= \frac{e}{m_e} \sum_\sigma \int \mathrm{d}\mathbf{r} \Psi^\dagger_\sigma \hat{\mathbf{A}} \cdot \hat{\mathbf{p}} \Psi_\sigma \\
&\approx \sqrt{\frac{1}{2L_z|\gamma(z<0)|} \frac{2\pi\hbar}{\omega S L(\omega)}} \sum_{\mathbf{q}n'n} \delta_{\mathbf{q}\mathbf{q}'} [\boldsymbol{\lambda}_\mathbf{k} \cdot e\langle \hat{\mathbf{v}} \rangle^{\mathbf{q}}_{n'n} a_k c^\dagger_{\mathbf{q}n'} c_{\mathbf{q}n} + h.c.] (\text{plasmon interband approx}) \\
&= \sqrt{\frac{\pi\hbar e^2}{\omega L(\omega)|\gamma(z<0)|L_z S}} \sum_{\mathbf{q}n'n} \delta_{\mathbf{q}\mathbf{q}'} [\boldsymbol{\lambda}_\mathbf{k} \cdot \langle \hat{\mathbf{v}} \rangle^{\mathbf{q}}_{n'n} a_k c^\dagger_{\mathbf{q}n'} c_{\mathbf{q}n} + h.c.]
\end{aligned}$$

$$\begin{aligned}
\hat{\mathbf{H}}_{e-\mathrm{ph}} &= \sum_{\mathbf{R}s} \hat{\mathbf{x}}_{\mathbf{R}s} \sum_\sigma \int_{N_\mathbf{R}\Omega} \mathrm{d}\mathbf{r} \Psi^\dagger_\sigma \partial_{\mathbf{R}s} V_{\mathrm{nuc}}(\mathbf{r}) \Psi_\sigma (\mathbf{R}s \,\text{label nuclear displacement modes}) \\
&= \frac{1}{\sqrt{N_{\mathbf{k}'}}} \sum_{\mathbf{k}'\alpha} \sum_{\mathbf{q}n} \sum_{\mathbf{q}'n'} \delta_{\mathbf{q}+\mathbf{k}',\mathbf{q}'} g^{\mathbf{k}'\alpha}_{n',\mathbf{q}n} (b^\dagger_{\mathbf{k}'\alpha} + b_{-\mathbf{k}'\alpha}) c^\dagger_{\mathbf{q}'n'} c_{\mathbf{q}n} (\text{in terms of phonon ladder operators})
\end{aligned}$$

$$\begin{aligned}
g^{\mathbf{k}'\alpha}_{n',\mathbf{q}n} &\equiv \int_\Omega \mathrm{d}\mathbf{r} \psi^*_{\mathbf{q}+\mathbf{k}',n'}(\mathbf{r}) \psi_{\mathbf{q}n}(\mathbf{r}) \sum_{\mathbf{R}s} f^{\mathbf{k}'}_{\alpha s} \sqrt{\frac{\hbar}{2m_s\omega_{\mathbf{k}'\alpha}}} e^{i\mathbf{k}'\cdot\mathbf{R}} \partial_{\mathbf{R}s} V_{\mathrm{nuc}}(\mathbf{r}) (\text{standard definition}) \\
&= \frac{M^{\mathbf{k}'\alpha}_{n',\mathbf{q}n}}{\sqrt{2\omega_{\mathbf{k}'\alpha}}} (\text{compared to the } M \text{ defined in the previous derivation})
\end{aligned}$$

Using the results of the final section below (done in a simpler notation without the extraneous indices), we can simplify:

$$\begin{aligned}
\mathcal{T}^{kk'\alpha+}_{qn,q'n'} &= \delta_{\mathbf{q}+\mathbf{k}',\mathbf{q}'}\sqrt{\frac{\pi\hbar e^2}{\omega L(\omega)|\gamma(z<0)|L_z S}\frac{1}{N_{\mathbf{k}'}}f_{\mathbf{q}n}(1-f_{\mathbf{q}'n'})n_{\mathrm{pl}}n_{\mathbf{k}'\alpha}} \\
&\quad \times\boldsymbol{\lambda}_{\mathbf{k}}\cdot\sum_l\left[\frac{\langle\hat{\mathbf{v}}\rangle^{\mathbf{q}'}_{n'l}g^{\mathbf{k}'\alpha}_{l,\mathbf{q}n}}{\bar{\varepsilon}_{\mathbf{q}'l}-(\varepsilon_{\mathbf{q}n}+\hbar\omega_{\mathbf{k}'\alpha})}+\frac{g^{\mathbf{k}'\alpha}_{n',\mathbf{q}l}\langle\hat{\mathbf{v}}\rangle^{\mathbf{q}}_{ln}}{\bar{\varepsilon}_{\mathbf{q}l}-(\varepsilon_{\mathbf{q}n}+\hbar\omega)}\right] \\
&= \delta_{\mathbf{q}+\mathbf{k}',\mathbf{q}'}\sqrt{\frac{\pi\hbar e^2}{\omega L(\omega)|\gamma(z<0)|N_{\mathbf{k}'}L_z S}f_{\mathbf{q}n}(1-f_{\mathbf{q}'n'})n_{\mathrm{pl}}n_{\mathbf{k}'\alpha}} \\
&\quad \times\boldsymbol{\lambda}_{\mathbf{k}}\cdot\sum_l\left[\frac{\langle\hat{\mathbf{v}}\rangle^{\mathbf{q}+\mathbf{k}'}_{n'l}g^{\mathbf{k}'\alpha}_{l,\mathbf{q}n}}{\bar{\varepsilon}_{\mathbf{q}+\mathbf{k}',l}-\varepsilon_{\mathbf{q}+\mathbf{k}',n'}+\hbar\omega}+\frac{g^{\mathbf{k}'\alpha}_{n',\mathbf{q}l}\langle\hat{\mathbf{v}}\rangle^{\mathbf{q}}_{ln}}{\bar{\varepsilon}_{\mathbf{q}l}-\varepsilon_{\mathbf{q}n}-\hbar\omega}\right] \\
&\quad \text{(using energy conservation)}
\end{aligned}$$

Similarly :

$$\begin{aligned}
\mathcal{T}^{kk'\alpha-}_{qn,q'n'} &= \delta_{\mathbf{q}+\mathbf{k}',\mathbf{q}'}\sqrt{\frac{\pi\hbar e^2}{\omega L(\omega)|\gamma(z<0)|N_{\mathbf{k}'}L_z S}f_{\mathbf{q}n}(1-f_{\mathbf{q}'n'})n_{\mathrm{pl}}(n_{\mathbf{k}'\alpha}+1)} \\
&\quad \times\boldsymbol{\lambda}_{\mathbf{k}}\cdot\sum_l\left[\frac{\langle\hat{\mathbf{v}}\rangle^{\mathbf{q}+\mathbf{k}'}_{n'l}g^{\mathbf{k}'\alpha}_{l,\mathbf{q}n}}{\bar{\varepsilon}_{\mathbf{q}+\mathbf{k}',l}-\varepsilon_{\mathbf{q}+\mathbf{k}',n'}+\hbar\omega}+\frac{g^{\mathbf{k}'\alpha}_{n',\mathbf{q}l}\langle\hat{\mathbf{v}}\rangle^{\mathbf{q}}_{ln}}{\bar{\varepsilon}_{\mathbf{q}l}-\varepsilon_{\mathbf{q}n}-\hbar\omega}\right] \\
&\quad \text{(in the way written, only change in phonon occupation!)}
\end{aligned}$$

$$\begin{aligned}
\Rightarrow \mathcal{T}^{kk'\alpha\pm}_{qn,q'n'} &= \delta_{\mathbf{q}+\mathbf{k}',\mathbf{q}'}\sqrt{\frac{\pi\hbar e^2}{\omega L(\omega)|\gamma(z<0)|N_{\mathbf{k}'}L_z S}f_{\mathbf{q}n}(1-f_{\mathbf{q}'n'})n_{\mathrm{pl}}\left(n_{\mathbf{k}'\alpha}+\frac{1}{2}\mp\frac{1}{2}\right)} \\
&\quad \times\boldsymbol{\lambda}_{\mathbf{k}}\cdot\sum_l\left[\frac{\langle\hat{\mathbf{v}}\rangle^{\mathbf{q}+\mathbf{k}'}_{n'l}g^{\mathbf{k}'\alpha}_{l,\mathbf{q}n}}{\bar{\varepsilon}_{\mathbf{q}+\mathbf{k}',l}-\varepsilon_{\mathbf{q}+\mathbf{k}',n'}+\hbar\omega}+\frac{g^{\mathbf{k}'\alpha}_{n',\mathbf{q}l}\langle\hat{\mathbf{v}}\rangle^{\mathbf{q}}_{ln}}{\bar{\varepsilon}_{\mathbf{q}l}-\varepsilon_{\mathbf{q}n}-\hbar\omega}\right]
\end{aligned}$$

Above, $\bar{\varepsilon}_{\mathbf{q}n} \equiv \varepsilon_{\mathbf{q}n} + i\,\mathrm{Im}\,\Sigma_{\mathbf{q}n}$ is the complex eigenvalue of the intermediate state.

$$
\begin{aligned}
\Rightarrow \Gamma_{\mathrm{indirect}} &= \frac{2\pi}{\hbar} \sum_{\mathbf{q}n\mathbf{q}'n'k'\alpha\pm} \delta(\varepsilon_{\mathbf{q}'n'} - \varepsilon_{\mathbf{q}n} - \hbar\omega \mp \hbar\omega_{\mathbf{k}'\alpha}) |\mathcal{T}^{kk'\alpha\pm}_{qn,q'n'}|^2 \\
&= \frac{2\pi}{\hbar} \frac{\pi\hbar e^2}{\omega L(\omega) |\gamma(z<0)| N_{\mathbf{k}'} L_z S} \sum_{\mathbf{q}nn'k'\alpha\pm} f_{\mathbf{q}n}(1 - f_{\mathbf{q}+\mathbf{k}',n'}) n_{\mathrm{pl}} \left( n_{\mathbf{k}'\alpha} + \frac{1}{2} \mp \frac{1}{2} \right) \\
&\quad \times \delta(\varepsilon_{\mathbf{q}+\mathbf{k}',n'} - \varepsilon_{\mathbf{q}n} - \hbar\omega \mp \hbar\omega_{\mathbf{k}'\alpha}) \left| \boldsymbol{\lambda}_{\mathbf{k}} \cdot \sum_l \left[ \frac{\langle \hat{\mathbf{v}} \rangle^{\mathbf{q}+\mathbf{k}'}_{n'l} g^{\mathbf{k}'\alpha}_{l,\mathbf{q}n}}{\bar{\varepsilon}_{\mathbf{q}+\mathbf{k}',l} - \varepsilon_{\mathbf{q}+\mathbf{k}',n'} + \hbar\omega} + \frac{g^{\mathbf{k}'\alpha}_{n',\mathbf{q}l} \langle \hat{\mathbf{v}} \rangle^{\mathbf{q}}_{ln}}{\bar{\varepsilon}_{\mathbf{q}l} - \varepsilon_{\mathbf{q}n} - \hbar\omega} \right] \right|^2 \\
&= \frac{2\pi^2 e^2}{\omega L(\omega) |\gamma(z<0)| \Omega} \times \frac{1}{N_{\mathbf{q}} N_{\mathbf{k}'}} \sum_{\mathbf{q}\mathbf{k}'nn'\alpha\pm} f_{\mathbf{q}n}(1 - f_{\mathbf{q}+\mathbf{k}',n'}) n_{\mathrm{pl}} \left( n_{\mathbf{k}'\alpha} + \frac{1}{2} \mp \frac{1}{2} \right) \\
&\quad \times \delta(\varepsilon_{\mathbf{q}+\mathbf{k}',n'} - \varepsilon_{\mathbf{q}n} - \hbar\omega \mp \hbar\omega_{\mathbf{k}'\alpha}) \left| \boldsymbol{\lambda}_{\mathbf{k}} \cdot \sum_l \left[ \frac{\langle \hat{\mathbf{v}} \rangle^{\mathbf{q}+\mathbf{k}'}_{n'l} g^{\mathbf{k}'\alpha}_{l,\mathbf{q}n}}{\bar{\varepsilon}_{\mathbf{q}+\mathbf{k}',l} - \varepsilon_{\mathbf{q}+\mathbf{k}',n'} + \hbar\omega} + \frac{g^{\mathbf{k}'\alpha}_{n',\mathbf{q}l} \langle \hat{\mathbf{v}} \rangle^{\mathbf{q}}_{ln}}{\bar{\varepsilon}_{\mathbf{q}l} - \varepsilon_{\mathbf{q}n} - \hbar\omega} \right] \right|^2 \\
\Gamma_{\mathrm{direct}} &= \frac{2\pi^2 e^2}{\omega L(\omega) |\gamma(z<0)| \Omega} \times \frac{1}{N_{\mathbf{q}}} \sum_{\mathbf{q}nn'} f_{\mathbf{q}n}(1 - f_{\mathbf{q}n'}) n_{\mathrm{pl}} \times \delta(\varepsilon_{\mathbf{q}n'} - \varepsilon_{\mathbf{q}n} - \hbar\omega) |\boldsymbol{\lambda}_{\mathbf{k}} \cdot \langle \hat{\mathbf{v}} \rangle^{\mathbf{q}}_{n'n}|^2
\end{aligned}
$$

Note the exact parallelism between the direct and indirect expressions now. The key difference was the redefinition of the electron-phonon coupling element $g$ to include the factor of $\sqrt{\frac{1}{2\omega_{\mathbf{k}'\alpha}}}$ arising from the phonon amplitude. (We need to make this change in the code to use this expression.) It also looks like the previous derivation had another factor of 2 error besides the $e/2m_e \to e/m_e$ fix. Finally, it was wrong to include the intermediate state occupation, which also affects multi-plasmon (which is where we originally derived it).

## B.3 Accounting for reverse transitions

Finally, if we want to look at the net transition rate from plasmon occupation number $n_{\mathrm{pl}} \to n_{\mathrm{pl}} - 1$, then we need to account for the above absorption process as well as the corresponding emission processes that go from $n_{\mathrm{pl}} - 1 \to n_{\mathrm{pl}}$. By detailed balance, the matrix element is exactly the same and only the occupation factors for the fermion change: $f_v(1 - f_c) \to (1 - f_v) f_c$. The difference between the two processes has a fermion factor of $f_v(1 - f_c) - (1 - f_v) f_c = f_v - f_c$. Thus the final

transition rates accounting for this are:

$$\Gamma_{\text{direct}} = \frac{2\pi^2 e^2}{\omega L(\omega)|\gamma(z<0)|\Omega} \times \frac{1}{N_{\mathbf{q}}} \sum_{\mathbf{q}nn'} (f_{\mathbf{q}n} - f_{\mathbf{q}n'}) n_{\text{pl}} \times \delta(\varepsilon_{\mathbf{q}n'} - \varepsilon_{\mathbf{q}n} - \hbar\omega) |\boldsymbol{\lambda}_{\mathbf{k}} \cdot \langle \hat{\mathbf{v}} \rangle_{n'n}^{\mathbf{q}}|^2$$

$$\begin{aligned}\Gamma_{\text{indirect}} = {} & \frac{2\pi^2 e^2}{\omega L(\omega)|\gamma(z<0)|\Omega} \times \frac{1}{N_{\mathbf{q}} N_{\mathbf{k}'}} \sum_{\mathbf{q}\mathbf{k}'nn'\alpha\pm} (f_{\mathbf{q}n} - f_{\mathbf{q}+\mathbf{k}',n'}) n_{\text{pl}} \left( n_{\mathbf{k}'\alpha} + \frac{1}{2} \mp \frac{1}{2} \right) \\ & \times \delta(\varepsilon_{\mathbf{q}+\mathbf{k}',n'} - \varepsilon_{\mathbf{q}n} - \hbar\omega \mp \hbar\omega_{\mathbf{k}'\alpha}) \left| \boldsymbol{\lambda}_{\mathbf{k}} \cdot \sum_{l} \left[ \frac{\langle \hat{\mathbf{v}} \rangle_{n'l}^{\mathbf{q}+\mathbf{k}'} g_{l,\mathbf{q}n}^{\mathbf{k}'\alpha}}{\bar{\varepsilon}_{\mathbf{q}+\mathbf{k}',l} - \varepsilon_{\mathbf{q}+\mathbf{k}',n'} + \hbar\omega} + \frac{g_{n',\mathbf{q}l}^{\mathbf{k}'\alpha} \langle \hat{\mathbf{v}} \rangle_{ln}^{\mathbf{q}}}{\bar{\varepsilon}_{\mathbf{q}l} - \varepsilon_{\mathbf{q}n} - \hbar\omega} \right] \right|^2\end{aligned}$$

## B.4 On-shell contributions

Let's look at the dominant on-shell contributions i.e. one where the energy denominators get close to singular. Note that there are second order poles from the diagonal terms in expanding the matrix elements, and first order poles from the off-diagonal terms. In the limit of long-lived states (the

regularization going to zero), the second order poles dominate, so let us focus on those:

$$
\begin{aligned}
\Gamma^{\text{singular}}_{\text{indirect}} &= \text{Singular}\left[\frac{2\pi^2 e^2}{\omega L(\omega)|\gamma(z<0)|\Omega}\times\frac{1}{N_{\mathbf{q}}N_{\mathbf{k}'}}\sum_{\mathbf{q}\mathbf{k}'nn'\alpha\pm}(f_{\mathbf{q}n}-f_{\mathbf{q}+\mathbf{k}',n'})n_{\text{pl}}\left(n_{\mathbf{k}'\alpha}+\frac{1}{2}\mp\frac{1}{2}\right)\right.\\
&\quad\left.\times\delta(\varepsilon_{\mathbf{q}+\mathbf{k}',n'}-\varepsilon_{\mathbf{q}n}-\hbar\omega\mp\hbar\omega_{\mathbf{k}'\alpha})\left|\boldsymbol{\lambda}_{\mathbf{k}}\cdot\sum_l\left[\frac{\langle\hat{\mathbf{v}}\rangle^{\mathbf{q}+\mathbf{k}'}_{n'l}g^{\mathbf{k}'\alpha}_{l,\mathbf{q}n}}{\bar{\varepsilon}_{\mathbf{q}+\mathbf{k}',l}-\varepsilon_{\mathbf{q}+\mathbf{k}',n'}+\hbar\omega}+\frac{g^{\mathbf{k}'\alpha}_{n',\mathbf{q}l}\langle\hat{\mathbf{v}}\rangle^{\mathbf{q}}_{ln}}{\bar{\varepsilon}_{\mathbf{q}l}-\varepsilon_{\mathbf{q}n}-\hbar\omega}\right]\right|^2\right]\\
&= \text{Sum}\left[\text{Singular}\left|\boldsymbol{\lambda}_{\mathbf{k}}\cdot\sum_l\left[\frac{\langle\hat{\mathbf{v}}\rangle^{\mathbf{q}+\mathbf{k}'}_{n'l}g^{\mathbf{k}'\alpha}_{l,\mathbf{q}n}}{\bar{\varepsilon}_{\mathbf{q}+\mathbf{k}',l}-\varepsilon_{\mathbf{q}+\mathbf{k}',n'}+\hbar\omega}+\frac{g^{\mathbf{k}'\alpha}_{n',\mathbf{q}l}\langle\hat{\mathbf{v}}\rangle^{\mathbf{q}}_{ln}}{\bar{\varepsilon}_{\mathbf{q}l}-\varepsilon_{\mathbf{q}n}-\hbar\omega}\right]\right|^2\right]\\
&\quad\text{(will put back all the prefactors and sums in } a \text{ few steps)}\\
&= \text{Sum}\left[\text{Singular}\sum_l\left[\left|\frac{\boldsymbol{\lambda}_{\mathbf{k}}\cdot\langle\hat{\mathbf{v}}\rangle^{\mathbf{q}+\mathbf{k}'}_{n'l}g^{\mathbf{k}'\alpha}_{l,\mathbf{q}n}}{\bar{\varepsilon}_{\mathbf{q}+\mathbf{k}',l}-\varepsilon_{\mathbf{q}+\mathbf{k}',n'}+\hbar\omega}\right|^2+\left|\frac{g^{\mathbf{k}'\alpha}_{n',\mathbf{q}l}\boldsymbol{\lambda}_{\mathbf{k}}\cdot\langle\hat{\mathbf{v}}\rangle^{\mathbf{q}}_{ln}}{\bar{\varepsilon}_{\mathbf{q}l}-\varepsilon_{\mathbf{q}n}-\hbar\omega}\right|^2\right]+\begin{pmatrix}\text{subdominant}\\ \text{off diagonals}\end{pmatrix}\right]\\
&\approx \text{Sum}\left[\text{Singular}\sum_l\left[\frac{|\boldsymbol{\lambda}_{\mathbf{k}}\cdot\langle\hat{\mathbf{v}}\rangle^{\mathbf{q}+\mathbf{k}'}_{n'l}|^2|g^{\mathbf{k}'\alpha}_{l,\mathbf{q}n}|^2}{(\varepsilon_{\mathbf{q}+\mathbf{k}',l}-\varepsilon_{\mathbf{q}+\mathbf{k}',n'}+\hbar\omega)^2+\text{Im}\,\Sigma^2_{\mathbf{q}+\mathbf{k}',l}}+\frac{|g^{\mathbf{k}'\alpha}_{n',\mathbf{q}l}|^2|\boldsymbol{\lambda}_{\mathbf{k}}\cdot\langle\hat{\mathbf{v}}\rangle^{\mathbf{q}}_{ln}|^2}{(\varepsilon_{\mathbf{q}l}-\varepsilon_{\mathbf{q}n}-\hbar\omega)^2+\text{Im}\,\Sigma^2_{\mathbf{q}l}}\right]\right]\\
&\quad\text{Singular}\left[\frac{1}{x^2+\eta^2},\eta\to 0\right]\\
&= \frac{\pi}{\eta}\,\text{Singular}\left[\frac{\eta/\pi}{x^2+\eta^2},\eta\to 0\right]\\
&= \frac{\pi}{\eta}\delta(x)(\text{as the argument is } a \text{ normalized Lorentzian with width}\to 0)
\end{aligned}
$$

$$
\begin{aligned}
\Gamma^{\text{singular}}_{\text{indirect}} &= \text{Sum}\left[\sum_l\left[\begin{array}{c}\frac{\pi}{\text{Im}\,\Sigma_{\mathbf{q}+\mathbf{k}',l}}|\boldsymbol{\lambda}_{\mathbf{k}}\cdot\langle\hat{\mathbf{v}}\rangle^{\mathbf{q}+\mathbf{k}'}_{n'l}|^2|g^{\mathbf{k}'\alpha}_{l,\mathbf{q}n}|^2\delta(\varepsilon_{\mathbf{q}+\mathbf{k}',l}-\varepsilon_{\mathbf{q}+\mathbf{k}',n'}+\hbar\omega)\\ +\frac{\pi}{\text{Im}\,\Sigma_{\mathbf{q}l}}|g^{\mathbf{k}'\alpha}_{n',\mathbf{q}l}|^2|\boldsymbol{\lambda}_{\mathbf{k}}\cdot\langle\hat{\mathbf{v}}\rangle^{\mathbf{q}}_{ln}|^2\delta(\varepsilon_{\mathbf{q}l}-\varepsilon_{\mathbf{q}n}-\hbar\omega)\end{array}\right]\right]\\
&= \frac{2\pi^2e^2}{\omega L(\omega)|\gamma(z<0)|\Omega}\times\frac{1}{N_{\mathbf{q}}N_{\mathbf{k}'}}\sum_{\mathbf{q}\mathbf{k}'nn'\alpha\pm}(f_{\mathbf{q}n}-f_{\mathbf{q}+\mathbf{k}',n'})n_{\text{pl}}\left(n_{\mathbf{k}'\alpha}+\frac{1}{2}\mp\frac{1}{2}\right)\\
&\quad\times\sum_l\left[\begin{array}{c}\frac{\pi}{\text{Im}\,\Sigma_{\mathbf{q}+\mathbf{k}',l}}|\boldsymbol{\lambda}_{\mathbf{k}}\cdot\langle\hat{\mathbf{v}}\rangle^{\mathbf{q}+\mathbf{k}'}_{n'l}|^2|g^{\mathbf{k}'\alpha}_{l,\mathbf{q}n}|^2\begin{pmatrix}\delta(\varepsilon_{\mathbf{q}+\mathbf{k}',l}-\varepsilon_{\mathbf{q}+\mathbf{k}',n'}+\hbar\omega)\times\\ \delta(\varepsilon_{\mathbf{q}+\mathbf{k}',n'}-\varepsilon_{\mathbf{q}n}-\hbar\omega\mp\hbar\omega_{\mathbf{k}'\alpha})\end{pmatrix}\\ +\frac{\pi}{\text{Im}\,\Sigma_{\mathbf{q}l}}|g^{\mathbf{k}'\alpha}_{n',\mathbf{q}l}|^2|\boldsymbol{\lambda}_{\mathbf{k}}\cdot\langle\hat{\mathbf{v}}\rangle^{\mathbf{q}}_{ln}|^2\begin{pmatrix}\delta(\varepsilon_{\mathbf{q}l}-\varepsilon_{\mathbf{q}n}-\hbar\omega)\times\\ \delta(\varepsilon_{\mathbf{q}+\mathbf{k}',n'}-\varepsilon_{\mathbf{q}n}-\hbar\omega\mp\hbar\omega_{\mathbf{k}'\alpha})\end{pmatrix}\end{array}\right]\\
&= \Gamma_1+\Gamma_2
\end{aligned}
$$

$$
\begin{aligned}
\Gamma_1 \equiv\ & \tfrac{2\pi^2e^2}{\omega L(\omega)|\gamma(z<0)|\Omega} \times \tfrac{1}{N_{\mathbf{q}}N_{\mathbf{k}'}} \textstyle\sum_{\mathbf{q}\mathbf{k}'nn'l\alpha\pm}(f_{\mathbf{q}n} - f_{\mathbf{q}+\mathbf{k}',n'})n_{\mathrm{pl}}\left(n_{\mathbf{k}'\alpha} + \tfrac{1}{2} \mp \tfrac{1}{2}\right) \\
& \times \tfrac{\pi}{\operatorname{Im}\Sigma_{\mathbf{q}+\mathbf{k}',l}} |\boldsymbol{\lambda}_{\mathbf{k}} \cdot \langle\hat{\mathbf{v}}\rangle_{n'l}^{\mathbf{q}+\mathbf{k}'}|^2 |g_{l,\mathbf{q}n}^{\mathbf{k}'\alpha}|^2 \delta(\varepsilon_{\mathbf{q}+\mathbf{k}',l} - \varepsilon_{\mathbf{q}+\mathbf{k}',n'} + \hbar\omega)\delta(\varepsilon_{\mathbf{q}+\mathbf{k}',n'} - \varepsilon_{\mathbf{q}n} - \hbar\omega \mp \hbar\omega_{\mathbf{k}'\alpha}) \\
=\ & \tfrac{2\pi^2e^2}{\omega L(\omega)|\gamma(z<0)|\Omega} \times \tfrac{1}{N_{\mathbf{q}}N_{\mathbf{k}'}} \textstyle\sum_{\mathbf{q}\mathbf{k}'nn'l\alpha\pm}(f_{\mathbf{q}n} - f_{\mathbf{q}+\mathbf{k}',n'})n_{\mathrm{pl}}\left(n_{\mathbf{k}'\alpha} + \tfrac{1}{2} \mp \tfrac{1}{2}\right) \\
& \times \tfrac{\pi}{\operatorname{Im}\Sigma_{\mathbf{q}+\mathbf{k}',l}} |\boldsymbol{\lambda}_{\mathbf{k}} \cdot \langle\hat{\mathbf{v}}\rangle_{n'l}^{\mathbf{q}+\mathbf{k}'}|^2 |g_{l,\mathbf{q}n}^{\mathbf{k}'\alpha}|^2 \delta(\varepsilon_{\mathbf{q}+\mathbf{k}',l} - \varepsilon_{\mathbf{q}+\mathbf{k}',n'} + \hbar\omega)\delta(\varepsilon_{\mathbf{q}+\mathbf{k}',l} - \varepsilon_{\mathbf{q}n} \mp \hbar\omega_{\mathbf{k}'\alpha}) \\
& \qquad \text{(Using identity } \delta(x)\delta(y) = \delta(x)\delta(x+y)\text{)} \\
\approx\ & \tfrac{2\pi^2e^2}{\omega L(\omega)|\gamma(z<0)|\Omega} \times \tfrac{1}{N_{\mathbf{q}}N_{\mathbf{k}'}} \textstyle\sum_{\mathbf{q}\mathbf{k}'nn'l\alpha\pm}(f_{\mathbf{q}+\mathbf{k}',l} - f_{\mathbf{q}+\mathbf{k}',n'})n_{\mathrm{pl}}\left(n_{\mathbf{k}'\alpha} + \tfrac{1}{2} \mp \tfrac{1}{2}\right) \\
& \times \tfrac{\pi}{\operatorname{Im}\Sigma_{\mathbf{q}+\mathbf{k}',l}} |\boldsymbol{\lambda}_{\mathbf{k}} \cdot \langle\hat{\mathbf{v}}\rangle_{n'l}^{\mathbf{q}+\mathbf{k}'}|^2 |g_{l,\mathbf{q}n}^{\mathbf{k}'\alpha}|^2 \delta(\varepsilon_{\mathbf{q}+\mathbf{k}',l} - \varepsilon_{\mathbf{q}+\mathbf{k}',n'} + \hbar\omega)\delta(\varepsilon_{\mathbf{q}+\mathbf{k}',l} - \varepsilon_{\mathbf{q}n} \mp \hbar\omega_{\mathbf{k}'\alpha}) \\
& \text{(Since } |\varepsilon_{\mathbf{q}n} - \varepsilon_F| \gg \hbar\omega_{\mathbf{k}'\alpha} \text{ for most of the contribution when } \omega \gg \omega_D\text{)} \\
=\ & \tfrac{2\pi^2e^2}{\omega L(\omega)|\gamma(z<0)|\Omega} \times \tfrac{1}{N_{\mathbf{q}}N_{\mathbf{k}'}} \textstyle\sum_{\mathbf{q}\mathbf{k}'nn'l\alpha\pm}(f_{\mathbf{q}n} - f_{\mathbf{q}n'})n_{\mathrm{pl}}\left(n_{\mathbf{k}'\alpha} + \tfrac{1}{2} \mp \tfrac{1}{2}\right) \\
& \times \tfrac{\pi}{\operatorname{Im}\Sigma_{\mathbf{q}n}} |\boldsymbol{\lambda}_{\mathbf{k}} \cdot \langle\hat{\mathbf{v}}\rangle_{n'n}^{\mathbf{q}}|^2 |g_{n,\mathbf{k}'+\mathbf{q},l}^{-\mathbf{k}'\alpha}|^2 \delta(\varepsilon_{\mathbf{q}n} - \varepsilon_{\mathbf{q}n'} + \hbar\omega)\delta(\varepsilon_{\mathbf{q}n} - \varepsilon_{\mathbf{q}+\mathbf{k},l} \mp \hbar\omega_{\mathbf{k}'\alpha}) \\
& \qquad \text{(Swapping dummy indices} (\mathbf{q}, \mathbf{k}', \mathbf{q}+\mathbf{k}') \to (\mathbf{q}+\mathbf{k}', -\mathbf{k}', \mathbf{q}) \text{ and } n \leftrightarrow l\text{)} \\
=\ & \tfrac{2\pi^2e^2}{\omega L(\omega)|\gamma(z<0)|\Omega} \times \tfrac{1}{N_{\mathbf{q}}} \textstyle\sum_{\mathbf{q}nn'}(f_{\mathbf{q}n} - f_{\mathbf{q}n'})n_{\mathrm{pl}}\delta(\varepsilon_{\mathbf{q}n} - \varepsilon_{\mathbf{q}n'} + \hbar\omega)|\boldsymbol{\lambda}_{\mathbf{k}} \cdot \langle\hat{\mathbf{v}}\rangle_{n'n}^{\mathbf{q}}|^2 \\
& \times \tfrac{1}{\operatorname{Im}\Sigma_{\mathbf{q}n}} \left[\pi \tfrac{1}{N_{\mathbf{k}'}} \textstyle\sum_{\mathbf{k}'l\alpha\pm} \left(n_{\mathbf{k}'\alpha} + \tfrac{1}{2} \mp \tfrac{1}{2}\right) \delta(\varepsilon_{\mathbf{q}n} - \varepsilon_{\mathbf{q}+\mathbf{k}',l} \mp \hbar\omega_{\mathbf{k}'\alpha}) |g_{l,\mathbf{q}n}^{-\mathbf{k}'\alpha}|^2\right] \\
& \qquad \text{(Since } g_{n,\mathbf{q}+\mathbf{k}',l}^{-\mathbf{k}'\alpha} = (g_{l,\mathbf{q}n}^{\mathbf{k}'\alpha})^* \text{ by hermiticity of } \hat{\mathbf{H}}_{e-\mathrm{ph}}\text{)} \\
=\ & \tfrac{2\pi^2e^2}{\omega L(\omega)|\gamma(z<0)|\Omega} \times \tfrac{1}{N_{\mathbf{q}}} \textstyle\sum_{\mathbf{q}nn'}(f_{\mathbf{q}n} - f_{\mathbf{q}n'})n_{\mathrm{pl}}\delta(\varepsilon_{\mathbf{q}n} - \varepsilon_{\mathbf{q}n'} + \hbar\omega)|\boldsymbol{\lambda}_{\mathbf{k}} \cdot \langle\hat{\mathbf{v}}\rangle_{n'n}^{\mathbf{q}}|^2 \tfrac{\operatorname{Im}\Sigma_{\mathbf{q}n}^{\mathrm{ePh}}}{\operatorname{Im}\Sigma_{\mathbf{q}n}} \\
\Gamma_2 \equiv\ & \tfrac{2\pi^2e^2}{\omega L(\omega)|\gamma(z<0)|\Omega} \times \tfrac{1}{N_{\mathbf{q}}N_{\mathbf{k}'}} \textstyle\sum_{\mathbf{q}\mathbf{k}'nn'l\alpha\pm}(f_{\mathbf{q}n} - f_{\mathbf{q}+\mathbf{k}',n'})n_{\mathrm{pl}}\left(n_{\mathbf{k}'\alpha} + \tfrac{1}{2} \mp \tfrac{1}{2}\right) \\
& \times \tfrac{\pi}{\operatorname{Im}\Sigma_{\mathbf{q}l}} |\boldsymbol{\lambda}_{\mathbf{k}} \cdot \langle\hat{\mathbf{v}}\rangle_{ln}^{\mathbf{q}}|^2 |g_{n',\mathbf{q}l}^{\mathbf{k}'\alpha}|^2 \delta(\varepsilon_{\mathbf{q}l} - \varepsilon_{\mathbf{q}n} - \hbar\omega)\delta(\varepsilon_{\mathbf{q}+\mathbf{k}',n'} - \varepsilon_{\mathbf{q}n} - \hbar\omega \mp \hbar\omega_{\mathbf{k}'\alpha}) \\
=\ & \tfrac{2\pi^2e^2}{\omega L(\omega)|\gamma(z<0)|\Omega} \times \tfrac{1}{N_{\mathbf{q}}N_{\mathbf{k}'}} \textstyle\sum_{\mathbf{q}\mathbf{k}'nn'l\alpha\pm}(f_{\mathbf{q}n} - f_{\mathbf{q}+\mathbf{k}',n'})n_{\mathrm{pl}}\left(n_{\mathbf{k}'\alpha} + \tfrac{1}{2} \mp \tfrac{1}{2}\right) \\
& \times \tfrac{\pi}{\operatorname{Im}\Sigma_{\mathbf{q}l}} |\boldsymbol{\lambda}_{\mathbf{k}} \cdot \langle\hat{\mathbf{v}}\rangle_{ln}^{\mathbf{q}}|^2 |g_{n',\mathbf{q}l}^{\mathbf{k}'\alpha}|^2 \delta(\varepsilon_{\mathbf{q}l} - \varepsilon_{\mathbf{q}n} - \hbar\omega)\delta(\varepsilon_{\mathbf{q}+\mathbf{k}',n'} - \varepsilon_{\mathbf{q}l} \mp \hbar\omega_{\mathbf{k}'\alpha}) \\
& \qquad \text{(Using identity } \delta(x)\delta(y) = \delta(x)\delta(y-x)\text{)} \\
\approx\ & \tfrac{2\pi^2e^2}{\omega L(\omega)|\gamma(z<0)|\Omega} \times \tfrac{1}{N_{\mathbf{q}}N_{\mathbf{k}'}} \textstyle\sum_{\mathbf{q}\mathbf{k}'nn'l\alpha\pm}(f_{\mathbf{q}n} - f_{\mathbf{q}l})n_{\mathrm{pl}}\left(n_{\mathbf{k}'\alpha} + \tfrac{1}{2} \mp \tfrac{1}{2}\right) \\
& \times \tfrac{\pi}{\operatorname{Im}\Sigma_{\mathbf{q}l}} |\boldsymbol{\lambda}_{\mathbf{k}} \cdot \langle\hat{\mathbf{v}}\rangle_{ln}^{\mathbf{q}}|^2 |g_{n',\mathbf{q}l}^{\mathbf{k}'\alpha}|^2 \delta(\varepsilon_{\mathbf{q}l} - \varepsilon_{\mathbf{q}n} - \hbar\omega)\delta(\varepsilon_{\mathbf{q}+\mathbf{k}',n'} - \varepsilon_{\mathbf{q}l} \mp \hbar\omega_{\mathbf{k}'\alpha}) \\
& \left(\text{Since } \left|\varepsilon_{\mathbf{q}+\mathbf{k}',n'} - \varepsilon_F\right| \gg \hbar\omega_{\mathbf{k}'\alpha} \text{ for most of the contribution when } \omega \gg \omega_D\right) \\
=\ & \tfrac{2\pi^2e^2}{\omega L(\omega)|\gamma(z<0)|\Omega} \times \tfrac{1}{N_{\mathbf{q}}N_{\mathbf{k}'}} \textstyle\sum_{\mathbf{q}\mathbf{k}'nn'l\alpha\pm}(f_{\mathbf{q}n} - f_{\mathbf{q}n'})n_{\mathrm{pl}}\left(n_{\mathbf{k}'\alpha} + \tfrac{1}{2} \mp \tfrac{1}{2}\right) \\
& \times \tfrac{\pi}{\operatorname{Im}\Sigma_{\mathbf{q}n'}} |\boldsymbol{\lambda}_{\mathbf{k}} \cdot \langle\hat{\mathbf{v}}\rangle_{n'n}^{\mathbf{q}}|^2 |g_{l,\mathbf{q}n'}^{\mathbf{k}'\alpha}|^2 \delta(\varepsilon_{\mathbf{q}n'} - \varepsilon_{\mathbf{q}n} - \hbar\omega)\delta(\varepsilon_{\mathbf{q}+\mathbf{k}',l} - \varepsilon_{\mathbf{q}n'} \mp \hbar\omega_{\mathbf{k}'\alpha}) \\
& \qquad \text{(Swapping dummy indices } n' \leftrightarrow l\text{)} \\
=\ & \tfrac{2\pi^2e^2}{\omega L(\omega)|\gamma(z<0)|\Omega} \times \tfrac{1}{N_{\mathbf{q}}} \textstyle\sum_{\mathbf{q}nn'}(f_{\mathbf{q}n} - f_{\mathbf{q}n'})n_{\mathrm{pl}}\delta(\varepsilon_{\mathbf{q}n'} - \varepsilon_{\mathbf{q}n} - \hbar\omega)|\boldsymbol{\lambda}_{\mathbf{k}} \cdot \langle\hat{\mathbf{v}}\rangle_{n'n}^{\mathbf{q}}|^2 \\
& \times \tfrac{1}{\operatorname{Im}\Sigma_{\mathbf{q}n'}} \left[\pi \tfrac{1}{N_{\mathbf{k}'}} \textstyle\sum_{\mathbf{k}'l\alpha\pm} \left(n_{\mathbf{k}'\alpha} + \tfrac{1}{2} \mp \tfrac{1}{2}\right) \delta(\varepsilon_{\mathbf{q}+\mathbf{k}',l} - \varepsilon_{\mathbf{q}n'} \mp \hbar\omega_{\mathbf{k}'\alpha}) |g_{l,\mathbf{q}n'}^{\mathbf{k}'\alpha}|^2\right] \\
=\ & \tfrac{2\pi^2e^2}{\omega L(\omega)|\gamma(z<0)|\Omega} \times \tfrac{1}{N_{\mathbf{q}}} \textstyle\sum_{\mathbf{q}nn'}(f_{\mathbf{q}n} - f_{\mathbf{q}n'})n_{\mathrm{pl}}\delta(\varepsilon_{\mathbf{q}n'} - \varepsilon_{\mathbf{q}n} - \hbar\omega)|\boldsymbol{\lambda}_{\mathbf{k}} \cdot \langle\hat{\mathbf{v}}\rangle_{n'n}^{\mathbf{q}}|^2 \tfrac{\operatorname{Im}\Sigma_{\mathbf{q}n'}^{e-\mathrm{ph}}}{\operatorname{Im}\Sigma_{\mathbf{q}n'}} \\
\Gamma_{\text{indirect}}^{\text{singular}} =\ & \tfrac{2\pi^2e^2}{\omega L(\omega)|\gamma(z<0)|\Omega} \times \tfrac{1}{N_{\mathbf{q}}} \textstyle\sum_{\mathbf{q}nn'}(f_{\mathbf{q}n} - f_{\mathbf{q}n'})n_{\mathrm{pl}}\delta(\varepsilon_{\mathbf{q}n'} - \varepsilon_{\mathbf{q}n} - \hbar\omega)|\boldsymbol{\lambda}_{\mathbf{k}} \cdot \langle\hat{\mathbf{v}}\rangle_{n'n}^{\mathbf{q}}|^2 \left(\tfrac{\operatorname{Im}\Sigma_{\mathbf{q}n}^{\mathrm{ePh}}}{\operatorname{Im}\Sigma_{\mathbf{q}n}} + \tfrac{\operatorname{Im}\Sigma_{\mathbf{q}n'}^{\mathrm{ePh}}}{\operatorname{Im}\Sigma_{\mathbf{q}n'}}\right)
\end{aligned}
$$

Therefore, if we had used only the $e$-phonon carrier linewidths in calculating $\Gamma_{\text{indirect}}$, we would have ended up with $\Gamma_{\text{indirect}}^{\text{singular}} = 2\Gamma_{\text{direct}}$. That is why we always see $\Gamma_{\text{indirect}} > 2\Gamma_{\text{direct}}$ for lower energies where $\Sigma_{\mathbf{q}n} \approx \Sigma_{\mathbf{q}n}^{\text{ePh}}$ for all accessible states.

## B.5 Intermediate state occupations in higher-order perturbations

Scratch: figure out how intermediate state occupations work. For simplicity just work with a lumped electron state index (not labeling $k$-points expliictly), and let the interaction hamiltonian be $H_1 = \sum_{i \neq j} \alpha_{1ij}(a_1 c_i^\dagger c_j + a_1^\dagger c_j^\dagger c_i)$ and similarly $H_2$.

$$\mathcal{T} = \underbrace{\sum_M \frac{\langle F|\hat{\mathbf{H}}_1|M\rangle\langle M|\hat{\mathbf{H}}_2|I\rangle}{E_M - E_I}}_{\mathcal{T}_{12}} + (1 \leftrightarrow 2)$$

where $I$, $M$ and $F$ are the many-body initial, intermediate and final states. Let $I = |0\rangle$ be the normalized initial state with some distribution of the electrons and both types of bosons (could be the Fermi sea + boson vacuum as a special case, but the following is more general), and set it as the reference energy, $E_I = 0$. Let $F = \frac{c_c^\dagger c_v a_1 a_2 |0\rangle}{\sqrt{(1-f_c)f_v n_1 n_2}}$ be the normalized final state with an electron-hole pair and two bosons less compared to the initial state, with relative energy $E_F = \varepsilon_c - \varepsilon_v - \omega_1 - \omega_2$.

The intermediate state should be summed over all possible many-body states. The $H_2$ expectation value will be non-zero only if $M$ differs from $I$ by a single electron-hole pair and a single boson of type 2. Likewise the $H_1$ expectation value will be non-zero only if $M$ differs from $F$ by a single electron-hole pair and a single boson of type 1. Therefore $M = \frac{c_l^\dagger c_m a_2 |0\rangle}{\sqrt{(1-f_l)f_m n_2}}$, indexed by two electron indices $l, m$ with $l \neq m$, and $E_M = \varepsilon_l - \varepsilon_m - \omega_2$.

$$\begin{aligned}
\mathcal{T}_{12} &\equiv \textstyle\sum_M \frac{\langle F|\hat{\mathbf{H}}_1|M\rangle\langle M|\hat{\mathbf{H}}_2|I\rangle}{E_M-E_I} \\
&= \textstyle\sum_{l\neq m,w\neq x,y\neq z} \frac{\alpha_{1wx}\alpha_{2yz}\langle 0|a_2^\dagger a_1^\dagger c_v^\dagger c_c a_1 c_w^\dagger c_x c_l^\dagger c_m a_2|0\rangle\langle 0|a_2^\dagger c_m^\dagger c_l a_2 c_y^\dagger c_z^\dagger|0\rangle}{(\varepsilon_l-\varepsilon_m-\omega_2)(1-f_l)f_m n_2\sqrt{(1-f_c)f_v n_1 n_2}} \\
&= \textstyle\sum_{l\neq m,w\neq x,y\neq z} \frac{\alpha_{1wx}\alpha_{2yz}n_2 n_1 n_2\langle 0|c_v^\dagger c_c c_w^\dagger c_x c_l^\dagger c_m|0\rangle\langle 0|c_m^\dagger c_l c_y^\dagger c_z|0\rangle}{(\varepsilon_l-\varepsilon_m-\omega_2)(1-f_l)f_m n_2\sqrt{(1-f_c)f_v n_1 n_2}} \\
&= \textstyle\sqrt{\frac{n_1 n_2}{(1-f_c)f_v}}\sum_{l\neq m,w\neq x,y\neq z}\alpha_{1wx}\alpha_{2yz}\frac{\langle 0|c_v^\dagger c_c c_w^\dagger c_x c_l^\dagger c_m|0\rangle\langle 0|c_m^\dagger c_l c_y^\dagger c_z|0\rangle}{(\varepsilon_l-\varepsilon_m-\omega_2)(1-f_l)f_m} \\
&\qquad\qquad\qquad\qquad\qquad\qquad\qquad\qquad\text{(Simplifying the bosonic sector first)} \\
&\quad\ \langle 0|c_m^\dagger c_l c_y^\dagger c_z|0\rangle \\
&= \langle 0|c_m^\dagger(\delta_{ly}-c_y^\dagger c_l)c_z|0\rangle \\
&= \langle 0|(c_m^\dagger c_z\delta_{ly}-c_m^\dagger c_y^\dagger c_l c_z)|0\rangle \\
&= \delta_{ly}\delta_{mz}f_m - f_m f_y(\delta_{mz}\delta_{ly}-\delta_{ml}\delta_{yz}) \\
&= \delta_{ly}\delta_{mz}f_m - f_m f_y\delta_{mz}\delta_{ly} \qquad\qquad\qquad\qquad (y\neq z, l\neq m) \\
&= f_m(1-f_l)\delta_{mz}\delta_{ly} \\
\mathcal{T}_{12} &= \textstyle\sqrt{\frac{n_1 n_2}{(1-f_c)f_v}}\sum_{l\neq m,w\neq x,y\neq z}\alpha_{1wx}\alpha_{2yz}\frac{\langle 0|c_v^\dagger c_c c_w^\dagger c_x c_l^\dagger c_m|0\rangle f_m(1-f_l)\delta_{mz}\delta_{ly}}{(\varepsilon_l-\varepsilon_m-\omega_2)(1-f_l)f_m} \\
&= \textstyle\sqrt{\frac{n_1 n_2}{(1-f_c)f_v}}\sum_{l\neq m,w\neq x}\alpha_{1wx}\alpha_{2lm}\frac{\langle 0|c_v^\dagger c_c c_w^\dagger c_x c_l^\dagger c_m|0\rangle}{\varepsilon_l-\varepsilon_m-\omega_2}
\end{aligned}$$

$$\begin{aligned}
&\quad\ \langle 0|c_v^\dagger c_c c_w^\dagger c_x c_l^\dagger c_m|0\rangle \\
&= \langle 0\,\Big|(\delta_{cw}c_v^\dagger c_x c_l^\dagger c_m - c_v^\dagger c_w^\dagger c_c c_x c_l^\dagger c_m)|0\rangle \\
&= \langle 0|(\delta_{cw}\delta_{lx}c_v^\dagger c_m - \delta_{cw}c_v^\dagger c_l^\dagger c_x c_m - \delta_{lx}c_v^\dagger c_w^\dagger c_c c_m + c_v^\dagger c_w^\dagger c_c c_l^\dagger c_x c_m)|0\rangle \\
&= \langle 0|(\delta_{cw}\delta_{lx}c_v^\dagger c_m - \delta_{cw}c_v^\dagger c_l^\dagger c_x c_m - \delta_{lx}c_v^\dagger c_w^\dagger c_c c_m + \delta_{lc}c_v^\dagger c_w^\dagger c_x c_m - c_v^\dagger c_w^\dagger c_l^\dagger c_c c_x c_m)|0\rangle \\
&= \delta_{cw}\delta_{lx}(\delta_{mv}f_v) - \delta_{cw}(\delta_{vm}\delta_{lx}f_v f_l) - \delta_{lx}(\delta_{vm}\delta_{wc}f_v f_c) + \delta_{lc}(-\delta_{vx}\delta_{wm}f_v f_m) \\
&\qquad\quad -(-\delta_{vx}\delta_{wm}\delta_{lc}f_v f_m f_c - \delta_{vm}\delta_{wc}\delta_{lx}f_v f_c f_l) \qquad \text{(using } l\neq m, w\neq x, y\neq z) \\
&= \delta_{vx}\delta_{wm}\delta_{lc}(-f_v f_m + f_v f_m f_c) + \delta_{vm}\delta_{wc}\delta_{lx}(f_v - f_v f_l - f_v f_c + f_v f_c f_l) \\
&= -\delta_{vx}\delta_{wm}\delta_{lc}f_v(1-f_c)f_m + \delta_{vm}\delta_{wc}\delta_{lx}f_v(1-f_l)(1-f_c) \\
&= f_v(1-f_c)[\delta_{vm}\delta_{wc}\delta_{lx}(1-f_l) - \delta_{vx}\delta_{wm}\delta_{lc}f_m]
\end{aligned}$$

$$
\begin{aligned}
\mathcal{T}_{12} &= \sqrt{\tfrac{n_1 n_2}{(1-f_c)f_v}} \sum_{l\neq m, w\neq x} \alpha_{1wx}\alpha_{2lm} \tfrac{f_v(1-f_c)[\delta_{vm}\delta_{wc}\delta_{lx}(1-f_l)-\delta_{vx}\delta_{wm}\delta_{lc}f_m]}{\varepsilon_l-\varepsilon_m-\omega_2} \\
&= \sqrt{n_1 n_2 f_v(1-f_c)} \sum_{l\neq m, w\neq x} \alpha_{1wx}\alpha_{2lm} \tfrac{[\delta_{vm}\delta_{wc}\delta_{lx}(1-f_l)-\delta_{vx}\delta_{wm}\delta_{lc}f_m]}{\varepsilon_l-\varepsilon_m-\omega_2} \\
&= \sqrt{n_1 n_2 f_v(1-f_c)} \left( \sum_{l\neq v,c} \alpha_{1cl}\alpha_{2lv} \tfrac{(1-f_l)}{\varepsilon_l-\varepsilon_v-\omega_2} - \sum_{m\neq v,c} \alpha_{1mv}\alpha_{2cm} \tfrac{f_m}{\varepsilon_c-\varepsilon_m-\omega_2} \right) \\
&= \sqrt{n_1 n_2 f_v(1-f_c)} \left( \sum_{l\neq v,c} (1-f_l) \tfrac{\alpha_{1cl}\alpha_{2lv}}{\varepsilon_l-\varepsilon_v-\omega_2} + \sum_{l\neq v,c} f_l \tfrac{\alpha_{2cl}\alpha_{1lv}}{\varepsilon_l-\varepsilon_c+\omega_2} \right) \\
&\qquad\qquad \text{(Relabeling dummy } m \to l\text{)} \\
&= \sqrt{n_1 n_2 f_v(1-f_c)} \sum_{l\neq v,c} \left[ (1-f_l) \tfrac{\alpha_{1cl}\alpha_{2lv}}{\varepsilon_l-\varepsilon_v-\omega_2} + f_l \tfrac{\alpha_{2cl}\alpha_{1lv}}{\varepsilon_l-\varepsilon_v-\omega_1} \right] \\
&\qquad\qquad \text{(energy conservation)}
\end{aligned}
$$

$$
\begin{aligned}
\mathcal{T} &= \mathcal{T}_{12} + \mathcal{T}_{21} \\
&= \sqrt{n_1 n_2 f_v(1-f_c)} \sum_{l\neq v,c} \left[ \begin{array}{c} (1-f_l) \tfrac{\alpha_{1cl}\alpha_{2lv}}{\varepsilon_l-\varepsilon_v-\omega_2} + f_l \tfrac{\alpha_{2cl}\alpha_{1lv}}{\varepsilon_l-\varepsilon_v-\omega_1} \\ +(1-f_l) \tfrac{\alpha_{2cl}\alpha_{1lv}}{\varepsilon_l-\varepsilon_v-\omega_1} + f_l \tfrac{\alpha_{1cl}\alpha_{2lv}}{\varepsilon_l-\varepsilon_v-\omega_2} \end{array} \right] \\
&= \sqrt{n_1 n_2 f_v(1-f_c)} \sum_{l\neq v,c} \left[ \tfrac{\alpha_{1cl}\alpha_{2lv}}{\varepsilon_l-\varepsilon_v-\omega_2} + \tfrac{\alpha_{2cl}\alpha_{1lv}}{\varepsilon_l-\varepsilon_v-\omega_1} \right] \\
&= \sqrt{n_1 n_2 f_v(1-f_c)} \sum_{l\neq v,c} \left[ \tfrac{\alpha_{1cl}\alpha_{2lv}}{\varepsilon_l-\varepsilon_v-\omega_2} + (1 \leftrightarrow 2) \right]
\end{aligned}
$$

Note that the occupation factors correspnd intuitively to whether the particle is being absorbed or emitted. Switch $n \to n+1$ for each boson, and $f \to 1-f$ for each fermion, when going from absorption to emission. Besides that, switch the signs on the corresponding energy in the denominator and energy-conserving delta, and complex conjugate the corresponding matrix element coefficient ($\alpha$).

# Appendix C

# Electron-electron Scattering Rate Derivation

## C.1 Kohn-Sham susceptibility

Starting from the detailed derivation we performed for the jellium response case:

$$\begin{aligned}\chi_{\mathrm{KS}}(\mathbf{r},\mathbf{r}',\omega) &= -w_s \sum_{i\neq j} f_i(1-f_j)\left[\frac{\psi_i^*(\mathbf{r})\psi_j(\mathbf{r})\psi_j^*(\mathbf{r}')\psi_i(\mathbf{r}')}{\varepsilon_j-\varepsilon_i-\tilde{\omega}}+\frac{\psi_i(\mathbf{r})\psi_j^*(\mathbf{r})\psi_j(\mathbf{r}')\psi_i^*(\mathbf{r}')}{\varepsilon_j-\varepsilon_i+\tilde{\omega}}\right] \\ &= -w_s \sum_{i\neq j} f_i(1-f_j)\left[\frac{n_{ij}(\mathbf{r})n_{ij}^*(\mathbf{r}')}{\varepsilon_j-\varepsilon_i-\tilde{\omega}}+\frac{n_{ij}^*(\mathbf{r})n_{ij}(\mathbf{r}')}{\varepsilon_j-\varepsilon_i+\tilde{\omega}}\right] \left(n_{ij}(\mathbf{r})\equiv\psi_i^*(\mathbf{r})\psi_j(\mathbf{r})\right)\end{aligned}$$

where $\tilde{\omega}=\omega+i\eta$ is the regularized frequency and $w_s$ is the spin weight (2 for regular unpolarized and 1 for spinorial calculations).

When $\omega\to-\omega$, $\tilde{\omega}\to-\tilde{\omega}^*$, so that the first term becomes the complex conjugate of the second term and vice versa. Therefore $\chi_{\mathrm{KS}}$ satisfies $\chi_{\mathrm{KS}}(-\omega)=\chi_{\mathrm{KS}}^*(\omega)$ exactly, as expected (and necessary for a real response function). We can therefore store the polarizability and dielectric functions for positive frequencies alone.

Further note that since the potential is real, $\psi^*$ is an eigenfunction with the same eigenvalue as $\psi$. Therefore, we can reindex the second term so that $i,j$ in the second term refer to the complex

conjugate states of $i, j$ in the first term. Hence:

$$\begin{aligned}
\chi_{\mathrm{KS}}(\mathbf{r},\mathbf{r}',\omega) &= -w_s \sum_{i\neq j} f_i(1-f_j)\left[\frac{1}{\varepsilon_j-\varepsilon_i-\tilde{\omega}}+\frac{1}{\varepsilon_j-\varepsilon_i+\tilde{\omega}}\right] n_{ij}(\mathbf{r})n_{ij}^*(\mathbf{r}') \\
&= -\frac{w_s}{2}\sum_{i\neq j}\left[f_i(1-f_j)\left[\frac{1}{\varepsilon_j-\varepsilon_i-\tilde{\omega}}+\frac{1}{\varepsilon_j-\varepsilon_i+\tilde{\omega}}\right] n_{ij}(\mathbf{r})n_{ij}^*(\mathbf{r}') + (i\leftrightarrow j)\right] \\
&\quad \text{(since } i \text{ and } j \text{ are dummy indices)} \\
&= -\frac{w_s}{2}\sum_{i\neq j}\left[\begin{array}{c} f_i(1-f_j)\left[\frac{1}{\varepsilon_j-\varepsilon_i-\tilde{\omega}}+\frac{1}{\varepsilon_j-\varepsilon_i+\tilde{\omega}}\right] n_{ij}(\mathbf{r})n_{ij}^*(\mathbf{r}') \\ +f_j(1-f_i)\left[\frac{1}{\varepsilon_i-\varepsilon_j-\tilde{\omega}}+\frac{1}{\varepsilon_i-\varepsilon_j+\tilde{\omega}}\right] n_{ij}^*(\mathbf{r})n_{ij}(\mathbf{r}') \end{array}\right] \\
&= -\frac{w_s}{2}\sum_{i\neq j} n_{ij}(\mathbf{r})n_{ij}^*(\mathbf{r}')\left[\begin{array}{c} f_i(1-f_j)\left[\frac{1}{\varepsilon_j-\varepsilon_i-\tilde{\omega}}+\frac{1}{\varepsilon_j-\varepsilon_i+\tilde{\omega}}\right] \\ +f_j(1-f_i)\left[\frac{1}{\varepsilon_i-\varepsilon_j-\tilde{\omega}}+\frac{1}{\varepsilon_i-\varepsilon_j+\tilde{\omega}}\right] \end{array}\right] \left(\begin{array}{c}\text{complex conjugate}\\ \text{reindexing as before}\end{array}\right) \\
&= -\frac{w_s}{2}\sum_{i\neq j} n_{ij}(\mathbf{r})n_{ij}^*(\mathbf{r}')\left[\begin{array}{c} f_i(1-f_j)\left[\frac{1}{\varepsilon_j-\varepsilon_i-\tilde{\omega}}+\frac{1}{\varepsilon_j-\varepsilon_i+\tilde{\omega}}\right] \\ -f_j(1-f_i)\left[\frac{1}{\varepsilon_j-\varepsilon_i+\tilde{\omega}}+\frac{1}{\varepsilon_j-\varepsilon_i-\tilde{\omega}}\right] \end{array}\right] \\
&= -w_s\sum_{i\neq j} n_{ij}(\mathbf{r})n_{ij}^*(\mathbf{r}')\left[\frac{1}{\varepsilon_j-\varepsilon_i-\tilde{\omega}}+\frac{1}{\varepsilon_j-\varepsilon_i+\tilde{\omega}}\right]\frac{f_i-f_j}{2}
\end{aligned}$$

This seems to be the nicest form that makes best use of the $n_{ij}$ computation, i.e. collect all energy denominator and filling combinations that correspond to it.

Now, specialize to a periodic system and let $i$ correspond to a band with crystal momentum $\mathbf{k}$ and let $j$ correspond to a band with crystal momentum $\mathbf{k}+\mathbf{q}$. Then, $n_{ij}^{\mathbf{kq}}(\mathbf{r}) \equiv \psi_i^{\mathbf{k}*}(\mathbf{r})\psi_j^{\mathbf{k}+\mathbf{q}}(\mathbf{r}) = u_i^{\mathbf{k}*}(\mathbf{r})u_j^{\mathbf{k}+\mathbf{q}}(\mathbf{r})e^{i\mathbf{q}\cdot\mathbf{r}}$. We can then put the periodic part back in reciprocal space and expand $n_{ij}^{\mathbf{kq}}(\mathbf{r}) = \sum_{\mathbf{G}} \tilde{n}_{ij}^{\mathbf{kq}}(\mathbf{G})e^{i(\mathbf{q}+\mathbf{G})\cdot\mathbf{r}}$. Here, $\tilde{n}_{ij}^{\mathbf{kq}}$ is the reciprocal space version of the periodic product density corresponding to the Bloch functions $u_i^{\mathbf{k}}$ and $u_j^{\mathbf{k}+\mathbf{q}}$. Also note that in a periodic system, there are states infinitesimally separated from any given state which are distinct (correspodning to an infinitesimally different Bloch phase for example). We can therefore drop the $i \neq j$ constraint for

periodic systems. Substituting above:

$$\begin{aligned}
\chi_{\mathrm{KS}}(\mathbf{r},\mathbf{r}',\omega) &= -\frac{w_s}{N_{\mathbf{k}}^2}\sum_{ij\mathbf{kq}}\sum_{\mathbf{GG}'}\tilde{n}_{ij}^{\mathbf{kq}}(\mathbf{G})\tilde{n}_{ij}^{\mathbf{kq}*}(\mathbf{G}')e^{i(\mathbf{q}+\mathbf{G})\cdot\mathbf{r}-i(\mathbf{q}+\mathbf{G}')\cdot\mathbf{r}'}\left[\frac{1}{\varepsilon_j-\varepsilon_i-\tilde{\omega}}+\frac{1}{\varepsilon_j-\varepsilon_i+\tilde{\omega}}\right]\frac{f_i-f_j}{2} \\
&\equiv \frac{1}{N_{\mathbf{k}}}\sum_{\mathbf{qGG}'}e^{i\mathbf{q}\cdot(\mathbf{r}-\mathbf{r}')}e^{i\mathbf{G}\cdot\mathbf{r}-i\mathbf{G}'\cdot\mathbf{r}'}\chi_{\mathrm{KS}}^{\mathbf{GG}'}(\mathbf{q},\omega) \\
\chi_{\mathrm{KS}}^{\mathbf{GG}'}(\mathbf{q},\omega) &= -\frac{w_s}{N_{\mathbf{k}}}\sum_{ij\mathbf{k}}\tilde{n}_{ij}^{\mathbf{kq}}(\mathbf{G})\tilde{n}_{ij}^{\mathbf{kq}*}(\mathbf{G}')\left[\frac{1}{\varepsilon_j-\varepsilon_i-\tilde{\omega}}+\frac{1}{\varepsilon_j-\varepsilon_i+\tilde{\omega}}\right]\frac{f_i-f_j}{2} \\
\hat{\boldsymbol{\chi}}_{\mathrm{KS}}(\mathbf{q},\omega) &= -\frac{w_s}{N_{\mathbf{k}}}\sum_{ij\mathbf{k}}\frac{f_i-f_j}{2}\left[\frac{1}{\varepsilon_j-\varepsilon_i-\tilde{\omega}}+\frac{1}{\varepsilon_j-\varepsilon_i+\tilde{\omega}}\right]\tilde{n}_{ij}^{\mathbf{kq}}\tilde{n}_{ij}^{\mathbf{kq}\dagger}(\mathbf{GG}'\,\text{matrix notation})
\end{aligned}$$

## C.2 Scattering time

Within the GW approximation, the imaginary part of the self energy is:

$$\begin{aligned}
\operatorname{Im}\Sigma_i^{\mathbf{k}} &= \frac{1}{2\pi^2}\sum_j\int_{\mathrm{BZ}}\mathrm{d}\mathbf{q}\sum_{\mathbf{GG}'}\frac{\tilde{n}_{ij}^{\mathbf{kq}*}(\mathbf{G})\tilde{n}_{ij}^{\mathbf{kq}}(\mathbf{G}')}{|\mathbf{q}+\mathbf{G}|^2}\operatorname{Im}[-\varepsilon^{-1}_{\mathbf{GG}'}(\mathbf{q},\varepsilon_i^{\mathbf{k}}-\varepsilon_j^{\mathbf{k}+\mathbf{q}})] \\
&= \sum_j\int_{\mathrm{BZ}}\frac{\Omega\mathrm{d}\mathbf{q}}{(2\pi)^3}\sum_{\mathbf{GG}'}\tilde{n}_{ij}^{\mathbf{kq}*}(\mathbf{G})\frac{4\pi}{\Omega|\mathbf{q}+\mathbf{G}|^2}\operatorname{Im}[-\varepsilon^{-1}_{\mathbf{GG}'}(\mathbf{q},\varepsilon_i^{\mathbf{k}}-\varepsilon_j^{\mathbf{k}+\mathbf{q}})]\tilde{n}_{ij}^{\mathbf{kq}}(\mathbf{G}') \\
&= \frac{1}{N_{\mathbf{k}}}\sum_{\mathbf{q}j}\tilde{n}_{ij}^{\mathbf{kq}\dagger}\hat{\mathbf{K}}(\mathbf{q})\operatorname{Im}[-\varepsilon^{-1}(\mathbf{q},\varepsilon_i^{\mathbf{k}}-\varepsilon_j^{\mathbf{k}+\mathbf{q}})]\tilde{n}_{ij}^{\mathbf{kq}}(\hat{\mathbf{K}}=\text{Coulomb operator}) \\
&= -\frac{1}{N_{\mathbf{k}}}\sum_{\mathbf{q}j}\tilde{n}_{ij}^{\mathbf{kq}\dagger}\hat{\mathbf{K}}(\mathbf{q})\operatorname{Im}[(1-\chi_{\mathrm{KS}}(\mathbf{q},\varepsilon_i^{\mathbf{k}}-\varepsilon_j^{\mathbf{k}+\mathbf{q}})\hat{\mathbf{K}}(\mathbf{q}))^{-1}]\tilde{n}_{ij}^{\mathbf{kq}}(\mathrm{RPA}) \\
&= -\frac{1}{N_{\mathbf{k}}}\sum_{\mathbf{q}j}\tilde{n}_{ij}^{\mathbf{kq}\dagger}\operatorname{Im}[\underbrace{(\hat{\mathbf{K}}^{-1}(\mathbf{q})-\chi_{\mathrm{KS}}(\mathbf{q},\varepsilon_i^{\mathbf{k}}-\varepsilon_j^{\mathbf{k}+\mathbf{q}}))^{-1}}_{\hat{\mathbf{K}}_{\mathrm{scr}}(\mathbf{q},\varepsilon_i^{\mathbf{k}}-\varepsilon_j^{\mathbf{k}+\mathbf{q}})}]\tilde{n}_{ij}^{\mathbf{kq}}
\end{aligned}$$

which has a very clear interpretation: it is the imaginary part of the sum of expectation values of the screened Coulomb operator taken on pair densities with all other single-particle states.

Next, we examine how best to exploit symmetries to reduce the computational effort. The scattering rate should be the same for states related by point group symmetries, so we only need to compute $\operatorname{Im}\Sigma_i^{\mathbf{k}}$ for $\mathbf{k}$ in the irreducible wedge of the Brillouin zone. Then, the sum over $\mathbf{q}$ would be over the entrire BZ, so we would need to calculate $\chi_{\mathrm{KS}}$ and $\varepsilon$ for all $\mathbf{q}$, and that is the most computationally expensive part.

Instead, let us try to reduce the calculation of the dielectric function to the irreducible BZ. Let

$M$ be the point group containing orthogonal rotation matrices $m$.

$$
\begin{aligned}
\operatorname{Im}\Sigma_i^{\mathbf{k}} &= -\frac{1}{N_{\mathbf{k}}}\sum_{\mathbf{q}\in \mathrm{BZ}}\sum_{j\mathbf{G}\mathbf{G}'}\tilde{n}_{ij}^{\mathbf{k}\mathbf{q}*}(\mathbf{G})\operatorname{Im}[\hat{\mathbf{K}}^{\mathrm{scr}}_{\mathbf{G}\mathbf{G}'}(\mathbf{q},\varepsilon_i^{\mathbf{k}}-\varepsilon_j^{\mathbf{k}+\mathbf{q}})]\tilde{n}_{ij}^{\mathbf{k}\mathbf{q}}(\mathbf{G}') \\
&= -\frac{1}{N_{\mathbf{k}}}\sum_{\mathbf{q}_0\in \mathrm{BZ}_0}\sum_{\mathbf{q}\in M\mathbf{q}_0}\sum_{j\mathbf{G}\mathbf{G}'}\tilde{n}_{ij}^{\mathbf{k}\mathbf{q}*}(\mathbf{G})\operatorname{Im}[\hat{\mathbf{K}}^{\mathrm{scr}}_{\mathbf{G}\mathbf{G}'}(\mathbf{q},\varepsilon_i^{\mathbf{k}}-\varepsilon_j^{\mathbf{k}+\mathbf{q}})]\tilde{n}_{ij}^{\mathbf{k}\mathbf{q}}(\mathbf{G}') \\
&\quad \left(\text{Split }\sum_{\mathbf{q}}\text{ into orbits of }\mathbf{q}_0\text{ in irreducible wedge }\mathrm{BZ}_0\right) \\
&= -\frac{1}{N_{\mathbf{k}}}\sum_{\mathbf{q}_0\in \mathrm{BZ}_0}\frac{|M\mathbf{q}_0|}{|M|}\sum_{m\in M}\sum_{j\mathbf{G}\mathbf{G}'}\tilde{n}_{ij}^{\mathbf{k}(m\mathbf{q}_0)*}(\mathbf{G})\operatorname{Im}[\hat{\mathbf{K}}^{\mathrm{scr}}_{\mathbf{G}\mathbf{G}'}(m\mathbf{q}_0,\varepsilon_i^{mm^T\mathbf{k}}-\varepsilon_j^{mm^T\mathbf{k}+m\mathbf{q}_0})]\tilde{n}_{ij}^{\mathbf{k}(m\mathbf{q}_0)}(\mathbf{G}') \\
&\quad (\text{orbit}-\text{stabilizer theorem}) \\
&= -\frac{1}{N_{\mathbf{k}}}\sum_{\mathbf{q}_0\in \mathrm{BZ}_0}\frac{|M\mathbf{q}_0|}{|M|}\sum_{m\in M}\sum_{j\mathbf{G}\mathbf{G}'}\tilde{n}_{ij}^{\mathbf{k}(m\mathbf{q}_0)*}(\mathbf{G})\operatorname{Im}[\hat{\mathbf{K}}^{\mathrm{scr}}_{\mathbf{G}\mathbf{G}'}(m\mathbf{q}_0,\varepsilon_i^{m^T\mathbf{k}}-\varepsilon_j^{m^T\mathbf{k}+\mathbf{q}_0})]\tilde{n}_{ij}^{\mathbf{k}(m\mathbf{q}_0)}(\mathbf{G}') \\
&\quad (\varepsilon' s\text{ are scalars})
\end{aligned}
$$

$$
\begin{aligned}
\tilde{n}_{ij}^{\mathbf{k}(m\mathbf{q})}(\mathbf{G}) &= \int_\Omega \frac{\mathrm{d}\mathbf{r}}{\Omega}u_i^{\mathbf{k}*}(\mathbf{r})u_j^{\mathbf{k}+m\mathbf{q}}(\mathbf{r})e^{-i\mathbf{G}\cdot\mathbf{r}} \\
&= \int_\Omega \frac{\mathrm{d}\mathbf{r}}{\Omega}u_i^{mm^T\mathbf{k}*}(\mathbf{r})u_j^{m(m^T\mathbf{k}+\mathbf{q})}(\mathbf{r})e^{-i\mathbf{G}\cdot\mathbf{r}} \\
&= \int_\Omega \frac{\mathrm{d}\mathbf{r}}{\Omega}u_i^{m^T\mathbf{k}*}(m^T\mathbf{r})u_j^{m^T\mathbf{k}+\mathbf{q}}(m^T\mathbf{r})e^{-im^T\mathbf{G}\cdot m^T\mathbf{r}} \\
&= \int_\Omega \frac{\mathrm{d}\mathbf{r}'}{\Omega}u_i^{m^T\mathbf{k}*}(\mathbf{r}')u_j^{m^T\mathbf{k}+\mathbf{q}}(\mathbf{r}')e^{-im^T\mathbf{G}\cdot\mathbf{r}'}(\mathbf{r}'\equiv m^Tr) \\
&= \tilde{n}_{ij}^{(m^T\mathbf{k})\mathbf{q}}(m^T\mathbf{G})
\end{aligned}
$$

$$
\begin{aligned}
\hat{\mathbf{K}}^{\mathrm{scr}}_{\mathbf{G}\mathbf{G}'}(m\mathbf{q},\omega) &= \int\frac{\mathrm{d}\mathbf{r}}{\Omega}e^{i(m\mathbf{q}+\mathbf{G})\cdot\mathbf{r}}\int\frac{\mathrm{d}\mathbf{r}'}{\Omega}e^{-i(m\mathbf{q}+\mathbf{G}')\cdot\mathbf{r}'}K^{\mathrm{scr}}(\mathbf{r},\mathbf{r}') \\
&= \int\frac{\mathrm{d}\mathbf{r}}{\Omega}e^{i(\mathbf{q}+m^T\mathbf{G})\cdot m^T\mathbf{r}}\int\frac{\mathrm{d}\mathbf{r}'}{\Omega}e^{-i(\mathbf{q}+m^T\mathbf{G}')\cdot m^T\mathbf{r}'}K^{\mathrm{scr}}(\mathbf{r},\mathbf{r}') \\
&= \int\frac{\mathrm{d}\mathbf{r}}{\Omega}e^{i(\mathbf{q}+m^T\mathbf{G})\cdot m^T\mathbf{r}}\int\frac{\mathrm{d}\mathbf{r}'}{\Omega}e^{-i(\mathbf{q}+m^T\mathbf{G}')\cdot m^T\mathbf{r}'}K^{\mathrm{scr}}(m^T\mathbf{r},m^T\mathbf{r}')(K^{\mathrm{scr}}\text{ symmetric on }M) \\
&= \hat{\mathbf{K}}^{\mathrm{scr}}_{(m^T\mathbf{G})(m^T\mathbf{G}')}(\mathbf{q})
\end{aligned}
$$

$$
\begin{aligned}
\operatorname{Im}\Sigma_i^{\mathbf{k}} &= -\frac{1}{N_{\mathbf{k}}}\sum_{\mathbf{q}_0\in \mathrm{BZ}_0}\frac{|M\mathbf{q}_0|}{|M|}\sum_{m\in M} \\
&\quad \times \sum_{j\mathbf{G}\mathbf{G}'} \tilde{n}_{ij}^{(m^T\mathbf{k})\mathbf{q}_0 *}(m^T\mathbf{G})\operatorname{Im}[\hat{\mathbf{K}}^{\mathrm{scr}}_{(m^T\mathbf{G})(m^T\mathbf{G}')}(\mathbf{q}_0, \varepsilon_i^{m^T\mathbf{k}} - \varepsilon_j^{m^T\mathbf{k}+\mathbf{q}_0})]\tilde{n}_{ij}^{(m^T\mathbf{k})\mathbf{q}_0}(m^T\mathbf{G}') \\
&= -\frac{1}{N_{\mathbf{k}}}\sum_{\mathbf{q}_0\in \mathrm{BZ}_0}\frac{|M\mathbf{q}_0|}{|M|}\sum_{m\in M}\sum_{j\mathbf{G}\mathbf{G}'} \tilde{n}_{ij}^{(m^T\mathbf{k})\mathbf{q}_0 *}(\mathbf{G})\operatorname{Im}[\hat{\mathbf{K}}^{\mathrm{scr}}_{\mathbf{G}\mathbf{G}'}(\mathbf{q}_0, \varepsilon_i^{m^T\mathbf{k}} - \varepsilon_j^{m^T\mathbf{k}+\mathbf{q}_0})]\tilde{n}_{ij}^{(m^T\mathbf{k})\mathbf{q}_0}(\mathbf{G}') \\
&\quad (\text{Relabeling dummy } \mathbf{G}\to m\mathbf{G}, \mathbf{G}'\to m\mathbf{G}') \\
&= -\frac{1}{|M|}\sum_{m\in M}\sum_{\mathbf{q}_0\in \mathrm{BZ}_0}\frac{|M\mathbf{q}_0|}{N_{\mathbf{k}}}\sum_{j\mathbf{G}\mathbf{G}'} \tilde{n}_{ij}^{(m^T\mathbf{k})\mathbf{q}_0 *}(\mathbf{G})\operatorname{Im}[\hat{\mathbf{K}}^{\mathrm{scr}}_{\mathbf{G}\mathbf{G}'}(\mathbf{q}_0, \varepsilon_i^{m^T\mathbf{k}} - \varepsilon_j^{m^T\mathbf{k}+\mathbf{q}_0})]\tilde{n}_{ij}^{(m^T\mathbf{k})\mathbf{q}_0}(\mathbf{G}') \\
&= \frac{1}{|M|}\sum_{m\in M}\operatorname{Im}\tilde{\Sigma}_i^{m^T\mathbf{k}} \\
\operatorname{Im}\tilde{\Sigma}_i^{\mathbf{k}} &\equiv -\sum_{\mathbf{q}\in \mathrm{BZ}_0} w_{\mathbf{q}}^0 \sum_{j\mathbf{G}\mathbf{G}'} \tilde{n}_{ij}^{\mathbf{k}\mathbf{q} *}(\mathbf{G})\operatorname{Im}[\hat{\mathbf{K}}^{\mathrm{scr}}_{\mathbf{G}\mathbf{G}'}(\mathbf{q}, \varepsilon_i^{\mathbf{k}} - \varepsilon_j^{\mathbf{k}+\mathbf{q}})]\tilde{n}_{ij}^{\mathbf{k}\mathbf{q}}(\mathbf{G}') \\
w_{\mathbf{q}}^0 &\equiv \frac{|M\mathbf{q}_0|}{N_{\mathbf{k}}}
\end{aligned}
$$

Therefore, we first compute the *unsymmetrized* scattering rates, $\operatorname{Im}\tilde{\Sigma}_i^{\mathbf{k}}$, for all $\mathbf{k}$ using the original formula, but summing over only $\mathbf{q}$ in the irreducible wedge of BZ but weighted by the cardinality of the corresponding orbits. We then simply symmetrize the scattering rates over the point group. This way we only need to compute the expensive dielectric matrix over the irreducible wedge.

Note: In degenerate subspaces, the symmetry that makes the eigenvalues equal will also ensure that the scattering rates are equal. So the above procedure is robust against unknown unitary rotations in degenerate subspaces.

## C.3 CEDA plasma frequency sum rule

$$
\begin{aligned}
\chi_{\mathrm{KS}}^{\mathbf{GG}}(\mathbf{q},\omega) &= -\frac{w_s}{N_{\mathbf{k}}}\sum_{\mathbf{k}}\sum_{ij=0}^{\infty}|\tilde{n}_{ij}^{\mathbf{kq}}(\mathbf{G})|^2\left[\frac{1}{\varepsilon_j-\varepsilon_i-\tilde{\omega}}+\frac{1}{\varepsilon_j-\varepsilon_i+\tilde{\omega}}\right]\frac{f_i-f_j}{2} \\
&= -\frac{w_s}{N_{\mathbf{k}}}\sum_{\mathbf{k}}\sum_{ij=0}^{N_b}|\tilde{n}_{ij}^{\mathbf{kq}}(\mathbf{G})|^2\left[\frac{1}{\varepsilon_j-\varepsilon_i-\tilde{\omega}}+\frac{1}{\varepsilon_j-\varepsilon_i+\tilde{\omega}}\right]\frac{f_i-f_j}{2} \\
&\quad -\frac{w_s}{N_{\mathbf{k}}}\sum_{\mathbf{k}}\sum_{i=0}^{N_b}\sum_{j=N_b}^{\infty}|\tilde{n}_{ij}^{\mathbf{kq}}(\mathbf{G})|^2\left[\frac{1}{\varepsilon_j-\varepsilon_i-\tilde{\omega}}+\frac{1}{\varepsilon_j-\varepsilon_i+\tilde{\omega}}\right]\frac{f_i}{2} \\
&\quad -\frac{w_s}{N_{\mathbf{k}}}\sum_{\mathbf{k}}\sum_{i=N_b}^{\infty}\sum_{j=0}^{N_b}|\tilde{n}_{ij}^{\mathbf{kq}}(\mathbf{G})|^2\left[\frac{1}{\varepsilon_j-\varepsilon_i-\tilde{\omega}}+\frac{1}{\varepsilon_j-\varepsilon_i+\tilde{\omega}}\right]\frac{-f_j}{2} \\
&\quad \text{(The term with } i,j>N_b \text{ has } f_i=f_j=0 \text{ and hence drops out)} \\
&= -\frac{w_s}{N_{\mathbf{k}}}\sum_{\mathbf{k}}\sum_{ij=0}^{N_b}|\tilde{n}_{ij}^{\mathbf{kq}}(\mathbf{G})|^2\left[\frac{1}{\varepsilon_j-\varepsilon_i-\tilde{\omega}}+\frac{1}{\varepsilon_j-\varepsilon_i+\tilde{\omega}}\right]\frac{f_i-f_j}{2} \\
&\quad -\frac{w_s}{N_{\mathbf{k}}}\sum_{\mathbf{k}}\sum_{i=0}^{N_b}f_i\sum_{j=N_b}^{\infty}|\tilde{n}_{ij}^{\mathbf{kq}}(\mathbf{G})|^2\left[\frac{1}{\varepsilon_j-\varepsilon_i-\tilde{\omega}}+\frac{1}{\varepsilon_j-\varepsilon_i+\tilde{\omega}}\right] \\
&\quad \text{(swapping } i\leftrightarrow j \text{ in third term above)} \\
&\approx -\frac{w_s}{N_{\mathbf{k}}}\sum_{\mathbf{k}}\sum_{ij=0}^{N_b}|\tilde{n}_{ij}^{\mathbf{kq}}(\mathbf{G})|^2\left[\frac{1}{\varepsilon_j-\varepsilon_i-\tilde{\omega}}+\frac{1}{\varepsilon_j-\varepsilon_i+\tilde{\omega}}\right]\frac{f_i-f_j}{2} \\
&\quad -\frac{w_s}{N_{\mathbf{k}}}\sum_{\mathbf{k}}\sum_{i=0}^{N_b}f_i\sum_{j=N_b}^{\infty}|\tilde{n}_{ij}^{\mathbf{kq}}(\mathbf{G})|^2\left[\frac{1}{\bar{\varepsilon}-\varepsilon_i-\tilde{\omega}}+\frac{1}{\bar{\varepsilon}-\varepsilon_i+\tilde{\omega}}\right] \text{(CEDA)} \\
&= -\frac{w_s}{N_{\mathbf{k}}}\sum_{\mathbf{k}}\sum_{ij=0}^{N_b}|\tilde{n}_{ij}^{\mathbf{kq}}(\mathbf{G})|^2\left[\frac{1}{\varepsilon_j-\varepsilon_i-\tilde{\omega}}+\frac{1}{\varepsilon_j-\varepsilon_i+\tilde{\omega}}\right]\frac{f_i-f_j}{2} \\
&\quad -\frac{w_s}{N_{\mathbf{k}}}\sum_{\mathbf{k}}\sum_{i=0}^{N_b}f_i\left[\frac{1}{\bar{\varepsilon}-\varepsilon_i-\tilde{\omega}}+\frac{1}{\bar{\varepsilon}-\varepsilon_i+\tilde{\omega}}\right]\left(\frac{1}{\Omega^2}-\sum_{j=0}^{N_b}|\tilde{n}_{ij}^{\mathbf{kq}}(\mathbf{G})|^2\right) \text{(completeness)} \\
&= -\frac{w_s}{N_{\mathbf{k}}}\sum_{\mathbf{k}}\sum_{ij=0}^{N_b}|\tilde{n}_{ij}^{\mathbf{kq}}(\mathbf{G})|^2\left(\left[\frac{1}{\varepsilon_j-\varepsilon_i-\tilde{\omega}}+\frac{1}{\varepsilon_j-\varepsilon_i+\tilde{\omega}}\right]\frac{f_i-f_j}{2}-f_i\left[\frac{1}{\bar{\varepsilon}-\varepsilon_i-\tilde{\omega}}+\frac{1}{\bar{\varepsilon}-\varepsilon_i+\tilde{\omega}}\right]\right) \\
&\quad -\frac{w_s}{N_{\mathbf{k}}}\frac{1}{\Omega^2}\sum_{\mathbf{k}}\sum_{i=0}^{N_b}f_i\left[\frac{1}{\bar{\varepsilon}-\varepsilon_i-\tilde{\omega}}+\frac{1}{\bar{\varepsilon}-\varepsilon_i+\tilde{\omega}}\right]
\end{aligned}
$$

Plasma frequency sum rule:

$$
\begin{aligned}
\frac{\pi\omega_p^2}{2} &= -\int_0^\infty \omega \mathrm{d}\omega \frac{4\pi\Omega}{|\mathbf{q}+\mathbf{G}|^2}\,\mathrm{Im}[\chi_{\mathrm{KS}}^{\mathbf{GG}}(\mathbf{q},\omega)] \\
N_{\mathrm{el}} &= -\frac{\Omega}{2\pi^2}\int_0^\infty \omega \mathrm{d}\omega \frac{4\pi\Omega}{|\mathbf{q}+\mathbf{G}|^2}\,\mathrm{Im}[\chi_{\mathrm{KS}}^{\mathbf{GG}}(\mathbf{q},\omega)] (\omega_p^2 = 4\pi N_{\mathrm{el}}) \\
&= \frac{1}{2\pi^2}\frac{4\pi}{|\mathbf{q}+\mathbf{G}|^2}\frac{w_s}{N_{\mathbf{k}}}\sum_{\mathbf{k}}\int_0^\infty \omega \mathrm{d}\omega \\
&\quad \times \mathrm{Im}\left[\begin{array}{c} \sum_{ij=0}^{N_b}\Omega^2|\tilde{n}_{ij}^{\mathbf{kq}}(\mathbf{G})|^2\left(\left[\frac{1}{\varepsilon_j-\varepsilon_i-\tilde{\omega}}+\frac{1}{\varepsilon_j-\varepsilon_i+\tilde{\omega}}\right]\frac{f_i-f_j}{2}-f_i\left[\frac{1}{\bar{\varepsilon}-\varepsilon_i-\tilde{\omega}}+\frac{1}{\bar{\varepsilon}-\varepsilon_i+\tilde{\omega}}\right]\right) \\ +\sum_{i=0}^{N_b} f_i\left[\frac{1}{\bar{\varepsilon}-\varepsilon_i-\tilde{\omega}}+\frac{1}{\bar{\varepsilon}-\varepsilon_i+\tilde{\omega}}\right] \end{array}\right] \\
&\quad \int_0^\infty \omega \mathrm{d}\omega\,\mathrm{Im}\left[\frac{1}{E-\tilde{\omega}}+\frac{1}{E+\tilde{\omega}}\right] \\
&= \int_0^\infty \omega \mathrm{d}\omega\,\mathrm{Im}\left[-\frac{1}{\omega-E+i\eta}+\frac{1}{\omega+E+i\eta}\right] \\
&= \int_0^\infty \omega \mathrm{d}\omega\,\mathrm{Im}\left[-\left(\mathcal{P}\frac{1}{\omega-E}-i\pi\delta(\omega-E)\right)+\left(\mathcal{P}\frac{1}{\omega+E}-i\pi\delta(\omega+E)\right)\right](\eta\to 0) \\
&= \pi\int_0^\infty \omega \mathrm{d}\omega[\delta(\omega-E)-\delta(\omega+E)] \\
&= \pi E
\end{aligned}
$$

$$
\begin{aligned}
N_{\mathrm{el}} &= \frac{1}{2\pi}\frac{4\pi}{|\mathbf{q}+\mathbf{G}|^2}\frac{w_s}{N_{\mathbf{k}}}\sum_{\mathbf{k}}\left[\sum_{ij=0}^{N_b}\Omega^2|\tilde{n}_{ij}^{\mathbf{kq}}(\mathbf{G})|^2\left((\varepsilon_j-\varepsilon_i)\frac{f_i-f_j}{2}-f_i(\bar{\varepsilon}-\varepsilon_i)\right)+\sum_{i=0}^{N_b} f_i(\bar{\varepsilon}-\varepsilon_i)\right] \\
&= \frac{1}{2\pi}\frac{4\pi}{|\mathbf{q}+\mathbf{G}|^2}\frac{w_s}{N_{\mathbf{k}}}\sum_{\mathbf{k}}\left[\sum_{ij=0}^{N_b}\Omega^2|\tilde{n}_{ij}^{\mathbf{kq}}(\mathbf{G})|^2\begin{pmatrix}(\varepsilon_j-\varepsilon_i)\frac{f_i-f_j}{2}\\ -\frac{f_i}{2}(\bar{\varepsilon}-\varepsilon_i)\\ -\frac{f_j}{2}(\bar{\varepsilon}-\varepsilon_j)\end{pmatrix}+\sum_{i/j=0}^{N_b}\begin{pmatrix}\frac{f_i}{2}(\bar{\varepsilon}-\varepsilon_i)\\ +\frac{f_j}{2}(\bar{\varepsilon}-\varepsilon_j)\end{pmatrix}\right] \\
&\quad \text{(Restoring } i\leftrightarrow j \text{ symmetry)} \\
&= \frac{1}{2\pi}\frac{4\pi}{|\mathbf{q}+\mathbf{G}|^2}\frac{w_s}{N_{\mathbf{k}}}\sum_{\mathbf{k}}\left[\sum_{ij=0}^{N_b}\Omega^2|\tilde{n}_{ij}^{\mathbf{kq}}(\mathbf{G})|^2\begin{pmatrix}\frac{f_i}{2}(\varepsilon_j-\bar{\varepsilon})\\ +\frac{f_j}{2}(\varepsilon_i-\bar{\varepsilon})\end{pmatrix}+\sum_{i/j=0}^{N_b}\begin{pmatrix}\frac{f_i}{2}(\bar{\varepsilon}-\varepsilon_i)\\ +\frac{f_j}{2}(\bar{\varepsilon}-\varepsilon_j)\end{pmatrix}\right] \\
&= \frac{1}{2\pi}\frac{4\pi}{|\mathbf{q}+\mathbf{G}|^2}\frac{w_s}{N_{\mathbf{k}}}\sum_{\mathbf{k}}\begin{bmatrix}-\left(\sum_i f_i\varepsilon_i-\sum_{ij}\Omega^2|\tilde{n}_{ij}^{\mathbf{kq}}(\mathbf{G})|^2\frac{f_i\varepsilon_j+f_j\varepsilon_i}{2}\right)\\ +\bar{\varepsilon}\left(\sum_i f_i-\sum_{ij}\Omega^2|\tilde{n}_{ij}^{\mathbf{kq}}(\mathbf{G})|^2\frac{f_i+f_j}{2}\right)\end{bmatrix}
\end{aligned}
$$

$$
\begin{aligned}
\frac{w_s}{N_{\mathbf{k}}}\sum_{\mathbf{k}i} f_i &= \frac{1}{2\pi}K_{\mathbf{q}}(\mathbf{G})\frac{w_s}{N_{\mathbf{k}}}\sum_{\mathbf{k}}\left[\begin{array}{c} -\left(\sum_i f_i\varepsilon_i - \sum_{ij}\Omega^2|\tilde{n}_{ij}^{\mathbf{kq}}(\mathbf{G})|^2\frac{f_i\varepsilon_j+f_j\varepsilon_i}{2}\right) \\ +\bar{\varepsilon}\left(\sum_i f_i - \sum_{ij}\Omega^2|\tilde{n}_{ij}^{\mathbf{kq}}(\mathbf{G})|^2\frac{f_i+f_j}{2}\right)\end{array}\right] \\
2\pi K_{\mathbf{q}}^{-1}(\mathbf{G})\sum_{\mathbf{k}i} f_i &= \bar{\varepsilon}\left(\sum_{\mathbf{k}i} f_i - \Omega^2\sum_{\mathbf{k}ij}|\tilde{n}_{ij}^{\mathbf{kq}}(\mathbf{G})|^2\frac{f_i+f_j}{2}\right) - \left(\sum_{\mathbf{k}i} f_i\varepsilon_i - \Omega^2\sum_{\mathbf{k}ij}|\tilde{n}_{ij}^{\mathbf{kq}}(\mathbf{G})|^2\frac{f_i\varepsilon_j+f_j\varepsilon_i}{2}\right) \\
\bar{\varepsilon} &= \frac{\sum_{\mathbf{qG}} w_{\mathbf{q}}(\mathbf{G})\left[2\pi K_{\mathbf{q}}^{-1}(\mathbf{G})\sum_{\mathbf{k}i} f_i + \sum_{\mathbf{k}i} f_i\varepsilon_i - \Omega^2\sum_{\mathbf{k}ij}|\tilde{n}_{ij}^{\mathbf{kq}}(\mathbf{G})|^2\frac{f_i\varepsilon_j+f_j\varepsilon_i}{2}\right]}{\sum_{\mathbf{qG}} w_{\mathbf{q}}(\mathbf{G})\left[\sum_{\mathbf{k}i} f_i - \Omega^2\sum_{\mathbf{k}ij}|\tilde{n}_{ij}^{\mathbf{kq}}(\mathbf{G})|^2\frac{f_i+f_j}{2}\right]} \\
&= \frac{\sum_{\mathbf{qG}} w_{\mathbf{q}}(\mathbf{G})[\mathrm{FEsum} - \Omega^2\,\mathrm{oNum} + 2\pi K_{\mathbf{q}}^{-1}(\mathbf{G})\,\mathrm{Fsum}]}{\sum_{\mathbf{qG}} w_{\mathbf{q}}(\mathbf{G})[\mathrm{Fsum} - \Omega^2\,\mathrm{oDen}]} \\
\mathrm{Fsum} &\equiv \sum_{\mathbf{k}i} f_i \\
\mathrm{FEsum} &\equiv \sum_{\mathbf{k}i} f_i\varepsilon_i \\
\mathrm{oNum} &\equiv \sum_{\mathbf{k}ij}|\tilde{n}_{ij}^{\mathbf{kq}}(\mathbf{G})|^2\frac{f_i\varepsilon_j+f_j\varepsilon_i}{2} \\
\mathrm{oDen} &\equiv \sum_{\mathbf{k}ij}|\tilde{n}_{ij}^{\mathbf{kq}}(\mathbf{G})|^2\frac{f_i+f_j}{2}
\end{aligned}
$$

# Appendix D

# $e^-$-phonon interactions in jellium

Consider a jellium solid consisting of uniform density $n_0$ of electrons in a background of compensating charge density $-n_0$ with mass-density $n_0 M$ (atomic units with electron-is-positive charge convention). In the bulk configuration, the electron potential is constant everywhere and hence the electronic states are simply plane waves with the dispersion $\varepsilon_{\mathbf{q}} = q^2/2$ . The number density of electrons with energy less than $\varepsilon$ is then $n(\varepsilon) = \sum_s \int \frac{d\mathbf{q}}{(2\pi)^3} \theta(\varepsilon - \varepsilon_{\mathbf{q}}) = 2 \int_0^{\sqrt{2\varepsilon}} \frac{4\pi q^2}{(2\pi)^3} \mathrm{d}q = \frac{(2\varepsilon)^{3/2}}{3\pi^2}$. Therefore, the Fermi energy is $\varepsilon_F = k_F^2/2$ with $k_F \equiv (3\pi^2 n_0)^{1/3}$.

## D.1 Jellium phonon dispersion

In order to derive the phonon dispersions, we will need to consider perturbations of the nuclear background from the above uniform configuration. This will require the self-consistent electron response to that perturbation. Let's first derive that electron response. Working within the Born-Oppenheimer approximations, the nuclear motion time scales are much larger than the electronic ones, so we can work with the time-independent perturbation of the electronic system.

Note: The most involved piece of the electronic response is the response of the electron density to the total electron (Kohn-Sham) potential, which we have previously derived in detail elsewhere.

$$
\begin{aligned}
\chi_{\mathrm{KS}}(\mathbf{r},\mathbf{r}',\omega) &= -2\sum_{m\neq n} f_n(1-f_m)\left[\frac{\psi_n^{0*}(\mathbf{r})\psi_m^0(\mathbf{r})\psi_m^{0*}(\mathbf{r}')\psi_n^0(\mathbf{r}')}{\varepsilon_m-\varepsilon_n-\omega}+\frac{\psi_n^0(\mathbf{r})\psi_m^{0*}(\mathbf{r})\psi_m^0(\mathbf{r}')\psi_n^{0*}(\mathbf{r}')}{\varepsilon_m-\varepsilon_n+\omega}\right]\\
&= -2\sum_{\mathbf{q}\neq\mathbf{q}'}\frac{1}{\Omega^2}f_{\mathbf{q}'}(1-f_{\mathbf{q}})\left[\frac{e^{i(\mathbf{q}-\mathbf{q}')\cdot(\mathbf{r}-\mathbf{r}')}}{q^2/2-q'^2/2-\omega}+\frac{e^{-i(\mathbf{q}-\mathbf{q}')\cdot(\mathbf{r}-\mathbf{r}')}}{q^2/2-q'^2/2+\omega}\right]\\
&= -2\sum_{\mathbf{q}\neq\mathbf{q}'}\frac{1}{\Omega^2}\left[\frac{f_{\mathbf{q}'}(1-f_{\mathbf{q}})e^{i(\mathbf{q}-\mathbf{q}')\cdot(\mathbf{r}-\mathbf{r}')}}{q^2/2-q'^2/2-\omega}+\frac{f_{\mathbf{q}}(1-f_{\mathbf{q}'})e^{i(\mathbf{q}-\mathbf{q}')\cdot(\mathbf{r}-\mathbf{r}')}}{q'^2/2-q^2/2+\omega}\right]\\
&\quad(\text{Swapping } q\leftrightarrow q' \text{ in second term})\\
&= -2\sum_{\mathbf{q}\neq\mathbf{q}'}\frac{1}{\Omega^2}\frac{e^{i(\mathbf{q}-\mathbf{q}')\cdot(\mathbf{r}-\mathbf{r}')}}{q^2/2-q'^2/2-\omega}[f_{\mathbf{q}'}(1-f_{\mathbf{q}})-f_{\mathbf{q}}(1-f_{\mathbf{q}'})]\\
&= -2\int\frac{d\mathbf{q}}{(2\pi)^3}\int\frac{d\mathbf{q}'}{(2\pi)^3}(f_{\mathbf{q}'}-f_{\mathbf{q}})\frac{e^{i(\mathbf{q}-\mathbf{q}')\cdot(\mathbf{r}-\mathbf{r}')}}{q^2/2-q'^2/2-\omega}\\
&= -2\int\frac{d\mathbf{k}}{(2\pi)^3}e^{i\mathbf{k}\cdot(\mathbf{r}-\mathbf{r}')}\int\frac{d\mathbf{q}}{(2\pi)^3}\frac{f_{\mathbf{q}}-f_{\mathbf{q}+\mathbf{k}}}{(\mathbf{q}+\mathbf{k})^2/2-q^2/2-\omega}((\mathbf{q},\mathbf{q}')\to(\mathbf{k}+\mathbf{q},\mathbf{q}))\\
\chi_{\mathrm{KS}}(\mathbf{k},\omega=0) &= -2\int\frac{d\mathbf{q}}{(2\pi)^3}\frac{f_{\mathbf{q}}-f_{\mathbf{q}+\mathbf{k}}}{(\mathbf{q}+\mathbf{k})^2/2-q^2/2}(\text{switching to reciprocal space})\\
&\approx -2\int\frac{d\mathbf{q}}{(2\pi)^3}\frac{\theta(k_F-q)-\theta(k_F-|\mathbf{q}+\mathbf{k}|)}{(\mathbf{q}+\mathbf{k})^2/2-q^2/2}(T=0\,\text{occupations})\\
&= -2\int\frac{d\mathbf{q}}{(2\pi)^3}\frac{\theta(|\mathbf{q}+\mathbf{k}|-k_F)\theta(k_F-q)-\theta(k_F-|\mathbf{q}+\mathbf{k}|)\theta(q-k_F)}{(\mathbf{q}+\mathbf{k})^2/2-q^2/2}\\
&= -4\int\frac{d\mathbf{q}}{(2\pi)^3}\frac{\theta(|\mathbf{q}+\mathbf{k}|-k_F)\theta(k_F-q)}{(\mathbf{q}+\mathbf{k})^2/2-q^2/2}(\text{Swapping } \mathbf{q}\leftrightarrow\mathbf{q}+\mathbf{k} \text{ in second term})\\
&= -4\int_0^{k_F}\frac{q^2\mathrm{d}q}{(2\pi)^3}\int d\phi_q\int_{-1}^{+1}\mathrm{d}\cos\theta_q\frac{\theta(|\mathbf{q}+\mathbf{k}|-k_F)}{qk\cos\theta_q+k^2/2}(\theta_q=\text{angle between }\mathbf{q}\text{ and }\mathbf{k})\\
&= -\frac{1}{\pi^2}\int_0^{k_F}q^2\mathrm{d}q\int_{-1}^{+1}\mathrm{d}\cos\theta_q\frac{\theta\left(\sqrt{q^2+k^2+2qk\cos\theta_q}-k_F\right)}{qk\cos\theta_q+k^2/2}\\
&= -\frac{1}{\pi^2}\int_0^{k_F}q^2\mathrm{d}q\begin{cases}0, & q<k_F-k\\ \int_{\frac{k_F^2-(q^2+k^2)}{2qk}}^{+1}\frac{\mathrm{d}\cos\theta_q}{qk\cos\theta_q+k^2/2}, & k-k_F<q<k_F-k\\ \int_{-1}^{+1}\frac{\mathrm{d}\cos\theta_q}{qk\cos\theta_q+k^2/2}, & q<k-k_F\end{cases}\\
&= -\frac{1}{\pi^2k}\int_0^{k_F}q\mathrm{d}q\begin{cases}0, & q<k_F-k\\ \log\left|\frac{k^2+2kq}{k_F^2-q^2}\right|, & k_F-k<q\text{ and }|q-k|<k_F\\ \log\left|\frac{k+2q}{k-2q}\right|, & k_F-k<q\text{ and }|q-k|>k_F\end{cases}\\
&= -\frac{k_F}{\pi^2}\int_0^1\frac{Q}{K}\mathrm{d}Q\begin{cases}0, & Q<1-K\\ \log\left|\frac{K^2+2KQ}{1-Q^2}\right|, & 1-K<Q\text{ and }|Q-K|<1\\ \log\left|\frac{K+2Q}{K-2Q}\right|, & 1-K<Q\text{ and }|Q-K|>1\end{cases}\quad\left(K\equiv\frac{k}{k_F},Q\equiv\frac{q}{k_F}\right)
\end{aligned}
$$

This can be integrated analytically (Mathematica) to a pretty complicated piecewise function that's very well approximated in the relevant region (small $k$ through $k \sim k_F$) by

$$\chi_{\rm KS}(\mathbf{k}, \omega = 0) \approx -\frac{1}{\pi^2} \begin{cases} \sqrt{k_F^2 - k^2/6}, & k < k_F\sqrt{6} \\ 0, & k \geqslant k_F\sqrt{6} \end{cases}$$

Check: the Thomas-Fermi model replaces each point in space with a homogeneous electron gas. Therefore, the response is independent of $k$. For a perturbation $V$, the Fermi energy $\varepsilon_F \to \varepsilon_F - V$, so that the density response is $\chi_{\rm KS} = -\frac{\partial}{\partial \varepsilon_F} \frac{(2\varepsilon_F)^{3/2}}{3\pi^2} = -\frac{3}{2}\frac{(2\varepsilon_F)^{1/2}}{3\pi^2} 3 = -\frac{k_F}{\pi^2}$. This agrees with the $k \to 0$ limit of the above nonlocal response.

Now consider the response of the system to a perturbation to the nuclear charge density $\delta N e^{i\mathbf{k}\cdot\mathbf{r}}$. Let the corresponding electronic response be $\delta n e^{i\mathbf{k}\cdot\mathbf{r}}$. Then the net electric potential is $\frac{4\pi}{k^2}(\delta N + \delta n)e^{i\mathbf{k}\cdot\mathbf{r}}$ and the exchange-correlation potential is $e''_{\rm XC}(n_0)\delta n e^{i\mathbf{k}\cdot\mathbf{r}}$ within the LDA approximation. Thus the total electron potential is $\delta V = \left(\frac{4\pi}{k^2}(\delta N + \delta n) + e''_{\rm XC}(n_0)\delta n\right) e^{i\mathbf{k}\cdot\mathbf{r}}$. Then by definition of $\chi_{\rm KS}$, $\delta n = \chi_{\rm KS}(k)\delta V$, so that

$$\begin{aligned} \delta n &= \chi_{\rm KS}(k)\delta V \\ &= \chi_{\rm KS}(k)\left(\frac{4\pi}{k^2}(\delta N + \delta n) + e''_{\rm XC}(n_0)\delta n\right) \\ \Rightarrow \delta n &= \frac{\chi_{\rm KS}(k)\frac{4\pi}{k^2}}{1 - \chi_{\rm KS}(k)\left(\frac{4\pi}{k^2} + e''_{\rm XC}(n_0)\right)}\delta N \end{aligned}$$

Now, consider a displacement field of the nuclear charge distribution, $\mathbf{x}e^{i\mathbf{k}\cdot\mathbf{r}}$. This essentially produces a dipole density $-n_0\mathbf{x}e^{i\mathbf{k}\cdot\mathbf{r}}$ (minus sign due to electron-is-positive convention). The corresponding nuclear charge density is $\delta N e^{i\mathbf{k}\cdot\mathbf{r}} = -\nabla\cdot(-n_0\mathbf{x}e^{i\mathbf{k}\cdot\mathbf{r}}) = i\mathbf{k}\cdot\mathbf{x}n_0 e^{i\mathbf{k}\cdot\mathbf{r}}$. The restoring force on the nuclei is due to the total electric field of the system and hence $-\left(-\nabla\frac{4\pi}{k^2}(\delta n + \delta N)e^{i\mathbf{k}\cdot\mathbf{r}}\right) = i\mathbf{k}\frac{4\pi}{k^2}(\delta n + \delta N)$. (First minus sign due to negative charge of nuclei, second sign for electric field from potential.)

Additionally, let the background jelly be intrinsically elastic with Young's modulus $Y$ and Poisson's ratio $\nu$. This implies a shear modulus $Y/2(1+\nu)$ and Bulk modulus $Y/3(1-2\nu)$. The strain tensor, $e_{ij} = \frac{1}{2}(\partial_i u_j + \partial_j u_i)$ in terms of the displacement field $u_i = x_i e^{i\mathbf{k}\cdot\mathbf{r}}$. Therefore $e_{ij} = \frac{i}{2}(x_i k_j + x_j k_i)e^{i\mathbf{k}\cdot\mathbf{r}}$. In terms of standard eleasticity theory for isotropic media, the stress tensor is then $\sigma_{ij} = \lambda e_{kk}\delta_{ij} + 2\mu e_{ij}$, where $\lambda = \frac{Y}{3(1-2\nu)} - \frac{2}{3}\frac{Y}{2(1+\nu)} = \frac{Y\nu}{(1+\nu)(1-2\nu)}$ and $\mu = \frac{Y}{2(1+\nu)}$.

Finally, the force per particle is

$$\begin{aligned}
\frac{1}{n_0}\partial_j\sigma_{ij} &= \frac{1}{n_0}\partial_j(\lambda e_{kk}\delta_{ij} + 2\mu e_{ij}) \\
&= \frac{i}{n_0}\partial_j(\lambda x_k k_k \delta_{ij} + \mu(x_i k_j + x_j k_i))e^{i\mathbf{k}\cdot\mathbf{r}} \\
&= -\frac{1}{n_0}(\lambda x_k k_k \delta_{ij} k_j + \mu(x_i k_j k_j + x_j k_i k_j))e^{i\mathbf{k}\cdot\mathbf{r}} \\
&= -\frac{1}{n_0}(\lambda x_j k_j k_i + \mu(x_j \delta_{ij} k^2 + x_j k_i k_j))e^{i\mathbf{k}\cdot\mathbf{r}} \\
&= -\frac{1}{n_0}((\lambda+\mu)k_i k_j + \mu k^2 \delta_{ij})x_j e^{i\mathbf{k}\cdot\mathbf{r}}
\end{aligned}$$

The equation of motion of nuclear background oscillations is therefore:

$$\begin{aligned}
M\ddot{x}_i &= ik_i\frac{4\pi}{k^2}(\delta n + \delta N) - \frac{1}{n_0}((\lambda+\mu)k_i k_j + \mu k^2\delta_{ij})x_j \\
&= ik_i\frac{4\pi}{k^2}\left(\frac{\chi_{\mathrm{KS}}(k)\frac{4\pi}{k^2}}{1-\chi_{\mathrm{KS}}(k)\left(\frac{4\pi}{k^2}+e''_{\mathrm{XC}}(n_0)\right)}+1\right)\delta N - \frac{1}{n_0}((\lambda+\mu)k_i k_j + \mu k^2\delta_{ij})x_j \\
&= ik_i\left(\frac{1}{\frac{k^2}{4\pi}-\frac{\chi_{\mathrm{KS}}(k)}{1-\chi_{\mathrm{KS}}(k)e''_{\mathrm{XC}}(n_0)}}\right)ik_j x_j n_0 - \frac{1}{n_0}\left(\frac{Y}{2(1+\nu)(1-2\nu)}k_i k_j + \frac{Y}{2(1+\nu)}k^2\delta_{ij}\right)x_j \\
\ddot{x}_i &= -\left[\left(\frac{n_0/M}{\frac{k^2}{4\pi}-\frac{\chi_{\mathrm{KS}}(k)}{1-\chi_{\mathrm{KS}}(k)e''_{\mathrm{XC}}(n_0)}}+\frac{\mu}{(1-2\nu)n_0 M}\right)k_i k_j + \frac{\mu}{n_0 M}k^2\delta_{ij}\right]x_j \\
&= -\left[\underbrace{\left(\frac{n_0/M}{\frac{k^2}{4\pi}-\frac{\chi_{\mathrm{KS}}(k)}{1-\chi_{\mathrm{KS}}(k)e''_{\mathrm{XC}}(n_0)}}+\frac{v_T^2}{1-2\nu}\right)}_{A}k_i k_j + v_T^2 k^2\delta_{ij}\right]x_j \left(v_T \equiv \sqrt{\frac{\mu}{n_0 M}}\right)
\end{aligned}$$

Diagonalizing this matrix reveals normal mode frequencies $\omega^2 = v_T^2k^2, v_T^2k^2, (v_T^2+A)k^2$, where the first two are transverse modes ($x \perp k$) and the last one is longitudinal ($x > k$). The transverse modes have linear dispersion with transverse sound velocity $v_T$ by construction, and the longitudinal

mode has dispersion:

$$\begin{aligned}
\omega_{\rm ph}(k) &= k\sqrt{\frac{4\pi n_0}{M\left(k^2-\frac{4\pi\chi_{\rm KS}(k)}{1-\chi_{\rm KS}(k)e''_{\rm XC}(n_0)}\right)}+\frac{v_T^2}{1-2\nu}+v_T^2} \\
v_L=\omega'_{\rm ph}(0) &= \sqrt{\frac{4\pi n_0}{M\left(\frac{-4\pi(-k_F/\pi^2)}{1-(-k_F/\pi^2)e''_{\rm XC}(n_0)}\right)}+\frac{2v_T^2(1-\nu)}{1-2\nu}} \\
&\approx \sqrt{\frac{\pi^2 n_0}{k_F M}+\frac{2v_T^2(1-\nu)}{1-2\nu}}(\text{Neglecting XC : TDDFT}\to\text{RPA}) \\
&= \sqrt{\frac{k_F^2}{3M}+\frac{2v_T^2(1-\nu)}{1-2\nu}}=\sqrt{\frac{v_F^2}{3M}+\frac{2v_T^2(1-\nu)}{1-2\nu}}(\text{since}\,\hbar=1)
\end{aligned}$$

For real metals, we can now select the Poisson ratio $\nu$ of the background to match the transverse and longitudinal sound velocities:

| Metal | $\varepsilon_F$ [eV] | $v_F$ [km/s] | Expt $v_T$ [km/s] | Expt $v_L$ [km/s] | $\nu$ fit |
|---|---|---|---|---|---|
| Gold | 9. | 1800 | 1.20 | 3.24 | 0.38 |
| Silver | 9. | 1800 | 1.61 | 3.65 | 0.26 |

## D.2 Electron-electron scattering

The electron scattering process $1+2\to 3+4$ involves the diagrams:

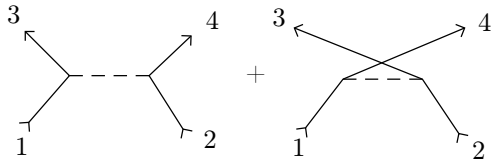


The virtual photon line has energy-momentum $\varepsilon_1-\varepsilon_3, \mathbf{k}_1-\mathbf{k}_3$ in the first diagram, and $\varepsilon_1-\varepsilon_4, \mathbf{k}_1-\overrightarrow{k}_4$ in the second diagram. The photon propagator is simply the screened Coulomb operator $K(\mathbf{q},\omega)=\frac{4\pi}{q^2\epsilon(q,\omega)}$. Define $K_{ij}\equiv K(\mathbf{k}_i-\mathbf{k}_j,\varepsilon_i-\varepsilon_j)$; note that $K_{13}=K_{24}$ and $K_{14}=K_{23}$ using energy and momentum conservation and the fact that $K(-\mathbf{q},\omega)=K(\mathbf{q},\omega)$. Then using the

Feynman rules for non-relativistic QED:

$$
\begin{aligned}
\mathcal{M} &= i[\delta_{s_1 s_3} K_{13} \delta_{s_2 s_4} - \delta_{s_1 s_4} K_{14} \delta_{s_2 s_3}] \\
\Gamma_1 &= 2\pi \sum_{s_2 s_3 s_4} \int \frac{d\mathbf{k}_2}{(2\pi)^3} \frac{d\mathbf{k}_3}{(2\pi)^3} \frac{d\mathbf{k}_4}{(2\pi)^3} f_2(1-f_3)(1-f_4)\delta(\varepsilon_1+\varepsilon_2-\varepsilon_3-\varepsilon_4)(2\pi)^3\delta(\mathbf{k}_1+\mathbf{k}_2-\mathbf{k}_3-\mathbf{k}_4)|\mathcal{M}|^2 \\
&= 2\pi \int \frac{d\mathbf{k}_2}{(2\pi)^3} \frac{d\mathbf{k}_3}{(2\pi)^3} f_2(1-f_3)(1-f_4)\delta(\varepsilon_1+\varepsilon_2-\varepsilon_3-\varepsilon_4) \sum_{s_2 s_3 s_4} |\delta_{s_1 s_3} K_{13} \delta_{s_2 s_4} - \delta_{s_1 s_4} K_{23} \delta_{s_2 s_3}|^2 \\
&\quad \text{(assuming all distributions and hence } f's \text{ are always spin balanced)} \\
&= 2\pi \int \frac{d\mathbf{k}_2}{(2\pi)^3} \frac{d\mathbf{k}_3}{(2\pi)^3} f_2(1-f_3)(1-f_4)\delta(\varepsilon_1+\varepsilon_2-\varepsilon_3-\varepsilon_4)[2|K_{13}|^2 + 2|K_{23}|^2 - 2\,\mathrm{Re}(K_{13}K_{23}^*)] \\
&= 4\pi \int \frac{d\mathbf{k}_2}{(2\pi)^3} \frac{d\mathbf{k}_3}{(2\pi)^3} f_2(1-f_3)(1-f_4)\delta(\varepsilon_1+\varepsilon_2-\varepsilon_3-\varepsilon_4)[|K_{13}|^2 + |K_{23}|^2 - \mathrm{Re}(K_{13}K_{23}^*)]
\end{aligned}
$$

Now for calculating the screened Coulomb interaction $K(q,\omega)$, we need $\epsilon(q,\omega)$, which in turn we get from $\chi_{\rm KS}(q,\omega)$ defined before.

$$
\begin{aligned}
V_{\rm out}(q,\omega) &\equiv \epsilon^{-1}(q,\omega)V_{\rm in}(q,\omega)\\
V_{\rm out}(q,\omega) &= V_{\rm in}(q,\omega)+\frac{4\pi}{q^2}\chi(q,\omega)V_{\rm in}(q,\omega)\\
&= \left[1+\frac{4\pi}{q^2}\frac{\chi_{\rm KS}(q,\omega)}{1-\chi_{\rm KS}(q,\omega)\left(\frac{4\pi}{q^2}+e^{''}_{\rm XC}(n_0)\right)}\right]V_{\rm in}(q,\omega)(\text{RPA like relation of TDDFT})\\
\epsilon^{-1}(q,\omega) &= 1+\frac{\chi_{\rm KS}(q,\omega)\frac{4\pi}{q^2}}{1-\chi_{\rm KS}(q,\omega)\left(\frac{4\pi}{q^2}+e^{''}_{\rm XC}(n_0)\right)}\\
&= \frac{1-\chi_{\rm KS}(q,\omega)e^{''}_{\rm XC}(n_0)}{1-\chi_{\rm KS}(q,\omega)e^{''}_{\rm XC}(n_0)-\chi_{\rm KS}(q,\omega)\frac{4\pi}{q^2}}\\
\epsilon(q,\omega) &= 1-\frac{4\pi/q^2}{\chi^{-1}_{\rm KS}(q,\omega)-e^{''}_{\rm XC}(n_0)}
\end{aligned}
$$

$$
\begin{aligned}
\chi_{\rm KS}(q,\omega) &= -2\int\frac{d\mathbf{k}}{(2\pi)^3}\frac{f_{\mathbf{k}}-f_{\mathbf{q}+\mathbf{k}}}{(\mathbf{q}+\mathbf{k})^2/2-k^2/2-\omega}\\
&= -2\int\frac{d\mathbf{k}}{(2\pi)^3}\frac{f_{\mathbf{k}}(1-f_{\mathbf{q}+\mathbf{k}})-f_{\mathbf{q}+\mathbf{k}}(1-f_{\mathbf{k}})}{(\mathbf{q}+\mathbf{k})^2/2-k^2/2-\omega}\\
&= -2\int\frac{d\mathbf{k}}{(2\pi)^3}\left[\frac{f_{\mathbf{k}}(1-f_{\mathbf{q}+\mathbf{k}})}{(\mathbf{q}+\mathbf{k})^2/2-k^2/2-\omega}-\frac{f_{\mathbf{k}}(1-f_{\mathbf{q}+\mathbf{k}})}{k^2/2-(\mathbf{q}+\mathbf{k})^2/2-\omega}\right]\\
&\quad(\text{swapping }\mathbf{k}\leftrightarrow\mathbf{k}+\mathbf{q}\text{ in second term})\\
&= -4\int\frac{d\mathbf{k}}{(2\pi)^3}f_{\mathbf{k}}(1-f_{\mathbf{q}+\mathbf{k}})\frac{(\mathbf{q}+\mathbf{k})^2/2-k^2/2}{((\mathbf{q}+\mathbf{k})^2/2-k^2/2)^2-\omega^2}\\
&= -\frac{4}{(2\pi)^2}\int_0^\infty k_\rho{\rm d}k_\rho\int_{-\infty}^{+\infty}{\rm d}k_z f_{\varepsilon_F}\left(\frac{k_\rho^2+k_z^2}{2}\right)\left(1-f_{\varepsilon_F}\left(\frac{k_\rho^2+(k_z+q)^2}{2}\right)\right)\frac{q^2/2+qk_z}{(q^2/2+qk_z)^2-\omega^2}\\
&\quad(\text{cylindrical coordinates for }k\text{ with axis along }q)\\
&= -\frac{1}{\pi^2}\int_{-\infty}^{+\infty}{\rm d}k_z\frac{q^2/2+qk_z}{(q^2/2+qk_z)^2-\omega^2}g(k_z,q)
\end{aligned}
$$

$$
\begin{aligned}
g(k_z,q) &\equiv \int_0^\infty k_\rho{\rm d}k_\rho f_{\varepsilon_F}\left(\frac{k_\rho^2+k_z^2}{2}\right)\left(1-f_{\varepsilon_F}\left(\frac{k_\rho^2+(k_z+q)^2}{2}\right)\right)\\
&= \int_0^\infty\frac{{\rm d}k_\rho^2}{2}\theta(k_F^2-k_z^2-k_\rho^2)\theta(k_\rho^2+(k_z+q)^2-k_F^2)(T\to 0\,\text{occupations})\\
&= \frac{\theta(k_F^2-k_z^2+(k_z+q)^2-k_F^2)}{2}\int_{\max(0,k_F^2-(k_z+q)^2)}^{\max(0,k_F^2-k_z^2)}{\rm d}k_\rho^2\\
&= \frac{\theta(k_z+q/2)}{2}[\max(0,k_F^2-k_z^2)-\max(0,k_F^2-(k_z+q)^2)](\text{too many cases to list explicitly})
\end{aligned}
$$



$$
\begin{aligned}
\chi_{\rm KS}(q,\omega) &= -\frac{1}{\pi^2}\int_{-\infty}^{+\infty}{\rm d}k_z\frac{q^2/2+qk_z}{(q^2/2+qk_z)^2-\omega^2}\frac{\theta(k_z+q/2)}{2}[\max(0,k_F^2-k_z^2)-\max(0,k_F^2-(k_z+q)^2)]\\
&= -\frac{q}{2\pi^2}\int_0^\infty{\rm d}y\frac{y}{q^2y^2-\omega^2}[\max(0,k_F^2-(y-q/2)^2)-\max(0,k_F^2-(y+q/2)^2)](y\equiv q/2+k_z)\\
&= -\frac{k_F}{\pi^2}\int_0^\infty{\rm d}Y\frac{Y^2}{Y^2-W^2}\underbrace{\left[\frac{\max(0,1-(Y-Q)^2)-\max(0,1-(Y+Q)^2)}{4QY}\right]}_{\equiv h(Y,Q)}
\end{aligned}
$$

The integral is divergent as written, and needs to be regularized as usual with $\omega \to \omega + i\delta$. Taking the limit $\delta \to 0$ after regularizing leaves behind the principal part of the above integral in the real contrbution along with an imaginary part. There are 6 cases in total, for the three ranges of $W$ for each of the two $Q$ cases. The integrals are analytically solvable in all cases (Mathematica), and can be collected together as:

$$\chi_{\rm KS}(q,\omega) = -\frac{k_F}{\pi^2}\left[\frac{1}{2} + \frac{\begin{array}{c}(1-(Q-W)^2)\log\left|\frac{Q-W+1}{Q-W-1}\right| + (1-(Q+W)^2)\log\left|\frac{Q+W+1}{Q+W-1}\right| \\ +i\pi[\min(1,(Q+W)^2) - \min(1,(Q-W)^2)]\end{array}}{8Q}\right]$$

## D.3 Electron-phonon scattering

Consider the matrix element fo the process: electron($\mathbf{k}$)+phonon($\mathbf{q}$)→electron($\mathbf{k}+\mathbf{q}$). The longitudinal phonon has a nuclear charge density $\frac{iqn_0}{\sqrt{\omega_q}}e^{i\mathbf{q}\cdot\mathbf{r}}$, with the denominator appearing due to the mode normaliztaion of a phonon quantum. With a longitudinal sound velocity $v_L$, $\omega_q \approx v_L q$ for small $q$, so that the effective nuclear charge density is $\delta N = in_0\sqrt{\frac{q}{v_L}}e^{i\mathbf{q}\cdot\mathbf{r}}$. The net electrostatic potential due to the phonon is:

$$\begin{aligned}
V^{\mathbf{q}}_{\rm ph}(\mathbf{r}) &= \frac{4\pi}{k^2}(\delta N + \delta n) \\
&= \frac{4\pi}{q^2}\left(\delta N + \frac{\chi_{\rm KS}(q)\frac{4\pi}{q^2}}{1-\chi_{\rm KS}(q)\left(\frac{4\pi}{q^2} + e''_{\rm XC}(n_0)\right)}\delta N\right) \\
&= \left(\frac{q^2}{4\pi} + (e''_{\rm XC}(n_0) - \chi^{-1}_{\rm KS}(q))^{-1}\right)^{-1}\delta N \\
&\approx \left(e''_{\rm XC}(n_0) + \frac{\pi^2}{k_F}\right)\delta N (\text{For small } q) \\
&= \left(e''_{\rm XC}(n_0) + \frac{\pi^2}{k_F}\right) in_0\sqrt{\frac{q}{v_L}}e^{i\mathbf{q}\cdot\mathbf{r}} \\
M_{e-\rm ph} &= \int d\mathbf{r}\psi^*_{\mathbf{k}+\mathbf{q}}(r)V^{\mathbf{q}}_{\rm ph}(\mathbf{r})\psi_{\mathbf{k}}(r) \\
&= \left(e''_{\rm XC}(n_0) + \frac{\pi^2}{k_F}\right) in_0\sqrt{\frac{q}{v_L}} (\psi' s \text{ are plane waves})
\end{aligned}$$

Thus $|M_{e-\rm ph}|^2 \propto q$ for small $q$, which cancels the $1/\omega_{\mathbf{q}}$ divergence in the Bose factors.

Now consider the Fermi golden rule expression for the total scattering rate of state $i$ (using the same notation as the phonon-assisted derivation, but eliminating the plasmon):

$$\begin{aligned}
\Gamma_{\text{abs}}^{e-\text{ph}} &= \frac{2\pi}{\hbar}\sum_{q_j b_j;\mathbf{k}\alpha}(1-f_{\mathbf{q}_j b_j})\delta\left(\varepsilon_{\mathbf{q}_j b_j}-\varepsilon_{\overrightarrow{q_i} b_i}-\hbar\omega_{\mathbf{k}\alpha}\right)\left|\boldsymbol{M}^{\mathbf{k}\alpha}_{\overrightarrow{q_i} b_i,\mathbf{q}_j b_j}\right|^2 \\
&= \frac{\pi}{N_{\mathbf{R}}}\sum_{q_j b_j;\alpha}(1-f_{\mathbf{q}_j b_j})n^{(\mathbf{q}_j-\mathbf{q}_i)\alpha}\frac{\delta\left(\varepsilon_{\mathbf{q}_j b_j}-\varepsilon_{\overrightarrow{q_i} b_i}-\hbar\omega_{(\mathbf{q}_j-\mathbf{q}_i)\alpha}\right)}{\hbar\omega_{(\mathbf{q}_j-\mathbf{q}_i)\alpha}}\left|M^{(\mathbf{q}_j-\mathbf{q}_i)\alpha}_{\overrightarrow{q_i} b_i,\mathbf{q}_j b_j}\right|^2 \\
&= \pi\Omega\sum_{b_j\alpha}\int\frac{d\mathbf{q}}{(2\pi)^3}(1-f_{\mathbf{q}_j b_j})n^{(\mathbf{q}_j-\mathbf{q}_i)\alpha}\frac{\delta\left(\varepsilon_{\mathbf{q}_j b_j}-\varepsilon_{\overrightarrow{q_i} b_i}-\hbar\omega_{(\mathbf{q}_j-\mathbf{q}_i)\alpha}\right)}{\hbar\omega_{(\mathbf{q}_j-\mathbf{q}_i)\alpha}}\left|M^{(\mathbf{q}_j-\mathbf{q}_i)\alpha}_{\overrightarrow{q_i} b_i,\mathbf{q}_j b_j}\right|^2 \\
\Gamma_{\text{emit}}^{e-\text{ph}} &= \pi\Omega\sum_{b_j\alpha}\int\frac{d\mathbf{q}}{(2\pi)^3}(1-f_{\mathbf{q}_j b_j})(n^{-(\mathbf{q}_j-\mathbf{q}_i)\alpha}+1)\frac{\delta\left(\varepsilon_{\mathbf{q}_j b_j}-\varepsilon_{\overrightarrow{q_i} b_i}+\hbar\omega_{-(\mathbf{q}_j-\mathbf{q}_i)\alpha}\right)}{\hbar\omega_{-(\mathbf{q}_j-\mathbf{q}_i)\alpha}}\left|M^{-(\mathbf{q}_j-\mathbf{q}_i)\alpha}_{\overrightarrow{q_i} b_i,\mathbf{q}_j b_j}\right|^2
\end{aligned}$$

Next assume that $\left|M^{-(\mathbf{q}_j-\mathbf{q}_i)\alpha}_{\overrightarrow{q_i} b_i,\mathbf{q}_j b_j}\right|^2 = M^2(k)$ where $k \equiv |\mathbf{q}_j-\mathbf{q}_i|$ i.e. it depends only on the phonon wave-vector, and for simplicity, assume a single acoustic phonon branch (lump the contributions into a single branch) with $\omega_q = v_L q$. Finally, neglect the energy of the phonon on the electronic scale, so that the absorption and emission processes couple to almost the same electronic state. Then the total rate is:

$$\begin{aligned}
\Gamma_{e-\text{ph}} &= \sum_{b_j}\int\frac{\Omega d\mathbf{q}}{(2\pi)^3}(1-f_{\mathbf{q}_j b_j})\delta\left(\varepsilon_{\mathbf{q}_j b_j}-\varepsilon_{\overrightarrow{q_i} b_i}\right)\underbrace{\frac{\pi(2n_k+1)}{\hbar v_L k}M^2(k)}_{\equiv M_0^2} \\
&= M_0^2 g\left(\varepsilon_{\overrightarrow{q_i} b_i}\right)
\end{aligned}$$

where $g(\varepsilon)$ is the density of states in the unit cell. From the drude model, close to the Fermi energy, $\Gamma_{e-\text{ph}} = n_0\rho$ in atomic units, where $\rho$ is the resistivity. Therefore, $M_0 = \sqrt{n_0\rho/g(\varepsilon_F)}$.

Now making the same approximations for the phonon-assisted plasmon decay, and additionally making the phonon-first and plasmon-first processes incoherent (since we don't have the phase for

the phonon matrix element; this sort of requires the phonon to behave classically and not interfere):

$$
\begin{aligned}
\Gamma &= \frac{\pi^2 e^2 \hbar^2}{4m_e^2 \Omega |\gamma_-| \omega_{\rm sp} L(\omega_{\rm sp})} \sum_{b_i b_j} \frac{1}{N_{\mathbf{k}}^2} \sum_{q_i q_j} f_{\overrightarrow{q_i} b_i} (1 - f_{\mathbf{q}_j b_j}) \delta \left( \varepsilon_{\mathbf{q}_j b_j} - \varepsilon_{\overrightarrow{q_i} b_i} - \hbar\omega_{\rm sp} \right) \frac{2n_k + 1}{v_L k} M^2(k) \\
&\quad \times \left( \left| \sum_{b_l} \left( 1 - f_{\overrightarrow{q_j}, b_l} \right) \frac{\left( \hat{\mathbf{k}}_{\rm sp} - \frac{k_{\rm sp}}{\gamma_-} \hat{\mathbf{z}} \right) \cdot \langle i \partial_{\mathbf{r}} \rangle_{b_j b_l}^{\mathbf{q}_j}}{\varepsilon_{\overrightarrow{q}_j b_l} - \varepsilon_{\overrightarrow{q}_i b_i}} \right|^2 + \left| \sum_{b_l} (1 - f_{\mathbf{q}_i, b_l}) \frac{\left( \hat{\mathbf{k}}_{\rm sp} - \frac{k_{\rm sp}}{\gamma_-} \hat{\mathbf{z}} \right) \cdot \langle i \partial_{\mathbf{r}} \rangle_{b_l b_i}^{\mathbf{q}_i}}{\varepsilon_{\mathbf{q}_i b_l} - (\varepsilon_{\mathbf{q}_i b_i} + \hbar\omega_{\rm sp})} \right|^2 \right) \\
\Gamma &= \frac{\pi e^2 \hbar^3 M_0^2}{4m_e^2 \Omega |\gamma_-| \omega_{\rm sp} L(\omega_{\rm sp})} \sum_{b_i b_j} \frac{1}{N_{\mathbf{k}}^2} \sum_{q_i q_j} f_{\overrightarrow{q_i} b_i} (1 - f_{\mathbf{q}_j b_j}) \delta \left( \varepsilon_{\mathbf{q}_j b_j} - \varepsilon_{\overrightarrow{q_i} b_i} - \hbar\omega_{\rm sp} \right) \\
&\quad \times \left( \left| \sum_{b_l} \left( 1 - f_{\overrightarrow{q_j}, b_l} \right) \frac{\left( \hat{\mathbf{k}}_{\rm sp} - \frac{k_{\rm sp}}{\gamma_-} \hat{\mathbf{z}} \right) \cdot \langle i \partial_{\mathbf{r}} \rangle_{b_j b_l}^{\mathbf{q}_j}}{\varepsilon_{\overrightarrow{q}_j b_l} - \varepsilon_{\overrightarrow{q}_i b_i}} \right|^2 + \left| \sum_{b_l} (1 - f_{\mathbf{q}_i, b_l}) \frac{\left( \hat{\mathbf{k}}_{\rm sp} - \frac{k_{\rm sp}}{\gamma_-} \hat{\mathbf{z}} \right) \cdot \langle i \partial_{\mathbf{r}} \rangle_{b_l b_i}^{\mathbf{q}_i}}{\varepsilon_{\mathbf{q}_i b_l} - (\varepsilon_{\mathbf{q}_i b_i} + \hbar\omega_{\rm sp})} \right|^2 \right) \\
&= \sum_{b_i b_j} \frac{1}{N_{\mathbf{k}}^2} \sum_{q_i q_j} f_{\overrightarrow{q_i} b_i} (1 - f_{\mathbf{q}_j b_j}) \delta \left( \varepsilon_{\mathbf{q}_j b_j} - \varepsilon_{\overrightarrow{q_i} b_i} - \hbar\omega_{\rm sp} \right) \\
&\quad \times \left( \left| \sum_{b_l} \left( 1 - f_{\overrightarrow{q_j}, b_l} \right) \frac{\mathbf{S}_\Gamma \cdot \langle i \partial_{\mathbf{r}} \rangle_{b_j b_l}^{\mathbf{q}_j}}{\varepsilon_{\overrightarrow{q}_j b_l} - \varepsilon_{\overrightarrow{q}_i b_i}} \right|^2 + \left| \sum_{b_l} (1 - f_{\mathbf{q}_i, b_l}) \frac{\mathbf{S}_\Gamma \cdot \langle i \partial_{\mathbf{r}} \rangle_{b_l b_i}^{\mathbf{q}_i}}{\varepsilon_{\mathbf{q}_i b_l} - (\varepsilon_{\mathbf{q}_i b_i} + \hbar\omega_{\rm sp})} \right|^2 \right) \\
\mathbf{S}_\Gamma &\equiv \sqrt{\frac{\pi M_0^2}{4\Omega |\gamma_-| \omega_{\rm sp} L(\omega_{\rm sp})}} \left( \hat{\mathbf{k}}_{\rm sp} - \frac{k_{\rm sp}}{\gamma_-} \hat{\mathbf{z}} \right) \text{ (sqrtGammaPrefac in atomic units)}
\end{aligned}
$$

Note that in the Metropolis implementation, $\mathbf{S}_\Gamma$ has an additional factor of $\sqrt{N_1/N_{\rm kpts}}$.

# Appendix E

# Phonon Vertex

For a phonon mode $\alpha\mathbf{k}$, we have displacements $x_{\mathbf{R}s} = X_s^{\alpha\mathbf{k}} e^{i\mathbf{k}\cdot\mathbf{R}}$ for the d.o.f $s$ in unit cell located at $\mathbf{R}$. The initial Hamiltonian is:

$$
\begin{aligned}
H &= \sum_{\mathbf{R}s} \frac{p_{\mathbf{R}s}^2}{2m_s} + \frac{1}{2} \sum_{\mathbf{R}s;\mathbf{R}'s'} x_{\mathbf{R}s} G_{ss'}(\mathbf{R}-\mathbf{R}') x_{\mathbf{R}'s'} \\
\text{Let } x_{\mathbf{R}s} &= \sum_{\alpha\mathbf{k}} X^{\alpha\mathbf{k}} \frac{f_{\alpha s}^{\mathbf{k}}}{\sqrt{m_s}} \frac{e^{i\mathbf{k}\cdot\mathbf{R}}}{\sqrt{N_{\mathbf{R}}}} (\text{where } f^{\mathbf{k}} \text{ is some unitary matrix}) \\
p_{\mathbf{R}s} &= \sum_{\alpha\mathbf{k}} P^{\alpha\mathbf{k}} \sqrt{m_s} f_{\alpha s}^{\mathbf{k}} \frac{e^{-i\mathbf{k}\cdot\mathbf{R}}}{\sqrt{N_{\mathbf{R}}}} (\text{canonical transformation so that } X \text{ and } P \text{ are conjugate}) \\
H &= \frac{1}{2} \sum_{\alpha\mathbf{k},\alpha'\overrightarrow{k'}} P^{\alpha\mathbf{k}} P^{\alpha'\mathbf{k}'} \sum_s f_{\alpha s}^{\mathbf{k}} f_{\alpha' s}^{\mathbf{k}'} \sum_{\mathbf{R}} \frac{e^{-i\mathbf{k}'\cdot\mathbf{R}} e^{-i\mathbf{k}\cdot\mathbf{R}}}{N_{\mathbf{R}}} \\
&\quad + \frac{1}{2} \sum_{\alpha\mathbf{k},\alpha'\overrightarrow{k'}} \sum_{\mathbf{R}s;\mathbf{R}'s'} X^{\alpha\mathbf{k}} X^{\alpha'\mathbf{k}'} f_{\alpha s}^{\mathbf{k}} f_{\alpha' s'}^{\mathbf{k}'} \frac{G_{ss'}(\mathbf{R}-\mathbf{R}')}{\sqrt{m_s m_{s'}}} \frac{e^{i\mathbf{k}'\cdot\mathbf{R}'} e^{i\mathbf{k}\cdot\mathbf{R}}}{N_{\mathbf{R}}} \\
&= \frac{1}{2} \sum_{\alpha\mathbf{k},\alpha'\overrightarrow{k'}} P^{\alpha\mathbf{k}} P^{\alpha'\mathbf{k}'} \sum_s f_{\alpha s}^{\mathbf{k}} f_{\alpha' s}^{\mathbf{k}'} \delta_{\mathbf{k},-\mathbf{k}'} + \frac{1}{2} \sum_{\alpha\mathbf{k},\alpha'\overrightarrow{k'}} \delta_{\mathbf{k},-\mathbf{k}'} X^{\alpha\mathbf{k}} X^{\alpha'\mathbf{k}'} \sum_{ss'} f_{\alpha s}^{\mathbf{k}} \frac{F_{ss'}(\mathbf{k}')}{\sqrt{m_s m_{s'}}} f_{\alpha' s'}^{\mathbf{k}'} \\
&= \frac{1}{2} \sum_{\alpha\alpha'\mathbf{k}} P^{\alpha\mathbf{k}} P^{\alpha'-\mathbf{k}} \sum_s f_{\alpha s}^{\mathbf{k}} f_{\alpha' s}^{-\mathbf{k}} + \frac{1}{2} \sum_{\alpha\alpha'\mathbf{k}} X^{\alpha\mathbf{k}} X^{\alpha'-\mathbf{k}} \sum_{ss'} f_{\alpha s}^{\mathbf{k}} \frac{F_{ss'}(-\mathbf{k})}{\sqrt{m_s m_{s'}}} f_{\alpha' s'}^{-\mathbf{k}}
\end{aligned}
$$

At this stage, pick the unitary matrix $f^{\mathbf{k}}$ to be the set of eigenvectors of $\frac{F_{ss'}(\mathbf{k})}{\sqrt{m_s m_{s'}}}$ with eigenvalues $\omega_{\mathbf{k}\alpha}^2$, so that $\sum_{s'} \frac{F_{ss'}(\mathbf{k})}{\sqrt{m_s m_{s'}}} f_{\alpha s'}^{\mathbf{k}} = \omega_{\mathbf{k}\alpha}^2 f_{\alpha s}^{\mathbf{k}}$ by definition. Also note that $G$ is real $\Rightarrow F(-\mathbf{k}) = F^*(\mathbf{k})$

and hence $f^{-\mathbf{k}} = f^{\mathbf{k}*}$ as well as $\omega_{\mathbf{k}\alpha} = \omega_{-\mathbf{k}\alpha}$. Continuing the simplification:

$$\begin{aligned}
H &= \frac{1}{2}\sum_{\alpha\alpha'\mathbf{k}} P^{\alpha\mathbf{k}}P^{\alpha'-\mathbf{k}}\sum_s f^{\mathbf{k}}_{\alpha s}f^{-\mathbf{k}}_{\alpha' s} + \frac{1}{2}\sum_{\alpha\alpha'\mathbf{k}} X^{\alpha\mathbf{k}}X^{\alpha'-\mathbf{k}}\sum_s f^{\mathbf{k}}_{\alpha s}\omega^2_{-\mathbf{k}\alpha'}f^{-\mathbf{k}}_{\alpha' s} \\
&= \frac{1}{2}\sum_{\alpha\alpha'\mathbf{k}} [P^{\alpha\mathbf{k}}P^{\alpha'-\mathbf{k}} + \omega^2_{\mathbf{k}\alpha'}X^{\alpha\mathbf{k}}X^{\alpha'-\mathbf{k}}]\sum_s f^{\mathbf{k}}_{\alpha s}f^{\mathbf{k}*}_{\alpha' s} \\
&= \frac{1}{2}\sum_{\alpha\alpha'\mathbf{k}} [P^{\alpha\mathbf{k}}P^{\alpha'-\mathbf{k}} + \omega^2_{\mathbf{k}\alpha'}X^{\alpha\mathbf{k}}X^{\alpha'-\mathbf{k}}]\delta_{\alpha\alpha'} \\
&= \frac{1}{2}\sum_{\alpha\mathbf{k}} [P^{\alpha\mathbf{k}}P^{\alpha-\mathbf{k}} + \omega^2_{\mathbf{k}\alpha}X^{\alpha\mathbf{k}}X^{\alpha-\mathbf{k}}]
\end{aligned}$$

which is a set of Harmonic oscillators with unit mass and frequencies $\omega^2_{\mathbf{k}\alpha}$. It is a little strange in the way the $\mathbf{k}$ and $-\mathbf{k}$ combine instead of having complex conjugates, but we can deal with that in the quantization with a slight modification to the substitution of the ladder operators:

$$\begin{aligned}
X^{\alpha\mathbf{k}} &= \frac{1}{\sqrt{2\omega_{\mathbf{k}\alpha}}}(b^\dagger_{\mathbf{k}\alpha} + b_{-\mathbf{k}\alpha}) \\
P^{\alpha\mathbf{k}} &= i\sqrt{\frac{\omega_{\mathbf{k}\alpha}}{2}}(b^\dagger_{\mathbf{k}\alpha} - b_{-\mathbf{k}\alpha}) \\
H &= \frac{1}{2}\sum_{\alpha\mathbf{k}} [P^{\alpha\mathbf{k}}P^{\alpha-\mathbf{k}} + \omega^2_{\mathbf{k}\alpha}X^{\alpha\mathbf{k}}X^{\alpha-\mathbf{k}}] \\
&= \frac{1}{2}\sum_{\alpha\mathbf{k}} \left[-\frac{\omega_{\mathbf{k}\alpha}}{2}(b^\dagger_{\mathbf{k}\alpha} - b_{-\mathbf{k}\alpha})(b^\dagger_{-\mathbf{k}\alpha} - b_{\mathbf{k}\alpha}) + \frac{\omega_{\mathbf{k}\alpha}}{2}(b^\dagger_{\mathbf{k}\alpha} + b_{-\mathbf{k}\alpha})(b^\dagger_{-\mathbf{k}\alpha} + b_{\mathbf{k}\alpha})\right] \\
&= \sum_{\alpha\mathbf{k}} \frac{\omega_{\mathbf{k}\alpha}}{4}[-b^\dagger_{\mathbf{k}\alpha}b^\dagger_{-\mathbf{k}\alpha} + b^\dagger_{\mathbf{k}\alpha}b_{\mathbf{k}\alpha} + b_{-\mathbf{k}\alpha}b^\dagger_{-\mathbf{k}\alpha} - b_{-\mathbf{k}\alpha}b_{\mathbf{k}\alpha} + b^\dagger_{\mathbf{k}\alpha}b^\dagger_{-\mathbf{k}\alpha} + b^\dagger_{\mathbf{k}\alpha}b_{\mathbf{k}\alpha} + b_{-\mathbf{k}\alpha}b^\dagger_{-\mathbf{k}\alpha} + b_{-\mathbf{k}\alpha}b_{\mathbf{k}\alpha}] \\
&= \sum_{\alpha\mathbf{k}} \frac{\omega_{\mathbf{k}\alpha}}{4}[2(b^\dagger_{\mathbf{k}\alpha}b_{\mathbf{k}\alpha} + b_{-\mathbf{k}\alpha}b^\dagger_{-\mathbf{k}\alpha})] \\
&= \sum_{\alpha\mathbf{k}} \frac{\omega_{\mathbf{k}\alpha}}{2}[b^\dagger_{\mathbf{k}\alpha}b_{\mathbf{k}\alpha} + b^\dagger_{-\mathbf{k}\alpha}b_{-\mathbf{k}\alpha} + 1](\text{using commutator}) \\
&= \sum_{\alpha\mathbf{k}} \frac{\omega_{\mathbf{k}\alpha}}{2}[b^\dagger_{\mathbf{k}\alpha}b_{\mathbf{k}\alpha} + b^\dagger_{\mathbf{k}\alpha}b_{\mathbf{k}\alpha} + 1](\text{Replace dummy index } \mathbf{k} \to -\mathbf{k} \text{ in second term}) \\
&= \sum_{\alpha\mathbf{k}} \omega_{\mathbf{k}\alpha}\left[b^\dagger_{\mathbf{k}\alpha}b_{\mathbf{k}\alpha} + \frac{1}{2}\right]
\end{aligned}$$

A brief aside on the electronic states: given the standard unit cell normalized wavefunctions in Bloch form $\psi_{\mathbf{q}b}(\mathbf{r}) = u_{\mathbf{q}b}(\mathbf{r})e^{i\mathbf{q}\cdot\mathbf{r}}$, the properly normalized wavefunctions on the supercell are $\frac{1}{\sqrt{N_{\mathbf{R}}}}\psi_{\mathbf{q}b}(\mathbf{r})$. Then, the many-body real-space annihilation operator (also called the field operator) can be written

as $\Psi(\mathbf{r}) = \sum_{\mathbf{q}b} \frac{1}{\sqrt{N_{\mathbf{R}}}} \psi_{\mathbf{q}b}(\mathbf{r}) c_{\mathbf{q}b}$, where $c_{\mathbf{q}b}$ is the fermionic annihilation operator for state $\mathbf{q}b$. Then the real-space density operator is:

$$\begin{aligned}
\hat{\mathbf{n}}(\mathbf{r}) &= \Psi^\dagger(\mathbf{r})\Psi(\mathbf{r}) \\
&= \sum_{\mathbf{q}b} \frac{1}{\sqrt{N_{\mathbf{R}}}} \psi^*_{\mathbf{q}b}(\mathbf{r}) c^\dagger_{\mathbf{q}b} \sum_{\mathbf{q}'b'} \frac{1}{\sqrt{N_{\mathbf{R}}}} \psi_{\mathbf{q}'b'}(\mathbf{r}) c_{\mathbf{q}'b'} \\
&= \sum_{\mathbf{q}b} \sum_{\mathbf{q}'b'} c^\dagger_{\mathbf{q}b} c_{\mathbf{q}'b'} \frac{\psi^*_{\mathbf{q}b}(\mathbf{r}) \psi_{\mathbf{q}'b'}(\mathbf{r})}{N_{\mathbf{R}}} \\
&= \sum_{\mathbf{q}b} \sum_{\mathbf{q}'b'} c^\dagger_{\mathbf{q}b} c_{\mathbf{q}'b'} \frac{u^*_{\mathbf{q}b}(\mathbf{r}) u_{\mathbf{q}'b'}(\mathbf{r})}{N_{\mathbf{R}}} e^{i(\mathbf{q}'-\mathbf{q})\cdot\mathbf{r}}
\end{aligned}$$

Now consider the interaction hamiltonian between the electrons and phonons, it is the potential due to the shift in nuclei acting on the electrons:

$$\begin{aligned}
H_{e-\mathrm{ph}} &= \sum_{\mathbf{R}s} x_{\mathbf{R}s} \int_{N_{\mathbf{R}}\Omega} \mathrm{d}\mathbf{r} \partial_{\mathbf{R}s} V_{\mathrm{nuc}}(\mathbf{r}) \hat{\mathbf{n}}(\mathbf{r}) \\
&= \sum_{\mathbf{R}s} \sum_{\alpha\mathbf{k}} X^{\alpha\mathbf{k}} \frac{f^{\mathbf{k}}_{\alpha s}}{\sqrt{m_s}} \frac{e^{i\mathbf{k}\cdot\mathbf{R}}}{\sqrt{N_{\mathbf{R}}}} \int_{N_{\mathbf{R}}\Omega} \mathrm{d}\mathbf{r} \partial_{\mathbf{R}s} V_{\mathrm{nuc}}(\mathbf{r}) \sum_{\mathbf{q}b} \sum_{\mathbf{q}'b'} c^\dagger_{\mathbf{q}b} c_{\mathbf{q}'b'} \frac{u^*_{\mathbf{q}b}(\mathbf{r}) u_{\mathbf{q}'b'}(\mathbf{r})}{N_{\mathbf{R}}} e^{i(\mathbf{q}'-\mathbf{q})\cdot\mathbf{r}} \\
&= \frac{1}{N_{\mathbf{R}}^{3/2}} \sum_{\alpha\mathbf{k}} \sum_{\mathbf{q}b} \sum_{\mathbf{q}'b'} X^{\alpha\mathbf{k}} c^\dagger_{\mathbf{q}b} c_{\mathbf{q}'b'} \int_{N_{\mathbf{R}}\Omega} \mathrm{d}\mathbf{r} \underbrace{\sum_{\mathbf{R}s} \frac{f^{\mathbf{k}}_{\alpha s}}{\sqrt{m_s}} e^{i\mathbf{k}\cdot\mathbf{R}} \partial_{\mathbf{R}s} V_{\mathrm{nuc}}(\mathbf{r})}_{\equiv g_{\mathbf{k}\alpha}(\mathbf{r})} u^*_{\mathbf{q}b}(\mathbf{r}) u_{\mathbf{q}'b'}(\mathbf{r}) e^{i(\mathbf{q}'-\mathbf{q})\cdot\mathbf{r}}
\end{aligned}$$

$$\begin{aligned}
g_{\mathbf{k}\alpha}(\mathbf{r}+\mathbf{R}') &= \sum_{\mathbf{R}s} \frac{f^{\mathbf{k}}_{\alpha s}}{\sqrt{m_s}} e^{i\mathbf{k}\cdot\mathbf{R}} \partial_{\mathbf{R}s} V_{\mathrm{nuc}}(\mathbf{r}+\mathbf{R}') \\
&= \sum_{\mathbf{R}s} \frac{f^{\mathbf{k}}_{\alpha s}}{\sqrt{m_s}} e^{i\mathbf{k}\cdot\mathbf{R}} \partial_{(\mathbf{R}+\mathbf{R}')s} V_{\mathrm{nuc}}(\mathbf{r}) \\
&= e^{-i\mathbf{k}\cdot\mathbf{R}'} \sum_{\mathbf{R}s} \frac{f^{\mathbf{k}}_{\alpha s}}{\sqrt{m_s}} e^{i\mathbf{k}\cdot(\mathbf{R}+\mathbf{R}')} \partial_{(\mathbf{R}-\mathbf{R}')s} V_{\mathrm{nuc}}(\mathbf{r}) \\
&= e^{-i\mathbf{k}\cdot\mathbf{R}'} g_{\mathbf{k}\alpha}(\mathbf{r}) \Rightarrow g_{\mathbf{k}\alpha}(\mathbf{r}) \text{ is in Bloch form with wavevector } -\mathbf{k} \\
g_{\mathbf{k}\alpha}(\mathbf{r}) &= h_{\mathbf{k}\alpha}(\mathbf{r}) e^{-i\mathbf{k}\cdot\mathbf{r}} (\text{with } h_{\mathbf{k}\alpha}(\mathbf{r}) \text{ periodic on unit cell}) \\
\Rightarrow h_{\mathbf{k}\alpha}(\mathbf{r}) &\equiv \sum_{\mathbf{R}s} \frac{f^{\mathbf{k}}_{\alpha s}}{\sqrt{m_s}} e^{i\mathbf{k}\cdot(\mathbf{R}+\mathbf{r})} \partial_{\mathbf{R}s} V_{\mathrm{nuc}}(\mathbf{r}) \text{ is periodic}
\end{aligned}$$

$$
\begin{aligned}
H_{e-\mathrm{ph}} &= \tfrac{1}{N_{\mathbf{R}}^{3/2}} \textstyle\sum_{\alpha\mathbf{k}} \sum_{\mathbf{q}b} \sum_{\mathbf{q}'b'} X^{\alpha\mathbf{k}} c^\dagger_{\mathbf{q}b} c_{\mathbf{q}'b'} \int_{N_{\mathbf{R}}\Omega} \mathrm{d}\mathbf{r} h_{\mathbf{k}\alpha}(\mathbf{r}) u^*_{\mathbf{q}b}(\mathbf{r}) u_{\mathbf{q}'b'}(\mathbf{r}) e^{i(\mathbf{q}'-\mathbf{k}-\mathbf{q})\cdot\mathbf{r}} \\
&= \tfrac{1}{N_{\mathbf{R}}^{3/2}} \textstyle\sum_{\alpha\mathbf{k}} \sum_{\mathbf{q}b} \sum_{\mathbf{q}'b'} X^{\alpha\mathbf{k}} c^\dagger_{\mathbf{q}b} c_{\mathbf{q}'b'} \sum_{\mathbf{R}} \int_{\Omega} \mathrm{d}\mathbf{r} h_{\mathbf{k}\alpha}(\mathbf{r}) u^*_{\mathbf{q}b}(\mathbf{r}) u_{\mathbf{q}'b'}(\mathbf{r}) e^{i(\mathbf{q}'-\mathbf{k}-\mathbf{q})\cdot(\mathbf{r}+\mathbf{R})} \\
&\qquad\qquad\qquad\qquad\qquad\qquad\qquad\qquad\qquad\qquad\qquad\qquad\qquad\qquad\qquad\qquad (\text{using periodicity of } h_{\mathbf{k}\alpha} \text{ and } u_{\mathbf{q}b}) \\
&= \tfrac{1}{\sqrt{N_{\mathbf{R}}}} \textstyle\sum_{\alpha\mathbf{k}} \sum_{\mathbf{q}b} \sum_{\mathbf{q}'b'} X^{\alpha\mathbf{k}} c^\dagger_{\mathbf{q}b} c_{\mathbf{q}'b'} \int_{\Omega} \mathrm{d}\mathbf{r} h_{\mathbf{k}\alpha}(\mathbf{r}) u^*_{\mathbf{q}b}(\mathbf{r}) u_{\mathbf{q}'b'}(\mathbf{r}) e^{i(\mathbf{q}'-\mathbf{k}-\mathbf{q})\cdot\mathbf{r}} \textstyle\sum_{\mathbf{R}} \frac{e^{i(\mathbf{q}'-\mathbf{k}-\mathbf{q})\cdot\mathbf{R})}}{N_{\mathbf{R}}} \\
&= \tfrac{1}{\sqrt{N_{\mathbf{R}}}} \textstyle\sum_{\alpha\mathbf{k}} \sum_{\mathbf{q}b} \sum_{\mathbf{q}'b'} X^{\alpha\mathbf{k}} c^\dagger_{\mathbf{q}b} c_{\mathbf{q}'b'} \int_{\Omega} \mathrm{d}\mathbf{r} h_{\mathbf{k}\alpha}(\mathbf{r}) u^*_{\mathbf{q}b}(\mathbf{r}) u_{\mathbf{q}'b'}(\mathbf{r}) e^{i(\mathbf{q}'-\mathbf{k}-\mathbf{q})\cdot\mathbf{r}} \delta_{\mathbf{q}+\mathbf{k},\mathbf{q}'} \\
&= \tfrac{1}{\sqrt{N_{\mathbf{R}}}} \textstyle\sum_{\alpha\mathbf{k}} \sum_{\mathbf{q}b} \sum_{\mathbf{q}'b'} X^{\alpha\mathbf{k}} c^\dagger_{\mathbf{q}b} c_{\mathbf{q}'b'} \delta_{\mathbf{q}+\mathbf{k},\mathbf{q}'} \underbrace{\int_{\Omega} \mathrm{d}\mathbf{r} u^*_{\mathbf{q}b}(\mathbf{r}) u_{\mathbf{q}'b'}(\mathbf{r}) \sum_{\mathbf{R}s} \frac{f^{\mathbf{k}}_{\alpha s}}{\sqrt{m_s}} e^{i\mathbf{k}\cdot(\mathbf{R}+\mathbf{r})} \partial_{\mathbf{R}s} V_{\mathrm{nuc}}(\mathbf{r})}_{\equiv M^{\mathbf{k}\alpha}_{\mathbf{q}b,\mathbf{q}'b'}} \\
&= \textstyle\sum_{\alpha\mathbf{k}} \sum_{\mathbf{q}bb'} \frac{M^{\mathbf{k}\alpha}_{\mathbf{q}b,(\mathbf{q}+\mathbf{k})b'}}{\sqrt{2N_{\mathbf{R}}\omega_{\mathbf{k}\alpha}}} (b^\dagger_{\mathbf{k}\alpha} + b_{-\mathbf{k}\alpha}) c^\dagger_{\mathbf{q}b} c_{(\mathbf{q}+\mathbf{k})b'}
\end{aligned}
$$

Here, $M^{\mathbf{k}\alpha}_{\mathbf{q}b,(\mathbf{q}+\mathbf{k})b'}$ are the non-zero matrix elements you will get from the DFT/phonon code. You can see that the momentum conservation works out properly for the emission and absorption processes, and the weird $\mathbf{k}$ and $-\mathbf{k}$ combinations during the phonon quantization was necessary for this to happen. Also note that the normalization has non-trivial modifications due to the 'amplitude of motion' per phonon quantum.

Summary: the matrix element for absorbing a phonon $\mathbf{k}\alpha$ between a pair of electronic states is exactly the same as emitting the phonon $-\mathbf{k}\alpha$ between the same pair of electronic states.

# Bibliography

Abe, Ryu, Masanobu Higashi, and Kazunari Domen. “Facile Fabrication of an Efficient Oxynitride TaON Photoanode for Overall Water Splitting into H(2) and O(2) under Visible Light Irradiation”. In: *J. Am. Chem. Soc.* 132.34 (2010), p. 11828.

Ágoston, P. et al. In: *Phys. Rev. Lett.* 103.24 (2009), p. 245501.

Akimov, A. V. et al. “Generation of single optical plasmons in metallic nanowires coupled to quantum dots”. In: *Nature* 450.7168 (Nov. 15, 2007), pp. 402–406. URL: http://dx.doi.org/10.1038/nature06230.

Altewischer, E., M. P. van Exter, and J. P. Woerdman. “Plasmon-assisted transmission of entangled photons”. In: *Nature* 418.6895 (July 18, 2002), pp. 304–306. URL: http://dx.doi.org/10.1038/nature00869.

Andrew, P. and W. L. Barnes. “Energy Transfer Across a Metal Film Mediated by Surface Plasmon Polaritons”. In: *Science* 306.5698 (Nov. 2004), pp. 1002–1005.

Archambault, Alexandre et al. “Quantum theory of spontaneous and stimulated emission of surface plasmons”. In: *Physical Review B* 82.3 (July 12, 2010), pp. 035411–. URL: http://link.aps.org/doi/10.1103/PhysRevB.82.035411.

Atwater, Harry A. and Albert Polman. “Plasmonics for improved photovoltaic devices”. In: *Nat Mater* 9.3 (Mar. 2010), pp. 205–213. URL: http://dx.doi.org/10.1038/nmat2629.

— “Plasmonics for improved photovoltaic devices”. In: *Nat Mater* 9.3 (Mar. 2010), pp. 205–213. URL: http://dx.doi.org/10.1038/nmat2629.

Ballester, D. et al. “Long-range surface-plasmon-polariton excitation at the quantum level”. In: *Physical Review A* 79.5 (May 26, 2009), pp. 053845–. URL: http://link.aps.org/doi/10.1103/PhysRevA.79.053845.

Barnes, William L., Alain Dereux, and Thomas W. Ebbesen. "Surface plasmon subwavelength optics". In: *Nature* 424.6950 (Aug. 14, 2003), pp. 824–830. URL: http://dx.doi.org/10.1038/nature01937.

— "Surface plasmon subwavelength optics". In: *Nature* 424.6950 (Aug. 14, 2003), pp. 824–830. URL: http://dx.doi.org/10.1038/nature01937.

Bernardi, M. et al. "Theory and Computation of Hot Carriers Generated by Surface Plasmon Polaritons in Noble Metals". In: *Nat. Commun.* In press (2015).

Bilc, D. I. et al. "Hybrid exchange-correlation functional for accurate prediction of the electronic and structural properties of ferroelectric oxides". In: *Phys. Rev. B* 77.16 (Apr. 2008), p. 165107. DOI: 10.1103/PhysRevB.77.165107.

Biswas, Koushik, Alberto Franceschetti, and Stephan Lany. "Generalized valence-force-field model of (Ga,In)(N,P) ternary alloys". In: *Phys. Rev. B* 78 (8 Aug. 2008), p. 085212. DOI: 10.1103/PhysRevB.78.085212. URL: http://link.aps.org/doi/10.1103/PhysRevB.78.085212.

Bohm, David and David Pines. "A Collective Description of Electron Interactions: III. Coulomb Interactions in a Degenerate Electron Gas". In: *Phys. Rev.* 92 (3 Nov. 1953), pp. 609–625. DOI: 10.1103/PhysRev.92.609. URL: http://link.aps.org/doi/10.1103/PhysRev.92.609.

Brongersma, Mark L., Naomi J. Halas, and Peter Nordlander. "Plasmon-induced hot carrier science and technology". In: *Nat Nano* 10.1 (Jan. 2015), pp. 25–34. URL: http://dx.doi.org/10.1038/nnano.2014.311.

— "Plasmon-induced hot carrier science and technology". In: *Nat Nano* 10.1 (Jan. 2015), pp. 25–34. URL: http://dx.doi.org/10.1038/nnano.2014.311.

Brueck, S. R. J. et al. "Enhanced quantum efficiency internal photoemission detectors by grating coupling to surface plasma waves". In: *Applied Physics Letters* 46.10 (May 15, 1985), pp. 915–917. URL: http://dx.doi.org/10.1063/1.95819.

Buckeridge, J. et al. "Automated procedure to determine the thermodynamic stability of a material and the range of chemical potentials necessary for its formation relative to competing phases and compounds". In: *Computer Physics Communications* 185.1 (2014), pp. 330–338. ISSN: 0010-4655. DOI: http://dx.doi.org/10.1016/j.cpc.2013.08.026. URL: http://www.sciencedirect.com/science/article/pii/S0010465513002993.

Carvalho, Luiz Cláudio de et al. "Distribution of cations in wurtzitic $In_xGa_{1-x}N$ and $In_xAl_{1-x}N$ alloys: Consequences for energetics and quasiparticle electronic structures". In: *Phys. Rev. B* 85

(11 Mar. 2012), p. 115121. DOI: 10.1103/PhysRevB.85.115121. URL: http://link.aps.org/doi/10.1103/PhysRevB.85.115121.

Chang, D. E. et al. "Quantum Optics with Surface Plasmons". In: *Physical Review Letters* 97.5 (Aug. 3, 2006), pp. 053002–. URL: http://link.aps.org/doi/10.1103/PhysRevLett.97.053002.

Chang, Darrick E. et al. "A single-photon transistor using nanoscale surface plasmons". In: *Nat Phys* 3.11 (Nov. 2007), pp. 807–812. URL: http://dx.doi.org/10.1038/nphys708.

Chen, Shiyou et al. In: *Phys. Rev. B* 79 (2009), p. 165211.

— "Crystal and electronic band structure of $Cu_2ZnSnX_4$ (X = S and Se) photovoltaic absorbers: First-principles insights". In: *Appl. Phys. Lett.* 94 (2009), p. 041903.

Chen, Shiyou et al. "Defect physics of the kesterite thin-film solar cell absorber Cu2ZnSnS4". In: *Applied Physics Letters* 96.2, 021902 (2010), pages. DOI: http://dx.doi.org/10.1063/1.3275796. URL: http://scitation.aip.org/content/aip/journal/apl/96/2/10.1063/1.3275796.

— "Electronic structure and stability of quaternary chalcogenide semiconductors derived from cation cross-substitution of II-VI and I-III-$VI_2$ compounds". In: *Phys. Rev. B* 79 (16 Apr. 2009), p. 165211. DOI: 10.1103/PhysRevB.79.165211. URL: http://link.aps.org/doi/10.1103/PhysRevB.79.165211.

Chen, Shiyou et al. "Intrinsic point defects and complexes in the quaternary kesterite semiconductor $Cu_2ZnSnS_4$". In: *Phys. Rev. B* 81.24 (June 2010), p. 245204. DOI: 10.1103/PhysRevB.81.245204.

Chen, Shiyou et al. "Wurtzite-derived polytypes of kesterite and stannite quaternary chalcogenide semiconductors". In: *Phys. Rev. B* 82 (2010), p. 195203.

Christopher, Phillip, Hongliang Xin, and Suljo Linic. "Visible-light-enhanced catalytic oxidation reactions on plasmonic silver nanostructures". In: *Nat Chem* 3.6 (June 2011), pp. 467–472. URL: http://dx.doi.org/10.1038/nchem.1032.

Clark, S. J. et al. "Intrinsic defects in ZnO calculated by screened exchange and hybrid density functionals". In: *Phys. Rev. B* 81.11 (2010), p. 115311.

Clavero, Cesar. "Plasmon-induced hot-electron generation at nanoparticle/metal-oxide interfaces for photovoltaic and photocatalytic devices". In: *Nat Photon* 8.2 (Feb. 2014), pp. 95–103. URL: http://dx.doi.org/10.1038/nphoton.2013.238.

— "Plasmon-induced hot-electron generation at nanoparticle/metal-oxide interfaces for photovoltaic and photocatalytic devices". In: *Nat Photon* 8.2 (Feb. 2014), pp. 95–103. URL: http://dx.doi.org/10.1038/nphoton.2013.238.

— "Plasmon-induced hot-electron generation at nanoparticle/metal-oxide interfaces for photovoltaic and photocatalytic devices". In: *Nat Photon* 8.2 (Feb. 2014), pp. 95–103. URL: http://dx.doi.org/10.1038/nphoton.2013.238.

Courths, R. and S. H ufner. "Photoemission experiments on copper". In: *Physics Reports* 112.2 (1984), pp. 53–171. ISSN: 0370-1573. DOI: http://dx.doi.org/10.1016/0370-1573(84)90167-4. URL: http://www.sciencedirect.com/science/article/pii/0370157384901674.

Deng, Fuling et al. "Determination of the basic optical parameters of ZnSnN2". In: *Opt. Lett.* 40.7 (Apr. 2015), pp. 1282–1285. DOI: 10.1364/OL.40.001282. URL: http://ol.osa.org/abstract.cfm?URI=ol-40-7-1282.

Di Martino, Giuliana et al. "Quantum Statistics of Surface Plasmon Polaritons in Metallic Stripe Waveguides". In: *Nano Letters* 12.5 (2014/10/20 2012), pp. 2504–2508. DOI: 10.1021/nl300671w. URL: http://dx.doi.org/10.1021/nl300671w.

Doppalapudi, D. et al. "Phase separation and ordering in InGaN alloys grown by molecular beam epitaxy". In: *Journal of Applied Physics* 84.3 (1998), pp. 1389–1395.

Du, K. et al. "Synthesis and characterization of ZnGeN2 grown from elemental Zn and Ge sources". In: *Journal of Crystal Growth* 310.6 (Mar. 15, 2008), pp. 1057–1061. DOI: http://dx.doi.org/10.1016/j.jcrysgro.2007.12.042. URL: http://www.sciencedirect.com/science/article/pii/S0022024807012560.

Du, Mao-Hua and S. B. Zhang. "Impurity-bound small polarons in ZnO: Hybrid density functional calculations". In: *Phys. Rev. B* 80.11 (Sept. 2009), p. 115217. DOI: 10.1103/PhysRevB.80.115217.

DuChene, Joseph S. et al. "Prolonged Hot Electron Dynamics in Plasmonic-Metal/Semiconductor Heterostructures with Implications for Solar Photocatalysis". In: *Angewandte Chemie International Edition* 53.30 (2014), pp. 7887–7891. ISSN: 1521-3773. DOI: 10.1002/anie.201404259. URL: http://dx.doi.org/10.1002/anie.201404259.

Duda, Laurent -C. et al. "Density of states, hybridization, and band-gap evolution in $Al_xGa_{1-x}N$ alloys". In: *Phys. Rev. B* 58 (4 July 1998), pp. 1928–1933. DOI: 10.1103/PhysRevB.58.1928. URL: http://link.aps.org/doi/10.1103/PhysRevB.58.1928.

Dudarev, S. L. et al. “Electron-energy-loss spectra and the structural stability of nickel oxide: An LSDA+U study”. In: *Phys. Rev. B* 57 (3 Jan. 1998), pp. 1505–1509. DOI: 10.1103/PhysRevB.57.1505. URL: http://link.aps.org/doi/10.1103/PhysRevB.57.1505.

Durante, Nicola et al. “Optical Properties of Au Nanoclusters from TD-DFT Calculations”. In: *The Journal of Physical Chemistry C* 115.14 (2013/11/11 2011), pp. 6277–6282. DOI: 10.1021/jp112217g. URL: http://dx.doi.org/10.1021/jp112217g.

Elson, J. M. and R. H. Ritchie. “Photon Interactions at a Rough Metal Surface”. In: *Phys. Rev. B* 4 (12 Dec. 1971), pp. 4129–4138. DOI: 10.1103/PhysRevB.4.4129. URL: http://link.aps.org/doi/10.1103/PhysRevB.4.4129.

— “Photon Interactions at a Rough Metal Surface”. In: *Physical Review B* 4.12 (Dec. 15, 1971), pp. 4129–4138. URL: http://link.aps.org/doi/10.1103/PhysRevB.4.4129.

Esteban, Ruben et al. “Bridging quantum and classical plasmonics with a quantum-corrected model”. In: *Nat Commun* 3 (May 8, 2012), p. 825. URL: http://dx.doi.org/10.1038/ncomms1806.

Etchegoin, P. G., E. C. Le Ru, and M. Meyer. “An analytic model for the optical properties of gold”. In: *The Journal of Chemical Physics* 125.16, 164705 (2006), pages. DOI: http://dx.doi.org/10.1063/1.2360270.

Fang, CM et al. “The electronic structure of tantalum (oxy)nitrides TaON and Ta3N5”. In: *J. Mater. Chem.* 11.4 (2001), p. 1248.

Fang, Zheyu et al. “Plasmon-Induced Doping of Graphene”. In: *ACS Nano* 6.11 (2014/08/28 2012), pp. 10222–10228. DOI: 10.1021/nn304028b. URL: http://dx.doi.org/10.1021/nn304028b.

Fedutik, Y. et al. “Exciton-Plasmon-Photon Conversion in Plasmonic Nanostructures”. In: *Physical Review Letters* 99.13 (Sept. 24, 2007), pp. 136802–. URL: http://link.aps.org/doi/10.1103/PhysRevLett.99.136802.

Feldberg, N. et al. “Growth of ZnSnN2 by Molecular Beam Epitaxy”. In: 43.4 (2014), pp. 884–888. DOI: 10.1007/s11664-013-2962-8. URL: http://dx.doi.org/10.1007/s11664-013-2962-8.

Fowler, R. H. “The Analysis of Photoelectric Sensitivity Curves for Clean Metals at Various Temperatures”. In: *Phys. Rev.* 38 (1 July 1931), pp. 45–56. DOI: 10.1103/PhysRev.38.45. URL: http://link.aps.org/doi/10.1103/PhysRev.38.45.

— “The Analysis of Photoelectric Sensitivity Curves for Clean Metals at Various Temperatures”. In: *Physical Review* 38.1 (July 1, 1931), pp. 45–56. URL: http://link.aps.org/doi/10.1103/PhysRev.38.45.

Fuchs, M. et al. “Cohesive properties of group-III nitrides: A comparative study of all-electron and pseudopotential calculations using the generalized gradient approximation”. In: *Phys. Rev. B* 65 (24 2002), p. 245212.

Gai, Yanqin et al. “Design of Narrow-Gap $TiO2$: A Passivated Codoping Approach for Enhanced Photoelectrochemical Activity”. In: *Phys. Rev. Lett.* 102.3 (Jan. 2009), p. 036402. DOI: 10.1103/PhysRevLett.102.036402.

Giannini, Vincenzo et al. “Plasmonic Nanoantennas: Fundamentals and Their Use in Controlling the Radiative Properties of Nanoemitters”. In: *Chemical Reviews* 111.6 (2014/08/28 2011), pp. 3888–3912. DOI: 10.1021/cr1002672. URL: http://dx.doi.org/10.1021/cr1002672.

GiugniA. et al. “Hot-electron nanoscopy using adiabatic compression of surface plasmons”. In: *Nat Nano* 8.11 (Nov. 2013), pp. 845–852. URL: http://dx.doi.org/10.1038/nnano.2013.207.

Giustino, Feliciano, Marvin L. Cohen, and Steven G. Louie. “Electron-phonon interaction using Wannier functions”. In: *Phys. Rev. B* 76 (16 Oct. 2007), p. 165108. DOI: 10.1103/PhysRevB.76.165108. URL: http://link.aps.org/doi/10.1103/PhysRevB.76.165108.

Goodman, C. H. L. “The prediction of semiconductor properties in inorganic compounds”. In: *J. Phys. Chem. Solids* 6 (1958), p. 305.

Govorov, Alexander O., Hui Zhang, and Yurii K. Gun’ko. “Theory of Photoinjection of Hot Plasmonic Carriers from Metal Nanostructures into Semiconductors and Surface Molecules”. In: *The Journal of Physical Chemistry C* 117.32 (Aug. 2013), pp. 16616–16631. DOI: 10.1021/jp405430m. URL: http://dx.doi.org/10.1021/jp405430m.

— “Theory of Photoinjection of Hot Plasmonic Carriers from Metal Nanostructures into Semiconductors and Surface Molecules”. In: *The Journal of Physical Chemistry C* 117.32 (2013/11/11 2013), pp. 16616–16631. DOI: 10.1021/jp405430m. URL: http://dx.doi.org/10.1021/jp405430m.

Goykhman, Ilya et al. “Locally Oxidized Silicon Surface-Plasmon Schottky Detector for Telecom Regime”. In: *Nano Letters* 11.6 (June 2011), pp. 2219–2224. DOI: 10.1021/nl200187v. URL: http://dx.doi.org/10.1021/nl200187v.

Gramotnev, Dmitri K. and Sergey I. Bozhevolnyi. “Plasmonics beyond the diffraction limit”. In: *Nat Photon* 4.2 (Feb. 2010), pp. 83–91. URL: http://dx.doi.org/10.1038/nphoton.2009.282.

Gratzel, M. “Photoelectrochemical cells”. In: *Nature* 414.6861 (2001), p. 338.

Groot, Frank de. "High-Resolution X-ray Emission and X-ray Absorption Spectroscopy". In: *Chemical Reviews* 101.6 (2001). PMID: 11709999, pp. 1779–1808. DOI: 10.1021/cr9900681. eprint: http://dx.doi.org/10.1021/cr9900681. URL: http://dx.doi.org/10.1021/cr9900681.

Hedin, Lars. "New Method for Calculating the One-Particle Green's Function with Application to the Electron-Gas Problem". In: *Phys. Rev.* 139 (3A Aug. 1965), A796–A823. DOI: 10.1103/PhysRev.139.A796. URL: http://link.aps.org/doi/10.1103/PhysRev.139.A796.

Heyd, J., G. E. Scuseria, and M. Ernzerhof. In: *J. Chem. Phys.* 118 (2003), p. 8207.

Hopfield, J. J. "Theory of the Contribution of Excitons to the Complex Dielectric Constant of Crystals". In: *Phys. Rev.* 112 (5 Dec. 1958), pp. 1555–1567. DOI: 10.1103/PhysRev.112.1555. URL: http://link.aps.org/doi/10.1103/PhysRev.112.1555.

— "Theory of the Contribution of Excitons to the Complex Dielectric Constant of Crystals". In: *Physical Review* 112.5 (Dec. 1, 1958), pp. 1555–1567. URL: http://link.aps.org/doi/10.1103/PhysRev.112.1555.

Huttner, Bruno and Stephen M. Barnett. "Quantization of the electromagnetic field in dielectrics". In: *Phys. Rev. A* 46 (7 Oct. 1992), pp. 4306–4322. DOI: 10.1103/PhysRevA.46.4306. URL: http://link.aps.org/doi/10.1103/PhysRevA.46.4306.

— "Quantization of the electromagnetic field in dielectrics". In: *Physical Review A* 46.7 (Oct. 1, 1992), pp. 4306–4322. URL: http://link.aps.org/doi/10.1103/PhysRevA.46.4306.

Ingram, David B. et al. "Predictive Model for the Design of Plasmonic Metal/Semiconductor Composite Photocatalysts". In: *ACS Catalysis* 1.10 (2013/11/11 2011), pp. 1441–1447. DOI: 10.1021/cs200320h. URL: http://dx.doi.org/10.1021/cs200320h.

Inouye, Hideyuki et al. "Ultrafast dynamics of nonequilibrium electrons in a gold nanoparticle system". In: *Phys. Rev. B* 57 (18 May 1998), pp. 11334–11340. DOI: 10.1103/PhysRevB.57.11334. URL: http://link.aps.org/doi/10.1103/PhysRevB.57.11334.

Ishitani, Yoshihiro. "Carrier dynamics and related electronic band properties of InN films". In: *Japanese Journal of Applied Physics* 53.10 (2014), p. 100204. URL: http://stacks.iop.org/1347-4065/53/i=10/a=100204.

Jacob, Zubin and Vladimir M. Shalaev. "Plasmonics Goes Quantum". In: *Science* 334.6055 (Oct. 2011), pp. 463–464. URL: http://www.sciencemag.org/content/334/6055/463.short.

Jacquemin, Denis, Benedetta Mennucci, and Carlo Adamo. "Excited-state calculations with TD-DFT: from benchmarks to simulations in complex environments". In: *Physical Chemistry Chemical*

*Physics* 13.38 (2011), pp. 16987–16998. DOI: 10.1039/C1CP22144B. URL: http://dx.doi.org/10.1039/C1CP22144B.

Janotti, A. et al. "Hybrid functional studies of the oxygen vacancy in $TiO2$". In: *Phys. Rev. B* 81.8 (Feb. 2010), p. 085212. DOI: 10.1103/PhysRevB.81.085212.

Kang, Yimin et al. "Plasmonic Hot Electron Induced Structural Phase Transition in a MoS2 Monolayer". In: *Advanced Materials* 26.37 (2014), pp. 6467–6471. ISSN: 1521-4095. DOI: 10.1002/adma.201401802. URL: http://dx.doi.org/10.1002/adma.201401802.

Khurgin, Jacob B. "How to deal with the loss in plasmonics and metamaterials". In: *Nat Nano* 10.1 (Jan. 2015), pp. 2–6. URL: http://dx.doi.org/10.1038/nnano.2014.310.

Khurgin, J.B. "Ultimate limit of field confinement by surface plasmon polaritons". preprint arXiv:1410.1226. 2014.

Kioupakis, Emmanouil et al. "Free-carrier absorption in nitrides from first principles". In: *Phys. Rev. B* 81 (24 June 2010), p. 241201. DOI: 10.1103/PhysRevB.81.241201. URL: http://link.aps.org/doi/10.1103/PhysRevB.81.241201.

Knight, Mark W. et al. "Embedding Plasmonic Nanostructure Diodes Enhances Hot Electron Emission". In: *Nano Letters* 13.4 (2013/07/23 2013), pp. 1687–1692. DOI: 10.1021/nl400196z. URL: http://dx.doi.org/10.1021/nl400196z.

Knight, Mark W. et al. "Photodetection with Active Optical Antennas". In: *Science* 332.6030 (May 2011), pp. 702–704. URL: http://www.sciencemag.org/content/332/6030/702.abstract.

Kolesov, Roman et al. "Wave-particle duality of single surface plasmon polaritons". In: *Nat Phys* 5.7 (July 2009), pp. 470–474. URL: http://dx.doi.org/10.1038/nphys1278.

Kresse, G. and J. Furthmueller. In: *Phys. Rev. B* 54 (1996), p. 11169.

Kresse, G. and J. Furthmüller. "Efficient iterative schemes for *ab initio* total-energy calculations using a plane-wave basis set". In: *Phys. Rev. B* 54 (16 Oct. 1996), pp. 11169–11186. DOI: 10.1103/PhysRevB.54.11169. URL: http://link.aps.org/doi/10.1103/PhysRevB.54.11169.

Kresse, G. and D. Joubert. In: *Phys. Rev. B* 59 (1999), p. 1758.

Kuisma, M. et al. "Kohn-Sham potential with discontinuity for band gap materials". In: *Phys. Rev. B* 82 (11 Sept. 2010), p. 115106. DOI: 10.1103/PhysRevB.82.115106. URL: http://link.aps.org/doi/10.1103/PhysRevB.82.115106.

Kuwabara, Akihide. "Theoretical investigation to thermal equilibrium concentration of point defect through first-principles calculation". In: *Science and Technology of Advanced Materials* 8.6 (2007), p. 519.

Ladstädter, Florian et al. "First-principles calculation of hot-electron scattering in metals". In: *Phys. Rev. B* 70 (23 Dec. 2004), p. 235125. DOI: 10.1103/PhysRevB.70.235125. URL: http://link.aps.org/doi/10.1103/PhysRevB.70.235125.

Lahourcade, Lise et al. "Structural and Optoelectronic Characterization of RF Sputtered ZnSnN2". In: *Advanced Materials* 25 (2013), pp. 2562–2566.

— "Structural and Optoelectronic Characterization of RF Sputtered ZnSnN2". In: *Advanced Materials* 25.18 (2013), pp. 2562–2566. ISSN: 1521-4095. DOI: 10.1002/adma.201204718. URL: http://dx.doi.org/10.1002/adma.201204718.

Landau, L. "On the vibration of the electronic plasma". In: *J. Phys. USSR* 10 (1946).

Lany, Stephan and Alex Zunger. "Assessment of correction methods for the band-gap problem and for finite-size effects in supercell defect calculations: Case studies for ZnO and GaAs". In: *Phys. Rev. B* 78.23 (Dec. 2008), p. 235104. DOI: 10.1103/PhysRevB.78.235104.

Leenheer, Andrew J. et al. "Solar energy conversion via hot electron internal photoemission in metallic nanostructures: Efficiency estimates". In: *Journal of Applied Physics* 115.13, 134301 (2014), pages. DOI: http://dx.doi.org/10.1063/1.4870040. URL: http://scitation.aip.org/content/aip/journal/jap/115/13/10.1063/1.4870040.

Lewis Jr, H Ralph and WB Riesenfeld. "An Exact Quantum Theory of the Time Dependent Harmonic Oscillator and of a Charged Particle in a Time Dependent Electromagnetic Field". In: *Journal of Mathematical Physics* 10 (1969), p. 1458.

Li, Pan et al. "First-Principles Study of the Electronic, Optical Properties and Lattice Dynamics of Tantalum Oxynitride". In: *Inorg. Chem.* 49.15 (2010), p. 6917.

Lide, D.R. *CRC Handbook of Chemistry and Physics, 84th Edition*. CRC HANDBOOK OF CHEMISTRY AND PHYSICS. Taylor & Francis, 2003. ISBN: 9780849304842.

Linic, Suljo, Phillip Christopher, and David B. Ingram. "Plasmonic-metal nanostructures for efficient conversion of solar to chemical energy". In: *Nat Mater* 10.12 (Dec. 2011), pp. 911–921. URL: http://dx.doi.org/10.1038/nmat3151.

— "Plasmonic-metal nanostructures for efficient conversion of solar to chemical energy". In: *Nat Mater* 10.12 (Dec. 2011), pp. 911–921. URL: http://dx.doi.org/10.1038/nmat3151.

Linic, Suljo et al. “Catalytic and Photocatalytic Transformations on Metal Nanoparticles with Targeted Geometric and Plasmonic Properties”. In: *Accounts of Chemical Research* 46.8 (Aug. 2013), pp. 1890–1899. DOI: 10.1021/ar3002393. URL: http://dx.doi.org/10.1021/ar3002393.

Łopuszyński, Michał and Jacek A. Majewski. “Ordering in ternary nitride semiconducting alloys”. In: *Phys. Rev. B* 85 (3 Jan. 2012), p. 035211. DOI: 10.1103/PhysRevB.85.035211. URL: http://link.aps.org/doi/10.1103/PhysRevB.85.035211.

Lumey, MW and R Dronskowski. “The electronic structure of tantalum oxynitride and the falsification of alpha-TaON”. In: *Z. Anorg. Allg. Chem.* 629.12-13 (2003), p. 2173.

Lyons, J. L., A. Janotti, and C. G. Van de Walle. “Carbon impurities and the yellow luminescence in GaN”. In: *Appl. Phys. Lett.* 97 (2010), p. 152108.

Madelung, O. M. *Semiconductors: Data Handbook*. 3rd. Berlin: Springer, 2004.

Maeda, Kazuhiko, Ryu Abe, and Kazunari Domen. “Role and Function of Ruthenium Species as Promoters with TaON-Based Photocatalysts for Oxygen Evolution in Two-Step Water Splitting under Visible Light”. In: *J. Phys. Chem. C* 115.7 (2011), p. 3057.

Maeda, Kazuhiko and Kazunari Domen. “New Non-Oxide Photocatalysts Designed for Overall Water Splitting under Visible Light”. In: *J. Phys. Chem. C* 111.22 (2007), p. 7851.

— “Photocatalytic Water Splitting: Recent Progress and Future Challenges”. In: *The Journal of Physical Chemistry Letters* 1.18 (2013/07/23 2010), pp. 2655–2661. DOI: 10.1021/jz1007966. URL: http://dx.doi.org/10.1021/jz1007966.

Maeda, Kazuhiko et al. “Efficient Nonsacrificial Water Splitting through Two-Step Photoexcitation by Visible Light using a Modified Oxynitride as a Hydrogen Evolution Photocatalyst”. In: *J. Am. Chem. Soc.* 132.16 (2010), p. 5858.

Maier, Stefan Alexander. *Plasmonics: fundamentals and applications*. Springer Science and Business Media, 2007.

Maier, Stefan A. et al. “Local detection of electromagnetic energy transport below the diffraction limit in metal nanoparticle plasmon waveguides”. In: *Nat Mater* 2.4 (Apr. 2003), pp. 229–232. URL: http://dx.doi.org/10.1038/nmat852.

Majumder, Subrata et al. “Bandgap tailoring of rutile TiO(2)(110) via surface patterning with electron cyclotron resonance sputtering”. In: *Appl. Phys. Lett.* 98 (2011).

Manjavacas, A., F. J. Garcia de Abajo, and P. Nordlander. "Quantum plexcitonics: strongly interacting plasmons and excitons". In: *Nano Lett.* 11.6 (June 2011), pp. 2318–2323.

Manjavacas, Alejandro et al. "Plasmon-Induced Hot Carriers in Metallic Nanoparticles". In: *ACS Nano* 8.8 (2014). PMID: 24960573, pp. 7630–7638. DOI: 10.1021/nn502445f. eprint: http://dx.doi.org/10.1021/nn502445f. URL: http://dx.doi.org/10.1021/nn502445f.

— "Plasmon-Induced Hot Carriers in Metallic Nanoparticles". In: *ACS Nano* 8.8 (2014/08/28 2014), pp. 7630–7638. DOI: 10.1021/nn502445f. URL: http://dx.doi.org/10.1021/nn502445f.

Marini, Andrea, Rodolfo Del Sole, and Giovanni Onida. "First-principles calculation of the plasmon resonance and of the reflectance spectrum of silver in the GW approximation". In: *Phys. Rev. B* 66 (11 Sept. 2002), p. 115101. DOI: 10.1103/PhysRevB.66.115101. URL: http://link.aps.org/doi/10.1103/PhysRevB.66.115101.

Marini, Andrea, Giovanni Onida, and Rodolfo Del Sole. "Plane-wave DFT-LDA calculation of the electronic structure and absorption spectrum of copper". In: *Phys. Rev. B* 64 (19 Oct. 2001), p. 195125. DOI: 10.1103/PhysRevB.64.195125. URL: http://link.aps.org/doi/10.1103/PhysRevB.64.195125.

— "Quasiparticle Electronic Structure of Copper in the GW Approximation". In: *Phys. Rev. Lett.* 88 (1 Dec. 2001), p. 016403. DOI: 10.1103/PhysRevLett.88.016403. URL: http://link.aps.org/doi/10.1103/PhysRevLett.88.016403.

Marinica, D.C. et al. "Quantum Plasmonics: Nonlinear Effects in the Field Enhancement of a Plasmonic Nanoparticle Dimer". In: *Nano Letters* 12.3 (2012), pp. 1333–1339. DOI: 10.1021/nl300269c. eprint: http://pubs.acs.org/doi/pdf/10.1021/nl300269c. URL: http://pubs.acs.org/doi/abs/10.1021/nl300269c.

Marzari, Nicola and David Vanderbilt. "Maximally localized generalized Wannier functions for composite energy bands". In: *Phys. Rev. B* 56 (20 Nov. 1997), pp. 12847–12865. DOI: 10.1103/PhysRevB.56.12847. URL: http://link.aps.org/doi/10.1103/PhysRevB.56.12847.

Marzari, Nicola et al. "Maximally localized Wannier functions: Theory and applications". In: *Rev. Mod. Phys.* 84 (4 Oct. 2012), pp. 1419–1475. DOI: 10.1103/RevModPhys.84.1419. URL: http://link.aps.org/doi/10.1103/RevModPhys.84.1419.

McFarland, Eric W. and Jing Tang. "A photovoltaic device structure based on internal electron emission". In: *Nature* 421.6923 (Feb. 6, 2003), pp. 616–618. URL: http://dx.doi.org/10.1038/nature01316.

— "A photovoltaic device structure based on internal electron emission". In: *Nature* 421.6923 (Feb. 6, 2003), pp. 616–618. URL: http://dx.doi.org/10.1038/nature01316.

Miller, Nate et al. "Effect of charged dislocation scattering on electrical and electrothermal transport in $n$-type InN". In: *Phys. Rev. B* 84 (7 Aug. 2011), p. 075315. DOI: 10.1103/PhysRevB.84.075315. URL: http://link.aps.org/doi/10.1103/PhysRevB.84.075315.

Mills, K. A. et al. "Angle-resolved photoemission determination of Λ-line valence bands in Pt and Au using synchrotron radiation". In: *Phys. Rev. B* 22 (2 July 1980), pp. 581–592. DOI: 10.1103/PhysRevB.22.581. URL: http://link.aps.org/doi/10.1103/PhysRevB.22.581.

Morikawa, Takeshi et al. "Dual functional modification by N doping of Ta(2)O(5): p-type conduction in visible-light-activated N-doped Ta(2)O(5)". In: *Appl. Phys. Lett.* 96 (2010), p. 142111.

Moskovits, Martin. "The case for plasmon-derived hot carrier devices". In: *Nat Nano* 10.1 (Jan. 2015), pp. 6–8. URL: http://dx.doi.org/10.1038/nnano.2014.280.

Mubeen, Syed et al. "An autonomous photosynthetic device in which all charge carriers derive from surface plasmons". In: *Nat Nano* 8.4 (Apr. 2013), pp. 247–251. URL: http://dx.doi.org/10.1038/nnano.2013.18.

Mukherjee, Shaunak et al. "Hot Electrons Do the Impossible: Plasmon-Induced Dissociation of H2 on Au". In: *Nano Letters* 13.1 (2013/07/23 2012), pp. 240–247. DOI: 10.1021/nl303940z. URL: http://dx.doi.org/10.1021/nl303940z.

— "Hot Electrons Do the Impossible: Plasmon-Induced Dissociation of H2 on Au". In: *Nano Letters* 13.1 (Jan. 2013), pp. 240–247. DOI: 10.1021/nl303940z. URL: http://dx.doi.org/10.1021/nl303940z.

Mukherjee, Shaunak et al. "Hot-Electron-Induced Dissociation of H2 on Gold Nanoparticles Supported on SiO2". In: *Journal of the American Chemical Society* 136.1 (Jan. 2014), pp. 64–67. DOI: 10.1021/ja411017b. URL: http://pubs.acs.org/doi/abs/10.1021/ja411017b.

Nakamura, Ryuhei, Tomoaki Tanaka, and Yoshihiro Nakato. "Oxygen Photoevolution on a Tantalum Oxynitride Photocatalyst under Visible-Light Irradiation: How Does Water Photooxidation Proceed on a Metal?Oxynitride Surface?" In: *J. Phys. Chem. B* 109.18 (2005), p. 8920.

Nakamura, Yoshiko Oi. "Quantization of Non-Radiative Surface Plasma Oscillations". In: *Progress of Theoretical Physics* 70.4 (Oct. 1983), pp. 908–919. URL: http://ptp.oxfordjournals.org/content/70/4/908.abstract%20N2%20-%20Non-radiative%20surface%20plasma%20oscillations%20in%20a%20semi-infinite%20metal%20are%20quantized%20by%20using%

20a%20hydrodynamic%20jellium%20model%20for%20electrons%20in%20the%20metal.%20In%20consequence%20of%20the%20quantization,%20the%20electron-SP%20(surface%20plasmon)%20vertex%20function%20is%20obtained%20for%20the%20overall%20region%20of%20the%20surface%20plasmon%20wave%20vector%20k.%20In%20the%20electrostatic%20limit,%20it%20coincides%20with%20the%20usual%20electrostatic%20vertex%20function%20obtained%20by%20others%20before.%20In%20the%20extremely%20retarded%20limit%20(k%20%E2%86%920),%20however,%20it%20has%20a%20different%20k%20dependence%20from%20the%20one%20predicted%20by%20a%20simple%20extrapolation%20of%20the%20electrostatic%20vertex%20function%20to%20the%20long%20wavelength%20region.%20Our%20vertex%20function%20diverges%20as%20k%20%E2%86%920,%20whereas%20the%20usual%20electrostatic%20one%20vanish%20at%20k=0%20if%20it%20is%20extrapolated%20to%20k=0.%20By%20using%20our%20vertex%20function,%20the%20long%20wavelength%20behavior%20of%20the%20surface%20loss%20intensity%20of%20scattered%20electrons%20passing%20through%20the%20metal%20foil%20is%20also%20predicted%20in%20the%20case%20of%20the%20normal%20incidence..

Narang, Prineha et al. "Bandgap Tunability in Zn(Sn,Ge)N2 Semiconductor Alloys". In: *Advanced Materials* 26.8 (2014), pp. 1235–1241. ISSN: 1521-4095. DOI: 10.1002/adma.201304473. URL: http://dx.doi.org/10.1002/adma.201304473.

Narang, P. et al. "Quasiparticle band structure of Zn-IV-N-2 compounds". In: *Un Published* (2013).

Noffsinger, Jesse et al. "Phonon-Assisted Optical Absorption in Silicon from First Principles". In: *Phys. Rev. Lett.* 108 (16 Apr. 2012), p. 167402. DOI: 10.1103/PhysRevLett.108.167402. URL: http://link.aps.org/doi/10.1103/PhysRevLett.108.167402.

Nozieres, P. and D. Pines. *Theory Of Quantum Liquids*. Advanced Books Classics Series. Westview Press, 1999. ISBN: 9780813346533.

Okumura, T. and K. N. Tu. "Electrical characterization of Schottky contacts of Au, Al, Gd, and Pt on n-type and p-type GaAs". In: *Journal of Applied Physics* 61.8 (1987), pp. 2955–2961. DOI: http://dx.doi.org/10.1063/1.337843. URL: http://scitation.aip.org/content/aip/journal/jap/61/8/10.1063/1.337843.

Ordal, M. A. et al. "Optical properties of the metals Al, Co, Cu, Au, Fe, Pb, Ni, Pd, Pt, Ag, Ti, and W in the infrared and far infrared". In: *Appl. Opt.* 22.7 (Apr. 1983), pp. 1099–1119. DOI: 10.1364/AO.22.001099. URL: http://ao.osa.org/abstract.cfm?URI=ao-22-7-1099.

Other, Anthony Norman. “Some things I did”. In: *J. Irrep. Res.* 1.1 (2014), pp. 1–10.

Pacifici, Domenico, Henri J. Lezec, and Harry A. Atwater. “All-optical modulation by plasmonic excitation of CdSe quantum dots”. In: *Nat Photon* 1.7 (July 2007), pp. 402–406. URL: http://dx.doi.org/10.1038/nphoton.2007.95.

Paier, J. et al. “Screened hybrid density functionals applied to solids”. In: *J. Chem. Phys.* 124.15 (2006), p. 154709.

Palik, E. D. *Handbook of Optical Constants of Solids*. New York: Academic, 1985.

Pamplin, B. R. “deriving new semi. compounds by structural analogy”. In: *J. Phys. Chem. Solids* 25 (1964), p. 675.

Pendry, John. “Playing Tricks with Light”. In: *Science* 285.5434 (Sept. 1999), pp. 1687–1688. URL: http://www.sciencemag.org/content/285/5434/1687.short.

Perdew, J. P. et al. In: *Phys. Rev. B* 46 (1992), p. 6671.

Perdew, John P. et al. “Restoring the Density-Gradient Expansion for Exchange in Solids and Surfaces”. In: *Phys. Rev. Lett.* 100.13 (Apr. 2008), p. 136406. DOI: 10.1103/PhysRevLett.100.136406.

— “Restoring the Density-Gradient Expansion for Exchange in Solids and Surfaces”. In: *Phys. Rev. Lett.* 100 (13 Apr. 2008), p. 136406. DOI: 10.1103/PhysRevLett.100.136406. URL: http://link.aps.org/doi/10.1103/PhysRevLett.100.136406.

Pillai, S. et al. “Surface plasmon enhanced silicon solar cells”. In: *Journal of Applied Physics* 101.9, 093105 (2007), pages. DOI: http://dx.doi.org/10.1063/1.2734885. URL: http://scitation.aip.org/content/aip/journal/jap/101/9/10.1063/1.2734885.

Piot, Adrien et al. “Collective excitation of plasmonic hot-spots for enhanced hot charge carrier transfer in metal/semiconductor contacts”. In: *Nanoscale* (2015), pages. DOI: 10.1039/C5NR01592H. URL: http://dx.doi.org/10.1039/C5NR01592H.

Punya, Atchara and Walter R. L. Lambrecht. “Band offsets between $ZnGeN_2$, GaN, ZnO, and $ZnSnN_2$ and their potential impact for solar cells”. In: *Phys. Rev. B* 88 (7 Aug. 2013), p. 075302. DOI: 10.1103/PhysRevB.88.075302. URL: http://link.aps.org/doi/10.1103/PhysRevB.88.075302.

Punya, Atchara, Walter R. L. Lambrecht, and Mark van Schilfgaarde. “Quasiparticle band structure of Zn-IV-N-2 compounds”. In: *Phys. Rev. B* 84 (2011), p. 165204.

Punya, Atchara, Walter R. L. Lambrecht, and Mark van Schilfgaarde. "Quasiparticle band structure of Zn-IV-$N_2$ compounds". In: *Phys. Rev. B* 84 (16 Oct. 2011), p. 165204. DOI: 10.1103/PhysRevB.84.165204. URL: http://link.aps.org/doi/10.1103/PhysRevB.84.165204.

Punya, Atchara, Tula R. Paudel, and Walter R. L. Lambrecht. "Electronic and lattice dynamical properties of II-IV-N2 semiconductors". In: *physica status solidi (c)* 8.7-8 (2011), pp. 2492–2499. ISSN: 1610-1642.

Qimin Yan et al. "Role of nitrogen vacancies in the luminescence of Mg-doped GaN". In: *Appl. Phys. Lett.* (2012), p. 142110.

Rakic, Aleksandar D. et al. "Optical Properties of Metallic Films for Vertical-Cavity Optoelectronic Devices". In: *Appl. Opt.* 37.22 (Aug. 1998), pp. 5271–5283. DOI: 10.1364/AO.37.005271. URL: http://ao.osa.org/abstract.cfm?URI=ao-37-22-5271.

Rakić, Aleksandar D. et al. "Optical properties of metallic films for vertical-cavity optoelectronic devices". In: *Appl. Opt.* 37.22 (Aug. 1998), pp. 5271–5283. DOI: 10.1364/AO.37.005271. URL: http://ao.osa.org/abstract.cfm?URI=ao-37-22-5271.

Rangel, T. et al. "Band structure of gold from many-body perturbation theory". In: *Phys. Rev. B* 86 (12 Sept. 2012), p. 125125. DOI: 10.1103/PhysRevB.86.125125. URL: http://link.aps.org/doi/10.1103/PhysRevB.86.125125.

Rehr, J. J. and R. C. Albers. "Theoretical approaches to x-ray absorption fine structure". In: *Rev. Mod. Phys.* 72 (3 July 2000), pp. 621–654. DOI: 10.1103/RevModPhys.72.621. URL: http://link.aps.org/doi/10.1103/RevModPhys.72.621.

Ritchie, R. H. "Plasma Losses by Fast Electrons in Thin Films". In: *Phys. Rev.* 106 (5 June 1957), pp. 874–881. DOI: 10.1103/PhysRev.106.874. URL: http://link.aps.org/doi/10.1103/PhysRev.106.874.

— "Plasma Losses by Fast Electrons in Thin Films". In: *Physical Review* 106.5 (June 1, 1957), pp. 874–881. URL: http://link.aps.org/doi/10.1103/PhysRev.106.874.

Ross, Robert T. and Arthur J. Nozik. "Efficiency of hot-carrier solar energy converters". In: *Journal of Applied Physics* 53.5 (1982), pp. 3813–3818.

S. Nakamura S. J. Pearton, G. Fasol. *The Blue Laser Diode: The Complete Story*. 2nd. Springer, 2000.

Sahu, B. R. and Leonard Kleinman. "Theoretical study of structural and electronic properties of $\beta - Ta2O5$ and $\delta - Ta2O5$". In: *Phys. Rev. B* 69.16 (Apr. 2004), p. 165202. DOI: 10.1103/PhysRevB.69.165202.

Salpeter, E. E. and H. A. Bethe. "A Relativistic Equation for Bound-State Problems". In: *Phys. Rev.* 84 (6 Dec. 1951), pp. 1232–1242. DOI: 10.1103/PhysRev.84.1232. URL: http://link.aps.org/doi/10.1103/PhysRev.84.1232.

Scanlon, David O. and Aron Walsh. "Bandgap engineering of ZnSnP2 for high-efficiency solar cells". In: *Appl. Phys. Lett.* 100 (2012), p. 251911.

Schilling, Heikko et al. "gamma-TaON: A metastable polymorph of tantalum oxynitride". In: *Angew. Chem.-Int. Edit.* 46.16 (2007), p. 2931.

Scholl, Jonathan A., Ai Leen Koh, and Jennifer A. Dionne. "Quantum plasmon resonances of individual metallic nanoparticles". In: *Nature* 483.7390 (Mar. 22, 2012), pp. 421–427. URL: http://dx.doi.org/10.1038/nature10904.

Schuck, P. James. "Nanoimaging: Hot electrons go through the barrier". In: *Nat Nano* 8.11 (Nov. 2013), pp. 799–800. URL: http://dx.doi.org/10.1038/nnano.2013.228.

Schuller, Jon A. et al. "Plasmonics for extreme light concentration and manipulation". In: *Nat Mater* 9.3 (Mar. 2010), pp. 193–204. URL: http://dx.doi.org/10.1038/nmat2630.

Shalaev, Vladimir M. et al. "Light-induced kinetic effects in solids". In: *Physical Review B* 53.17 (May 1, 1996), pp. 11388–11402. URL: http://link.aps.org/doi/10.1103/PhysRevB.53.11388.

Shelah, Saharon. "Note on a min-max problem of Leo Moser". In: *Journal of Combinatorial Theory* 6 (1969), pp. 298–300.

— "Stable theories". In: *Israel Journal of Mathematics* 7 (1969), pp. 187–202.

Shin, Hyunho et al. "Defect energy levels in Ta(2)O(5) and nitrogen-doped Ta(2)O(5)". In: *J. Appl. Phys.* 104 (2008), p. 116108.

Shockley, W. and H. J. Queisser. In: *J. Appl. Phys.* 32 (1961), p. 510.

Shockley, William and Hans J. Queisser. "Detailed Balance Limit of Efficiency of p-n Junction Solar Cells". In: *Journal of Applied Physics* 32.3 (1961), pp. 510–519.

Singh, R. et al. "Phase separation in InGaN thick films and formation of InGaN/GaN double heterostructures in the entire alloy composition". In: *Applied Physics Letters* 70.9 (1997), pp. 1089–1091.

Sobhani, Ali et al. “Narrowband photodetection in the near-infrared with a plasmon-induced hot electron device”. In: *Nat Commun* 4 (Mar. 27, 2013), p. 1643. URL: http://dx.doi.org/10.1038/ncomms2642.

Song, P., P. Nordlander, and S. Gao. “Quantum mechanical study of the coupling of plasmon excitations to atomic-scale electron transport”. In: *J Chem Phys* 134.7 (Feb. 2011), p. 074701.

Souza, Ivo, Nicola Marzari, and David Vanderbilt. “Maximally localized Wannier functions for entangled energy bands”. In: *Phys. Rev. B* 65 (3 Dec. 2001), p. 035109. DOI: 10.1103/PhysRevB.65.035109. URL: http://link.aps.org/doi/10.1103/PhysRevB.65.035109.

Stanley, Ross. “Plasmonics in the mid-infrared”. In: *Nat Photon* 6.7 (July 2012), pp. 409–411. URL: http://dx.doi.org/10.1038/nphoton.2012.161.

Stevanovi ć, Vladan et al. “Correcting density functional theory for accurate predictions of compound enthalpies of formation: Fitted elemental-phase reference energies”. In: *Phys. Rev. B* 85 (11 2012), p. 115104.

Sundararaman, Ravishankar et al. “Theoretical Predictions for Hot-carrier Generation from Surface Plasmon Decay”. In: *Nat. Commun.* 5 (5788 Apr. 2014). DOI: 10.1038/ncomms6788. URL: http://dx.doi.org/10.1038/ncomms6788.

— “Theoretical predictions for hot-carrier generation from surface plasmon decay”. In: *Nat Commun* 5 (Dec. 16, 2014). URL: http://dx.doi.org/10.1038/ncomms6788.

Sundararaman, R. et al. *JDFTx*. http://jdftx.sourceforge.net. 2012.

Sweatlock, Luke A. “Plasmonics: Numerical Methods and Device Applications”. PhD thesis. California Institute of Technology, 2008.

Takahashi, Yukina and Tetsu Tatsuma. “Solid state photovoltaic cells based on localized surface plasmon-induced charge separation”. In: *Applied Physics Letters* 99.18 (Oct. 31, 2011), pp. 182110–3. URL: http://dx.doi.org/10.1063/1.3659476.

Tame, M. S. et al. “Quantum plasmonics”. In: *Nat Phys* 9.6 (June 2013), pp. 329–340. URL: http://dx.doi.org/10.1038/nphys2615.

Tame, M. S. et al. “Single-Photon Excitation of Surface Plasmon Polaritons”. In: *Physical Review Letters* 101.19 (Nov. 7, 2008), pp. 190504–. URL: http://link.aps.org/doi/10.1103/PhysRevLett.101.190504.

Tassin, Philippe et al. "A comparison of graphene, superconductors and metals as conductors for metamaterials and plasmonics". In: *Nat Photon* 6.4 (Apr. 2012), pp. 259–264. URL: http://dx.doi.org/10.1038/nphoton.2012.27.

Thomann, Isabell et al. "Plasmon Enhanced Solar-to-Fuel Energy Conversion". In: *Nano Letters* 11.8 (Aug. 2011), pp. 3440–3446. DOI: 10.1021/nl201908s. URL: http://dx.doi.org/10.1021/nl201908s.

Van de Walle, C. G. and Neugebauer J. In: *J. Appl. Phys.* 95 (2004), p. 3851.

Walsh, Aron et al. "Nature of the Band Gap of $In_2O_3$ Revealed by First-Principles Calculations and X-Ray Spectroscopy". In: *Phys. Rev. Lett.* 100 (16 2008), p. 167402.

Walter, Michael G. et al. "Solar Water Splitting Cells". In: *Chem. Rev.* 110.11 (2010), p. 6446.

Wang, Fuming and Nicholas A. Melosh. "Plasmonic Energy Collection through Hot Carrier Extraction". In: *Nano Letters* 11.12 (2011). PMID: 22023372, pp. 5426–5430. DOI: 10.1021/nl203196z. eprint: http://dx.doi.org/10.1021/nl203196z. URL: http://dx.doi.org/10.1021/nl203196z.

— "Plasmonic Energy Collection through Hot Carrier Extraction". In: *Nano Letters* 11.12 (2013/07/23 2011), pp. 5426–5430. DOI: 10.1021/nl203196z. URL: http://dx.doi.org/10.1021/nl203196z.

— "Power-independent wavelength determination by hot carrier collection in metal-insulator-metal devices". In: *Nat Commun* 4 (Apr. 16, 2013), p. 1711. URL: http://dx.doi.org/10.1038/ncomms2728.

Wang, Shuzhi and Lin-Wang Wang. "Atomic and Electronic Structures of $GaN/ZnO$ Alloys". In: *Phys. Rev. Lett.* 104.6 (2010), p. 065501.

Warwick, Tony et al. "A new bend-magnet beamline for scanning transmission X-ray microscopy at the Advanced Light Source". In: *Journal of Synchrotron Radiation* 9.4 (July 2002), pp. 254–257. DOI: 10.1107/S0909049502005502. URL: http://dx.doi.org/10.1107/S0909049502005502.

Wehner, P. S. et al. "Valence-band structure of silver along $\Lambda$ from angle-resolved photoemission". In: *Phys. Rev. B* 19 (12 June 1979), pp. 6164–6171. DOI: 10.1103/PhysRevB.19.6164. URL: http://link.aps.org/doi/10.1103/PhysRevB.19.6164.

Wei, Su-Huai. In: *Comp. Mater. Sci.* 30 (2004), p. 337.

Wei, S.-H. et al. “Electronic properties of random alloys: Special quasirandom structures”. In: *Phys. Rev. B* 42 (15 Nov. 1990), pp. 9622–9649. DOI: 10.1103/PhysRevB.42.9622. URL: http://link.aps.org/doi/10.1103/PhysRevB.42.9622.

Welch, Adam W. et al. “Self-regulated growth and tunable properties of CuSbS2 solar absorbers”. In: *Solar Energy Materials and Solar Cells* 132 (2015), pp. 499–506. ISSN: 0927-0248. DOI: http://dx.doi.org/10.1016/j.solmat.2014.09.041. URL: http://www.sciencedirect.com/science/article/pii/S0927024814005297.

White, Thomas P. and Kylie R. Catchpole. “Plasmon-enhanced internal photoemission for photovoltaics: Theoretical efficiency limits”. In: *Applied Physics Letters* 101.7, 073905 (2012), pages. DOI: http://dx.doi.org/10.1063/1.4746425.

— “Plasmon-enhanced internal photoemission for photovoltaics: Theoretical efficiency limits”. In: *Applied Physics Letters* 101.7 (Aug. 13, 2012), pp. 073905–4. URL: http://dx.doi.org/10.1063/1.4746425.

— “Plasmon-enhanced internal photoemission for photovoltaics: Theoretical efficiency limits”. In: *Applied Physics Letters* 101.7, 073905 (2012), pages. DOI: http://dx.doi.org/10.1063/1.4746425. URL: http://scitation.aip.org/content/aip/journal/apl/101/7/10.1063/1.4746425.

Wyckoff, R. W. G. In: *Crystal Structures Vol. 1, Second Edition, Wiley & Sons* (1963).

Yan, Jun, Karsten W. Jacobsen, and Kristian S. Thygesen. “Conventional and acoustic surface plasmons on noble metal surfaces: A time-dependent density functional theory study”. In: *Phys. Rev. B* 86 (24 Dec. 2012), p. 241404. DOI: 10.1103/PhysRevB.86.241404. URL: http://link.aps.org/doi/10.1103/PhysRevB.86.241404.

Yashima, Masatomo, Yungi Lee, and Kazunari Domen. “Crystal structure and electron density of tantalum oxynitride, a visible light responsive photocatalyst”. In: *Chem. Mat.* 19.3 (2007), p. 588.

Yeh, J.J. and I. Lindau. “Atomic subshell photoionization cross sections and asymmetry parameters: $1 \leq Z \leq 103$”. In: *Atomic Data and Nuclear Data Tables* 32.1 (1985), pp. 1–155. ISSN: 0092-640X. DOI: http://dx.doi.org/10.1016/0092-640X(85)90016-6. URL: http://www.sciencedirect.com/science/article/pii/0092640X85900166.

Zhang, Hui and Alexander O. Govorov. “Optical Generation of Hot Plasmonic Carriers in Metal Nanocrystals: The Effects of Shape and Field Enhancement”. In: *The Journal of Physical*

*Chemistry C* 118.14 (Apr. 2014), pp. 7606–7614. DOI: 10.1021/jp500009k. URL: http://dx.doi.org/10.1021/jp500009k.

Zhang, S. B. et al. "Defect physics of the CuInSe2 chalcopyrite semiconductor". In: *Phys. Rev. B* 57.16 (1998), p. 9642.

Zia, Rashid and Mark L. Brongersma. "Surface plasmon polariton analogue to Young's double-slit experiment". In: *Nat Nano* 2.7 (July 2007), pp. 426–429. URL: http://dx.doi.org/10.1038/nnano.2007.185.

Ziman, J. M. *Principles of the Theory of Solids*. Cambridge University Press, 1964.

Zuloaga, J., E. Prodan, and P. Nordlander. "Quantum description of the plasmon resonances of a nanoparticle dimer". In: *Nano Lett.* 9.2 (Feb. 2009), pp. 887–891.

Zunger, Alex et al. "Special quasirandom structures". In: *Phys. Rev. Lett.* 65 (3 July 1990), pp. 353–356. DOI: 10.1103/PhysRevLett.65.353. URL: http://link.aps.org/doi/10.1103/PhysRevLett.65.353.